REPUBLIC OF TURKEY
YILDIZ TECHNICAL UNIVERSITY
GRADUATE SCHOOL OF SCIENCE AND ENGINEERING

PREDICTION OF RESPONSE AND DAMAGE IN REINFORCED CONCRETE JOINTS THROUGH ARTIFICIAL INTELLIGENCE TECHNIQUES

Mehmet Ozan YILMAZ

DOCTOR OF PHILOSOPHY THESIS
Department of Civil Engineering
Program of Structural Engineering

Supervisor
Prof. Dr. Serkan BEKİROĞLU

July, 2023

REPUBLIC OF TURKEY
YILDIZ TECHNICAL UNIVERSITY
GRADUATE SCHOOL OF SCIENCE AND ENGINEERING

PREDICTION OF RESPONSE AND DAMAGE IN REINFORCED CONCRETE JOINTS THROUGH ARTIFICIAL INTELLIGENCE TECHNIQUES

A thesis submitted by Mehmet Ozan YILMAZ in partial fulfillment of the requirements for the degree of **DOCTOR OF PHILOSOPHY** is approved by the committee on 24.07.2023 in Department of Civil Engineering, Program of Structural Engineering.

Prof. Dr. Serkan BEKİROĞLU
Yildiz Technical University
Supervisor

Approved By the Examining Committee

Prof. Dr. Serkan BEKİROĞLU, Supervisor
Yildiz Technical University _____

Assoc. Prof. Dr. Murat Serdar KIRÇIL, Member
Yıldız Technical University _____

Assoc. Prof. Dr. Ahmet Anıl DİNDAR, Member
Gebze Technical University _____

Assoc. Prof. Dr. Çağrı MOLLAMAHMUTOĞLU, Member
Yıldız Technical University _____

Assoc. Prof. Dr. Sadık Can GİRGİN, Member
Dokuz Eylül University _____

I hereby declare that I have obtained the required legal permissions during data collection and exploitation procedures, that I have made the in-text citations and cited the references properly, that I haven't falsified and/or fabricated research data and results of the study and that I have abided by the principles of the scientific research and ethics during my Thesis Study under the title of Prediction of Response and Damage in Reinforced Concrete Joints Through Artificial Intelligence Techniques supervised by my supervisor, Prof. Dr. Serkan BEKİROĞLU. In the case of a discovery of false statement, I am to acknowledge any legal consequence.

Mehmet Ozan YILMAZ

Signature

Dedicated to my beloved family

ACKNOWLEDGEMENTS

I would like to express my deepest gratitude and appreciation to all those who have contributed to the completion of this doctoral thesis. It is with their support, guidance, and encouragement that I have been able to accomplish this significant milestone in my academic journey.

First and foremost, I am immensely grateful to my supervisor, Professor Serkan Bekiroğlu. Your guidance, expertise, and unwavering support throughout this research project have been invaluable. Your constructive feedback, insightful discussions, and dedication to excellence have shaped me into a better researcher. I am grateful for the opportunities you provided me to grow intellectually and for your constant encouragement to pursue innovative ideas.

I am also indebted to the members of my thesis committee, Associate Professor Murat Serdar Kırçıl and Associate Professor Ahmet Anıl Dindar. Your invaluable feedback, suggestions, and critical insights have greatly enriched my research work. I am grateful for the time and effort you invested in evaluating my thesis and for the constructive discussions that have contributed to its refinement.

I extend my heartfelt appreciation to my colleagues and fellow researchers at Yıldız Technical University. Their stimulating discussions, collaborative spirit, and willingness to share knowledge have played a vital role in shaping my research ideas. I am thankful for the friendly and supportive environment that fostered intellectual growth and made this journey enjoyable.

I am grateful to the staff members at the Department of Civil Engineering for their assistance and cooperation throughout my studies. Their prompt administrative support, technical assistance, and willingness to go the extra mile have been instrumental in facilitating the smooth progress of my research.

I would like to express my deep gratitude to my family for their unwavering love, encouragement, and belief in my abilities. Their constant support, understanding, and patience have been a source of strength throughout my academic pursuits. I am truly grateful for their sacrifices and the countless ways they have stood by me.

Last but not least, I want to acknowledge the countless researchers, authors, and scholars whose work has laid the foundation for my research. I am indebted to the contributions of those who have dedicated their lives to advancing knowledge in my field of study. Their insights, discoveries, and publications have shaped my understanding and inspired me to embark on this research journey.

In conclusion, the completion of this thesis would not have been possible without the support and contributions of all those mentioned above, as well as many others who have played a part in my academic and personal development. While it is not possible to name everyone individually, please know that your influence has made a significant impact on my journey, and for that, I am eternally grateful.

Mehmet Ozan YILMAZ

TABLE OF CONTENTS

LIST OF SYMBOLS

a_i^l	activation of neuron i in layer l
A_{jh}	Joint area in horizontal direction (mm2)
A_c	Column cross-sectional area (mm2)
b_i^l	bias term of neuron i in layer l
b_b	Beam width (mm)
b_c	Column width (mm)
b_j	Joint width (mm)
c	Nonlocal interaction range parameter (mm2)
c_j	Center of jth radial basis function
D	Hardening material constant
d_{max}	Maximum historic deformation demand
d_{mic}	Total damage parameter
d_{mic}^c	Compressive damage parameter
d_{mic}^t	Tensile damage parameter
d_{min}	Minimum historic deformation demand
E	Modulus of elasticity (MPa)
e	Eccentricity (mm)
f_{bc}	Biaxial compressive strength (MPa)
f_{by}	Beam reinforcement yielding strength (MPa)
f_{ct}	Concrete tensile strength (MPa)
f_{uc}	Uniaxial compressive strength (MPa)
f_{ut}	Uniaxial tensile strength (MPa)
f_{yb}	Yielding strength of beam reinforcement (MPa)

f_{yc}	Yielding strength of column reinforcement (MPa)
f_{yj}	Joint reinforcement yielding strength (MPa)
f_{yj}	Yielding strength of joint reinforcement (MPa)
f_c	Compressive strength of the concrete material (MPa)
G^{mic}	Shear modulus in microplane scale
h_b	Beam height (mm)
h_c	Column height (mm)
K^{mic}	Bulk modulus in microplane scale
k_0, k_1, k_2	Elastic microplane damage surface parameters
m	Over-nonlocal averaging parameter
n	Normalized axial force
n_b	Neumann boundary normal vector
Q	plastic potential
R	Ratio between the major and minor axes of the cap
R_T	Tension cap hardening constant
r_w	Split weight factor
v	Normalized axial force
$v_{j,c}$	compressive normalized joint shear strength (MPa)
$v_{j,t}$	tensile normalized joint shear strength (MPa)
V_{jh}	Horizontal joint shear force (kN)
V_{jv}	Vertical joint shear force (kN)
v_j	Joint shear strength (MPa)
V_j	Joint shear strength (kN)
w_{ji}^l	weight connecting neuron i in layer l-1 to neuron j in layer l
α	Joint aspect ratio
α^{mic}	Maximum degradation rate
$\alpha_1 - \alpha_4$	Experimental fit parameters for degradation in stiffness and strength
β^{mic}	Damage rate
β_c	Compression damage evolution constant

β_t	Tension damage evolution constant
γ	Shear factor in joint zone
γ^{mic}	Maximum history equivalent strain
γ_{c0}	Compressive strain damage threshold
γ_{t0}	Tensile strain damage threshold
γ_0	Equivalent strain threshold for damage initialization
$\gamma_A - \gamma_E$	Joint shear strain values corresponding to points A - E
$\gamma_I - \gamma_V$	Joint shear strain values corresponding to points I - V
δ_{lim}	Maximum possible damage index value
ϵ_{el}	Elastic strain in decomposed total strain
ϵ_{pl}	Plastic strain in decomposed total strain
ϵ_D	Deviatoric strain in decomposed total strain
ϵ_s	Total strain in reinforcement
ϵ_V	Deviatoric strain in decomposed total strain
ϵ_y	Yielding strain of reinforcement material
η_m	local variable
κ	plastic strain
κ_{cm}	plastic strain value at peak strength
κ_{cr}	critical plastic strain threshold
λ	plastic strain increment
μ_{ce}	Bond strength in compression in elastic regime (MPa)
μ_{cp}	Bond strength in compression in post-yield regime (MPa)
μ_{te}	Bond strength in tension in elastic regime (MPa)
μ_{tp}	Bond strength in tension in post-yield regime (MPa)
ν	Poisson's ratio
ξ	vector of internal variables that effect yielding surface
ρ_b	Beam longitudinal reinforcement ratio
ρ_c	Column longitudinal reinforcement ratio
ρ_j	Joint transverse reinforcement ratio

σ	Normal stress (MPa)
σ_{II}	Second principle stress (MPa)
σ_{I}	First principle stress (MPa)
σ_{V}^{c}	Intersection point abscissa between compression cap and Drucker-Prager yield function (MPa)
σ_{y}	stress value at yielding surface (MPa)
τ	Shear stress (MPa)
$\tau_{A} - \tau_{E}$	Joint shear stress values corresponding to points A - E (MPa)
$\tau_{I} - \tau_{V}$	Joint shear stress values corresponding to points I - V (MPa)
ϕ	Radial basis function
Ω_{c}	Yield function in compression
Ω_{ci}	Onset of nonlinear hardening
Ω_{cr}	Normalized strength when critical plastic strain exceeded

LIST OF ABBREVIATIONS

MCFT	Modified Compression Field Theory
ANN	Artificial Neural Network
FFNN	Feed-Forward Neural Network
GRNN	Generalized Regression Neural Network
RBFN	Radial Basis Function Network
LHS	Latin Hypercube Sampling
PBSD	Performance Based Seismic Design
PSHA	Probabilistic Seismic Hazard Analysis
NSGA	Non-dominated Sorting Algorithm
FEM	Finite Element Method
RC	Reinforced Concrete
CPT	Coupled Pore-Pressure-Thermal
IP	Identification Parameter
MD	Measured Data
RNN	Recurrent Neural Network
MLP	Multilayer Perceptron
SOM	Self Organizing Networks
LSTM	Long Short-Term Memory
GRU	Gated Recurrent Unit
GA	Genetic Algorithm
MSE	Mean Squared Error
APDL	ANSYS Parametric Design Language
MPC	Multi-point constraint

LIST OF FIGURES

LIST OF TABLES

ABSTRACT

Prediction of Response and Damage in Reinforced Concrete Joints Through Artificial Intelligence Techniques

Mehmet Ozan YILMAZ

Department of Civil Engineering
Doctor of Philosophy Thesis

Supervisor: Prof. Dr. Serkan BEKİROĞLU

The modern approach to design of earthquake resistant reinforced concrete structures is based on predictable ductile failure of structures. The most basic principle in the operation of the ductile damage mechanism is to maintain the redistribution of plastic strains in beams under earthquake effects up to ductility levels that can meet high displacement demands. The design of columns to be stronger than beams in terms of bearing capacity has been introduced in order to ensure that plastic deformations occur in beams and has been accepted as the strongest guarantee of the aforementioned damage mechanism in many cases. In addition, it has been accepted in the analysis and design that the joints of reinforced concrete beams-columns, where large shear forces are transmitted, do not produce nonlinear deformations.

It is clear that the occurrence of nonlinear deformations in the joint regions is an obstacle to the ductile response of the frame. In recent years, some experimental studies have shown that nonlinear reactions may develop in frame members where these conditions are met, as well as in joints where the conditions set forth by modern codes are not met. This situation reveals the necessity of taking into account the nonlinear deflections occurring in the joints in the calculations performed both in the evaluation of existing structures and in the design of new structural systems.

In the literature, the models proposed for the prediction of internal forces and deformations under cyclic effects in joint regions can be categorised into two different

main groups. The first one is the models in which the results of a limited number of experimental studies, each with different experimental conditions, are used in calibration and the so-called super-elements, which are formed by one or more uniaxial springs are used. The second class of models is the plane and space models in which concrete and reinforcement are represented using more advanced finite element and constitutive relations. Both model classes are studied, and the reasons they are not commonly used in practical structural engineering evaluation and design applications are revealed.

It has been evaluated that the ability of the super-elements presented in the literature to simulate with acceptable approximation the nonlinear strain responses of a given reinforced concrete column-beam joint region under cyclic effects is directly related to the a priori estimation of the unidirectional incremental rotation-shear force relationship of the relevant reinforced concrete column-beam region. Due to this, two distinct models have been introduced which take the fundamental physical variables of any joint region sample as input and estimate shear strain-stress. The first one is an advanced artificial neural network model that utilises the results of experimental studies reported in the literature. A second prediction model, which serves the same purpose, is constructed by nonlinear regression between shear strain-stress relationships obtained from numerical simulation models using advanced finite element techniques and physical variables related to the joint region. Utilizing a non-dominated sorting genetic algorithm, scalars based on the joint type have been proposed to estimate the reduction in strength and stiffness of reinforced concrete column-beam joints under cyclic effects.

Keywords: reinforced concrete joints, nonlinear finite element analysis, artificial neural networks, genetic algorithm

ÖZET

Betonarme Birleşim Bölgelerinde Tepki ve Hasarın Yapay Zekâ Teknikleri Kullanılarak Tahmini

Mehmet Ozan YILMAZ

İnşaat Mühendisliği Anabilim Dalı
Doktora Tezi

Danışman: Prof. Dr. Serkan BEKİROĞLU

Depreme dayanıklı betonarme yapı tasarımda çağdaş yaklaşım, yapıların öngörülebilir sünek hasar alması üzerine kurulmuştur. Deprem etkileri altında plastik şekildeğiştirmelerin kirişlerde oluşarak yeniden dağılımın, yüksek yerdeğiştirme taleplerini karşılayabilecek süneklik seviyelerine kadar sürdürülebilmesi sünek hasar mekanizmasının çalıştırılmasındaki en temel ilke olarak görülebilir. Kolonların taşıma gücü bakımından kirişlerden daha güçlü olarak tasarlanması, plastik şekildeğiştirmelerin kirişlerde oluşmasını sağlamak amacıyla ortaya konmuş ve birçok durumda anılan hasar mekanizmasının en güçlü güvencesi olarak kabul edilmiştir. Bunun yanında, çözümlemede ve tasarımda, büyük kesme kuvvetlerinin aktarıldığı betonarme kiriş-kolonların birleşim bölgelerinin doğrusal olmayan şekildeğiştirmeler yapmadığı kabul görmüştür.

Birleşim bölgelerinde doğrusal olmayan şekildeğiştirmelerin oluşumunun, çerçevenin sünek tepkiler oluşturmasının önünde bir engel olduğu açıktır. Son yıllarda deneysel olarak gerçekleştirilen bazı çalışmalarda, çağdaş yönetmeliklerce ortaya konan şartların sağlanmadığı birleşimlerin yanında, bu koşulların sağlandığı çerçeve elemanlarında da doğrusal olmayan tepkilerin gelişebileceğine dair sonuçlara ulaşmıştır. Bu durum, gerek mevcut yapıların değerlendirilmesinde, gerekse yeni taşıyıcı sistemlerin tasarlanmasında yapılan hesaplarda birleşim bölgelerinde oluşan doğrusal olmayan şekildeğiştirmelerin gözönüne alınması gerekliliğini ortaya koymaktadır.

Literatürde, birleşim bölgelerinde çevrimsel etkiler altında oluşan iç kuvvet ve şekildeğiştirmelerin kestirim için ortaya konan modeller iki farklı temel sınıfta incelenebilir. Bunlardan ilki, her biri farklı deney koşullarına sahip sınırlı sayıda deneysel çalışmaya ait sonuçların kalibrasyonda kullanıldığı ve tek eksende çalışan bir veya birden fazla yayın bir araya gelerek oluşturduğu süper-eleman olarak adlandırılan elemanların kullanıldığı modellerdir. İkinci sınıf ise, betonun ve donatının kıyasla daha gelişmiş sonlu eleman ve bünye bağıntıları kullanılarak temsil edildiği, düzlemde ve uzayda oluşturulan modellerdir. Her iki sınıftaki modeller incelenerek, yapı mühendisliğinde pratik değerlendirme ve tasarım uygulamalarında yer bulmamalarında etkili olduğu değerlendirilen nedenler ortaya konmuştur.

Yapılan irdelemelerde, literatürde ortaya konmuş süper-elemanların, çevrimsel etkiler altındaki belli bir betonarme kolon-kiriş birleşim bölgesine ait doğrusal olmayan şekildeğiştirme tepkilerine kabul edilebilir yaklaşıklıkta benzetim kurabilme yetisinin, ilgili betonarme kolon-kiriş bölgesinin tek yönlü artımsal dönme-kesme kuvveti ilişkisinin önsel kestirimi ile doğrudan ilintili olduğu değerlendirilmiştir. Bu sebeple, herhangi bir birleşim bölgesi örneğini tanımlayan temel fiziksel değişkenleri girdi olarak kabul eden ve kayma şekil değiştirme-gerilme kestirimi yapan iki farklı model ileri sürülmüştür. Bunlardan ilki, literatürde sonuçları raporlanmış deneysel çalışmaların sonuçlarından faydalanan bir gelişmiş yapay sinir ağları modelidir. Aynı amaca hizmet eden ikinci bir kestirim modeli, güncel sonlu eleman tekniği kullanılarak oluşturulan sayısal benzetim modellerinden elde edilen kayma şekildeğiştirme-gerilme ilişkileri ile birleşim bölgesine ilişkin fiziksel değişkenler arasında yapılan doğrusal olmayan regresyon yoluyla oluşturulmuştur. Betonarme kolon-kiriş birleşim bölgelerinin çevrimsel etkiler altında dayanımda ve rijitlikte gösterdiği azalımın tahmini için ise baskın olmayan sıralama genetik algoritmayı kullanan bir kestirim modeli ortaya konmuştur.

Anahtar Kelimeler: betonarme birleşim bölgeleri, doğrusal olmayan sonlu eleman çözümlemesi, yapay sinir ağları, genetik algoritma

1
INTRODUCTION

1.1 Research Background

Performance-Based Seismic Design (PBSD) is an advanced engineering approach, that aims to achieve a desired level of structural performance and reliability under seismic loading. This methodology grounded in probabilistic seismic hazard analysis and structural response assessment, provides a comprehensive framework for addressing the complex interactions between ground motion, structural behavior and damage potential. By integrating both qualitative and quantitative aspects, PBSD allows for efficient and sustainable designs that are tailored to specific performance objectives and risk tolerance levels. The Structural Engineering Association of California [1] made an effort to establish a relationship between performance levels and the anticipated damage in the overall building, while simultaneously correlating these performance levels and seismic hazards with a triad of performance objectives (see Figure 1.1).

The initial stage involves the identification and quantification of seismic hazards pertinent to the site under consideration. Probabilistic Seismic Hazard Analysis (PSHA) is typically employed to estimate the likelihood of different levels of ground motion occurring at the site over a specified time period. The methodology generates a hazard curve which represents the relationship between ground motion intensity and

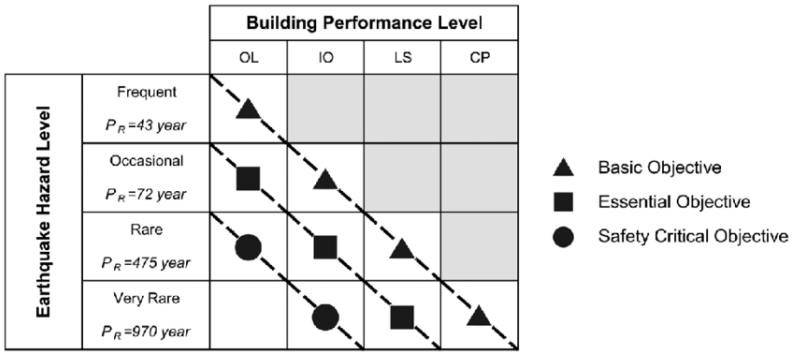

Figure 1.1 Performance levels defined in SEAOC [1]

the corresponding annual rate of exceedance. In the following stage, the structural system response to the defined seismic hazard is analysed using appropriate analytical models. Structural analysis methods can be linear or nonlinear depending on the desired accuracy and complexity. The final component entails evaluating the structural performance under different seismic demand scenarios [2]. This evaluation is based on predefined performance objectives which are typically categorized into operational, life safety, and collapse prevention levels. By comparing the structural response to these objectives, engineers can determine if the design meets the desired performance criteria. In case of non-compliance, an iterative design process is undertaken until the objectives are satisfied.

A crucial aspect of PBSD is the development of performance-based acceptance criteria, which involve the establishment of performance levels and corresponding limit states. These criteria are essential for quantifying structural damage and for ensuring that the design meets the intended risk tolerance. The selection of appropriate performance levels and limit states is guided by factors such as building occupancy, structural importance, and societal expectations.

The methodology underpinning Performance-Based Seismic Design (PBSD) is predicated on the assumption that structural members should adhere to ductile behavior criteria. This ductility allows for the redistribution of forces and increased energy dissipation, ultimately enhancing the overall seismic performance of the structure. However, it is important to recognize the inherent brittleness of beam-column joints, which arises due to the substantial shear forces they are subjected to during seismic events [3]. This brittle nature presents a challenge in reconciling the ductile behavior objectives of PBSD with the actual behavior of joints, necessitating careful consideration and innovative design solutions to ensure adequate performance under seismic loading.

A significant challenge concerning reinforced concrete joints emerges when conducting performance assessments of existing buildings. It has been observed that a considerable number of these structures lack appropriate reinforcement detailing. Consequently, they are prone to joint failures, which can lead to substantial structural damages. This underscores the need for diligent evaluation and retrofitting strategies to mitigate potential hazards in such buildings.

Following the February 2023 earthquakes in Turkey and Syria, post-earthquake investigations revealed significant damage not only in older buildings with inadequate reinforcement detailing in joint regions, but also in more recent reinforced concrete frames. Yılmaz *et al.* [4] reported that joint failure was evident in

Figure 1.2 Joint failure in a building built in mid-2000s from Samandağ, Hatay [4]

numerous buildings constructed in compliance with contemporary seismic design requirements. Interestingly, only a subset of these structures displayed discernible faulty workmanship. This finding highlights the need to reevaluate current seismic design standards and construction practices to ensure greater structural resilience. In addition to field observations, there is a large amount of experimental evidence indicating that deformations of both reinforced and unreinforced joints can control the response of reinforced concrete frames [5–11].

The ACI318-71 [12] building code was the first to recommend transverse reinforcement within the joint core for regions with high seismic activity. However, Park and Paulay (1973) argued that the provisions set forth in [12] were insufficient. Subsequently, numerous studies in the field prompted the development of ACI352-76 [13], which put forth a design guideline for beam-column joints. This guideline introduced new criteria, such as moment strength ratio, shear strength, confinement, and development length within the joint region, in order to achieve the necessary strength and ductility [14].

Joint design in structural engineering primarily follows an approach that involves maintaining joint dimensions within a specified range to reduce the acting shear stress and ensure the provision of adequate reinforcement, which serves to confine the concrete material in the core region [15]. The load transmission mechanism is typically idealized as a concrete compression strut and reinforcement truss in proximity to the joint core [16]. Furthermore, the force couple that forms the bending moment at the joint face is transmitted to the joint core via bond force between the concrete material and the reinforcement.

However, there are inconsistent findings concerning the critical factors influencing

the actual stress state in the joint core [17, 18]. This may suggest that the prevailing design approach may be an oversimplification of the complex behavior of joint regions. Although this analogy might yield safe designs when the acting internal forces are predicted accurately, it neglects non-linear inelastic deformations and the intricate stress state present within the joint region, potentially limiting its applicability in certain cases.

Numerous experimental studies conducted in recent decades, as well as post-earthquake investigations, have underscored the need to reevaluate the role of reinforced concrete joints within the framework of performance-based design and assessment methodologies [3, 19]. The advancements in modern technology, including sophisticated finite element analysis and soft computing techniques, offer promising opportunities to facilitate this reevaluation process.

The idealization of the joint region should be scrutinized using state-of-the-art techniques, such as advanced finite element analysis, to better understand and represent their behavior under seismic loading. A comprehensive assessment of the factors influencing joint seismic performance is necessary for designing more resilient structures [16]. Consequently, it is essential to establish and incorporate well-defined limits for joint elements in the evaluation of their performance.

Additionally, it is crucial to examine the uncertainties arising from the omission of joint inelastic deformations and their impact on the overall structural system and load redistribution [20]. By addressing these concerns, the field of earthquake engineering can develop more accurate and reliable methodologies for designing and assessing the seismic performance of reinforced concrete structures.

1.2 Objective and Scope

The primary goal of the research is to advance the understanding of reinforced concrete joint modelling by thoroughly examining existing numerical methods and identifying areas for improvement. For this purpose, the research is aimed to develop novel approaches that facilitate the integration of joint inelastic deformations into performance-based design and assessment processes. To accomplish this, the creation of a prediction model for shear strain-stress behavior that accurately reflects the complex deformation states in the joint region is intended, drawing upon experimental results from the literature. In an effort to minimize reliance on experimental data, an alternative prediction model using finite element simulations will also be developed.

Recognizing the significance of strength and stiffness deterioration due to cyclic effects

associated with strong ground motions, the thesis will further aim to create the other prediction model for these specific parameters.

1.3 Hypothesis

Employing an optimized artificial neural network architecture will enable the development of a model that accurately estimates the shear strain-stress behavior of reinforced concrete joints using their physical properties as input parameters. Parametric finite element models, when subjected to monotonic simulations up to severe damage conditions, will validate the microplane material and element formulation against experimental results. From this, a secondary predictive model for joint shear strain-stress relationships can be derived from regression analysis of the finite element outcomes.

The use of the genetic algorithm and Non-dominated Sorting Genetic Algorithm II (NSGA-II) will effectively assess the hysteresis model parameters necessary for estimating strength and stiffness degradation due to cyclic loads.

Finally, integrating these predictive models will significantly enhance our understanding of the seismic performance of reinforced concrete structures.

1.4 Organization of the Thesis

The thesis is organized into a rational sequence of chapters, beginning with a comprehensive literature review in Chapter 2. This chapter provides an in-depth exploration of current modelling techniques for reinforced concrete joints, including spring-based elements, advanced finite element formulations, hysteresis models, artificial intelligence fundamentals, and applications in structural engineering and joint modelling. The chapter also covers calibration of joint models and fragility curves of reinforced concrete frames and joints. Chapter 3 delves into the finite element implementation of the joint super-element model, outlining the assumptions regarding material behavior, hysteresis models, and calibration of joint parameters and introduction the object oriented simulation framework used in simulations. The focus of this chapter is the development of a practical super-element model for use in structural engineering applications. Chapter 4 introduces the artificial neural network models employed for the development of the prediction model for joint deformation characteristics. In Chapter 5, the thesis examines the use of 2D and 3D finite element analysis for joint simulation, presenting a description of the finite element models generated within the scope of the research and the results obtained from the analyses.

Chapter 6 proposes a methodology to calibrate fit-to-experiment parameters of a commonly used hysteresis model and aims to provide insight for the nature of these parameters to reduce dependency to the experimentation. In this chapter, results from the prediction models proposed in Chapter 4 and Chapter 5 are used and their efficiency are indirectly tested. Finally, Chapter 7 presents a discussion of the findings, shedding light on the implications of the results and offering suggestions for further research on the subject.

2
LITERATURE REVIEW

The increasing loss due to seismic events around the world in recent decades has emphasized the need to design earthquake-resistant structures, a concept that has garnered significant interest from engineers. This research focuses on examining the behavior of reinforced concrete (RC) joints under quasi-static cyclic and seismic loading. Cutting-edge methods are utilized to adjust the model parameters necessary for numerical simulations, assess different stages of structural damage, and determine seismic fragility curves for various structural performance levels. As part of this investigation, an extensive literature review has been carried out, offering a thorough summary of the current state-of-the-art and key findings, which are explored in the sections that follow.

Over the past several decades, there has been a comprehensive investigation into understanding the behavior of joints under seismic conditions, utilizing a variety of methods including experimental, statistical, analytical, and numerical approaches. Within this chapter, a presentation of general definitions related to the concepts utilized in the thesis is provided while referencing the relevant contemporary literature.

2.1 Analytical Definition on RC Joint Problem

Joints within reinforced concrete frames are characterized as the spatial region encompassing the depth of the deepest beam connecting to the column. These joints are classified according to ACI352-R02 [21] into three categories: interior, exterior, and corner, as depicted in Figure 2.1. In order to analyze the internal forces of a reinforced concrete space frame subjected to lateral effects in orthogonal directions, the beams framed to the column can be subdivided into plane frame beams (represented by the color blue in Figure 2.1) and transverse beams (represented by the color white in Figure 2.1). Considering the influence of transverse beams on the stress distribution within the joint region as confinement [22], the number of joint region

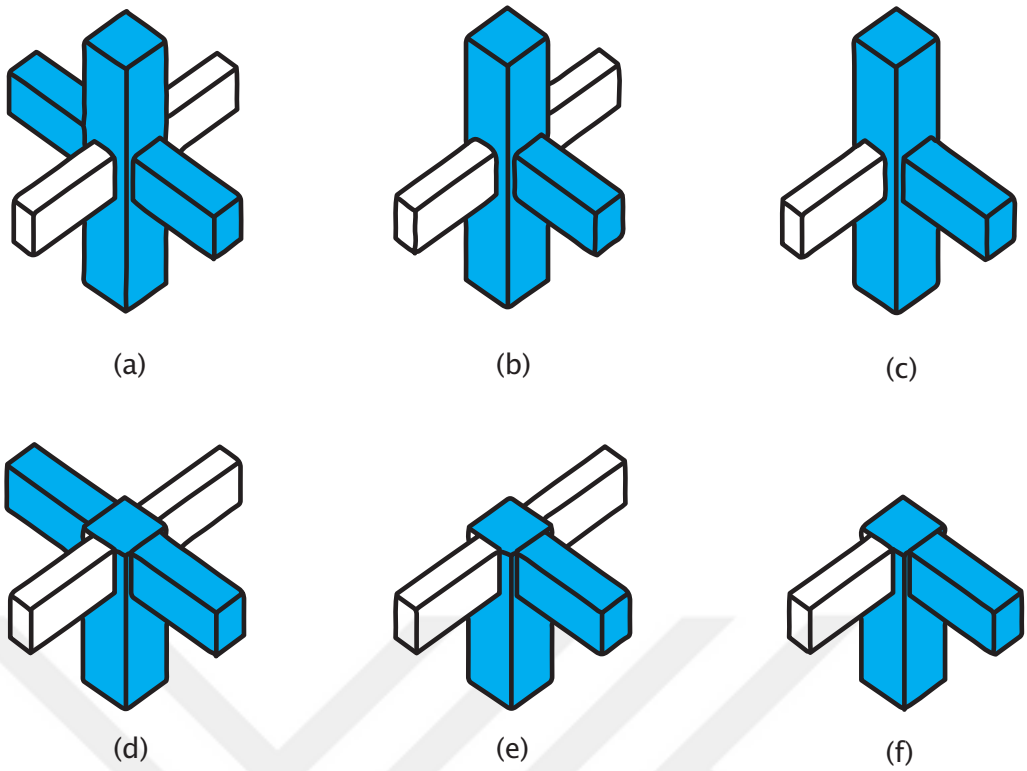

Figure 2.1 Joint types according to ACI352-R02 [21]: (a) interior, (b) exterior, (c) corner, (d) roof-interior, (e) roof-exterior, (f) roof-corner

types defined by ACI352-R02 [21] can be minimized. In the existing literature, it is commonly observed that the joint regions are analyzed as interior (Figure 2.1.(a)-(d)), exterior (Figure 2.1.(b)-(c)), and knee (Figure 2.1.(e)-(f)) types in nearly all studies. Consequently, the investigations conducted within the scope of this study align with this established classification framework.

The considerable forces and performance requisites imposed on these joints necessitate an enhanced comprehension of their seismic behavior. These forces engender intricate mechanisms encompassing bond and shear interactions within the joint. The first ever analytical effort to quantify joint response is carried out by W Hanson and W Conner [23] determined joint shear force through a free-body diagram from the mid-height section of the joint. Park and Paulay [24] postulated a strut-truss mechanism includes a concrete struts which sustains only compression to transfer shear forces and assumed to be formed in the potential failure plane. Paulay *et al.* [22] improved the compression strut approach which is formed in the diagonal direction between compression fields of beam and the column and tension forces are assumed to be carried by joint reinforcement at horizontal direction and column reinforcement at vertical direction. Vertical and horizontal reinforcement in the joint core region form a truss mechanism to contribute to the shear resistance. Horizontal and vertical forces transferred by bond form the beam and column flexural reinforcement are transmitted

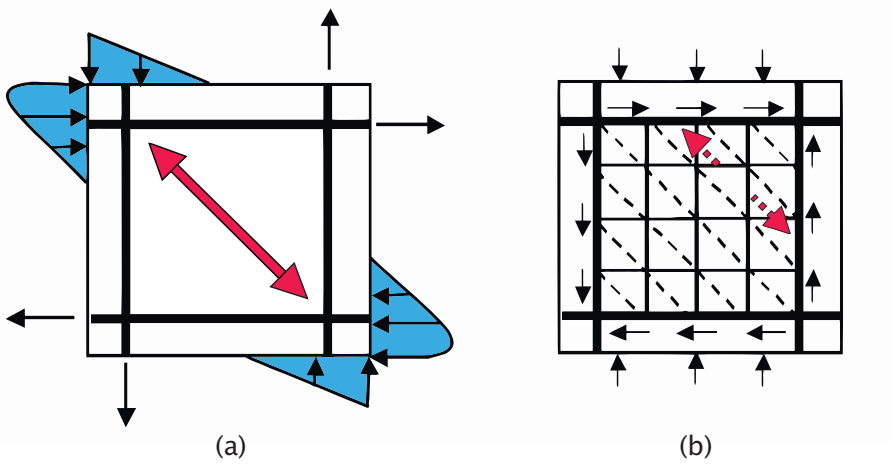

Figure 2.2 Joint shear resistance mechanisms: (a) concrete strut, (b) concrete truss (per Kim and LaFave [25])

to the core concrete. The shear resistance mechanisms idealized by Paulay *et al.* [22] are shown in Figure 2.2. In the existing literature, various versions of strut-tie models with minor adjustments are available, which are based on the traditional form of this approach.

In the out-of-plane direction, the torsional resistance of beams contributes to the shear stiffness of the joint region. Similarly, torsional strength also contributes to shear strength. The warping occurring in these beams causes a confinement effect in the joint region.

Hwang and Lee [26] proposed a softened strut-and-tie model capable of estimating the shear strength of reinforced concrete joints for both interior and exterior connections. The proposed softened strut-and-tie model adheres to the principles of mechanics, namely equilibrium, compatibility, and constitutive relations for cracked reinforced concrete. However, this version of the softened strut-and-tie model gives up the advantage of simplicity that is characteristic of traditional strut-and-tie models in order to adhere to these fundamental mechanical principles.

Murakami *et al.* [27] put forth a joint shear strength model exclusively for interior connections, lacking out-of-plane members and joint eccentricity. The model employed regression analysis to establish a joint shear strength model, taking into account the concrete compressive strength. FEMA356 [28] recommended an envelope curve for RC joint shear behavior, predominantly influenced by factors such as column axial load, joint transverse reinforcement quantity and spacing, out-of-plane geometry, and in-plane geometry. [29] introduced an analytical model to foresee joint shear behavior in both interior and exterior connections, by specifying plane strain conditions for the joint panel. They maintained that a joint panel's shear

resistance emanates from the bearing of beam and column compression zones, as well as from the bond between reinforcement and the surrounding concrete. Attaalla [30] offered an analytical equation to estimate joint shear strength for interior and exterior connections, developed from the assumption of a stress distribution around the joint panel satisfying equilibrium and taking into consideration a compression-softening phenomenon correlated with cracked reinforced concrete. The parameters included in the proposed equation consisted of the axial force in the beam and column, joint reinforcement ratio in the longitudinal and transverse directions of the joint, and geometry. Russo and Somma [31] recently proposed a joint shear strength model solely for exterior connections, in the absence of out-of-plane members and joint eccentricity. Shiohara [32] proposed a mathematical model to determine the joint shear strength of interior, exterior, and knee connections. In this suggestion, the so-called "quadruple flexural resistance" within a joint panel played an important role in defining joint shear failures. Joint shear strength was determined from satisfying force equilibrium in four rigid segments within the joint panel. They chose a deterministic model, comprising the contribution of vertical stress transmitted by the column, longitudinal beam reinforcement, and passive confinement of the joint due to transverse reinforcement. Tsonos [8] suggested a shear strength model contingent on concrete compressive strength and joint aspect ratio, grounded in the concrete material model put forward by Scott *et al.* [33].

Kamimura *et al.* [18] also claimed that joint shear strength is not significantly affected by the joint transverse reinforcement. Bonacci and Pantazoupoulou [17] reported the same result on axial load effect while had opposite findings on the joint transverse reinforcement. Joh *et al.* [34] claimed that the most influential factor is the compressive strength of the concrete after a large experimental examination on 75 setups.

Tsonos [8] carried out an experimental and analytical study on beam-column joints. He concluded shear strength values given by design codes are based on Paulay *et al.* [22] and yields to overestimations. Tsonos [8] summarized the load transfer mechanism and determination of shear strength of a joint region via following formulation. The summation of vertical forces equals the vertical joint shear force V_{jv}

$$V_{jv} = D_{cy} + D_{sy} = D_{cy} + (T_1 + ...T_4) \tag{2.1}$$

where subindice T_i denotes forces acting on longitudinal steel bars and D_{cy} is the compression strut in vertical direction. In horizontal direction joint shear force V_{jh}

$$V_{jh} = D_{cx} + D_{sx} = D_{cx} + (D_{1x} + ... + D_{vx}) \tag{2.2}$$

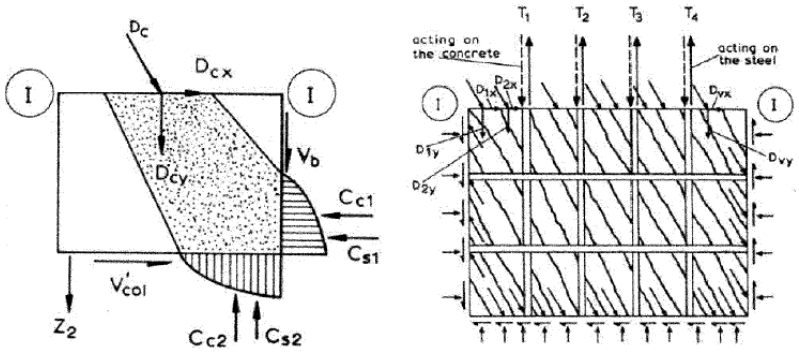

Figure 2.3 Forces acting on joint core concrete through strut and truss mechanism

Scheme shown in Figure 2.3 shows the forces acting on joint core region. Vertical normal compressive stress σ and shear stress τ uniformly distributed over the plane are given by

$$\sigma = \frac{V_{jv}}{h'_c b'_c} \tag{2.3}$$

$$\tau = \frac{V_{jh}}{h'_c b'_c} \tag{2.4}$$

where h'_c and b'_c denotes the length and the width of joint core respectively. Following relationship given in 2.5 between σ and τ can be established.

$$\sigma = \frac{V_{jv}}{V_{jh}} \times \tau \tag{2.5}$$

It has been shown that

$$\frac{V_{jv}}{V_{jh}} = \frac{h_b}{h_c} = \alpha \tag{2.6}$$

where α is the joint aspect ratio. Concrete biaxial strength curve is represented by a fifth-degree parabola as a function of increased joint concrete compressive strength due to confinement and first and second principle stresses; thus σ and τ.

$$-10\frac{\sigma_I}{f_c} + (\frac{\sigma_{II}}{f_c})^5 = 1 \tag{2.7}$$

Substituting Eq. 2.5 into Eq. 2.7 and using $\tau = \gamma\sqrt{f_c}$ gives following expression

$$\left[\frac{\alpha}{2\sqrt{f_c}}\left(1+\sqrt{1+\frac{4}{\alpha^2}}\right)\right]^5+\frac{5\alpha\gamma}{\sqrt{f_c}}\left[\sqrt{1+\frac{4}{\alpha^2}}-1\right]=1 \tag{2.8}$$

Assuming here

$$x=\frac{\alpha\gamma}{2\sqrt{f_c}} \tag{2.9}$$

and

$$\psi=\frac{\alpha\gamma}{2\sqrt{f_c}}\sqrt{1+\frac{4}{\alpha^2}} \tag{2.10}$$

Eq. 2.8 can be transformed into

$$(x+\psi)^5+10\psi-10x=1 \tag{2.11}$$

The solution of system of Eq. 2.11 gives the ultimate shear strength $\tau=\gamma\sqrt{f_c}$.

Over recent decades, advancements in finite element technology have built upon earlier analytical studies to facilitate a more comprehensive understanding of complex stress states within reinforced concrete joints. This progression has led to research utilizing springs with varying deformation capabilities, membrane elements and truss analogy. A detailed presentation of such research can be found in Section 2.3.

2.1.1 Code recommendations

In design specifications, it is generally assumed that the joints will not undergo any inelastic strain, as mentioned in the previous section. Therefore, the design process is strength-based and the shear forces assumed to occur in the joint zone, which do not exceed the shear strengths recommended by the specifications, may be considered sufficient for the joint zone to be considered safe.

Within the parameters of ACI352-R02 [21], as well as ASCE41-17 [35] the shear strength of the joint is ascertained by utilizing Equation 2.12

$$V_n=\gamma\sqrt{f_c}b_j h_c \tag{2.12}$$

where γ is the shear factor for the joint zone, f_c is the compressive strength of the concrete, b_j is the effective width of the joint zone as determined by the column and beam width; and h_c is the depth of the column. The shear factor functions as

a coefficient subject to variation, dependent on confinement of the joint by transverse beams. It is worth to note that ACI318-19 [36] adopts an analogous methodology for both external and knee-type joint zones, without discerning between the two. In Turkish Design Code [37], joint shear strength is defined in a similar fashion described in ACI352-R02 [21] with alterations in the coefficient takes into account the effect of the transverse beams.

AIJ1999 suggested Equation 2.14 to determine the joint shear strength.

$$V_j = k\phi F_j b_j D_j \tag{2.13}$$

$$F_j = 0.8 \times (f_c)^{0.7} \tag{2.14}$$

The coefficient k pertains to the geometric properties of the joint region in the plane, while the coefficient ϕ relates to the joint region's out-of-plane geometry. The concrete compressive strength coefficient, F_j, is determined using Equation 2.14, and the effective joint zone width, b_j, is dependent on the widths of the column and beam while D_j is the column depth or beam reinforcement anchorage length.

EC8 [38], the draft code to supercede EC8 [39], the principle stress criterion is employed to evaluate joint strength by assuming that the joint volume is in a plane stress condition. Equation 2.15 defines the joint stress by incorporating the reinforcement ratio ρ_{sh} between joint horizontal transverse reinforcement and beam longitudinal reinforcement ratio, the normalized axial force denoted as ν and f_{ct}, concrete tensile strength.

$$\tau_p = f_c \sqrt{\left(\nu\rho_{sh} + \frac{f_{ct}}{f_c}\right)\left(\nu + \frac{f_{ct}}{f_c}\right)} \tag{2.15}$$

Presuming that ρ_{sh} is equal to zero for an unreinforced joint, the tensile normalized joint shear strength, denoted as ν_{jt}, can be derived from Equation 2.16. Similar to the process employed for extracting Equation 2.16, Mohr's Circle is utilized to find out the compressive normalized joint shear strength, which is expressed in Equation 2.17. In this context, η represents a reduction factor that accounts for the negative impact of transverse tensile strains.

$$v_{j,t} = \frac{f_{ct}}{\sqrt{f_c}} \sqrt{1 + \frac{\nu f_c}{f_{ct}}} \tag{2.16}$$

$$v_{j,c} = \eta \frac{f_c}{\sqrt{f_c}} \sqrt{1 - \frac{\nu}{\eta}} \tag{2.17}$$

Similar to EC8 [38], NZSEE-17 [40] describes strength with respect to shear stress, as expressed in Equation 2.15, which assumes the utilization of the principal stress method for assessing joint shear strength. Meanwhile, the normalized shear strength for tensile and compressive forces is presented in Equations 2.16 and 2.17, respectively. Within these equations, k_j serves as an empirical coefficient that accommodates the increased strength of the interior joint relative to the exterior, as well as the strength reduction at a prescribed ductility level as noted by Hakuto *et al.* [3].

$$v_j = \frac{f_c}{6\alpha} \frac{f_{yj} A_{jh}}{f_{by} A_s^*} \tag{2.18}$$

$$v_{j,t} = \frac{0.85}{\sqrt{f_c}} \sqrt{(k_j \sqrt{f_c})^2 + k_j \sqrt{f_c} \nu f_c} \tag{2.19}$$

$$v_{j,c} = \frac{0.85}{\sqrt{f_c}} \sqrt{(0.60 f c)^2 - 0.6 f_c^2 \nu} \tag{2.20}$$

Unlike the strength-based approaches, in FEMA356 [28] and later ASCE41-17 [35], the nonlinear response of the joint zones is described as rotation and the corresponding generalised force, enabling the consideration of their effects on the behaviour of the structural system in nonlinear static and dynamic analysis procedures.

While the inclusion of joint regions as distinct structural elements within the FEMA356 [28] regulations represents a notable advancement, allowing for the consideration of these elements' deformations in the analysis of structural systems under seismic impacts and the evaluation of their plastic rotations as damage in the performance-based design process, a deficiency in the rational underpinnings of the modeling parameters and acceptance criteria has been identified. For non-linear dynamic procedure, complete hysteresis representation of each component is suggested including stiffness and strength deterioration. Kim and LaFave [25] highlighted that modelling parameters and acceptance criteria may alter significantly

than proposed in the code depending on the physical parameters defining the joint. This shortcoming hinders the approach from serving a restrictive and determinative function in earthquake specifications applied across seismically active regions worldwide.

2.2 Experimental Studies on RC Joint Testing

Since the early 1970s, it can be said that a significant portion of the scientific research conducted on reinforced concrete joint regions has been on an experimental basis. Although recent studies have focused on retrofitting joint regions with different materials and applications, many of the experimental studies aim to interpret the responses of the joint region under stress and deformation levels that can cause damage, which can also be considered as the main objective of this study. Within the scope of this study, the experiments conducted on only non-retrofitted specimens in both classes were examined, and the data obtained from these experiments were included in the databases used in the study.

By examining load transfer and damage mechanisms in joint regions, some pioneering studies of their time are presented chronologically, attempting to convey the historical development of experimental studies in identifying factors affecting the strength and deformation properties of joint regions.

Joint shear demand was identified as a crucial parameter in determining if a joint will exhibit brittle failure under earthquake loading by Higashi and Ohwada [41]. Minimal lateral confinement of the joint and an increase in joint shear strength are provided by interior column bars, as found by Meinheit and Jirsa [42]. They also concluded that column axial load influences shear cracking stress magnitude and shear crack inclination in the beam-column joint but not joint shear strength, and shear strength is not a linear function of joint hoop reinforcement volume.

It was concluded by Birss [43] that the joint load transfer mechanism, proposed by Paulay *et al.* [22], is satisfactory for design, and the beam-column joint region remains within the elastic regime when beam hinges are relocated away from the column face. Beckingsale [44] observed that specimens with low column axial load failed due to bar-slip, while specimens with higher column axial loads did not. The development of the two joint load-transfer mechanisms proposed by Paulay *et al.* [22] was also confirmed.

Improved joint behavior resulted from relocating beam plastic hinges away from the face of the joint, as found by Park and Milburn [45]. The conclusion of Otani *et al.* [46]

was that the number of column middle reinforcements doesn't significantly affect joint response. However, the joint shear failure behavior can be improved by increasing joint hoop steel and reducing joint shear stress demand.

The importance of joint transverse reinforcement for maintaining ductility levels in reinforced concrete beam-to-column connections was determined by Durrani and Wight [47]. They also found that joint shear stress significantly influences seismic performance. More hoops with lower yield strength improve seismic performance, as discovered by Ehsani and Wight [48]. They also concluded that when the moment strength ratio (M_r) is greater than 1.4, plastic hinges in the joint are prevented or prolonged.

Restrictions on beam bar diameter through the joint, joint shear stress demand, and minimum lateral reinforcement in the joint region were suggested by Kitayama *et al.* [49]. Their conclusions also stated that column axial load ratios below 0.3 do not exhibit a beneficial effect on bond resistance along beam reinforcement within the joint region, and those below 0.5 do not influence joint shear strength.

Endoh *et al.* [50] concluded that strength loss in post-peak load-deformation response was more significant for lightweight concrete compared to normal strength concrete. Additionally, they found that joint shear strengths of lightweight concrete were smaller due to reduced compressive strength.

Interior frames were discovered to have higher displacement ductility compared to exterior frames by Fujii and Morita [51]. Their conclusions also stated that column axial load ratio does not impact joint shear strength, an increase in joint transverse reinforcement ratio enhances joint shear capacity, and degradation of shear rigidity accelerates once joint shear strain reaches 0.5%.

It was observed by Joh *et al.* [34] that higher joint transverse reinforcement ratios reduce bond deterioration of longitudinal beam bars in the joint. Additionally, they noted that a large volume of transverse joint reinforcement can enhance joint stiffness after cracking and prevent bond deterioration by relocating the beam plastic hinge. Ductility was found to increase with higher joint hoop reinforcement and axial loads by Kaku and Asakusa [52]. Factors affecting bond behavior, such as column axial load, transverse reinforcement in the connection region, and the ratio of bottom beam reinforcement to top bar amount, were identified by Kaku and Asakusa [53]. They also found the anchorage length of beam bars to be significant. Ehsani and Alameddine [54] discovered that high concrete compressive strength results in higher shear capacity but lower ductility.

Noguchi and Kashiwazaki [55] found that maximum joint shear strength did not increase significantly with higher concrete compressive strength. They also discovered that the confinement effect of joint lateral reinforcement became significant only at large deformation levels, specifically drift angles exceeding 1/50 rad. Joint shear capacity was found to increase with higher concrete compressive strength and percentage of longitudinal reinforcement in beams by Oka and Shiohara [56], but the relationship was not linear.

In tests on two interior beam-column-slab connection subassemblies, Guimaraes *et al.* [57] observed that joint shear strength is a function of approximately the square root of concrete compressive strength. Hayashi *et al.* [58] developed a model relating bond strength to bar slip for beam longitudinal reinforcing steel, showing that both beam bar bond and joint shear stress demand play roles in joint failure under earthquake loading.

The ultimate shear strength of the joint panel and the shear panel envelope were successfully predicted using a proposed empirical equation by Teraoka *et al.* [59]. Walker [60] found that joints maintain strength and adequate stiffness when drift demand is under 1.5% and shear stress is under $10\sqrt{f_c}$ psi, where f_c represents concrete compressive strength. Column interior bars were concluded to be necessary for low axial load ratios by Park and Ruitong [61], who also recommended limiting the diameter of longitudinal bars in interior beam-column joints to reduce bond stress demand.

Zaid [62] confirmed conclusions of Shiohara [63] that the lever arm distance between tension and compression forces at the joint perimeter changes with loading, indicating that joint shear stress cannot be assumed to be proportional to the story shear. Pantelides *et al.* [64] found that joint shear strength capacities were approximately 8 % higher for specimens with higher axial load, and specimens with an axial load of $0.1f_cA_c$ dissipated about 20 % more energy than those with $0.25f_cA_c$ axial load.

Attaalla [30] concluded that using joint shear strength as a function of the square root of concrete compressive strength is an inappropriate measure of shear demand for joints with high-strength concrete.

The existing literature reports some contradictory or inconsistent findings on the behavior of reinforced concrete joints, which may be attributed to variations in the sampling space of the specimens examined, boundary conditions, reinforcement arrangements, and loading protocols across experimental studies. However, it is widely accepted that certain parameters, such as concrete compressive strength, beam longitudinal area and yield strength, column longitudinal reinforcement area, joint

transverse reinforcement area, and column axial load, have a significant impact on the response of the joints [65].

2.3 Numerical Studies on RC Joint Modelling

From the 1970s to the early 2000s, analytical and experimental investigations on joint regions have led to the evolution of models used to calculate the response of joint regions under earthquake effects, from strut-tie models exemplified within analytical models to more complex deformation mechanisms that can be numerically expressed in finite element solutions.

2.3.1 Super-element models

In the design of reinforced concrete (RC) frames, it is customary to assume rigid joints regardless of the detailing provided as it is discussed in Chapter 1. However, this assumption may not always hold true, particularly when evaluating the seismic performance of non-ductile RC frames, as detailing deficiencies can lead to a substantial reduction in joint stiffness. Moreover, joint failure might precede the ultimate capacity attainment of adjoining beams and columns. Consequently, accurately modeling joint inelastic behavior is crucial when assessing the seismic performance of non-ductile RC frames, requiring the consideration of two primary mechanisms: the shear response of the joint core, and bond-slip of longitudinal beam bars.

Following the development of strut-tie models, various finite element formulations have emerged to integrate joint behavior into the global modeling of frames. A category of joint models, known as "super-elements," comprises solutions that incorporate collections of finite elements representing different load transmission mechanisms Cook *et al.* [66]. The aim of devising super-elements is to decrease the number of degrees of freedom in large-scale finite element method problems while preserving accuracy. By merging these elements, the number of degrees of freedom can be reduced compared to representing the problem domain with plane or space finite elements, significantly lowering computational costs.

In structural engineering, the prevailing practice involves using either centerline (Figure 2.4.a) or rigid (Figure 2.4.b) joints, both of which disregard the effects of joint flexibility [67]. El-Metwally and Chen [68] introduced one of the earliest models incorporating zero-length rotational spring elements, positioned at the intersection of beam and column members, to define the joint's inelastic behavior through a load-deformation response. This model, occasionally termed the scissors model

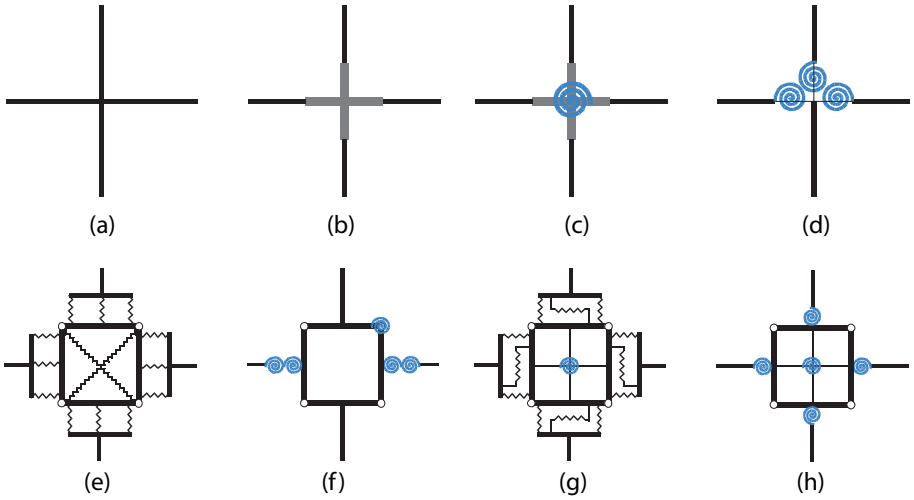

Figure 2.4 Spring-based super-elements used for joint modelling

without rigid joints, was later refined by Alath and Kunnath [69] and became known as the scissors model (Figure 2.4.c). While the cyclic response of the rotational spring was calibrated to experimental shear stress-strain data, the bond-slip mechanism was not considered.

Biddah and Ghobarah [70] employed distinct rotational springs to represent joint shear and bond-slip responses, defining the joint shear envelope using Hsu [71] softened truss model and calibrating bond-slip springs with experimental data (Figure 2.4.d). Youssef and Ghobarah [72] incorporated 12 translational springs forming a truss at the panel zone and introduced separate bar-slip mechanisms (Figure 2.4.e), calibrating each spring based on experimental findings.

Celik and Ellingwood [73] noted that the need for defining separate constitutive rules and the availability of experimental data limit the applicability of the element model. Shin and LaFave [74] proposed a joint element composed of hinged rigid links at the joint perimeter, a rotational spring embedded in a hinge forming a panel zone, and rotational springs at the member ends representing the bond-slip mechanism (Figure 2.4.f).

More recently, Lowes and Altoontash [16] introduced a continuum-type element combined with transition interface elements for compatibility with beam-column line elements (Figure 2.4.g). This model explicitly simulates three inelastic joint mechanisms: (i) a rotational spring for the joint core's shear response, (ii) eight bar-slip springs for bond failure in longitudinal bars within beams and columns, and (iii) four interface-shear springs to model shear load transfer loss at beam-joint and column-joint interfaces due to concrete crushing. Despite offering high control over various inputs, the model's drawback is increased computational effort and limited

availability of detailed response models for specific components (e.g., bond-slip). Consequently, Altoontash [75] simplified the Lowes and Altoontash [16] model, resulting in the commonly referred Joint2D model (Figure 2.4.h). Joint2D includes a rotational spring for joint core shear deformations and four zero-length rotational springs at beam-joint and column-joint interfaces to model the bond-slip behavior of longitudinal beam and column bars. Both the Lowes and Altoontash [16] model and Altoontash [75] model have been implemented in OpenSEES [76].

In the models proposed by Lowes and Altoontash [16] and Altoontash [75], the strain behaviour of the finite element representing the joint region as a panel is assigned by the Modified Compression Field Theory developed by Vecchio and Collins [77]. Shear stress-strain envelope of the panel zone was approximated with Modified Compression Field Theory and stiffness/strength deterioration properties were assigned through experimental data provided by [78].

The Modified Compression Field Theory (MCFT) is a model for evaluating the load-deformation response of cracked reinforced concrete under shear stress [38]. It considers concrete stresses in principal directions and reinforcing stresses, which are assumed to be axial. The MCFT model treats cracked concrete as a distinct material with empirically determined stress-strain behavior, potentially deviating from traditional stress-strain curves. The model takes into account average strains and stresses, which encompass local strains at cracks, strains between cracks, stresses between and at cracks. The validity of this assumption depends on including multiple cracks when determining average behavior. Mitra and Lowes [79] stated that the use of MCFT is not suitable especially for joints where transverse reinforcement is limited and proposed another strut-tie based model.

In the estimation of shear stress-deformation characteristics at joint regions, the simplifications made by strut-tie based understandings have proven to be inadequate in reflecting the stress conditions formed under earthquake effects within the joint region. Consequently, the models proposed in this field rely more on the examination of various experimental studies using statistical methods rather than on mechanistic approaches.

The backbone curve, shown in Figure 2.5, is typically characterized by four key points Celik and Ellingwood [73]. Point τ_1 signifies the shear stress at cracking, while points τ_2 and τ_3 correspond to the shear stress in the joint when beams or columns reach their yield and ultimate capacities, respectively, with both values limited by the joint's shear strength. Point τ_4 represents the residual strength, and the associated gamma (γ) values indicate shear strain. The combined effects of the joint panel's

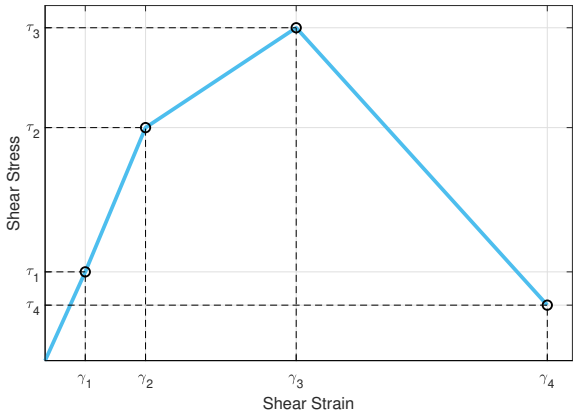

Figure 2.5 Multi-linear definition of shear strain - shear stress envelope for spring-based super-elements used for joint modelling

shear response and bar-slip of the lower longitudinal beam bars are integrated into a single stress-strain relationship. Bar-slip is considered by diminishing the yield and ultimate moment capacities of the beam under positive bending, utilizing a reduction factor obtained from extensive experiments. To ascertain stress values for points two and three, it is essential to identify the nature of joint failure: whether hinges develop in the beams or column or if the joint shear strength is reached preceding the adjoining members attaining their yield and ultimate capacities.

The backbone curve determination necessitates defining angular shear strain values for key shear stress values, which dictates the joint's deformation response Park and Mosalam [80]. Literature primarily focuses on joint shear stress capacity rather than deformation capacity. For primary lateral load-resisting systems, a 20% reduction in peak strength is typically used to define joint failure; however, this may be too conservative for secondary structural systems. Experimental testing on non-ductile joints generally ceases upon observing significant joint damage and lateral load-carrying capacity loss. Lower strain limits exhibit relatively constant joint strain, implying shear strain values are less impacted by joint detailing Park and Mosalam [80]. Park and Mosalam [81] noted joint aspect ratio's influence on joint shear strain response, and Jeon *et al.* [82] found exterior joints have lower deformation capacity compared to interior joints, also accounting for bar-slip effects on exterior joints' deformation response.

Hassan [83] and Hassan and Moehle [84] investigated the response of joints lacking transverse reinforcement up to axial load failure, focusing solely on exterior joints. They reported that the residual capacity of the joint at significant damage should be considered as 70-80% of its peak capacity. Moreover, the maximum recommended shear strain for the positive envelope (when the bottom beam bars experience tension)

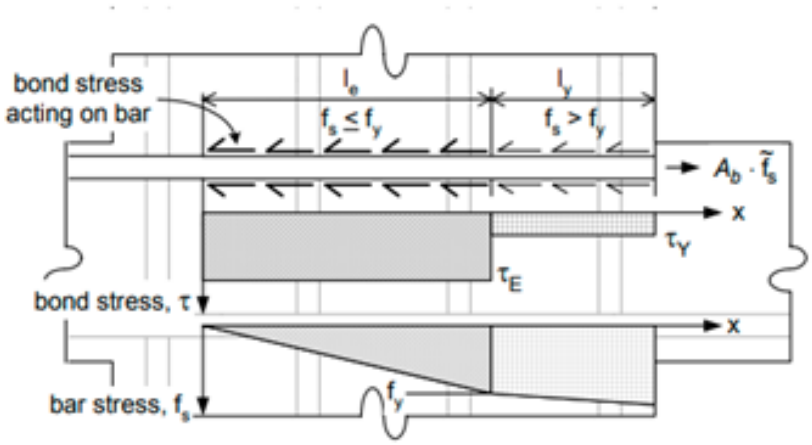

Figure 2.6 Illustration of bond stress across the anchored bar in joint [16]

Table 2.1 Average bond stresses for anchorage-zone

Notation	μ_{avg}	Steel Strain	Description
μ_{te}	$2\sqrt{f_c}$	$0 < \epsilon_s \leq \epsilon_y$	Tension in elastic regime
μ_{tp}	$0.5\sqrt{f_c}$	$\epsilon > \epsilon_y$	Tension in post yield regime
μ_{ce}	$3.1\sqrt{f_c}$	$-\epsilon_y \leq \epsilon_s < 0$	Compression in elastic regime
μ_{cp}	$3.1\sqrt{f_c}$	$\epsilon_s < -\epsilon_y$	Compression in post yield regime

is 0.03. They also suggested that if axial load failure is of specific interest, the final point on the backbone curve could be extended to the shear strain corresponding to 50% of the joint's peak capacity.

Another crucial mechanism impacting joint subassemblage response is the bond-slip of the flexural reinforcement of the beams. Lowes and Altoontash [16] suggested a constitutive model to delineate the load-deformation history of bond-slip, employing uniaxial springs to simulate the inelastic anchorage zone response (see Figure 2.6). Accurate reporting of bar-slip data is scarce in experimental investigations, as it necessitates sophisticated instrumentation setups and the adoption of a definition for slip. Due to challenges in conducting experiments and observing bar-slip response in joints, experimental data is limited. Since available experimental results on bond-slip behaviour in frame joints are limited in the literature, anchorage-zone cyclic loading test results were used to define bar stress–slip envelope and cyclic deterioration properties. Average bond strength (μ_{avg}) values are established based on experimental data from Eligehausen *et al.* [85] and Eligehausen *et al.* [86]. Experimental evidence indicates bond stress deterioration after exceeding a slip limit. Assuming the concrete surrounding a beam longitudinal reinforcement bar anchored in a joint and stressed in tension does not exceed yield stress, it is considered to be in compression or tension with a defined crack width. Table 2.1 provides average bond stress values for various

steel strain states. In the models by Celik and Ellingwood [73] and Jeon *et al.* [82], the bond-slip mechanism is not explicitly considered but is incorporated in the shear response of the panel spring.

To extend the monotonic bar stress with respect to slip history cyclically, calibration of the unload-reload path and damage rules is required. Lowes and Altoontash [16] introduced a set of rules to complete the definition of the model.

1. The unloading stiffness is presumed to be the same as the elastic stiffness,
2. Residual bar stress is calculated by assuming a uniform residual bond stress of $0.15\sqrt{f_c}$,
3. The slip at which reloading transpires is considered to be one fourth of the maximum historical slip,
4. The force at which reloading occurs is estimated to be be one fourth of the force developed at the maximum historical slip, based on experimental data provided by Eligehausen *et al.* [85] and Hawkins *et al.* [87].

Experimental results provided by Ma *et al.* [88] indicated that as the cracks initiated at the joint faces, flexibility of the shear transfer mechanism increases. This mechanism is idealized with interface springs in the super-element definition. Walraven [89] remarked that unloading stiffness does not deteriorate as a function of loading history and reloading stiffness is approximately identical to the initial stiffness. Based upon these facts, in numerical studies conducted by Altoontash [75], Lowes *et al.* [90] and Mitra and Lowes [79], interface springs are assumed elastic and extremely stiff thus the contribution of the shear transfer mechanism to the overall response of the joint is neglected. However, calibration of the load transfer mechanism using experimental data is recommended by Lowes *et al.* [90], while remarking the lack of experimental data.

Lowes and Altoontash [16], Lowes *et al.* [90] and Mitra and Lowes [79] assumed a very stiff uniaxial elastic spring and ignored interface flexibility remarking the lack of available experimental data describing the phenomenon. Lowes *et al.* [90] stated that interface shear stiffness can significantly decrease with increasing crack width at beam end. All element models were validated through a set of experiments; however, it should be noted all element models require a calibration process using the varying level of data provided from the experiment itself. This fact makes the element formulations useful to model any particular unit with available experimental

data, but impractical for general use in design or performance assessment purposes when specific experimental data is not available.

The shear stress strain models proposed for the introduced models should be complemented by hysteretic response rules describing the characteristics such as loading, unloading, deterioration in strength and stiffness under cyclic effects. Studies on this subject are discussed in the next subsection.

Alternatively, Ning *et al.* [91] and Sengupta and Li [92] used Modified Bouc-Wen-Baber-Noori (BWBN) model to replicate experimental response of columns and joints respectively. Despite well-matched results after calibration through experiments; generalization of calibration process is quite complicated since BWBN models are defined with parameters that have little or no physical meaning.

2.3.2 Considerations on Hysteretic Response

For the definition of the response of any structural component to a cyclic effect, hysteretic behaviour including unloading and reloading features should be established. For reinforced concrete joint instance, pinching and degradation in stiffness and strength should be covered as well. These parameters indeed are dependent on the material properties, reinforcement configuration and geometry of the specimen of interest [93]. Nevertheless, relation between parameters required to generate one of the hysteretic models available in the literature and the mentioned physical properties is questionable [67].

Numerous hysteresis models have been proposed over the years, such as the Takeda model [94], Ibarra-Medina-Krawinkler Deterioration model [95], and Pinching4 model [16, 96]. Among these, the *pinching4* model, available as a uniaxial material model in OpenSEES, has gained popularity due to its versatility. Nonetheless, recent research has critiqued the *pinching4* model's practicality, as it necessitates defining 39 parameters for characterizing hysteretic behavior, prompting suggestions for alternative models with fewer required parameters [91]. A key advantage of the *pinching4* model is its ability to directly define four critical points for the positive and negative backbone, allowing for easy calibration of envelope responses in joints. In contrast, other available hysteretic models enable direct definition of only up to three critical points for the positive and negative envelope, often resulting in inaccurate initial stiffness estimations due to the simplification of using three points instead of four to define the backbone.

Lowes and Altoontash [16] suggested model parameters for cyclic response of

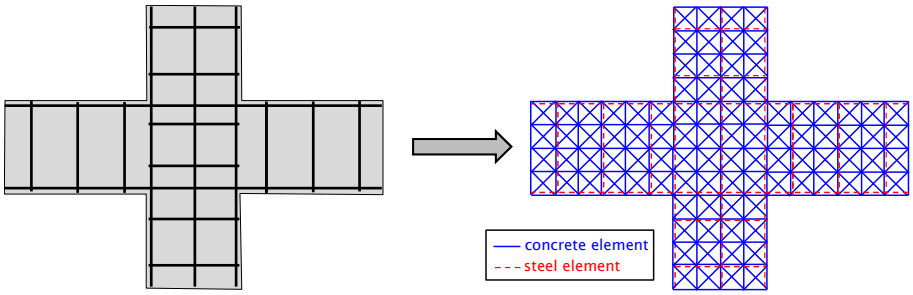

Figure 2.7 Truss analogy approach to model an interior joint [100]

pinching4 based on the experimental findings in [97] and [78]. Mitra and Lowes [79] proposed constant values for a set of parameters controlling hysteretic response of the pinching4 material and proposed empirical equations for degradation parameters based on the statistical evaluation of 57 sub-assemblages from 12 different experimental studies. Hysteretic parameters related to bond-slip spring response, in a similar fashion with the introduced in *pinching4* material, calibrated with the experimental results of the test carried out by Viwathanatepa *et al.* [98] and Stevens *et al.* [78]. Based on the investigation of the experimental results and analytical point of view introduced by Shiohara [99], Celik and Ellingwood [73] postulated an approach that is based on the reduction of joint strength due to poor bonding conditions. A further detailed discussion on the model parameters governing the pinching4 material is held in Section 3.2.1.1.

2.3.3 Nonlinear Truss Analogy

The truss analogy in the finite element method refers to a simplified approach used to analyze and design structural elements, such as beams, columns, or joints, subjected to various loading conditions like shear, flexure, and axial forces. In this approach, the structural elements are modeled as a series of interconnected truss elements, which are simple bar elements capable of resisting axial forces. Truss analogy simplifies the complexity of real structural behavior by assuming that the forces are distributed through the interconnected truss elements, which can deform only in the axial direction.

Research on truss-based modeling approaches has been conducted for the design and analysis of reinforced concrete (RC) members subjected to shear, flexure, and axial forces [101–103]. Panagiotou *et al.* [104] refined existing truss modeling methods by incorporating mesh size effects and biaxial effects for diagonal elements in compression. Moharrami *et al.* [105] further improved the truss model for the analysis of shear-critical RC columns, considering the contribution of aggregate interlock effects. Bowers [106] and Xing *et al.* [100] proposed a hybrid numerical model for

beam-column joints in non-ductile frames, including a nonlinear cyclic truss model for the connection region and a distributed plasticity model for beams and columns.

2.3.4 2D and 3D FE Analysis of RC Joints

The use of advanced constitutive and finite element formulations has become increasingly common in contemporary research and engineering applications, as they enable more accurate and robust analyses of complex material behavior. A comprehensive understanding of these formulations necessitates a solid foundation in plasticity theory, which serves as the cornerstone of many advanced material models, particularly for concrete and other quasi-brittle materials.

In this overview, the basic principles of plasticity theory and its utilization in concrete material modeling are to be briefly examined. Additionally, a review will be provided on the latest advancements that include damage-based models, improvements that have the potential to amplify the predictive proficiency of these models. Finally, recent instances of finite element analyses that are applied to reinforced concrete joints are to be illustrated, showcasing the proficiency of these cutting-edge constitutive models in encapsulating the intricate behavior of such structural elements.

2.3.4.1 Plasticity Theory Fundamentals

The theory of plasticity is commonly employed by researchers to characterize the behavior of materials that exhibit permanent deformations under the influence of external forces. However, concrete or similar materials possess unique characteristics that make them challenging to represent solely through plasticity theory. Despite these complexities, plasticity theory is still utilized to approximate the behavior of concrete, albeit with varying degrees of accuracy.

Plasticity was initially introduced for metals subjected to loading beyond their elastic limits, where deformation is proportional to the applied load. As the load surpasses the elastic limit, materials begin to exhibit plastic (irreversible) strains. Unlike metals, which maintain continuity until rupture, even with high levels of plastic strains, concrete is a composite material comprising aggregates of varying sizes and interstitial mortar, and tends to lose continuity more easily after only a portion of its strength limit is reached (due to cracking and crushing). Furthermore, in contrast to metals that harden after yielding, concrete softens after exceeding its strength limit, allowing lower stresses with increasing levels of plastic strains. Consequently, a plasticity model for concrete must be used in conjunction with a damage model to adequately represent its behavior.

In the literature, the definition of plasticity frequently commences with the decomposition of strains into two distinct components: elastic strains (ε_e) and plastic strains (ε_p).

$$\varepsilon = \varepsilon_{el} + \varepsilon_{pl} \tag{2.21}$$

The stress generated is directly proportional to the elastic strains, while plastic strains are assessed based on a specified yield criterion and flow rule.

$$\sigma = D\varepsilon_{el} \tag{2.22}$$

The yield criterion is a function that incorporates stress σ, and internal variables, denoted by ξ.

$$f(\sigma, \xi) = 0 \tag{2.23}$$

Function f represents a particular form of yield criterion for each plasticity model and gives a surface in stress space which an example is illustrated in Figure 2.8.(a)

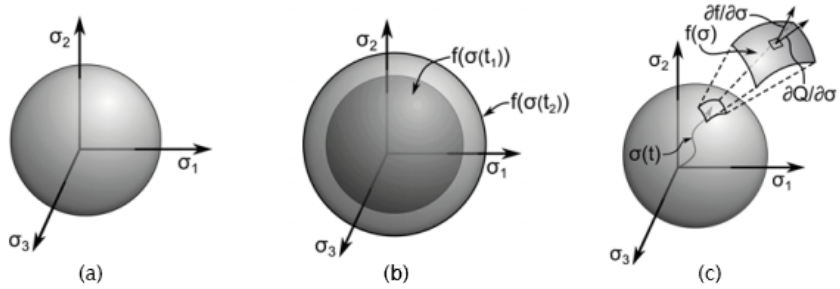

Figure 2.8 Illustration of (a) yield surface in stress space, (b) flow rule, (c) hardening (ANSYS 18.2 Material Reference

Yield condition, defines the stress states where the plastic strains occur. In elastic conditions, stress state in principle stress space is in the area or volume bounded by Equation 2.23. After reaching yield surface it is not possible for the material to produce higher levels of stress. Following conditions often referred as Karush-Kuhn-Tucker conditions must be satisfied in material behavior.

$$f \leq 0, \dot{\lambda} \geq 0, f\dot{\lambda} = 0 \tag{2.24}$$

where λ is plastic strain increment. This conditions force material to remain in *elastic region* ($\dot{\lambda} = 0$) when $f < 0$ is satisfied. If $f = 0$, stress state is reached to yield surface and increase in plastic strains ($\dot{\lambda} > 0$) are expected.

Material yielding decision must be independent of the coordinate system that the calculations performed. For isotropic materials, yield condition depends only on stress invariants (not necessarily all of them at once): trace of the stress tensor (I_1) and deviator invariants (J_2,J_3).

Once material starts to yield according to the condition given in Equation (2.24), amount and direction of the plastic strain increment should be determined. Evolution of plastic strains are determined by the following flow rule:

$$\dot{\varepsilon_{pl}} = \dot{\lambda}\frac{\partial Q}{\partial \sigma} \tag{2.25}$$

where Q is plastic potential which is again a scalar function. In most cases, plastic potential may be selected as the same function with the yield criterion. Plastic strain increment is normal to the yield surface as it is illustrated in Figure 2.8.(b).

The yield criterion is not defined by a constant surface but a function of a set of parameters and it is dependent on the history of loading and evolution of plastic strains. The increase in yield criterion is called hardening. Isotropic hardening which the stress state change from $\sigma(t_1)$ to $\sigma(t_2)$ as it is shown in Figure 2.8.(c) is defined in the form:

$$F(\sigma) - \sigma_y(\xi) = 0 \tag{2.26}$$

where $\sigma_y(\xi)$ is the stress limit that yielding starts.

Isotropic hardening is often useful under monotonic loading but often does not give realistic results for materials subjected to cyclic loads and plastic deformation after a load reversal from a plastic stress state. For this cases, kinematic hardening is introduced in the form

$$f(\sigma - \alpha, \xi) = 0 \tag{2.27}$$

where α is back stress tensor. Since softening phenomenon causes a decrease in strength/stiffness, it is a significant and relatively complex feature of concrete material modeling. A brief discussion about softening will be presented in the concrete

constitutive models.

In addition to analytical and experimental investigations, numerous numerical studies have employed finite element analysis as an approximation method for addressing the issue of joint behavior. The thesis focuses on the most accurate and up-to-date research in this domain. Generally, numerical solutions can be categorized into two primary groups: those utilizing frame, spring, and plane elements in their numerical models, and those implementing three-dimensional solid elements within the finite element analysis.

Nonetheless, it is crucial to acknowledge that endeavors employing solid models have frequently encountered inherent challenges related to the numerical representation of concrete material. Consequently, the loading conditions in these studies have predominantly remained monotonic, owing to the intricate nature of stress state evaluation. While this research does not delve into the results derived from numerical models, it does provide a comprehensive review of the modeling techniques employed.

Atta *et al.* [107] applied the concrete failure model proposed by William and Warnke (1975) utilizing ANSYS software to replicate the experimental study conducted by Scott [108]. Notably, even without specifying a bond rule between the concrete and reinforcement elements, a strong correlation with the experimental results was observed. A parametric investigation encompassing column axial load, reinforcement detailing, concrete strength, and beam dimensions was executed. The focus of the investigation remained on the strength basis, as the employed model demonstrated instability in instances where strength loss occurred within the concrete material. Subsequent to the emergence of tensile cracks, localized strains were not regularized via a smeared crack approach in this analysis, rendering the results dependent on the size of the finite elements and thus lacking objectivity. Additionally, it is important to highlight that the models under investigation did not exhibit abrupt strength loss attributable to a brittle failure mode; rather, they demonstrated a combination of beam and joint failure.

Mitra [65] employed a Drucker-Prager-based continuum formulation, utilizing DIANA 9.1 software, to simulate the response of an interior reinforced concrete joint. However, it was concluded that the simulation relies on an excessive number of parameters, many of which possess minimal or no physical significance, indicating that an enhanced comprehension of modeling parameters is necessary for the continuum formulation of any reinforced concrete structure. Furthermore, Mitra [65] observed that the continuum methodology is beset with convergence issues and necessitates a considerable amount of computational time and complexity. This underscores the

need for ongoing research to develop computationally stable and robust continuum methods for structural analysis in this domain.

Allam *et al.* [109] performed finite element analysis utilizing concrete damage plasticity (CDP), a modified version of the Drucker-Prager formulation, implemented through ABAQUS software, to simulate the response of an exterior reinforced concrete joint.

Kaliske and Zreid [110] employed a coupled plasticity-damage microplane model [111] through ANSYS software to replicate the experimental study findings of a reinforced concrete joint devoid of transverse reinforcement [112]. illustrates the concurrence between experimental and numerical outcomes, as well as the efficacy of the constitutive model in capturing the softening behavior of concrete material.

Ozbolt *et al.* [113] implemented a microplane relaxed kinematic constraint model to simulate the cyclic response of two exterior joints. In this investigation, Ozbolt *et al.* [113] obtained favorable outcomes (refer to Figure 8) employing a relatively coarse mesh in comparison to contemporary studies, adopting an approach grounded in crack band regularization. In addition to strain regularization, Ozbolt *et al.* [113] incorporated a smeared slip approach in their work via calibrated contact elements. Nevertheless, the authors did not provide further elaboration regarding the calibration process.

Yılmaz *et al.* [114] presented closely aligned load-displacement histories under monotonic loading up to 6.5% drift. Although there was concurrence between the observed and computed reaction forces, a more in-depth examination of the results disclosed that the calculated failure mode did not entirely correspond with the experimental observations.

Comparison of the results of studies on modelling of reinforced concrete joints with advanced finite element techniques with the results obtained experimentally indicates that, as a common point, a large number of model parameters contained in the complex constitutive and element relations used need to be calibrated by fine-tuning on an experiment-specific basis, which indicates that the mentioned techniques are not suitable for practical purposes. This emphasises the need for generalised calibration methods in the use of these methods.

2.3.4.2 Constitutive Models used for Concrete Material in RC Joint Modelling

In the literature, there is a vast amount of studies which defines the features of plasticity described in Section 2.3.4.1 according to the experiments carried out over

concrete specimens. Dislike metals, internal friction materials such as rock and concrete exhibits decrease in yield criterion after tension and compression strength of the material exceeded. This phenomenon is named softening. Overall behavior includes perfect elasto-plasticity and a non-smooth softening where further loading does not experience any resistance to deformation. This fact often cause numerical difficulties which lead to non-convergent results. Softening behavior is slightly different than hardening since it is initiated and its evolution is maintained by *localization* [115]. After exceeding the strength limit of concrete in tension or compression, contrary to hardening phenomena; some parts of material stops to resist deformations and stress is dissipated and localized in other parts. Hence, the primary issue with the concrete plasticity modelling is introducing a feasible numerical solution to the softening phenomenon.

Grassl [116] noted that associated flow rule produce overestimated maximum stress for concrete-like materials which deform due to internal frictional sliding, remarking that concrete material does not follow an associated flow rule. In non-associated flow rule, plastic potential is not proportional to the yield surface and strain increment is not in the same direction as the stress increments.

In ANSYS Mechanical APDL Material Reference [117] a set of generalized rules described to be used in combination with applicable yield criterion and flow rules. Yield function in compression Ω_c is given by a nonlinear hardening function and a linear softening function. Relative stress level at the onset of nonlinear hardening is Ω_{ci} with a hardening yield function:

$$\Omega_c = \Omega_{ci} + (1-\Omega_{ci})\sqrt{2\frac{\kappa}{\kappa_{cm}} - \frac{\kappa^2}{\kappa_{cm}^2}} \tag{2.28}$$

where κ and κ_{cm} denote actual plastic strain value and plastic strain value when the material strength is exceeded, respectively. After the state that peak compression strength is exceeded, softening starts with the function:

$$\Omega_c = 1 - \frac{1-\Omega_{cr}}{\kappa_{cr}-\kappa_{cm}}(\kappa-\kappa_{cm}) \tag{2.29}$$

when κ exceeds defined critical plastic strain threshold κ_{cr} compression strength is reduced to the pre-defined residual stress. Piece-wise set of equation 2.28 and 2.29 are plotted in figure 2.9.(a).

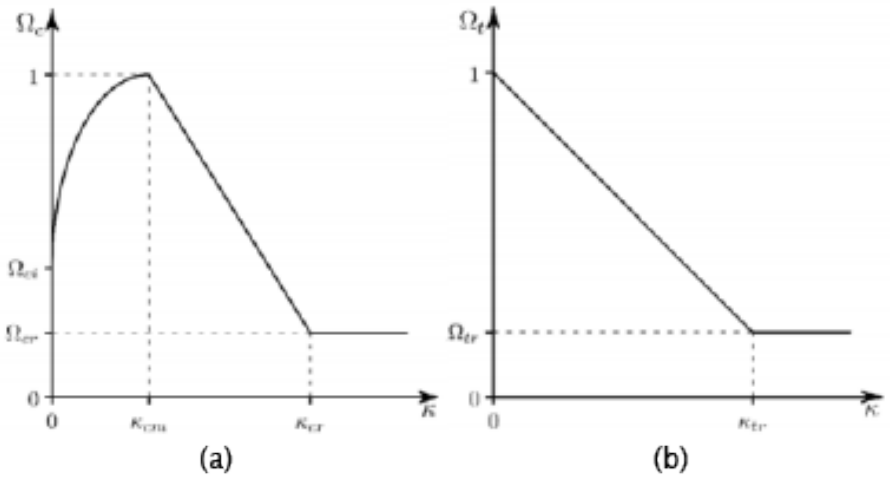

Figure 2.9 Hardening and Softening Rule under (a) Compression (b) Tension (ANSYS Material Reference, 2019)

Under tension, yield function Ω_t is given by a linear softening function where relative yield stress equal to 1 at initial yielding and decreases to the given residual relative stress Ω_{tr} when effective plastic strain is κ_{tr}. Described function is plotted in Figure 2.9.(b). Softening can be defined in an *exponential* form as well, surely that definition requires intermediate parameters that control the skewness of the curve. A better presentation might be defined based on *Fracture Energy* as Moharrami and Koutromanos [118] suggests; but it is known that formulation is based on mesh area and thus dependent on the mesh size. Only linear softening rule is used in this research, but other mentioned rules may be included in further steps of the study.

Mises [119] introduced well-known yield criterion shown in Eq 2.30 which is only dependent on J_2 and material parameter.

$$f(J_2) = \sqrt{J_2} - \tau = 0 \tag{2.30}$$

Materials with internal friction, slip surfaces are rough and shear stress needed to activate slip is affected by the stress normal to the slip plane. Feenstra and De Borst [120] states that to combine von Mises criterion with Rankine surface for tension may yield realistic results for concrete material. Another well-known surface is proposed by Drucker and Prager [121] in the form of

$$f(I_1, J_2) = \alpha I_1 + \sqrt{J_2} - \tau_0 \tag{2.31}$$

where α and τ_0 are material parameters. This indicates that the Drucker-Prager

Table 2.2 Plasticity Features of ANSYS APDL Plasticity Material Models ANSYS Mechanical APDL Material Reference [117]

Name	TB Lab	Yield Criterion	Flow Rule	Hardening Rule	Material Response
Bilinear Isotropic Hardening	BISO	von Mises/Hill	associative	work hardening	bilinear
Nonlinear Isotropic Hardening	NLISO	von Mises/Hill	associative	work hardening	nonlinear
Classical Bilinear Kinematic Hardening	BKIN	von Mises/Hill	associative (Prandtl- Reuss equations)	kinematic hardening	bilinear
Nonlinear Kinematic Hardening	CHAB	von Mises/Hill	associative	kinematic hardening	nonlinear
Drucker - Prager	DP	von Mises with dependence on hydrostatic stress	associative or non- associative	none	elastic- perfectly plastic
Extended Drucker - Prager	EDP	von Mises with dependence on hydrostatic stress	associative or non- associative	work hardening	multilinear
Cast Iron	CAST	von Mises with dependence on hydrostatic stress	non- associative	work hardening	multilinear
Gurson	GURS	von Mises with dependence pressure and porosity	associative	work hardening	multilinear
Menetrey - Willam	MW	von Mises with dependence on hydrostatic stress	non-associative	work hardening	multilinear

yield criterion is the same with von Mises, except with the slight difference about the fact that shear yield stress is adjusted to hydrostatic (volumetric) stress. Jirasek and Bazant [122] notes that for concrete material, it is possible to obtain better matching results in comparison with von Mises surface, however in tension, large deviations are still observed. Available constitutive models representing plastic behavior of concrete mostly rely on extension, combination or slight modification on Drucker-Prager model.

Available plasticity based concrete models offered in ANSYS Mechanical APDL Material Reference [117] is shown in Table 2.2 with their plasticity features.

2.3.4.3 Microplane Plasticity-Damage Model

An unconventional but powerful approach is introduced by Zreid and Kaliske [111] to overcome numerical issues due to localization of strains. Their formulation uses microplane quantities which replaces tensorial formulation with uniaxial stress states on planes with varying orientations. The main advantages of such approach are (1) providing a constitutive model that the modeler need not worry about tensorial invariance since it is satisfied by the summation of responses from microplanes of various orientations; (2) ability to capture deviations from normality caused by dilatancy in frictional materials and (3) direct characterization physical phenomena associated with surfaces, i.e. slip friction, lateral confinement etc.

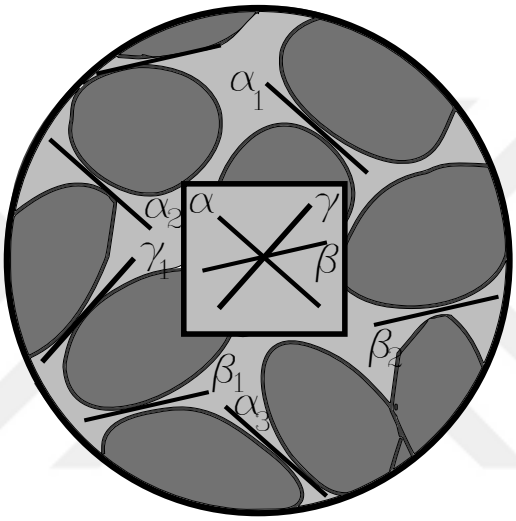

Figure 2.10 Microplanes [122]

It is assumed that macroscopic (conventional) quantities are computed through numerical integration over the sphere formed by micro-planes (see Fig. 2.10) using Equation 2.32.

$$\frac{3}{4\pi}\int_{\Omega}(.)d\Omega = \sum_{mic=1}^{21}(.)w^{mic} \tag{2.32}$$

Microplane counterpart of any yield criterion can be defined to establish a microplane plasticity model. In this case, Drucker-Prager Drucker and Prager [121] yield function is given in Equation 2.33.

$$f_{DP}^{mic} = \sqrt{\frac{3}{2}\sigma_D^e\sigma_D^e} + \alpha\sigma_V^e - \sigma_0 \tag{2.33}$$

where σ_D^e is effective deviatoric stress, σ_V^e is effective volumetric stress, α is friction

angle and σ_0 is initial yield strength. Introduced function forms an open surface in stress space. To cover all possible stress states, its form is bounded by compression and tension caps as it is described in Equation 2.34 and ensured a continuous derivative.

$$f^{mic}(\sigma_D^e, \sigma_V^e, \kappa) = \frac{3}{2}\sigma_D^e \sigma_D^e - f_1^2(\sigma_V^e, \kappa) f_c(\sigma_V^e, \kappa) f_t(\sigma_V^e, \kappa) \tag{2.34}$$

where f_1 is the plain Drucker-Prager yield surface. Compression bound function is given by Equation 2.35 and 2.36.

$$f_c = 1 - H_c(\sigma_V^C - \sigma_V^e)\frac{(\sigma_V^e - \sigma_V^C)^2}{X^2} \tag{2.35}$$

$$X = R f_1(\sigma_V^C) \tag{2.36}$$

where σ_V^C is abscissa of the intersection point between the compression cap and the Drucker-Prager yield function and R is ratio between volumetric and minor axes of the cap, H is the Heaviside function. Equation 2.37 and 2.38 reads the tension cap,

$$f_t = 1 - H_t(\sigma_V^e - \sigma_V^e)\frac{(\sigma_V^e - \sigma_V^T)^2}{(T - \sigma_V^T)^2} \tag{2.37}$$

$$T = T_0 + R_t f_h(\kappa) \tag{2.38}$$

where σ_V^T is abscissa of the intersection of tension cap and Drucker-Prager yield function and T_0 is the initial intersection of the cap with the major axis. Hardening is defined by Equation 2.39 where D is a material constant retrieved as a material input.

$$f_h(\kappa) = D\kappa \tag{2.39}$$

Figure 2.11 shows a schematic representation of the yield surface generated by the Equation 2.34.

Evaluation of plastic strains under monotonic loading is straightforward using the theory presented above. However, under cyclic loading, realistic representation without stiffness degradation is not possible. Equation 2.40 - 2.42 defines the damage rule,

$$1 - d_{mic} = (1 - d_c^{mic})(1 - r_w d_t^{mic}) \tag{2.40}$$

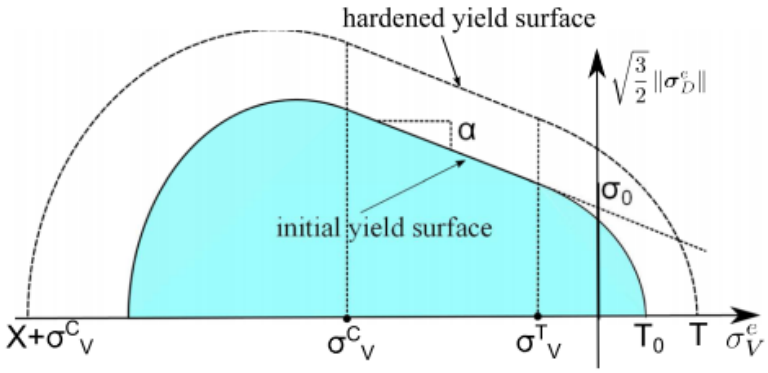

Figure 2.11 Drucker-Prager Cap Surface [111]

$$d_{mic}^{t} = 1 - exp(-\beta_t \gamma_{mic}^{t}) \tag{2.41}$$

$$d_{mic}^{c} = 1 - exp(-\beta_c \gamma_{mic}^{c}) \tag{2.42}$$

where c and t index note split compression and tension damage parameters respectively and they are controlled with user input β and γ. r_w is split weight factor and used to create distinct damage behavior under tension and compression. In transition from tension to compression, stiffness degradation due to cracks is recovered by crack closure mechanism r_w is a function of principal strains.

Since the introduced constitutive model aims to reproduce concrete response including softening branch, it is not possible to obtain any practical results due to the numerical instability issues associated with plasticity models with negative hardening. The main reason is that the softening region is infinitely small and total amount of energy dissipated during the failure process is zero [123], thus there is no trivial solution for the boundary value problem. In this context, this region is infinitely small, akin to a mere theoretical point, rather than a physically measurable size. This is pivotal because, in most systems, when a failure occurs, energy is typically lost or dissipated into another form. However, in this scenario, the total energy dissipated during the failure process is zero, implying no energy conversion. This combination of a minuscule softening region and absence of energy dissipation makes the boundary value problem particularly complex, ruling out a simple or "trivial" solution.

Several solutions to this problem were introduced in literature; a very effective one among them is implicit gradient enhancement which replaces local variables that make the solution unstable with non-local counterparts to prevent localization. The non-local average of a local variable is computed assuming the non-local value

governed by Helmholtz-type equation (see Eq. 2.43) with the homogenous Neumann boundary condition (see Eq. 2.44).

$$\bar{\eta_m} - c\nabla^2\bar{\eta_m} = \eta_m \tag{2.43}$$

$$\nabla\bar{\eta_m} n_b = 0 \tag{2.44}$$

where η_m is the local variable (e.g. equivalent strain) to be enhanced and $\hat{\eta_m}$ is the non-local counterpart. c is the length-scale parameter which controls the radius of interaction (or localization) and n_b is the boundary normal vector. Implicit regularization is obtained by the weighted combination of local and non-local variables as it is described in Equation 2.45.

$$\hat{\eta_i^{mic}} = m\bar{\eta_{mi}} + (1-m)\eta_{mi} \tag{2.45}$$

where $i = t, c$ note tension and compression respectively. m is regularization parameter. Prevention of the localization or with other words homogenization of the local variables over an interaction range requires two (for compression and tension) additional degree of freedom for each element. This feature is available in CPT215 8-node coupled pore-pressure solid element [124].

2.3.4.4 Elastic Microplane Damage Model

Plasticity theory is used to describe the inelastic behavior of concrete materials, specifically when they experience loading beyond their elastic limits, resulting in permanent deformation. Damage theory, on the other hand, accounts for the degradation of material properties due to the formation and growth of microcracks and voids in the concrete structure. Combining these two theories provides a more comprehensive representation of concrete behavior, as it takes into account both irreversible deformations and material deterioration. In a concrete plasticity damage model, the stress-strain relationship of concrete is described by considering the elastic, plastic, and damage components. The model typically incorporates a yield criterion to define the onset of plastic deformation and a flow rule to govern the evolution of plastic strains. Simultaneously, the model includes a damage variable to quantify the loss of material stiffness and strength due to crack formation and propagation.

Alternative to the tensorial definitions, Bazant and Prat [125] proposed a novel approach that the material behavior is modelled through uniaxial stress-strain laws

on various planes which are referred as microplanes.

Following the formulation presented in ANSYS Material Reference [117], Microplane theory is based on the assumption that microscopic free energy on the microplane level exists and its integral over all pre-defined microplanes is identical to the macroscopic free Helmholtz energy, defined as;

$$\Psi^{mac} = \frac{3}{4\pi} \int_{\Omega} \Psi^{mic} d\Omega \tag{2.46}$$

In thermodynamics, free energy is a measure of the amount of energy in a system that can perform work when temperature and volume are uniform throughout the system. It represents the energy that is "free" or available to be used.Summing up these energies from all microplanes yields a total corresponding to the macroscopic Helmholtz free energy. The Helmholtz free energy, defined as , represents the energy available to do work in a system at constant volume and temperature. Different thermodynamic potentials, like the Helmholtz free energy, are used to simplify analyses of specific conditions. In the case of the Helmholtz free energy, it is particularly useful for systems with fixed volume and temperature, indicating the maximum work obtainable excluding volume expansion.

The strains and stresses on microplanes are decomposed into volumetric and deviatoric parts based on the V-D split in which the strain is expressed as

$$\epsilon = \epsilon_D + \epsilon_V 1 \tag{2.47}$$

$$\epsilon_V = V : \epsilon \tag{2.48}$$

$$V = \frac{1}{3} 1 \tag{2.49}$$

$$\epsilon_D = Dev : \epsilon \tag{2.50}$$

$$Dev = n \cdot \Pi - \frac{1}{3} n \cdot 1 \otimes 1 = n \cdot \Pi^{dev} \tag{2.51}$$

where ϵ_D and ϵ_V correspond to deviatoric and volumetric components of the total calculated strain; V is the second-order volumetric projection tensor, 1 is second order identity tensor, Pi is the fourth-order symmetric identity tensor and n is the normal vector of the microplane. The stresses are evaluated by free energy derivative with respect to the strain as

$$\sigma = \frac{3}{4\pi}\int_{\Omega}\frac{\delta\psi^{mic}}{\delta\epsilon}d\Omega = \frac{3}{4\pi}\int_{\Omega}(V\sigma_V + 2Dev_T\sigma_D)d\Omega \tag{2.52}$$

where σ_v and σ_D are volumetric and deviatoric stresses respectively. Assuming isotropic elasticity, they can be described respectively as

$$\sigma_V = \frac{\delta\psi^{mic}}{\delta\epsilon_V} = K^{mic}\epsilon_V \tag{2.53}$$

$$\sigma_D = \frac{\delta\psi^{mic}}{\delta\epsilon_D} = D^{mic}\epsilon_D \tag{2.54}$$

where K_{mic} and G_{mic} are microplane elasticity parameters, bulk and shear moduli respectively and they can be related with the macroscopic properties as

$$K^{mic} = 3KG^{mic} = G \tag{2.55}$$

Integration over the approximate sphere surface (microplanes) to calculate the homogenized stresses and strains is obtained by numerical integration

$$\frac{3}{4\pi}\int(.)^{mic}d\Omega = \sum_{i=1}^{N_p}(.^{mic})^i w^i \tag{2.56}$$

where w_i is the weight factor stands for the contribution weight of each microplane vector to the calculated quatity. This formulation leads to anisotropic behavior even though the elastic uniaxial laws are defined for individual microplane vectors.

Strain-softening material models typically cause numerical instability due to stress singularities which can be mitigated by implicit gradient regularization in some cases [111, 123]. Implicit gradient regularization enhances a local variable by considering its non-local counterpart as an extra degree of freedom governed by a Helmholtz-type equation. Governing equations are given by the linear momentum-balance equation

and modified Helmholtz equation defining the non-local equivalent strain field η_m.

$$\nabla \cdot \sigma + f = 0 \tag{2.57}$$

$$\hat{\eta}_m - c\nabla^2 \hat{\eta}_m = \eta_m \tag{2.58}$$

where σ is the Cauchy stress tensor, f is the body force vector, ∇ is the divergence, ∇^2 is the gradient and is the Laplace operator. The gradient parameter c is the variable governs the range of non-local interaction. With the homogenous Neumann boundary condition defined as follows;

$$\nabla \hat{\eta_m} \cdot n_b = 0 \tag{2.59}$$

where n_b is the normal to the outer boundary of the non-local field, no explicit definition of boundary conditions for the extra degree of freeom is required.

Bazant and Pijaudier-Cabot [126] suggests to identifiy the gradient parameter c through the comparison of homogenous and nonhomogenous tensile tests of concrete while the first specimen is subjected to a distributed damage field and the second is a notched specimen and subjected to a localized damage. In such case, damage parameter is obtained by calibrating distributed and localized damage specimens force-displacement curves while keeping other parameters effecting material damage as constant. However, experiments representing distributed damage field for complex failure modes may not be possible. For such cases, Lehky and Novak [127] proposes inverse calibration of force-deflection curves.

Damage is considered through modification of microscopic free energy function which includes a damage parameter, d_{mic} which is a normalized damage variable d_{mic}.

$$\Psi^{mic}(\epsilon_V, \epsilon_D, d^{mic}) = (1 - d^{mic})\Psi^{mic}(\epsilon_V, \epsilon_D) \tag{2.60}$$

The damage status of the material is described by the equivalent strain based damage function $\phi^{mic} = \phi(\eta^{mic}) - d_{mic} \leq 0$ where η^{mic} is the equivalent strain which is a scalar measure that controls the damage initialization and evolution. Among other definitions, Bazant [123] defines equivalent strain as follows

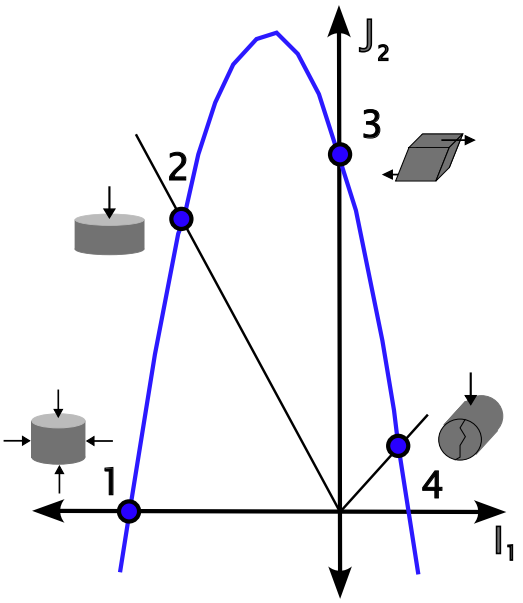

Figure 2.12 Failure surface of microplane material in invariant space

$$\eta^{mic} = k_0 I_1 + \sqrt{k_1^2 l_1^2 + k_2 J_2} \tag{2.61}$$

Isotropic damage model does not take into account the diffirent behavior of the material under tension and compression. $k0$, $k1$, $k2$ are the result of the adoptation of the model to different response of the material under different deformation states defined by invariants I_1 and J_2 as it is illustrated in Figure 2.12. Figure 2.12 also shows allowable deformation domain in invariant space where material behaves elastic (in microplane level) while beyond the envelope, material is damaged.

The damage variable d_{mic} itself is expressed with damage evolution law

$$d_{mic} = 1 - \frac{\gamma_0^{mic}}{\gamma^{mic}}\left(1 - \alpha^{mic} + \alpha^{mic} \exp(\beta^{mic}(\gamma_0^{mic} - \gamma^{mic}))\right) \tag{2.62}$$

where γ^{mic}, α^{mic} and β^{mic} respectively represent maximum history equivalent strain maximum degradation and damage rate while γ_0 is the equivalent strain threshold for damage initialization.

2.4 Parameter Identification with Soft-Computing Methods

In structural mechanics, the parameter identification (i.e. inverse analysis) problem is a crucial challenge that involves determining the material and geometrical properties

of a structure or its components. These properties, often referred to as parameters, are essential for accurate modeling, analysis, and prediction of structural behavior under various loading conditions. The parameter identification problem can be approached through a combination of experimental and computational methods. Experimental data, such as displacement, stress, and strain measurements are acquired from physical tests on the structure or its components. Computational methods, including the finite element method and other numerical techniques are employed to develop mathematical models that represent the structural behavior. The objective is to calibrate these models to match the experimental data by adjusting the parameters within their physically feasible ranges [128].

Kučerová [129] describes the solution to an inverse analysis into two distinct directions: forward mode and inverse mode. The forward mode is characterized by the minimization of an error function $F(x)$, defined as the discrepancy between the outputs of the model y^M, a function of the model parameters and the experimental output y^E, i.e.

$$minF(x) = min\|y^E - M(x)\| \tag{2.63}$$

Conversely, the inverse mode assumes the existence of an inverse model M^{INV} associated with the model M, satisfying

$$x = M^{INV}(y) \tag{2.64}$$

for all possible values of y.

In the context of the forward mode, which can be viewed as a solution to an optimization problem, gradient-based optimization techniques are commonly employed. Approaches inspired by simulated annealing methods [130], which utilize a single solution at a time, or evolutionary algorithms [131–133], which operate with populations of solutions, are typically adopted. Various genetic algorithm solutions have been proposed for this class of problems in the literature [134, 135], including multi-objective optimization techniques [136, 137]. Any solution offered which is based on approximating the assumed inverse model, traditional artificial neural network applications serve as an example for inverse mode inverse analysis [138]. A strong interest has been developed for formulating inverse analysis methods to determine the quasi-brittle fracture behaviour of concrete [139–150].

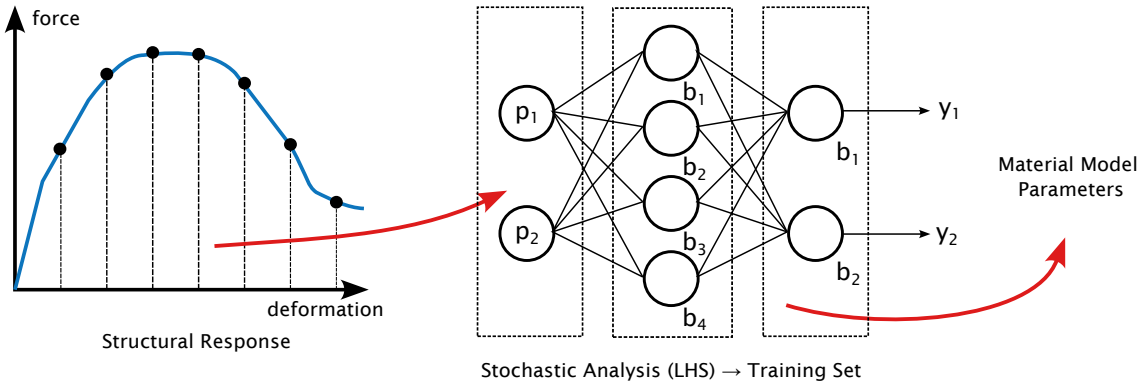

Figure 2.13 Illustration of inverse analysis through neural networks

Novak and Lehky [138] presented an approach to inverse analysis, integrating stratified Monte Carlo simulations with artificial neural networks. The process consists of several essential stages. Initially, a computational model for a specific issue is formulated using suitable finite element method tools. The model undergoes calibration via a trial-and-error method with model parameters (i.e. identification parameters: IP) and preliminary computations, leading to an approximate alignment with experimental measurement data (MD). Initial IP estimations rely on testing, engineering discernment, and virtual computational simulations, with refinements occurring in later stages. IP is regarded as random variables represented by probability distributions, such as rectangular or Gaussian distributions. Monte Carlo simulations are utilized to produce random IP realizations, with Latin Hypercube Sampling (LHS) being the favored technique. Probable statistical correlations among parameters are also taken into account to enhance inverse analysis and preserve computational model coherence. Several deterministic calculations are executed using random IP realizations (y), resulting in a statistical set of virtual responses (p). The suitable number of simulations is contingent upon factors like problem intricacy, neural network configuration, and IP variability. Random realizations (y) and computational model responses (p) serve as the basis for training an artificial neural network. This vital step is exemplified by a nonlinear load-deflection curve encompassing both pre-peak and post-peak behaviors. The trained ANN is employed to pinpoint the optimal IP set (y_{opt}) that achieves the highest concordance with MD when used as input for network simulations. Lastly, the results are validated by computing the computational model with the optimal parameters (y_{opt}) and contrasting the output with MD to evaluate the effectiveness of the inverse analysis.

2.4.1 Artificial Neural Networks

Artificial neural networks (ANNs) are a type of computational model inspired by the structure and function of the human brain. ANNs are composed of a large number

of simple processing elements, or neurons, which are connected to each other via weighted connections. Each neuron receives input signals from other neurons or from external sources, processes these signals using a mathematical function, and produces an output signal that is transmitted to other neurons in the network. There are numerous terms used to describe the field of artificial neural networks, including connectionism, parallel distributed processing, neurocomputing, natural intelligent systems, machine learning algorithms, and more [129].

Artificial neural networks have a long and rich history, dating back to the early days of computing. In the 1940s, researchers such as McCulloch and Pitts [151] began to explore the idea of modeling biological neurons using electronic circuits. This led to the development of the first artificial neuron model, which consisted of a simple binary threshold function that could be used to model logical operations. In the 1950s and 1960s, sophisticated neural network models are introduced, such as the perceptron and the adaptive linear neuron [152, 153]. These models were capable of learning from examples and could be used for pattern recognition and classification tasks. In the 1970s and 1980s, new types of neural network models are introduced, such as the Hopfield network [154] and the backpropagation algorithm [155]. These models were capable of learning more complex patterns and could be used for tasks such as image and speech recognition. In the 1990s, the field of ANNs experienced a resurgence of interest, driven in part by the development of more powerful computers and the availability of large datasets. Researchers began to develop new types of neural network models, such as the radial basis function network and the self-organizing map. In recent years, the field of ANNs has continued to evolve and grow, with new developments such as deep learning and convolutional neural networks. These models have achieved impressive results in a variety of fields, such as computer vision, natural language processing, and speech recognition.

The structure and function of ANNs can vary widely depending on the specific application, but they typically consist of multiple layers of neurons organized in a hierarchical fashion. The input layer receives raw data from the outside world, while the output layer produces the final output of the network. In between the input and output layers, there may be one or more hidden layers of neurons that process the input signals in increasingly complex ways. The interconnections within an artificial neural network are typically denoted by numerical weights, signifying the magnitude and direction of signal transmission between neurons. Throughout the training process, these weights are modified according to the input-output pairs from a dataset, enabling the network to generate accurate outputs for specific inputs. ANNs are a potent method for addressing numerous real-world challenges. They can enhance performance and adapt to environmental changes through experiential learning.

Moreover, ANNs can manage incomplete or noisy data and excel in scenarios where problem-solving rules or steps are undefined. Their straightforward implementation and substantial parallelism render them highly efficient. The most significant advantage of ANNs is their capacity to function as an arbitrary approximation mechanism that learns from observed data. However, their utilization necessitates a solid comprehension of the underlying theory. With proper selection of the model, cost function, and learning algorithm, the resulting ANN can exhibit remarkable robustness. The following subsection provides a review of several typical types of artificial neural networks.

2.4.1.1 Feed-Forward Neural Networks

Feedforward neural networks (FFNNs) are a class of artificial neural networks characterized by the unidirectional flow of information from input to output layers without any feedback loops [156]. These networks consist of multiple layers of interconnected neurons, including an input layer, one or more hidden layers, and an output layer [157]. Each neuron within a layer is connected to every neuron in the subsequent layer through weighted connections, where the weights signify the strength and direction of the signal transmission.

In a feedforward neural network, the input data traverses through the network in a single direction, undergoing a series of transformations as it passes from one layer to the next. The neurons in the hidden layers apply activation functions to the weighted sum of their inputs, introducing nonlinearity into the network [158]. Common activation functions include the sigmoid, hyperbolic tangent, and rectified linear unit (ReLU) functions [159].

Training a feedforward neural network entails adjusting the weights of the connections to minimize a predefined cost function, which quantifies the discrepancy between the network's predicted output and the actual target values [160]. Gradient-based optimization methods, such as stochastic gradient descent (SGD) or more advanced variants like Adam, are typically employed to optimize the weights during the training process [161]. The backpropagation algorithm, a fundamental technique in training feedforward neural networks, computes the gradient of the cost function with respect to each weight by applying the chain rule of calculus [155].

Feedforward neural networks have found extensive applications across various domains, including image and speech recognition [162], natural language processing [163], and financial forecasting [164]. Despite their simplicity and lack of recurrent connections, FFNNs have demonstrated the ability to solve complex problems by

approximating arbitrary functions [165]. However, their performance is limited when addressing tasks that require the processing of sequential or temporal data, as they lack the inherent memory and feedback mechanisms present in recurrent neural networks (RNNs) and other more sophisticated architectures [166].

The information in a feed-forward network flows from the input layer through the hidden layers to the output layer, without any feedback loops. The output of a neuron in a layer is computed using the following equations:

$$z_j^{(l)} = \sum_{i=1}^{N_{l-1}} w_{ji}^{(l)} a_i^{(l-1)} + b_j^{(l)}, \tag{2.65}$$

$$a_j^{(l)} = f^{(l)}(z_j^{(l)}), \tag{2.66}$$

where l denotes the layer number, N_{l-1} is the number of neurons in layer $l-1$, $w_{ji}^{(l)}$ is the weight connecting neuron i in layer $l-1$ to neuron j in layer l, $a_i^{(l-1)}$ is the activation of neuron i in layer $l-1$, $b_j^{(l)}$ is the bias term of neuron j in layer l, $z_j^{(l)}$ is the weighted input to neuron j in layer l, $a_j^{(l)}$ is the activation of neuron j in layer l, and $f^{(l)}(\cdot)$ is the activation function of layer l.

Training a feed-forward neural network involves adjusting the weights and biases to minimize the difference between the predicted outputs and the actual outputs for a given set of training examples. This process is typically done using a supervised learning algorithm, such as gradient descent combined with backpropagation. The objective is to minimize a loss function, $E_v(w, b)$, which measures the error between the predicted outputs and the true outputs:

$$E_v(w, b) = \frac{1}{N} \sum_{i=1}^{N} \frac{1}{2} (\hat{y}_i - y_i), \tag{2.67}$$

where N is the number of training examples, $\hat{y}_i$ is the predicted output and y_i is the true output for the i-th training example. A flowchart for definition, training and validation of a back-propagation feed-forward neural network is given in Figure 2.14.

During the training process, the dataset is often split into two or more parts: a training set and a validation set. The training set is used to adjust the weights and biases of the network, while the validation set is used to evaluate the performance of the trained model and to prevent overfitting. Overfitting occurs when the model learns to perform very well on the training set but does not generalize well to new, unseen data. By

monitoring the performance on the validation set, we can stop the training process when the performance on the validation set starts to degrade, a technique known as early stopping.

2.4.1.2 Radial Basis Function Networks

Radial basis function networks (RBFNs) are a specific class of feedforward artificial neural networks that utilize radial basis functions (RBFs) as activation functions within the hidden layer neurons. RBFNs have gained significant attention in the field of machine learning and pattern recognition due to their excellent approximation capabilities, fast training process, and simple structure [167–169].

The architecture of RBFNs typically consists of three layers: an input layer, a hidden layer with RBF neurons, and an output layer. In the hidden layer, each neuron computes the Euclidean distance between the input vector and its center vector, then applies a radial basis function to this distance. The most commonly used RBF is the Gaussian function, which has the advantage of smoothness and locality [167]. The output layer consists of linear neurons that perform a weighted sum of the hidden layer outputs to generate the final output [170].

RBFNs have been employed in various applications such as function approximation, classification, regression, and time series prediction [157, 171]. One of the primary advantages of RBFNs is their ability to approximate any continuous function to arbitrary accuracy, given sufficient hidden layer neurons [169]. Additionally, RBFNs offer a more localized response in comparison to other feedforward networks, such as multilayer perceptrons (MLPs), which rely on global basis functions [168].

The output of a radial basis function network (RBFN) can be defined as a function of the inputs, weights, and centers of the radial basis functions. Specifically, the predicted output for class k, denoted y_k, is given by:

$$y_k = \sum_{j=1}^{H} w_{kj} * \phi(\|x - c_j\|) \tag{2.68}$$

where x represents the input vector, c_j is the center of the jth radial basis function, w_{kj} is the weight associated with the jth radial basis function for class k, and $\phi(\cdot)$ is the radial basis function.

To train an RBFN, the error between the predicted outputs and the true outputs is minimized using a least squares approach. The error is given by:

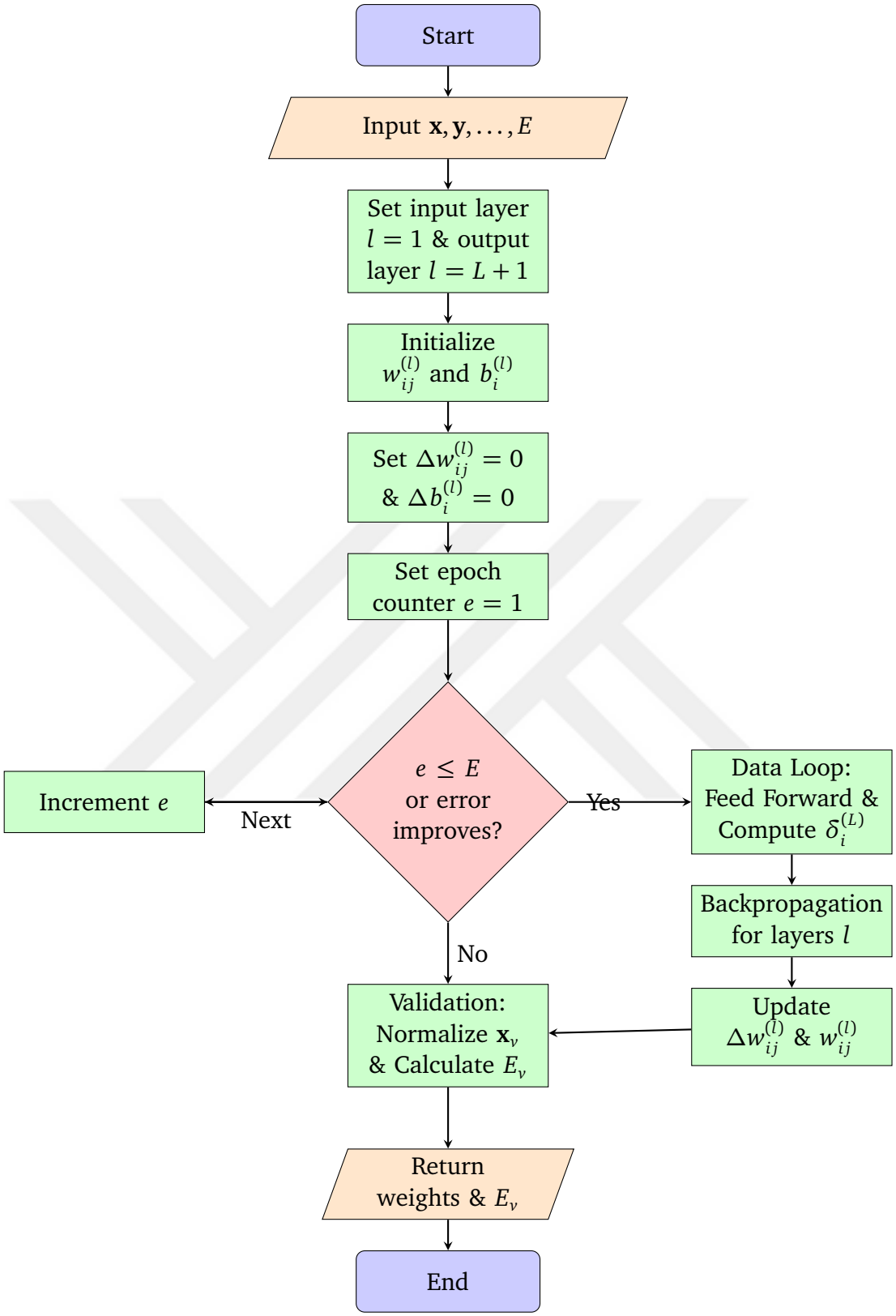

Figure 2.14 Backpropagation Feedforward Neural Network

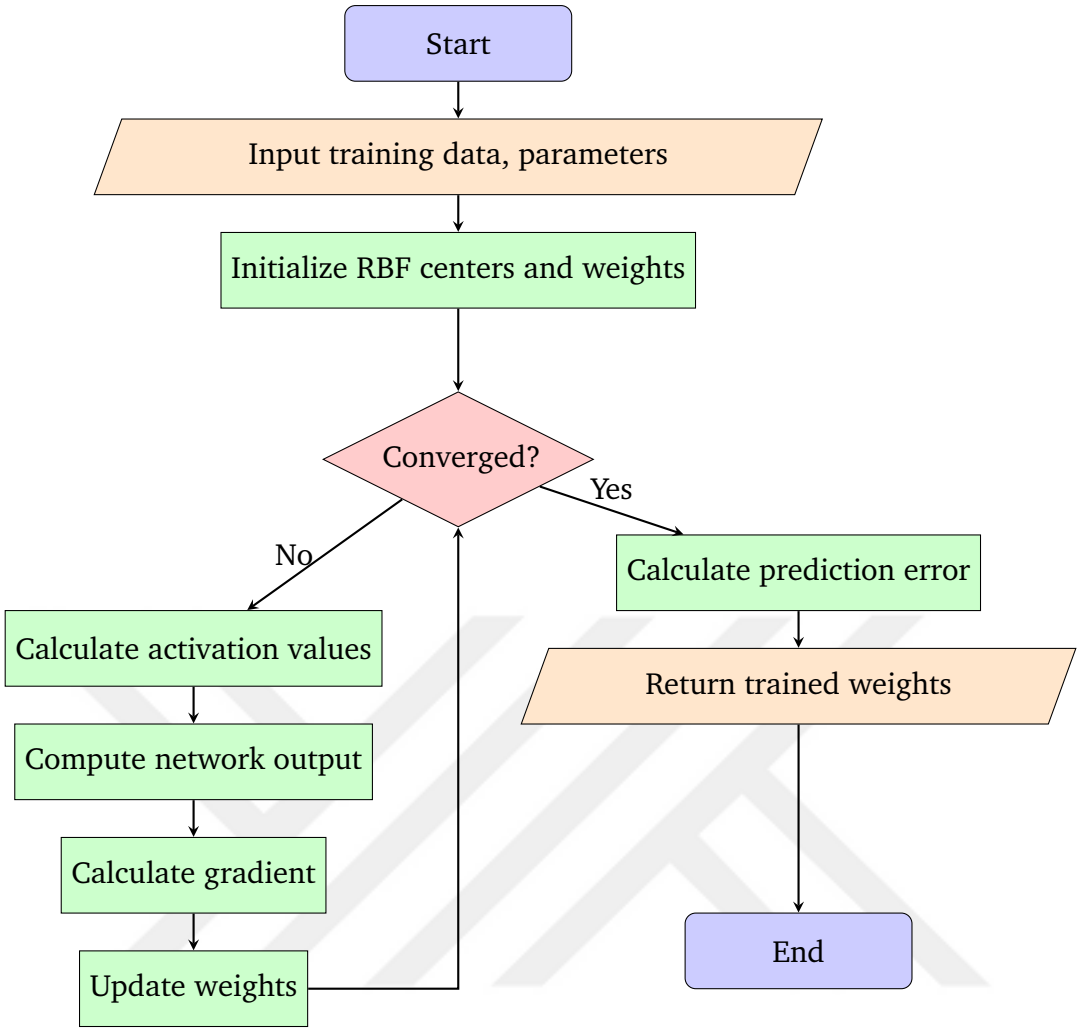

Figure 2.15 Radial Basis Neural Network

$$E = \frac{1}{2} * \sum_{n=1}^{N} \sum_{k=1}^{K} (y_{nk} - \hat{y}_{nk})^2 \tag{2.69}$$

where N is the number of training samples, K is the number of classes, y_{nk} is the true output for the nth sample and kth class, and $\hat{y}_{nk}$ is the predicted output for the nth sample and kth class. A flowchart for definition, training and validation of a radial basis function neural network is given in Figure 2.15.

A General Regression Neural Network (GRNN) is a type of radial basis function network that is specifically designed for regression tasks. GRNN is a one-pass learning algorithm that offers fast learning and smooth function approximation [172]. GRNN is a single-pass learning algorithm with excellent generalization capabilities, making it well-suited for function approximation, prediction, and classification tasks.

In GRNN, the pattern layer consists of neurons, each representing a data point from

the training set. These neurons employ radial basis functions, such as Gaussian functions, as activation functions to measure the similarity or distance between the input and the stored data points [172]. The width of the radial basis functions, known as the smoothing parameter or spread constant, influences the network's performance and can be optimized based on the problem at hand. The summation layer consists of two sets of neurons, one for the weighted sum of the radial basis function outputs (the numerator) and another for the sum of the activation values (the denominator). The output layer computes the ratio of the weighted sum and the sum of the activation values, yielding the network's final output, which corresponds to the function approximation or prediction.

GRNN's single-pass learning algorithm, smooth decision boundaries, and ability to avoid overfitting make it an attractive choice for various applications, including time series forecasting, classification, and regression tasks.

Architecture of GRNN consists of an input layer, a pattern (or radial basis) layer, a summation layer, and an output layer. The output of a GRNN is calculated using the following equation:

$$y(\mathbf{x}) = \frac{\sum_{i=1}^{N} w_i K(\frac{\|\mathbf{x}-\mathbf{x}_i\|}{\sigma}) y_i}{\sum_{i=1}^{N} K(\frac{\|\mathbf{x}-\mathbf{x}_i\|}{\sigma})}, \tag{2.70}$$

where N is the number of training examples, $\mathbf{x}$ is the input vector, $\mathbf{x}_i$ is the i-th training input vector, y_i is the corresponding target output, w_i is the weight associated with the i-th training example, σ is the kernel width parameter, and $K(\cdot)$ is the radial basis function kernel.

Training a GRNN is straightforward, as it is a one-pass learning algorithm. The training phase consists of setting the centers of the radial basis functions to the input vectors of the training examples and the corresponding weights to the target output values. The only parameter that needs to be determined during the training process is the kernel width parameter, σ, which controls the smoothness of the function approximation. The selection of σ can be done using techniques such as cross-validation or trial and error.

Similar to other neural networks, the dataset for training a GRNN is usually divided into a training set and a validation set. The training set is used to determine the centers of the radial basis functions and the corresponding weights, while the validation set is employed to evaluate the performance of the trained model and to select the optimal kernel width parameter, σ. By monitoring the performance on the validation set,

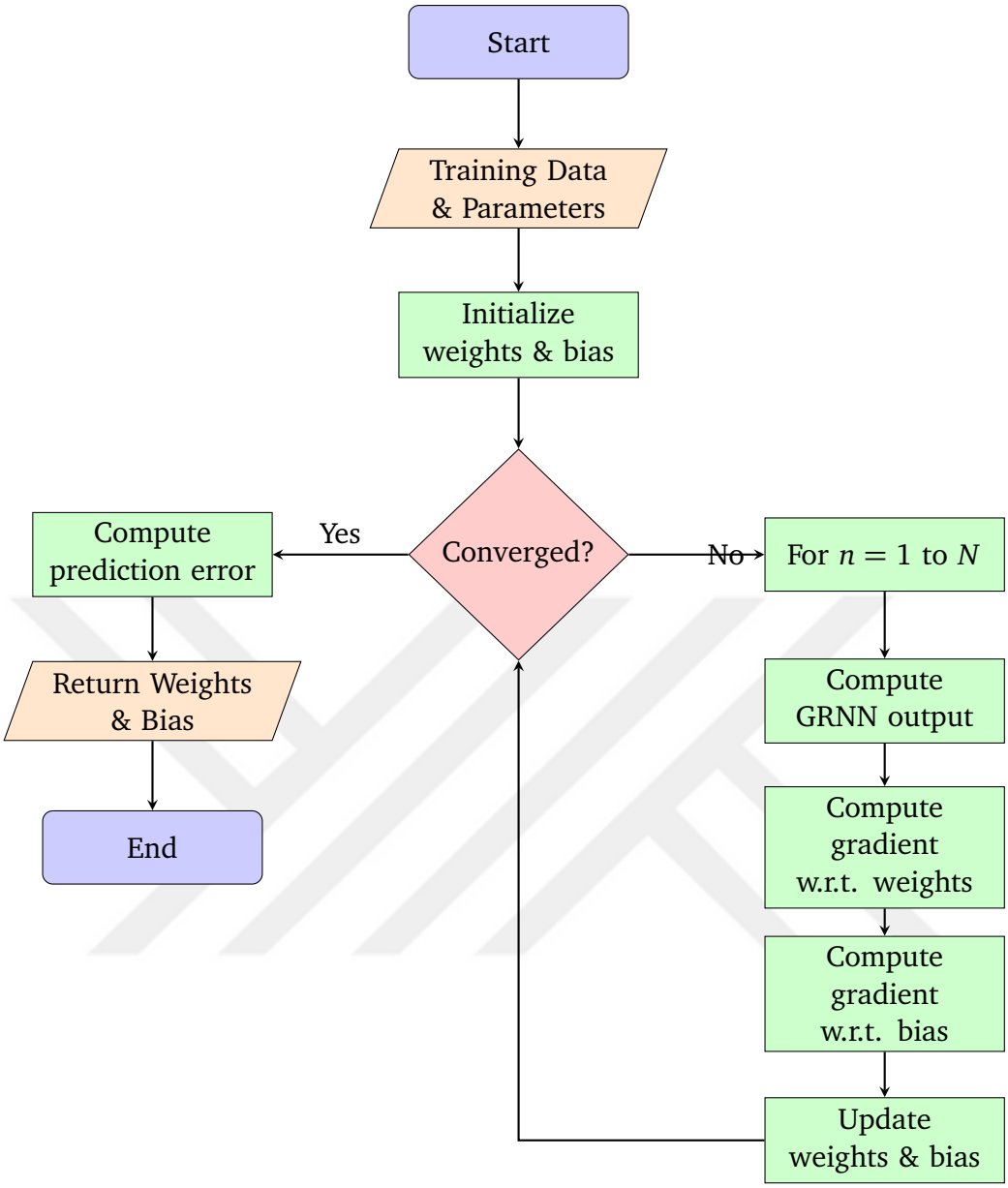

Figure 2.16 Generalized Regression Neural Network

we can avoid overfitting and choose the best value for σ that provides a balance between fitting the training data and generalizing to new, unseen data. A flowchart for definition, training and validation of a radial basis function neural network is given in Figure 2.16.

2.4.1.3 Other Types of Artificial Neural Networks

Kohonen Self-Organizing Networks, also known as Self-Organizing Maps (SOMs), are a type of unsupervised learning algorithm introduced by Teuvo Kohonen in the early 1980s [173]. SOMs are employed primarily for dimensionality reduction and data visualization tasks, where they preserve the topology and relative distances of the

input data in a lower-dimensional space. SOMs consist of an array of interconnected neurons organized in a grid-like structure that adapt to the input patterns through competitive learning, thereby forming a spatial representation of the input data [174].

Recurrent Neural Networks (RNNs) are a class of artificial neural networks characterized by the presence of feedback connections, which allow the network to exhibit dynamic temporal behavior and store information over time [175]. RNNs are particularly effective in dealing with sequential data and have been widely applied to tasks such as natural language processing, time series prediction, and speech recognition [176, 177]. The most popular RNN architectures, Long Short-Term Memory (LSTM) [166] and Gated Recurrent Units (GRU) [178], address the vanishing gradient problem commonly faced by traditional RNNs.

Hopfield Networks, introduced by John Hopfield in 1982, are a type of recurrent neural network that function as associative memory systems [154]. Hopfield networks store patterns in their weight matrix and can recall the stored patterns when provided with partial or noisy input. These networks are characterized by their symmetrical weight matrix, which ensures energy minimization and convergence to stable states. Hopfield networks have been applied to various tasks, including optimization problems and image recognition [179].

Fuzzy Neural Networks are a hybrid approach that combines the principles of fuzzy logic and artificial neural networks, aiming to overcome the limitations of both techniques and improve the learning and generalization capabilities [180]. FNNs employ fuzzy reasoning within the network structure, enabling them to handle imprecise, uncertain, or noisy data more effectively than traditional neural networks. Applications of FNNs include control systems, decision-making, and pattern recognition [181].

2.4.1.4 Training Set Preparation and Partitioning Techniques

The training and validation of artificial neural networks require a careful selection of the dataset partitioning technique. This section provides an overview of the various partitioning techniques commonly used in ANNs.

Proper partitioning of a dataset is crucial for training and validating artificial neural networks (ANNs) to ensure the generalization of learned models in regression tasks [157]. There are several approaches to divide the dataset into training and validation sets:

The holdout technique entails randomly splitting the dataset into two separate subsets

for training and validation purposes. The ANN is trained using the training subset and validated against the validation subset to evaluate its performance and generalization capabilities. While simple, this method may result in a high variance performance assessment, particularly for smaller datasets [158].

k-Fold cross-validation addresses the variance issue of the holdout method by dividing the dataset into k equal-sized folds. The ANN is trained and validated k times, with each fold being used as a validation set exactly once while the remaining $k-1$ folds serve as the training set. The overall performance estimate is obtained by averaging the performance metrics across the k iterations [158]. This method provides a more reliable estimate of the model's performance, especially for small datasets.

This method represents a specific case of k-fold cross-validation where k is equal to the dataset's total number of data points [182]. The ANN is trained on the entire dataset, excluding one data point, and validated against the single excluded point. This process is repeated for every data point in the dataset. While leave-one-out cross-validation offers a low-bias performance evaluation, it can be computationally demanding for larger datasets.

The bootstrap method generates multiple resampled datasets by drawing samples with replacement from the original dataset. Each resampled dataset is used to train an ANN, and the model's performance is assessed using out-of-bag samples not included in the resampled dataset. Although the bootstrap method can yield a robust performance evaluation, it may introduce bias due to the replacement sampling [182].

The choice of a partitioning technique depends on several factors, including the size of the dataset, the distribution of the data, and the computational resources available for training and validation. A careful selection of the partitioning technique is crucial in ensuring that the ANN is properly trained and can generalize well to new data.

2.4.2 Latin Hypercube Sampling

Latin hypercube sampling (LHS) is a statistical technique commonly used for generating well-spaced, representative samples from high-dimensional data spaces. LHS has been applied in various fields such as optimization, simulation, and uncertainty quantification [183–185]. In the context of artificial neural networks, LHS can be used as a random sampling technique for training data preparation. By randomly selecting input values from an LHS distribution, the resulting training data is more likely to capture the full range of input space and avoid overfitting, resulting in better generalization performance [182, 186].

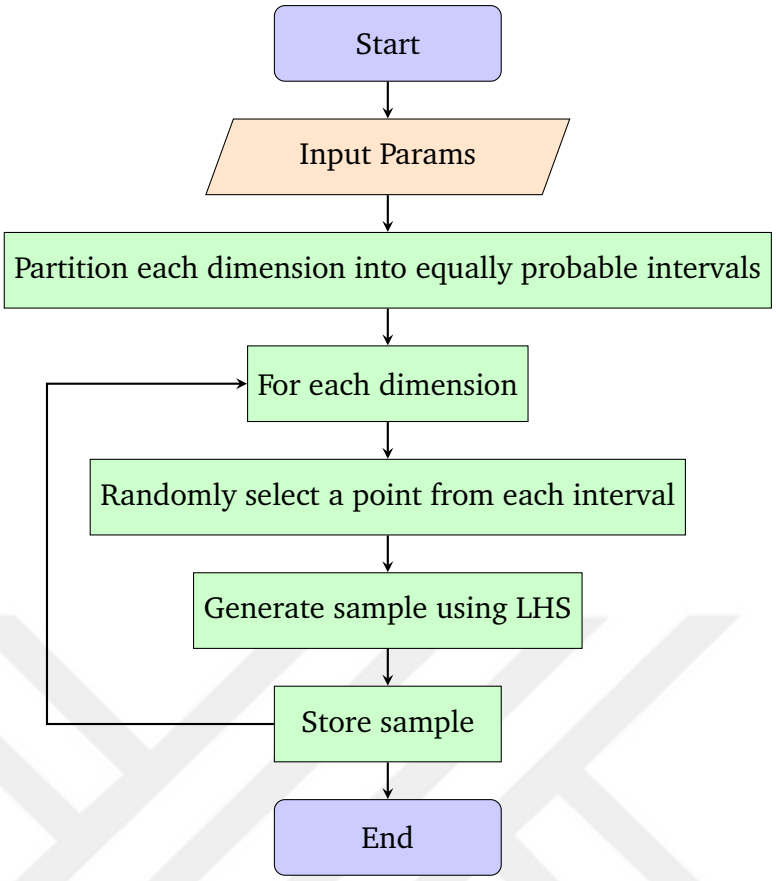

Figure 2.17 Latin Hypercube Sampling (LHS) for creating random population

LHS works by dividing each input variable range into equal intervals and randomly selecting one sample from each interval. This ensures that each sample is well-spaced and representative of the input space. There are various techniques for generating LHS samples, including the algorithm proposed by [183], which iteratively generates a set of Latin hypercube samples by randomly selecting one sample per column, and then shuffling the rows.

In summary, LHS is a powerful and widely used statistical technique for generating well-spaced, representative samples from high-dimensional data spaces. In the context of artificial neural networks, LHS can be used as a random sampling technique for training data preparation, leading to improved generalization performance. Several techniques for generating LHS samples exist, including the algorithm proposed by [183]. A simplified flowchart describing the LHS procedure is given with Figure 2.17.

2.4.3 Genetic Algorithms

Genetic algorithms (GAs) are a family of optimization techniques inspired by the process of natural selection and evolution [131]. These algorithms have been widely

applied to solve various optimization problems due to their ability to search large and complex solution spaces effectively [187]. GAs employ a population-based approach, and their primary components include selection, crossover, and mutation operations, which mimic the principles of survival of the fittest, recombination, and random genetic variations, respectively [188].

There are several types of genetic algorithms, including the canonical genetic algorithm, the steady-state genetic algorithm, and parallel and distributed genetic algorithms [189]. The canonical genetic algorithm is the most basic form, which uses a fixed-size population and applies genetic operations to generate offspring, replacing a portion of the population in each generation. In contrast, the steady-state genetic algorithm updates the population continuously by replacing one or a few individuals at a time. Parallel and distributed GAs exploit the power of parallel computing to perform multiple searches simultaneously, improving the efficiency and effectiveness of the search process.

Genetic algorithms differ from traditional optimization methods in several ways. First, GAs work with a population of solutions, whereas traditional methods typically focus on a single solution. This population-based approach allows GAs to explore multiple regions of the search space simultaneously, reducing the risk of converging to a local optimum [190]. Second, GAs operate on encoded representations of solutions rather than the solutions themselves, allowing them to handle discrete and combinatorial problems more effectively than gradient-based methods, which require continuous and differentiable objective functions [131]. Third, GAs are adaptive and stochastic in nature, which makes them more robust to changes in the problem and less sensitive to the initial conditions, in contrast to deterministic methods that can be heavily influenced by the starting point [189].

A typical genetic algorithm formulation consists of several key steps that guide the search process towards an optimal solution in a systematic and efficient manner [131]:

- **Initialization:** The first step in a GA is to create an initial population of candidate solutions, often generated randomly [187]. The population size, which is an essential parameter, is determined based on the problem complexity and computational resources available [189].
- **Evaluation:** Each individual in the population is evaluated using a fitness function that quantifies the quality of the solution concerning the optimization objective(s) [188]. The fitness function plays a crucial role in guiding the search process, and its design significantly influences the algorithm's performance

[190].

- **Selection:** The selection operator chooses individuals from the current population to create a mating pool, favoring those with higher fitness values. Various selection strategies exist, such as roulette wheel selection, tournament selection, and rank-based selection, each with its advantages and drawbacks [189]. Roulette wheel selection, also known as fitness proportionate selection, is one of the earliest and most widely used selection techniques [187]. In this method, the probability of selecting an individual is proportional to its fitness relative to the total fitness of the population. This approach ensures that fitter individuals have a higher chance of being chosen for reproduction, but it may lead to premature convergence if a small number of individuals dominate the selection process [131]. Tournament selection, introduced by Goldberg and Deb [191], addresses some of the issues associated with roulette wheel selection. In this method, a fixed number of individuals are randomly chosen from the population to participate in a "tournament," with the winner being the fittest among them. By adjusting the tournament size, the selection pressure can be controlled, allowing for a balance between exploration and exploitation [189]. Rank-based selection, proposed by Baker [192], focuses on the relative fitness of individuals rather than their absolute fitness. The population is sorted according to their fitness values, and the selection probability is assigned based on their rank. This method reduces the impact of extremely fit individuals on the selection process, promoting diversity and preventing premature convergence [189]. Elitism, though not a standalone selection method, is often incorporated into other selection techniques to ensure that the best individuals in the population are preserved across generations [193]. By retaining the fittest individuals, elitism can prevent the overall fitness from decreasing and help maintain the search's direction towards optimal solutions [188].

- **Crossover:** The crossover operator combines the genetic material of selected parents to generate offspring, mimicking the process of recombination in natural evolution [187]. Crossover methods include single-point, multi-point, and uniform crossover, among others, and the choice of a suitable crossover operator depends on the problem representation and the desired exploration-exploitation trade-off [188]. Single-point crossover, introduced by Holland (1975), is the simplest and most intuitive crossover method. In this technique, a random crossover point is chosen along the parent chromosomes, and the genetic material is exchanged after this point to create the offspring. Although easy to implement, single-point crossover can disrupt beneficial building blocks in the solutions, known as schemata, which may hinder the GA's performance.

Multi-point crossover, or n-point crossover, generalizes single-point crossover by using multiple crossover points [131]. By exchanging genetic information at several points along the chromosomes, multi-point crossover aims to preserve schemata more effectively and reduce the disruptive effect of the recombination process. Uniform crossover, proposed by Syswerda [194], is another popular crossover technique that operates at the gene level. Instead of using fixed crossover points, uniform crossover randomly chooses which parent contributes each gene to the offspring, with a predefined mixing ratio. This method allows for a more fine-grained exploration of the search space and can be particularly beneficial when the problem representation does not exhibit strong locality. Order-based crossover methods, such as partially mapped crossover (PMX) by Goldberg and Lingle [195] and cycle crossover by Oliver *et al.* [196], have been specifically designed for permutation-based problems.

- **Mutation:** The mutation operator introduces small random perturbations in the offspring's genetic material to maintain diversity in the population and prevent premature convergence [131]. Mutation rates and strategies vary depending on the problem and representation, with common approaches including bit-flip, swap, and Gaussian mutation [189].
- **Replacement:** The new offspring are integrated into the population, replacing some or all of the current individuals, depending on the GA variant (canonical, steady-state, or others) [190]. Replacement strategies can be generational, where the entire population is replaced, or elitist, where the best individuals are preserved to ensure that the overall fitness does not decrease [188].
- **Termination:** The algorithm iterates through steps 2-6 until a termination criterion is met, which could be a predefined number of generations, a convergence threshold, or a combination of factors.

A simplified flowchart of the process is also given in the Figure 2.18. The main challenge in inverse analysis lies in the ill-posed nature of the problems, which often exhibit non-uniqueness, instability, or non-linearity in the solution space [197]. Genetic algorithms (GAs) have been employed as a popular and effective optimization technique to address these challenges in inverse analysis [198]. The population-based search mechanism and global optimization capabilities of GAs make them well-suited for solving ill-posed inverse problems [199]. GAs have been used in various applications, including the identification of material parameters in solid mechanics [200].

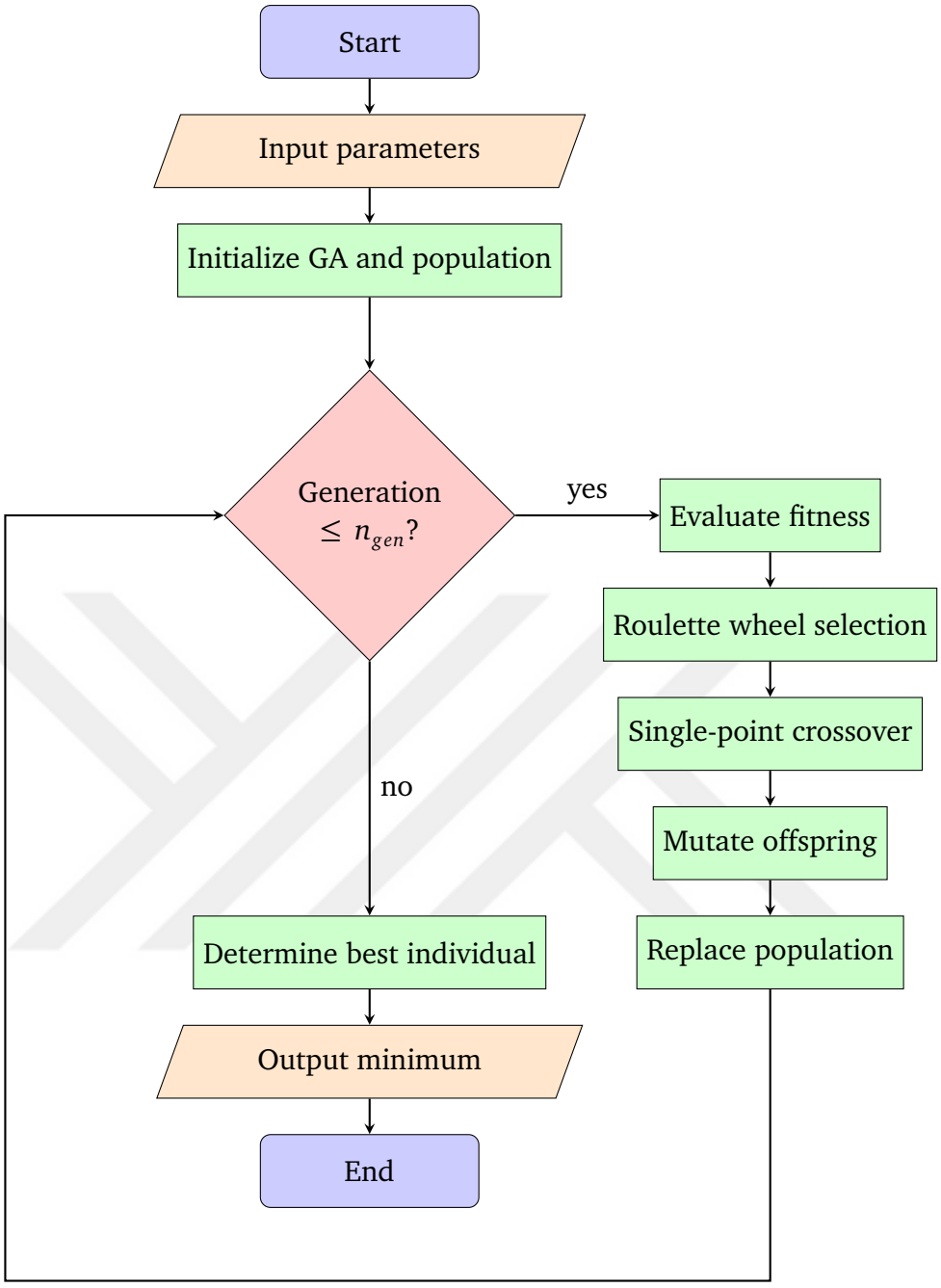

Figure 2.18 Genetic Algorithm with Single Point Crossover

2.4.3.1 Multiobjective Optimization

In practice, the process of calibrating or validating models typically involves minimizing discrepancies between observed and simulated data across several performance metrics. These metrics can be in conflict with one another, and optimizing one may lead to the deterioration of another. Multi-objective optimization algorithms, such as NSGA-II, provide a means to navigate these trade-offs and identify a diverse set of Pareto-optimal solutions that represent the best compromise between the competing objectives.

Multiobjective optimization, also known as multi-criteria or multi-objective decision making, is an optimization process where multiple conflicting objectives must be optimized simultaneously [190]. In real-world applications, it is often necessary to balance trade-offs between various objectives, as improving one may result in the degradation of another. Genetic algorithms (GAs) have emerged as a powerful tool for solving multiobjective optimization problems due to their population-based search mechanism and inherent parallelism [201].

In multiobjective optimization, the concept of Pareto optimality is of critical importance. A solution is said to be Pareto optimal if no other solution can improve one objective without worsening another [190]. The goal of multiobjective optimization using GAs is to identify a set of Pareto-optimal solutions that provide decision-makers with a range of alternatives, thereby enabling a better understanding of the problem's solution landscape [202]. Multi-objective optimization encourages the consideration of multiple performance criteria during the inverse analysis process. This can lead to better model performance, as calibrating a model to multiple objectives simultaneously can help identify deficiencies or biases that might be overlooked when optimizing for a single objective.

Several multiobjective genetic algorithms have been proposed in the literature, such as the Non-dominated Sorting Genetic Algorithm (NSGA-II) [203], the Strength Pareto Evolutionary Algorithm (SPEA2) [204], and the Multiobjective Evolutionary Algorithm based on Decomposition (MOEA/D) [205]. These algorithms differ in their selection, crossover, and mutation operators, as well as their strategies for handling the Pareto front and maintaining diversity among the solutions [201].

A critical aspect of multiobjective optimization with GAs is the selection of appropriate performance metrics to assess the quality of the obtained Pareto front. Common performance metrics include the hypervolume indicator, the generational distance, the inverted generational distance, and the epsilon indicator [206]. These metrics provide insights into the convergence, diversity, and distribution of the solutions along

the Pareto front [201].

The optimization performance of genetic algorithms is influenced by multiple factors, each playing a critical role in determining the efficiency and effectiveness of the search process [131, 207]. Appropriate population size and initialization are vital for adequate search space exploration and convergence [208]. The fitness function should be well-designed to guide the GA towards optimal solutions [131]. Selection strategy, crossover operator, and mutation operator and rate are crucial for balancing exploration and exploitation [190]. Furthermore, the replacement strategy determines the integration of offspring into the population, affecting convergence behavior [208]. Termination criteria control the stopping point of the algorithm, impacting overall performance. Additionally, algorithm variants and problem representation can influence the efficiency of the search process [207].

2.4.3.2 Non-dominated Sorting Genetic Algorithm II (NSGA-II)

The Non-dominated Sorting Genetic Algorithm II is a multi-objective optimization algorithm that has gained widespread recognition in recent years due to its robust performance and adaptability in solving various optimization problems. Introduced by Deb *et al.* [203], the algorithm is designed to tackle the challenges posed by multiple conflicting objectives in the optimization landscape. It employs a non-dominated sorting approach coupled with a crowding distance measure to maintain diversity in the population while evolving towards the Pareto-optimal front. The main procedure of NSGA-II involves the following steps:

- **Initialization:** A population of candidate solutions is randomly generated, where each solution is represented by a set of decision variables.
- **Evaluation:** Each candidate solution is evaluated by computing its fitness based on multiple objective functions. The objective functions are typically conflicting, meaning that improving one objective may lead to a decrease in another objective.
- **Non-dominated sorting:** The candidate solutions are sorted into multiple levels based on their non-domination relationships. A solution is non-dominated if there is no other solution that is better in all objectives. Solutions in the first level are non-dominated by all other solutions, solutions in the second level are non-dominated by all solutions in the first level and so on.
- **Crowding distance assignment:** Solutions in the same level are then assigned a crowding distance metric based on their distance to neighboring solutions.

This metric is used to ensure that the diversity of the population is maintained during selection.

- **Selection:** A new population is then created by selecting solutions from the different levels and based on their crowding distance metric.
- **Variation:** The selected solutions are then subjected to genetic operators such as crossover and mutation to create new candidate solutions.
- Repeat steps 2 to 6 until a termination criterion is met, such as reaching a maximum number of generations or a satisfactory level of convergence.

The main difference between NSGA-II and the standard multi-objective optimization procedure lies in the non-dominated sorting and crowding distance assignment steps. These steps are used to maintain the diversity of the population and avoid premature convergence to a single optimal solution. In contrast, the standard multi-objective optimization procedure typically uses a weighted sum method to combine the objectives into a single fitness function, which can lead to a biased search towards a particular region of the solution space.

The non-dominated sorting step is a crucial component of the NSGA-II algorithm, which is used to partition the population of candidate solutions into different levels of non-dominated fronts. Non-dominated sorting is performed based on the concept of Pareto dominance, which is a fundamental principle in multi-objective optimization that characterizes the superiority of one solution over another in terms of objective function values.

2.4.4 Meta-Modelling in Inverse Analysis

Meta-modelling, also known as surrogate modelling, has become an essential tool for addressing complex and computationally expensive engineering problems, particularly in inverse analysis applications [209, 210]. Inverse analysis seeks to estimate unknown parameters or system properties based on observed data, often involving the minimization of a discrepancy between model predictions and measurements [197]. Any instance of artificial neural network application intended to establish relation between input and output parameters of an engineering problem is also an example of meta-modelling.

Meta-modelling process for an inverse analysis problem, which aims to approximate the objective function (e.g., cost) is done through several key steps. First, an approximative model, such as an artificial neural network, is estimated, requiring

numerous simulations, appropriate topology determination, and training to minimize the error between the original and approximative models. This model maps a few inputs to tens or hundreds of outputs, presenting a complex task for the artificial neural network. Secondly, optimization is performed on the approximative model using either experimental or reference simulated data to determine the corresponding inputs. Following this, the first verification step involves comparing the identified inputs with the original input data for a reference data pair, ensuring the accuracy of the identification procedure. The second verification step entails simulating the computational model using the identified input data and comparing the resulting outputs to the reference outputs. Lastly, validation is conducted by executing the optimization process on experimental data and using the identified inputs to simulate the computational model. The obtained outputs are then compared with the experimental outputs to assess the performance of the meta-model [129].

An interesting approach in meta-modelling involves the approximation of the error function rather than the objective function [211]. By constructing a surrogate model that captures the relationship between the input parameters and the error in the model predictions, researchers can focus on minimizing the error directly. This approach can lead to improved accuracy and robustness in the inverse analysis, especially when dealing with noisy or incomplete data [212].

The main difference between meta-modeling of an error function and meta-modeling of an objective function lies in the nature of the mapping between inputs and outputs. In the case of meta-modeling the error function, an approximative function (FF) is established to represent the error function (F). The inputs to this function remain unchanged, but the number of outputs typically reduces to a single value, representing the error. This process simplifies the task of approximating the error function compared to the objective function. In certain situations, multiple objectives may be incorporated into the error function, leading to a multi-objective formulation. However, even in these cases, determining an approximative error function (FF) is generally less complex than determining an approximative model (M).

On the other hand, when meta-modeling the objective function, the focus is on approximating the original model (M) with its multiple outputs. This task can be more complicated due to the increased complexity of the mapping between inputs and outputs, and the need to accurately represent the relationships between them.

3
IMPLEMENTATION OF THE SIMULATION FRAMEWORK

3.1 Overview

The literature survey presented in Chapter 2 revealed that the finite element method provides possibilities for reinforced concrete joint modeling with varying degrees of complexity. The complexity range starts with a single uniaxial spring and goes to various plasticity models coupled with damage definitions. The survey also points out that the complex is not always the best under every condition. Once the complexity of the physical phenomenon increases, the numerical model representing it is often computationally more expensive and requires more parameters, some of which are not measurable directly from the physical definition of the problem. This often requires a parametric search of the mentioned parameters for each individual simulation, where the aim is to calibrate the simulation model parameters so that they can represent the experimentally observed response.

A significant conceptual issue arises at this point: simulation models are created to avoid costly experiments. Improving the fundamental understanding of a physical problem (i.e., damage initiation and evolution in reinforced concrete beam-to-column joints) requires the exploration of a large domain of effective variables that define the problem of interest and its corresponding output. In other words, simulations are done to imitate and replace experiments, but they need more and more experiments to be refined.

Depending on the nature of the problem, this exploration process can be conducted using a variety of methods. It is possible to conduct only experimental investigations, but experiments can be expensive, time-consuming, and sometimes impractical, especially in scenarios involving large-scale systems or hazardous conditions. Additionally, certain phenomena may be challenging to capture experimentally due to technical constraints. On the other hand, simulations offer the opportunity for extensive parametric studies, enabling researchers to systematically vary input parameters and observe their effects on the system's behavior. This ability to

explore the problem domain enhances the understanding of the underlying processes, facilitates optimization efforts, and guides the design of experiments by identifying critical variables and refining experimental protocols. Nevertheless, simulations must be appropriately validated and verified to ensure their accuracy and reliability. Validation involves comparing simulation results against experimental data to assess the model's ability to reproduce observed phenomena. Verification, on the other hand, focuses on confirming the correctness of the simulation implementation. While verification and validation establish the correctness and accuracy of the simulation models, calibration ensures their ability to replicate experimental results. The extent of calibration required may vary depending on the complexity of the simulation models employed.

In complex simulation models (e.g., advanced finite element models employed in the studies introduced in Chapter 5), calibration plays a crucial role due to the complicated nature of the phenomena being studied. These models typically involve a variety of variables, and in such cases, calibration becomes essential to refine the model's behavior and achieve agreement with experimental observations. By iteratively adjusting model parameters, calibration seeks to minimize the discrepancies between simulated and experimental results. This process helps improve the model's predictive capabilities and enhances its ability to capture the complex aspects of the real-world system. However, it is crucial to consider the risks associated with calibration, particularly the dangers of overfitting the model to specific experimental data. Overfitting occurs when a simulation model becomes excessively tailored to match experimental results, losing its generalization capabilities. This can lead to an overly complex model that is unable to accurately predict outcomes beyond the specific calibration data. Therefore, caution must be exercised to strike a balance between fitting the model to experimental data and maintaining its ability to generalize to broader scenarios. In contrast, relatively simplified simulation models (e.g., finite element models composed of uniaxial springs employed in the investigations introduced in Chapter 4), often employed to handle computationally challenging problems, may require less extensive calibration. These models, which will be referred to as "simplified models" or "super-element models" in this manuscript, aim to capture only the essential characteristics of the system while omitting relatively less significant details and complexities. Due to their reduced complexity, simplified models may rely on fewer adjustable parameters and exhibit less sensitivity to calibration. By focusing on the fundamental aspects and key trends, these models can offer insights into the underlying mechanisms. However, even in simplified models, calibration is necessary to ensure that the fundamental behavior and key trends observed in experiments are adequately represented. Simplified models often require fewer

calibration parameters, making them less susceptible to overfitting and reducing the risk of tailoring the model excessively to specific calibration data. On the other hand, complex models, while capable of providing a more detailed representation, inherently carry a higher risk of overfitting during the calibration process. With a larger number of adjustable parameters, complex models possess a greater capacity to fit the model's behavior closely to the calibration data. However, this level of calibration precision may come at the expense of generalization as the model becomes too finely tuned to the specific calibration dataset. The lack of generalization in the existing model poses a challenge for accurately representing the desired task. To achieve generalization, calibration using a substantial amount of experimentally observed data is necessary. However, conducting a large number of experiments is both difficult and costly.

This thesis proposes a solution by expanding the calibration dataset through the application of artificial intelligence techniques. This approach is crucial in developing a practical and robust joint element simulation, particularly for withstanding the severe effects of earthquakes. By considering joint inelastic deformations, the proposed method contributes to the advancement of performance-based design and assessment processes. Complex models with sophisticated definitions often fail to provide generalized solutions due to the need for extensive fine-tuning and high computational costs. However, with instance specific calibration, the beamcolumnjoint element in OpenSees, combined with the pinching4 material definition, is explicitly proven to lead to realistic inelastic deformations in concrete (shear), reinforcement, and bar-slip mechanisms [16, 65, 75, 79, 213]. The use of explicit elements for joints has been recognized as a valuable strategy for enhancing predictions regarding the failure mode and characteristic behavior of reinforced concrete frames. By explicitly considering joint behavior, a more comprehensive evaluation of the structural response can be achieved [9, 10, 214].

The thesis focuses on developing and evaluating a calibration approach that is supported by a larger domain of model parameters that can be covered solely by experimental investigations. The Figure 3.1 illustrates the research concept. As it is discussed in detail in Section 2, it is essential to emphasize that the accuracy of this representation heavily relies on the proper definition of the pinching4 model parameters. The material model requires two sets of model parameters: the first is the definition of joint shear strain and shear stress envelope *(envelopeParams)*, and the second is the calibration parameters controlling the deterioration equations *(deteriorationParams)*. In Chapter 5 and Chapter 4, two distinct prediction models on *envelopeParams* are proposed based on advanced finite element techniques and artificial neural networks, respectively. For accurate calibration of *deteriorationParams* for a given reinforced concrete joint sub-assemblage, another prediction model

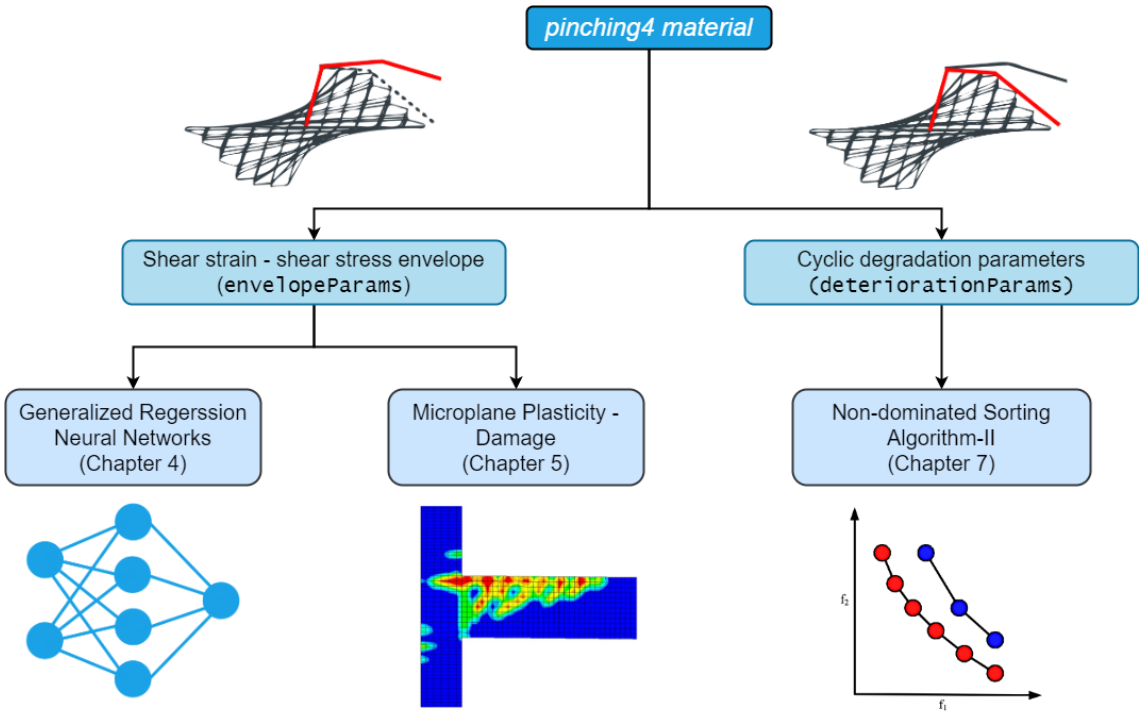

Figure 3.1 General organization diagram of the present research

which utilizes multi-objective optimization and artificial neural network techniques is introduced in Chapter 6.

The MATLAB implementation of the simulation framework used in this investigation is designed to be object-oriented, meaning that it uses objects to represent different components of the simulation model. This approach allows for greater flexibility and modularity in the code, making it easier to modify and extend as needed. A brief introduction of the class structure and workflow of the simulation framework is introduced in this chapter. Also, the *beamcolumjoint* element and *pinching4* material formulations and the theoretical foundations on which they are based will be explained in addition to the details given in Section 2.3.1.

3.2 The Open System for Earthquake Engineering Simulation (OpenSees)

OpenSees, or Open System for Earthquake Engineering Simulation, is an open-source software framework that specializes in simulating the behavior of structural and geotechnical systems under seismic loading, developed by the Pacific Earthquake Engineering Research Center (PEER) at the University of California, Berkeley. OpenSees provides researchers and engineers with a powerful and flexible tool for advancing the field of earthquake engineering through the development of innovative

simulation models and techniques. The software is designed with a modular architecture, allowing users to build complex, large-scale models using a combination of pre-built and user-defined elements, materials, and solution algorithms.

One of the significant capabilities of OpenSees is its ability to simulate reinforced concrete (RC) structures and joints. The software offers a wide array of element types and material models specifically tailored for RC components. These elements and models can accurately capture the non-linear behavior of concrete and reinforcing steel, such as cracking, crushing, and yielding. Additionally, OpenSees can handle the complex interaction between the reinforcement and the surrounding concrete, which is crucial for understanding the behavior of joints under various loading conditions.

In the context of reinforced concrete joint simulation, OpenSees enables researchers and engineers to study the performance of beam-column joints, slab-column joints, and other types of connections commonly found in RC structures. The software can account for various joint configurations and reinforcement detailing practices, making it possible to evaluate the influence of different design choices on the overall performance of the joint. Furthermore, OpenSees can simulate the impact of confinement, shear transfer mechanisms, and bond-slip effects on joint behavior, which are essential factors to consider in seismic design.

In structural engineering problems with any level of plasticity involved, consideration of the assumption on the dissipation of plastic strains is quite important in terms of accuracy and computational cost. Distributed plasticity models, also known as continuous or fiber-based plasticity models, consider the plastic behavior distributed along the entire length of the element. These models account for the gradual spread of plasticity and provide a detailed representation of the strain distribution across the cross section and along the length of the member. They typically involve the integration of the stress-strain response of many individual fibers within a cross-section to accurately capture the overall behavior. This method can provide a more accurate and realistic representation of the structural response, but it comes with higher computational cost due to the increased complexity and number of computations involved [215]. Lumped plasticity models, or concentrated plasticity models, assume that plastic deformation occurs only at discrete points within the structure, usually at the ends of the elements. In these models, the interior of the member is assumed to remain elastic, and all the inelastic behavior is concentrated into these plastic hinge regions. These models are simpler and more computationally efficient than distributed plasticity models, making them suitable for large scale problems or for preliminary design studies where a detailed representation of the strain distribution is not required. However, they might not be able to capture the detailed strain distribution as

accurately as the distributed plasticity models [216]. The choice between lumped and distributed plasticity models is a trade-off between computational efficiency and the level of detail in the representation of the strain distribution. The choice of the appropriate model will depend on the specific requirements of the analysis and the characteristics of the problem. In the present study, beams and columns framing to the joint element are modelled with distributed plasticity approach.

OpenSees is also widely acknowledged for its impressive assortment of capabilities regarding material and element formulations. This software platform, with its diverse methodologies for approximating plastic deformations, has found extensive use in academic literature for simulating joint responses under cyclical effects. The versatility and applicability of OpenSees in a variety of research contexts is demonstrated by its extensive use in exploring the complexities of material behavior under different loading conditions.

In this section, a comprehensive discussion is conducted on the general assumptions and formulations that are essential for the finite element analysis of reinforced concrete joints, with a focus on the application of super-elements. The objective is to illuminate the nuances of selecting and using appropriate elements within the broader context of OpenSees simulations. The impact that various assumptions and element formulations can have on the accuracy and realism of simulated joint responses is of particular interest.

3.2.1 Material definition

One of the standout features of OpenSees is its extensive material modeling capabilities, which cover a broad range of material behaviors, allowing for various simulation cases. Among many material models, a wide range of constitutive formulations are given in *uniaxialMaterial* class where the stress-strain (i.e. force-displacement) relationship is represented by a uni-axial implementation. Discussion in this subsection will be introducing material models commonly used in the simulation of reinforced concrete elements including beam-to-column joints.

Beyond the implementations provided for simple uniaxial constitutive relations provided for linear elastic, elastic and perfectly plastic and elastic with no tension material (e.g. *Elastic*, *ElasticPP*, *ENT* respectively), a large variety of material formulations for complex non-linear constitutive stress strain relationship of concrete and steel materials is implemented (or contributed by various researchers) in OpenSees. For instance, *Concrete01* material uses formulation provided by Scott *et al.* [33] model with degraded linear unloading-reloading stiffness based on the findings

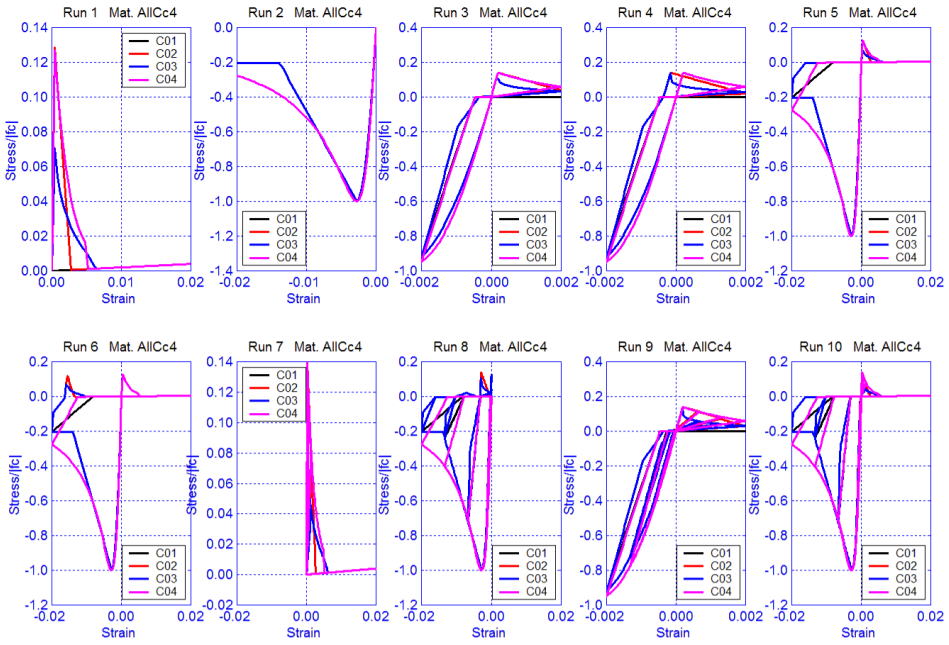

Figure 3.2 Comparison of the response of the concrete material classes implemented in Opensees for different loading histories

of Karsan and Jirsa [217] while assuming zero tensile strength. *Concrete02* provides a similar formulation but adding tension strength to the material with capability of linear tension softening while *Concrete03* uses a control parameter β that enables non-linear definition for tension softening. An advanced implementation of concrete material under cyclic loads is provided with *Concrete04* material class using the compressive strain stress path proposed by Popovics [218].

Similar to the concrete, various material classes for steel (or reinforcement steel) with varying degrees of sophistication are provided. *Steel01* is implemented based on the bi-linear force deformation relation with kinematic hardening. The *Steel02* material class is similarly takes into account a bilinear deformation curve with smoother transition. The theoretical formulation used in formulation introduced by Menegotto and Pinto [219] and later improved by Filippou *et al.* [220]. As the simulation results of uniaxial spring units with *Steel01* and *Steel02* material models shown in Figure 3.3 present, there is very slight difference between the responses produced by two material classes, mainly on the smoothing of the transition between elastic and elastoplastic regime [221]. However, it is worth noting that smooth transition between two regimes might help to solve convergence issues in finite element simulations of complex numerical models.

Figure 3.2 and Figure 3.3 show the comparison of the concrete and steel material

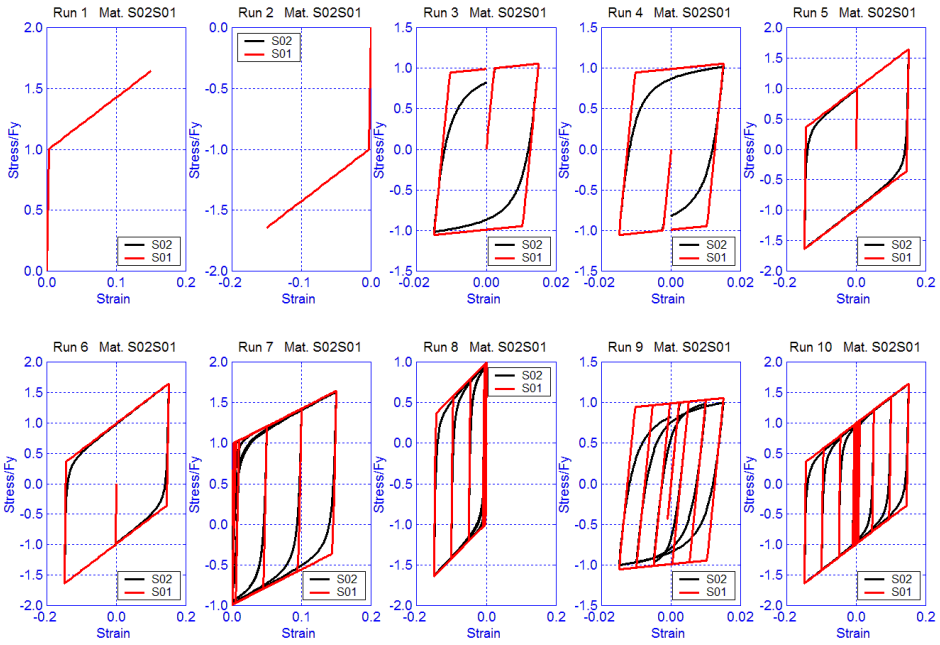

Figure 3.3 Comparison of the response of the steel material classes implemented in Opensees for different loading histories

classes strain stress response under a series of displacement loading histories, respectively. In the first run, strain is applied in one direction, specifically tension, unveiling how the material deforms and responds to unidirectional tensile stress. This contrasts to the second run, where strain is applied solely in compression, providing insight into the material's behavior under the opposing stress. The third and fourth runs introduce cycling of tension and compression at a low maximum-strain level. Here, the distinction lies in the starting point of the cycle, with the third run beginning with tension and the fourth with compression. These runs grant us the opportunity to explore the material's hysteresis behavior and understand its capacity to regain its original shape after deformation. Run five and six escalate the previous procedure to a higher maximum strain level, testing the material's resilience under larger deformations. Again, the difference lies in the starting point, tension for the fifth run and compression for the sixth. Runs seven through ten introduce a more complex scenario. Here, numerous cycles with increasing amplitude are applied. In the seventh run, these cycles go up to a high maximum-strain level but remain solely in tension. This pattern is expected to repeat in the eighth run, assuming it might be intended to be applied in compression. The last two runs add another level of complexity by applying these increasing amplitude cycles in both tension and compression. Run nine goes up to a low maximum strain level, while run ten goes up to a high maximum-strain level. These latter runs particularly shed light on the material's fatigue behavior under both tensile and compressive loads. Through these diverse

loading patterns, a comprehensive overview of the material's mechanical behavior under various conditions is obtained.

3.2.1.1 *pinching4* class

Beyond the representation of the relation between strain and stress for the various materials, uni-axial material class in OpenSees is also commonly used to define the force-displacement of macro-models (e.g. super-elements) which are intended to simulate the response of the structural elements but requiring model parameters do not correspond to direct measurable physical quantities.

In Section 2.3.2, a brief discussion is made on the *pinching4* material class, its assumptions and formulation since it is commonly used in a wide range of macro-models for reinforced concrete elements including joints. Among other material classes implemented in the software, *pinching4* is found particularly suitable for modeling the hysteretic response of reinforced concrete joints or masonry structures where significant pinching of the hysteresis loops is typically observed due to crack opening and closing, shear distortion and bond deterioration [16, 75].

In this study, the focus has been centered on the simulation of reinforced concrete joints, a critical component in structures that often exhibits complex behavior under cyclic loading. To capture this nuanced response, the *pinching4* material model in OpenSees was chosen, largely due to its inherent ability to replicate the characteristic 'pinching' phenomenon frequently observed in such joints. This phenomenon, typically resulting from bond deterioration or other related mechanisms, manifests as a narrowed or pinched shape of the hysteresis loops in the stress-strain behavior of the material.

The *pinching4* model through its detailed mathematical formulation presented in Mazzoni *et al.* [222], allows for the accurate representation of this behavior, thereby providing a reliable tool for predicting the response of reinforced concrete joints under various loading conditions. It should be noted that, while other material models exist within the literature that are capable of capturing complex hysteretic behavior, the *pinching4* model was selected specifically for its suitability for joint simulations. As such, a comparative evaluation of these alternative material models was not undertaken as part of this study.

pinching4 material is introduced following its definition in Mitra [65] since it is used within the scope of the present study due to its proven reliability and stronger connection of its parameters to the observable measures of a joint specimen.

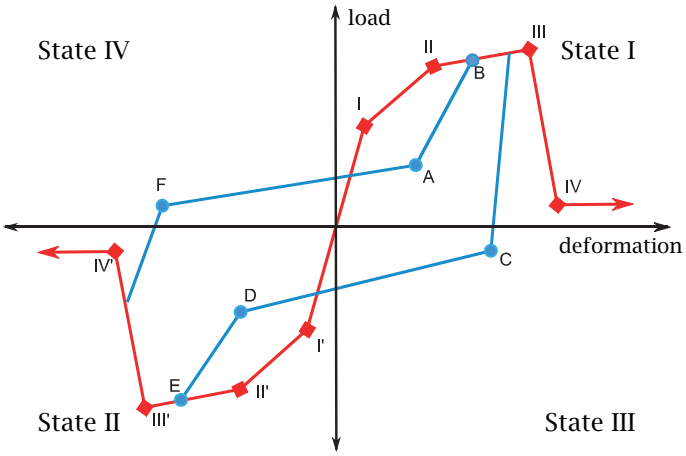

Figure 3.4 Backbone (red) and hysteretic response of *pinching4* material [65]

The four material states in Figure 3.4 define the material model's behavior under diverse loading conditions. States I and II, user-defined input parameters, represent the loading response envelope and can be adjusted to simulate hysteretic strength degradation. The load-paths for states III and IV are redefined with each deformation reversal. Additional load-deformation points establish state III and state IV load paths: one reached during significant unloading and another where considerable reloading occurs. For states III and IV, the load during unloading is defined as a fraction of the absolute maximum attainable. This sets the end of the substantial unload phase. The load-deformation point for substantial reloading in states III and IV is determined as a fraction of the absolute maximum historic deformation demand and a fraction of the load developed at the absolute maximum deformation demand.

Deformation history impact on response is determined by three damage rules that govern degradation in unloading stiffness, deterioration in strength achieved at previously unattained deformation demands, and deterioration in strength near maximum and minimum deformation demands. Each rule utilizes a damage index, δ defined with Equations 3.1 and 3.2.

$$\delta = \left(\alpha_1(\dot{d}_{max})^{\alpha_3} + \alpha_2(\kappa)^{\alpha_4}\right) \leq \delta_{lim} \tag{3.1}$$

$$\hat{d}_{max} = max\left(\frac{d_{max}}{D_{max}}, \frac{d_{min}}{D_{min}}\right) \tag{3.2}$$

In equation 3.1, α are parameters tailored to fit experimental data, δ_{lim} represents the maximum possible damage index value which is used for numerical stability, d_{max} and d_{min} denote the maximum and minimum historic deformation demands, D_{max} and

D_{min} indicate the positive and negative deformations at which strength loss starts in states I and II, subscript i pertains to the current load step, and κ measures energy dissipation under cyclic loading, as outlined in Equations 3.3 and 3.4. Accumulated hysteretic energy is given by 3.5

$$\kappa = \frac{E_i}{E_{monotonic}} \tag{3.3}$$

$$\kappa = \sum \left| \frac{du}{4u_{max}} \right| \tag{3.4}$$

$$E_i = \int_{history} dE \tag{3.5}$$

$E_{monotonic}$ equals the energy required to achieve D_{max} under monotonic loading, du corresponds to the displacement in a load-deformation history, and u_{max} refers to the deformation achieved up to the current load step i.

Stiffness and strength degradation are defined in Equations 3.6, 3.7, and 3.8. k represents the unloading stiffness, d_{max} is the unloading stiffness damage index, f_{max} is the maximum strength of the response envelope, δ_i^f is the strength damage index, d_{max} is the maximum historic deformation demand and reloading target, δ_i^d is the reloading stiffness damage index, and subscripts i and 0 refer to load step i and the initial load step, respectively.

$$k_i = k_0(1 - \delta_i^k) \tag{3.6}$$

$$f_{max,i} = f_{max,0}(1 - \delta_i^f) \tag{3.7}$$

$$d_{max,i} = d_{max,0}(1 + \delta_i^d) \tag{3.8}$$

In OpenSees, *pinching4* model is implemented as a material class that its constructor requires inputs to utilize the formulation described by Equations 3.1 - 3.8. The first set of input parameters (referred to as *envelopeParams* in this study) control the basic strain-stress behavior of the material. Brief description of the first set is given below.

- *stress1p, stress2p, stress1n, stress2n:* These parameters represent the stress levels at specific points on the stress-strain curve. *stress1p* and *stress2p* refer to positive (tensile) stress levels, and *stress1n* and *stress2n* refer to negative (compressive) stress levels.

- *strain1p, strain2p, strain1n, strain2n:* These parameters represent the strain levels at specific points on the stress-strain curve. *strain1p* and *strain2p* refer to positive (tensile) strain levels, and *strain1n* and *strain2n* refer to negative (compressive) strain levels.

The second set of parameters are for controlling the deterioration (referred to as *deteriorationParams* in this study) features of the material

- *rDispP, rForceP, uForceP, rDispN, rForceN, uForceN:* These parameters represent control points on the hysteresis loop, which describe the material's behavior under cyclic loading. The "P" parameters are for the positive (tensile) direction, and the "N" parameters are for the negative (compressive) direction.

- *gammaK1, gammaK2, gammaK3, gammaK4, gammaKLimit:* These parameters control the rate of deterioration in stiffness under cyclic loading. Different values of gammaK correspond to different stages of deterioration.

- *gammaD1, gammaD2, gammaD3, gammaD4, gammaDLimit:* These parameters control the rate of deterioration in energy dissipation capacity under cyclic loading. Different values of gammaD correspond to different stages of deterioration.

- *gammaF1, gammaF2, gammaF3, gammaF4, gammaFLimit:* These parameters control the rate of deterioration in strength under cyclic loading. Different values of gammaF correspond to different stages of deterioration.

- *gammaE:* This parameter controls the final asymptotic value of cyclic deterioration.

Existing literature suggests that researchers have identified potential values for the parameters of the 'pinching4' material model (see Section 2.3.2). These parameters are grouped into two sets, serving different purposes in the modeling process. The first set forms the definition of the joint panel deformation, a crucial component for a realistic simulation of the overall response envelope and inelastic joint deformations. The second set corresponds to parameters recommended for calibration based on

actual experimental data, although analytical approximations with varying level of accuracy for the first set are also available. The ultimate goal of this study, as stated in the Section 1.2, is to establish prediction models for *pinching4* material usage, thereby removing the need for experimental investigation for any given joint sub-assemblage.

3.2.2 Element Formulations

The Force Method and the Displacement Method are the two primary approaches to structural analysis, as well as finite element analysis. Both are fundamentally about solving the system of equations that comes from equilibrium, compatibility, and constitutive relations. However, they differ in the primary unknowns they consider and the procedures they use to solve the system.

The Force (flexibility) Method takes forces (or moments, in the case of rotational degrees of freedom) as the primary unknowns. In this method, one assembles a flexibility matrix and then solves the system of equations to obtain the forces. Displacements are then computed as secondary results from these forces. This method can be more computationally expensive than the displacement method, especially for large structures, because it requires the inversion of the flexibility matrix. However, it can be more accurate for certain types of problems, such as those involving large displacements or nonlinear material behavior.

In the Displacement Method (also known as the stiffness method), displacements are the primary unknowns. The procedure involves assembling a stiffness matrix (which characterizes how resistant the structure is to deformation) and solving a system of equations to obtain the displacements. Forces are then computed as secondary results from the displacements. This method is most often used in practice, and it is particularly well-suited to computer-based solutions due to its matrix structure.

In the domain of finite element structural analysis, a variety of structures are analyzed, including trusses, beams, plates, shells, or combinations thereof. The stiffness method is a common approach in this field, which involves discretizing the displacement field of the structure and interpolating it in terms of n_{dof} generalized displacement degrees of freedom, symbolized by q. Under the framework of the stiffness method, the displacement field $u(x)$ is formulated as

$$u(x) = N(x)q \tag{3.9}$$

The matrix N is defined as:

$$N = \begin{bmatrix} Nu(x) & 0 & 0 \\ 0 & Nw(x) & 0 \\ 0 & 0 & Nv(x) \end{bmatrix} \tag{3.10}$$

It is a $3 \times n_{dof}$ matrix which encompasses the interpolation function vectors Nu, Nw and Nv for displacement fields u, w and v respectively. For the deformation field $d(x)$, the following expression holds:

$$d(x) = B(x)q \tag{3.11}$$

Here, the strain-displacement transformation matrix B houses first and second derivatives of displacement shape functions, respecting kinematic relationships. On incorporating the differential form Δd of the deformation field equation into the constitutive relation $\Delta D = k\Delta d$, the ensuing relation is:

$$\Delta D(x) = k(x)\Delta d(x) = k(x)B(x)\Delta q \tag{3.12}$$

This gives the force field increment $\Delta D(x)$. By invoking the principle of virtual displacement, we obtain the equilibrium condition:

$$Q = \int_0^L B^T(x)D(x)dx \tag{3.13}$$

This leads to its linearized form:

$$k\delta q = R \tag{3.14}$$

It signifies a force-displacement relation where Q stands for the element resisting forces. The element stiffness matrix is given by:

$$K = \frac{\partial Q}{\partial q} = \int_0^L B^T(x)k(x)B(x)dx \tag{3.15}$$

In this equation, Δq and R are vectors signifying displacement increments and residual forces respectively. The parameter L denotes the element length.

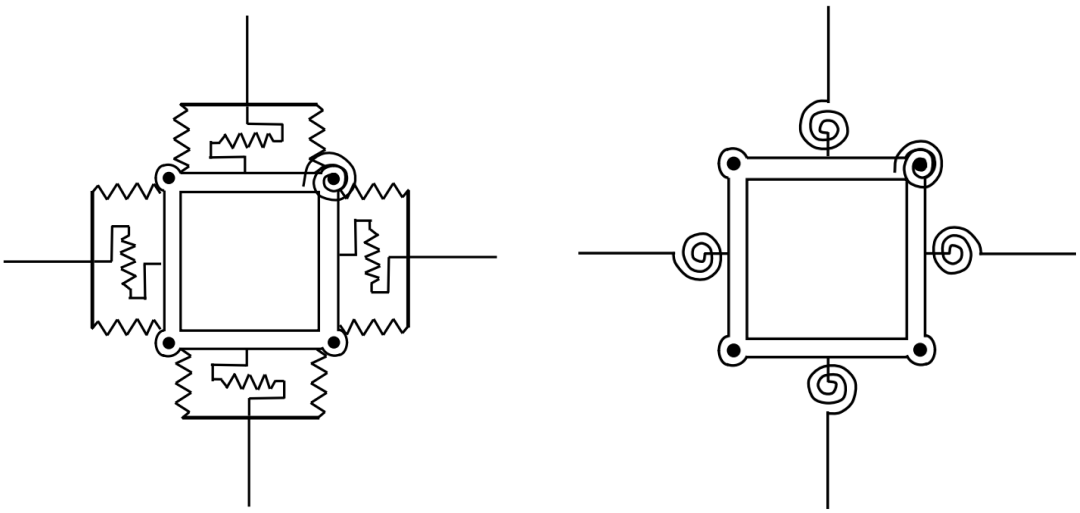

Figure 3.5 Joint model proposed by (a) Lowes and Altoontash [16] and (b) Altoontash [75]

3.2.2.1 Lowes - Altoontash Model

Lowes and Altoontash [16] proposed a comprehensive methodology to model the response of reinforced concrete beam–column joints under two-dimensional structural analyses. The strategy was to introduce a four-node super-element characterized by twelve degrees of freedom. The super-element encapsulated three essential components: a shear-panel component, bar-slip springs, and interface-shear springs, each contributing to the overall behavior of the joint in distinct manners. An illustration of the model is given in Figure 3.5.(a).

The shear-panel component primarily modeled the loss of strength and stiffness, which is attributed to the failure of the joint core. Bar-slip springs, which comprised eight in total, emulated the loss of stiffness and strength induced by damage within the anchorage zone. Lastly, the model also incorporated four interface-shear springs. These were particularly crucial in capturing the diminished capacity for shear transfer at the joint perimeter, a phenomenon that arises due to crack development.

The Lowes and Altoontash [16] employed a one-dimensional load-deformation response model to predict the behavior of these constituent components within the joint element [16]. This model manifested through a multi-linear response envelope, a tri-linear unload-reload path, and three damage rules, each of which played a pivotal role in governing the evolution of the response path. The specific unload-reload path adhered to the definition of the *pinching4* material, a concept extensively discussed in Section 3.2.1.1.

To implement this general load-deformation response model successfully, specific

calibration procedures were deemed necessary for each component of the element. In cases where the joints possess moderate to high volumes of transverse reinforcement, the researchers advocate the utilization of the modified compression field theory (MCFT) [77]. This theory is instrumental in delineating the response of the shear panel and supplying necessary parameters to simulate cyclic response effectively. The bond-slip spring response was defined based on the assumption of a constant or piece-wise constant bond-stress distribution within the joint. Various bond strength values, contingent on different bond-zone conditions, were provided alongside parameters that aid in simulating response under cyclic loading conditions. Lastly, the interface-shear springs were assumed to possess an elastic behavior, largely attributed to the dearth of experimental data available to calibrate these components.

Altoontash [75] presents a refinement to the Lowes and Altoontash [16] Joint Model, a schematic representation of which is depicted in Figure 3.5.(b). This streamlined version features four zero-length rotational springs situated at the interfaces of the beam-column. The purpose of these springs is to replicate the end-rotations of the member arising from bond-slip phenomena. In addition to this, a panel zone rotational spring is incorporated to mimic the shear deformation that occurs within the joint. The constitutive relation for the panel zone remains the same to the model developed by Lowes and Altoontash [16]. This similarity ensures that the calculation of the constitutive parameters, derived from structural properties and experimental responses, remains consistent and comparable. This simplified model, therefore, provides a more streamlined and efficient approach, while maintaining the key features and accuracy of the original formulation.

3.2.2.2 Mitra - Lowes Model

Mitra and Lowes [213] proposed several key modifications to the joint model, initially presented by Lowes and Altoontash [16], aiming to enhance the accuracy of response predictions across a wide range of design parameters. These amendments included a reconfiguration of the joint element where bar-slip springs are now located at the centroid of the beam and column flexural tension and compression zones, an advancement that augments the simulation of bar-slip spring force demands. Simultaneously, a novel model was proposed for calibrating the joint-panel component which, diverging from the uniform shear stress field in the previous model, adopts a diagonal compression strut mechanism for internal load transfer. This effectively simulates strength losses due to cyclic loading and anchorage-zone damage. Lastly, a new bar-slip response model was proposed, which combines hysteretic strength-loss with a model that evades negative stiffness until the reinforcing steel reaches its

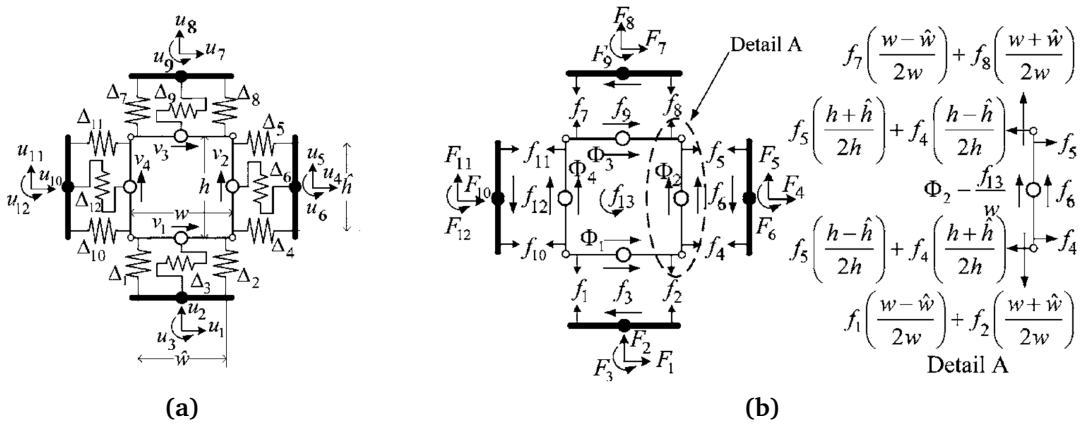

Figure 3.6 External and internal (a) nodal displacements and component deformations (b) nodal forces and component forces [79]

ultimate strength. This approach mitigates numerical instability issues and also refines the unload-reload model to provide an accurate simulation of frictional resistance for bars under tension and compression.

The joint element formulation, as proposed by Lowes and Altoontash [16], was refined to enhance the simulation of the response in the anchorage zone. This was accomplished by transitioning the position of the bar-slip springs from the joint element's periphery to the centroid of the compression and tension zones in the beam and column flexural. Figure a illustrates the component deformations Δ_i, internal nodal displacements v_i, and external nodal displacements u_i. It is essential to note that while the external nodes are shared between the joint element and the surrounding beam-column elements, the internal nodes are exclusive to the joint element. Standard sign conventions apply to the deformations of the bar-slip spring and shear-panel. For the interface-shear springs, a positive shear deformation is associated with positive external and null internal displacement. The component deformations can be expressed in Equation 3.16.

h, w, $\hat{h}$, $\hat{w}$ are as defined in Figure 3.6.(a). The bar-slip spring separation distance, $\hat{h}$ and $\hat{w}$, incorporated into Equation 3.16, provides an improved depiction of the bar-slip response. Figure b presents the component forces f_i, internal nodal resultants Φ_i, and external nodal resultants F_i. The component forces are linked to the component deformations via the one-dimensional load-deformation response relationships. Imposing equilibrium at the internal and external degrees of freedom allows the computation of the external nodal resultants and internal nodal resultants from component forces in Equation 3.17.

$$
\begin{bmatrix}
0 & -1 & \frac{\hat{w}}{2} & 0 & 0 & 0 & 0 & 0 & 0 & 0 & 0 & 0 & 0 & \frac{w-\hat{w}}{2w} & 0 & \frac{w-\hat{w}}{2w} \\
0 & -1 & \frac{-\hat{w}}{2} & 0 & 0 & 0 & 0 & 0 & 0 & 0 & 0 & 0 & 0 & \frac{w-\hat{w}}{2w} & 0 & \frac{w-\hat{w}}{2w} \\
1 & 0 & 0 & 0 & 0 & 0 & 0 & 0 & 0 & 0 & 0 & 0 & -1 & 0 & 0 & 0 \\
0 & 0 & 0 & 1 & 0 & \frac{\hat{h}}{2} & 0 & 0 & 0 & 0 & 0 & 0 & -\frac{h+\hat{h}}{2h} & 0 & -\frac{h+\hat{h}}{2h} & 0 \\
0 & 0 & 0 & 1 & 0 & -\frac{\hat{h}}{2} & 0 & 0 & 0 & 0 & 0 & 0 & -\frac{h+\hat{h}}{2h} & 0 & -\frac{h+\hat{h}}{2h} & 0 \\
0 & 0 & 0 & 0 & 1 & 0 & 0 & 0 & 0 & 0 & -1 & 0 & 0 & & & \\
0 & 0 & 0 & 0 & 0 & 0 & 0 & 1 & -\frac{\hat{w}}{2} & 0 & 0 & 0 & 0 & -\frac{w-\hat{w}}{2w} & 0 & -\frac{w-\hat{w}}{2w} \\
0 & 0 & 0 & 0 & 0 & 0 & 0 & 1 & \frac{\hat{w}}{2} & 0 & 0 & 0 & 0 & -\frac{w-\hat{w}}{2w} & 0 & -\frac{w-\hat{w}}{2w} \\
0 & 0 & 0 & 0 & 0 & 0 & 1 & 0 & 0 & 0 & 0 & 0 & 0 & 0 & -1 & 0 \\
0 & 0 & 0 & 0 & 0 & 0 & 0 & 0 & 0 & -1 & 0 & -\frac{\hat{h}}{2} & \frac{h+\hat{h}}{2h} & 0 & \frac{h+\hat{h}}{2h} & 0 \\
0 & 0 & 0 & 0 & 0 & 0 & 0 & 0 & 0 & -1 & 0 & \frac{\hat{h}}{2} & \frac{h+\hat{h}}{2h} & 0 & \frac{h+\hat{h}}{2h} & 0 \\
0 & 0 & 0 & 0 & 0 & 0 & 0 & 0 & 0 & 1 & 0 & 0 & 0 & 0 & 0 & -1 \\
0 & 0 & 0 & 0 & 0 & 0 & 0 & 0 & 0 & 0 & 0 & 0 & -\frac{1}{h} & \frac{1}{w} & \frac{1}{h} & -\frac{1}{2}
\end{bmatrix}
\begin{bmatrix} u_1 \\ u_2 \\ u_3 \\ u_4 \\ u_5 \\ u_6 \\ u_7 \\ u_8 \\ u_9 \\ u_{10} \\ u_{11} \\ u_{12} \\ v_1 \\ v_2 \\ v_3 \\ v_4 \end{bmatrix}
=
\begin{bmatrix} \Delta_1 \\ \Delta_2 \\ \Delta_3 \\ \Delta_4 \\ \Delta_5 \\ \Delta_6 \\ \Delta_7 \\ \Delta_8 \\ \Delta_9 \\ \Delta_{10} \\ \Delta_{11} \\ \Delta_{12} \\ \Delta_{13} \end{bmatrix}
\tag{3.16}
$$

$$
\begin{bmatrix}
0 & 0 & 1 & 0 & 0 & 0 & 0 & 0 & 0 & 0 & 0 & 0 & 0 \\
-1 & -1 & 0 & 0 & 0 & 0 & 0 & 0 & 0 & 0 & 0 & 0 & 0 \\
\frac{\hat{w}}{2} & \frac{-\hat{w}}{2} & 0 & 0 & 0 & 0 & 0 & -\frac{\hat{w}}{2} & \frac{\hat{w}}{2} & 0 & 0 & 0 & 0 \\
0 & 0 & 0 & 1 & 1 & 0 & 0 & 0 & 0 & 0 & 0 & 0 & 0 \\
0 & 0 & 0 & 0 & 0 & 1 & 0 & 0 & 0 & 0 & 0 & 0 & 0 \\
0 & 0 & 0 & \frac{\hat{h}}{2} & -\frac{\hat{h}}{2} & 0 & 0 & 0 & 0 & -\frac{\hat{h}}{2} & \frac{\hat{h}}{2} & 0 & 0 \\
0 & 0 & 0 & 0 & 0 & 0 & 0 & 0 & 1 & 0 & 0 & 0 & 0 \\
0 & 0 & 0 & 0 & 0 & 0 & 1 & 1 & 0 & 0 & 0 & 1 & 0 \\
0 & 0 & 0 & 0 & 0 & 0 & -\frac{\hat{w}}{2} & \frac{\hat{w}}{2} & 0 & 0 & 0 & 0 & 0 \\
0 & 0 & 0 & 0 & 0 & 0 & 0 & 0 & 0 & -1 & -1 & 1 & 0 \\
0 & 0 & 0 & 0 & 0 & -1 & 0 & 0 & 0 & 0 & 0 & 0 & 0 \\
0 & 0 & 0 & -\frac{h+\hat{h}}{2h} & -\frac{h+\hat{h}}{2h} & 0 & 0 & 0 & 0 & -\frac{h+\hat{h}}{2h} & \frac{h+\hat{h}}{2h} & 0 & 0 \\
0 & 0 & -1 & 0 & 0 & 0 & -1 & 0 & 0 & \frac{h+\hat{h}}{2h} & \frac{h+\hat{h}}{2h} & 0 & -\frac{1}{h} \\
\frac{w-\hat{w}}{2w} & \frac{w-\hat{w}}{2w} & 0 & 0 & 0 & 0 & -\frac{w-\hat{w}}{2w} & -\frac{w-\hat{w}}{2w} & 0 & 0 & 0 & 0 & \frac{1}{w} \\
0 & 0 & 0 & 0 & 0 & 0 & 0 & 0 & -1 & 0 & 0 & 0 & \frac{1}{h} \\
\frac{w-\hat{w}}{2w} & \frac{w-\hat{w}}{2w} & 0 & 0 & 0 & 0 & -\frac{w-\hat{w}}{2w} & -\frac{w-\hat{w}}{2w} & 0 & 0 & 0 & -1 & -\frac{1}{2}
\end{bmatrix}
\begin{bmatrix} f_1 \\ f_2 \\ f_3 \\ f_4 \\ f_5 \\ f_6 \\ f_7 \\ f_8 \\ f_9 \\ f_{10} \\ f_{11} \\ f_{12} \end{bmatrix}
=
\begin{bmatrix} F_1 \\ F_2 \\ F_3 \\ F_4 \\ F_5 \\ F_6 \\ F_7 \\ F_8 \\ F_9 \\ F_{10} \\ F_{11} \\ F_{12} \\ \Phi_1 \\ \Phi_2 \\ \Phi_3 \\ \Phi_4 \end{bmatrix}
\tag{3.17}
$$

The uniqueness of the internal element nodes to the joint element requires that a valid element state is realized when the internal nodal resultants are null. This condition can be employed to compute the four internal nodal displacements, v_i, given the external nodal displacements, u_i, which are computed as part of the global solution algorithm. Further details on the formulation can be found in Mitra [65].

3.3 Implementation of the Analysis Framework

Within the scope of this study, an object-oriented framework is implemented in MATLAB to effectively utilize the capabilities provided by the beamcolumnjoint element and pinching4 material formulations provided in OpenSees. The framework is designed to facilitate the manipulation of stored data and consists of a set of class structures that hold the necessary information of the relevant objects and method functions.

The central component of the framework is the *Joint* class, which serves as the main entry point and is responsible for generating object instances. Each object instance represents a specific joint specimen from the experimental database. These joint objects have several capabilities:

- Retrieve and store measured displacement and force data from *.csv* file,
- Retrieve and parameter values associated to the physical features of the joint sub-assemblage,
- Generate and store beam and column objects (instances of *Frame* class) associated with the stored physical features,
- Generate and store *beamcolumnjoint* and *pinching4material* objects associated with the physical features,
- Generate a *tcl* script file that creates beam and column sections, beam and column elements framing to the joint, a joint element, boundary conditions, displacement loading history and analysis options.

Once the *tcl* scripts are generated for all the joint specimens, the framework proceeds with simulating the response of each instance. During the analyses, multiple instances may be created for each experimental specimen, particularly when conducting a parametric search focused on the pinching4 model parameters. After completing the analyses, the simulated response for each instance is stored within the *Joint* object. This allows for a detailed comparison between the experimental and simulated responses, which is essential for evaluating the accuracy and performance of the simulation. The criteria for evaluating the difference between experimental and simulated responses are described in Chapter 6, and the accuracy of the simulation is assessed based on these criteria.

A diagram which illustrates the simplified object interaction of between the relevant classes are presented in Figure 3.3. The most basic unit in the framework is a

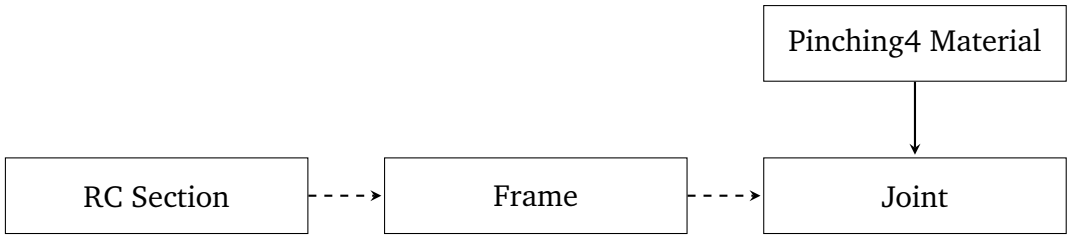

Figure 3.7 Simplified class diagram of the *beamColumnJoint-pinching4* analysis framework

RCSection object which consists the information related to concrete material and reinforcement configuration. Any instance of *RCSection* class can be associated to an instance of a Frame class. For example, using *RCSection* constructor function, two different rectangular section (with varying geometrical dimensions and reinforcement configurations) can be created and related information can be inherited to an instance of *Frame* class, which corresponds to an object represents a beam or column. Methods defined in *RCSection* can compute confined strain-stress curve and create a rectangular section which consists of rectangular *Patch* layers for concrete material and *Straight* fibers for longitudinal reinforcement, and return a string variable that can be executed in OpenSees *tcl* script to create a *Fiber* section.

A *Frame* object has the inherited properties of an *RCSection* as well as the spatial definition of the member. It has a method to generate a OpenSees *tcl* command to create *nonlinearBeamColumn* elements. Three or four frame objects can be constructed as the subclass of a *Joint* object and one or two of them should be defined as beam to construct a *Joint* object. Additionally, material properties and related methods are inherited by a subclass named *Pinching4Material* which is capable of storing model parameters of a particular pinching4 material definition and return OpenSees command as string to generate related material.

In accordance with Section 3.2.1.1, the primary approach relies on the calibration of the *pinching4* material. In relation to the experiments outlined in Table 4.1, a collection of *Joint* entities is created, each associated with distinct *pinching4* objects possessing different model parameters while the properties of the corresponding *Frame* objects remain constant throughout this process. Matlab script which defines the Pinching4Material class including its constructor function and the method function that returns OpenSees command is given in Listing 3.8

Overall, the framework provides a systematic approach to analyze and assess the behavior of beam-column joints using the beamcolumnjoint element and pinching4 material in OpenSees. By leveraging the object-oriented nature of the framework and the capabilities of the associated classes, it enables efficient data management, model generation, and simulation for multiple joint specimens in the experimental database.

```matlab
        classdef Pinching4Material < handle
            properties
                stress1p; stress2p; stress1n; stress2n;
                strain1p; strain2p; strain1n; strain2n;
                rDispP; rForceP; uForceP; rDispN; rForceN; uForceN;
                gammaK1; gammaK2; gammaK3; gammaK4; gammaKLimit;
                gammaD1; gammaD2; gammaD3; gammaD4; gammaDLimit;
                gammaF1; gammaF2; gammaF3; gammaF4; gammaFLimit; gammaE;
                materialId
            end
            methods

        % Constructor
        function obj = Pinching4Material(materialId, envelopeParams, deteriorationParams)
            obj.materialId = materialId;
            if length(envelopeParams) ~= 8
                error('envelopeParams vector should contain 8 parameters')
            end
            if length(deteriorationParams) ~= 22
                error('deteriorationParams vector should contain 22 parameters')
            end
            [obj.stress1p, obj.stress2p, obj.stress1n, obj.stress2n, ...
            obj.strain1p, obj.strain2p, obj.strain1n, obj.strain2n] = envelopeParams{:};
            [obj.rDispP, obj.rForceP, obj.uForceP, obj.rDispN, obj.rForceN, obj.uForceN, ...
            obj.gammaK1, obj.gammaK2, obj.gammaK3, obj.gammaK4, obj.gammaKLimit, ...
            obj.gammaD1, obj.gammaD2, obj.gammaD3, obj.gammaD4, obj.gammaDLimit, ...
            obj.gammaF1, obj.gammaF2, obj.gammaF3, obj.gammaF4, obj.gammaFLimit, obj.gammaE] = deteriorationParams{:};
        end

        % Method to generate OpenSees command
        function cmdStr = getOpenSeesCommand(obj)
            cmdStr = sprintf('uniaxialMaterial Pinching4 %d %f %f %f %f %f %f %f %f %f %f %f %f %f %f %f %f %f %f %f %f %f %f %f %f %f %f %f %f %f %f %f %f %f', ...
            obj.materialId, obj.stress1p, obj.stress2p, obj.stress1n, obj.stress2n, obj.strain1p, obj.strain2p, obj.strain1n, obj.strain2n, ...
            obj.rDispP, obj.rForceP, obj.uForceP, obj.rDispN, obj.rForceN, obj.uForceN, ...
            obj.gammaK1, obj.gammaK2, obj.gammaK3, obj.gammaK4, obj.gammaKLimit, ...
            obj.gammaD1, obj.gammaD2, obj.gammaD3, obj.gammaD4, obj.gammaDLimit, ...
            obj.gammaF1, obj.gammaF2, obj.gammaF3, obj.gammaF4, obj.gammaFLimit, obj.gammaE);
        end
    end
end
```

Figure 3.8 Class Definition for Pinching4Material Class

4
ARTIFICIAL NEURAL NETWORKS IN JOINT MODEL PARAMETER IDENTIFICATION

4.1 Overview

In this study, a predictive model for the shear strain-shear stress response in joint cores using artificial neural network methods was developed. To achieve this, an experimental database was collected from the available literature based on a set of selection criteria, including material type, loading conditions, and joint geometry. The most influential parameters on the shear strain-stress response were identified using correlation matrices, which were then used as input parameters for the neural network models. Several neural network models were trained using various architectures and training algorithms, and their performance was evaluated using a range of metrics, including mean squared error and coefficient of determination. The best-performing neural network model was selected based on its ability to accurately predict the shear strain-stress response for new input parameters. This model was validated using a hold-out dataset and compared to the available prediction models in the literature, demonstrating superior performance.

4.2 Problem Definition and Experimental Database

As Chapter 3 discusses, definition of reinforced concrete joint deformation in any particular numerical model requires a priori information of shear strain-stress information of the joint core. A comprehensive review on the available prediction models including analytical, statistical and numerical is presented in Chapter 2. Review on the available literature has shown that analytical approaches have limitations to define a generalized behaviour taking all of the relevant parameters into account. Despite the fact all of these models led to satisfactory results within their calibration databases, their applicability to an arbitrary joint configuration is disputable [223]. Empirical models are typically dependent on the dataset and the used statistical method; thus, generalization is remained as an issue so far. Empirical

models have other issues associated to their scope and reliability [224]. In this study, a generalized solution for this problem through machine learning techniques is sought. Ability of this methodology to provide a global and reliable solution is also investigated.

The problem defined in the Chapter 3 is processed as a meta-modelling problem. The major objective is assigned as building a collection of meta-models which predict shear strain and stress values using characteristic physical properties of an arbitrary joint sub-assemblage. Training and validation data for the prediction model is provided from the experimental studies available in the literature.

In collection of experimental data, 120 reinforced concrete joint sub-assemblages tested under monotonic or cyclic conditions carried out by Joh *et al.* [34], Ehsani and Wight [48], Endoh *et al.* [50], Fujii and Morita [51], Kaku and Asakusa [52], Kaku and Asakusa [53], Ehsani and Alameddine [54], Noguchi and Kashiwazaki [55], Oka and Shiohara [56], Guimaraes *et al.* [57], Walker [60], Shin and LaFave [74], Leon [97], Megget [225], Joh *et al.* [226], Kitayama *et al.* [227], Kurose *et al.* [228], Meinheit and Jirsa [229], Kitayama *et al.* [230], Tsubosaki *et al.* [231], Raffaelle and Wight [232], Goto and Joh [233], Ishida *et al.* [234], Yoshino *et al.* [235], Suzuki and al. [236], Goto and Joh [237], Teng and Zhou [238], Kusuhara *et al.* [239], Morita *et al.* [240], Watanabe *et al.* [241], Noguchi and Kurusu [242], and Joh *et al.* [243–245] are gathered through following criteria:

- The sub-assemblage is tested under quasi-static loading conditions,
- No retrofitting material (e.g. FRP) is introduced to the sub-assemblage,
- The load is applied to the beam free-end while the column ends are simply supported both for interior and exterior joint sub-assemblages,
- Joint shear stress with respect to the strain is reported,
- The sub-assemblage is loaded only in-plane,
- Reinforcement detailing is not changed between framing beams for exterior joints and framing columns for both exterior and interior joints.
- Tested sub-assemblage experienced joint shear failure (J) or joint shear failure in conjunction with beam yielding (BJ).

The basic statistical information about the experimental database is presented in Table 4.1. The detailed information of the collected data is provided in Table A in Section

A. It is worth noting that the provided dataset includes different experimental sources introduced in Section 2 considering the defined selection criteria listed above.

Table 4.1 Statistical description of the continuous variables

Var.	Min	Max	Mean	SD	Histogram	Var.	Min	Max	Mean	SD	Histogram
f_c	17.10	92.10	37.27	15.14	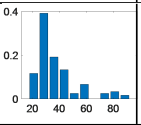	f_{yj}	235	955	442.27	171.81	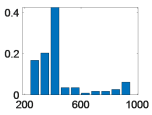
f_{yb}	325	1091	516.52	187.90	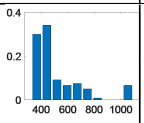	f_{yc}	245	1091	482.86	147.73	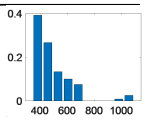
ρ_j	0	0.024	0.006	0.0045	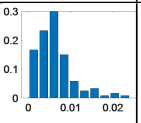	ρ_b	0.006	0.032	0.017	0.0058	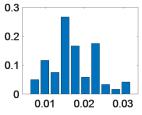
ρ_c	0.011	0.068	0.030	0.012	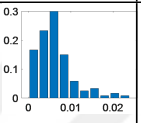	b_j	190	457	286.61	69.94	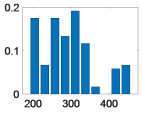
e	0	140	17.45	38.49	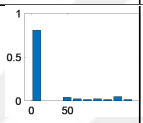	n	0	0.48	0.12	0.12	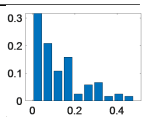
b_b	150	406	237.48	76.17	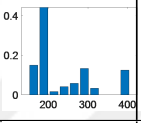	h_b	220	559	365.23	95.01	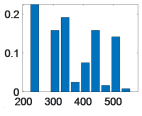
b_c	220	508	335.60	80.72	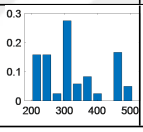	h_c	200	508	325.05	87.70	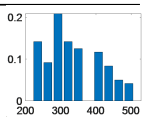

The basic statistical information about the physical parameters included in the experimental database is presented in Table 4.1. f_c is the compressive strength of the concrete material, f_{yj} is the yielding strength of the joint transverse reinforcement, f_{yb} is the yielding strength of the beam longitudinal reinforcement, f_{yc} is the yielding strength of the column longitudinal reinforcement, ρ_j is the volumetric reinforcement ratio in joint core, ρ_b is the longitudinal reinforcement ratio of the beam, ρ_c is the longitudinal reinforcement ratio of the column, b_j is effective joint width [37], e is the eccentricity, n is the ratio between the applied axial force and capacity, b_b and h_b are the beam width and depth, b_c and h_c are the column width and depth in respective order.

Figure 4.1 presents visual representations of the correlation values between the introduced parameters and the observed shear strength (a) as well as the shear strain (b) recorded at the point of shear strength exceedance in an effort to simplify the dataset for the prediction model and improve a preliminary understanding of the parameters affecting the targeted values. The results of the correlation analysis

indicate that the compressive strength of the concrete material, denoted as f_c, has a significant impact on joint strength. Additionally, the axial load ratio n, joint transverse reinforcement ratio ρ_j, beam transverse reinforcement ratio ρ_b, and yield strength of the beam longitudinal reinforcement f_{yb} exhibit a moderate level of influence on joint strength while the remaining parameters have a relatively insignificant impact on the ultimate stress attained in the core of the joint. In addition to the stress response, the shear strain values corresponding to the point of ultimate stress measurement are examined. Findings indicate that it can be inferred that the joint shear strain response is moderately influenced by several parameters, including f_{yj}, b_j, b_b, and h_b, in addition to the other parameters that were identified as impacting the stress response. It is noteworthy that the influence of f_c on the shear strain is comparatively lower than its effect on the stress.

It is important to acknowledge that the distribution of variables in the sampling space, as depicted in Table 4.1, is non-uniform. Therefore, it is possible that a correlation analysis that includes a more comprehensive representation of all relevant parameters may produce slightly different outcomes. However, it is essential to bear in consideration that the correlation analysis primarily provides a preliminary assessment of the most influential input variables for the objective of the proposed predictive model.

The methodology employed involves the identification of three crucial points on the curve that represents the stress-strain relationship within the joint core. Point A represents the initial significant change in the slope (stiffness) of the curve. The aforementioned alteration is indicating of the initiation of shear crack propagation within the joint's core. At this point, the strain and stress values are denoted as γ_A and τ_A correspondingly. In this study, the process of identifying Point A is aided by the determination of the peak value of the first derivative of the curve.

Point B is identified as the location where the greatest stress response is observed throughout the recorded history. The values of strain and stress at this particular location are denoted as γ_B and τ_B, respectively. It is noteworthy that the symbol τ_B denotes the shear capacity. The reliability of the proposed model can be evaluated by comparing its τ_B predictions with those of previous studies, which can provide valuable insights.

The final point of interest is Point C, which is characterized by the highest observed deformation level. The values of strain and stress at this particular point have been designated as γ_C and τ_C, respectively. A significant obstacle in determining this juncture pertains to its correlation with the intrinsic mechanical characteristics of the

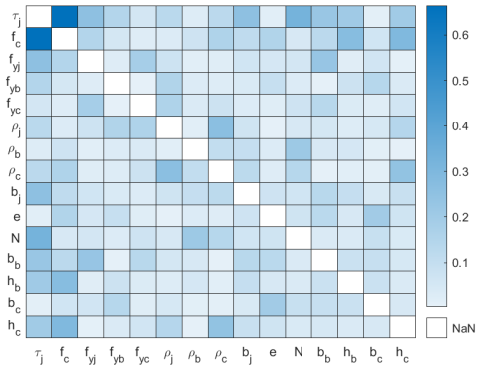

(a)

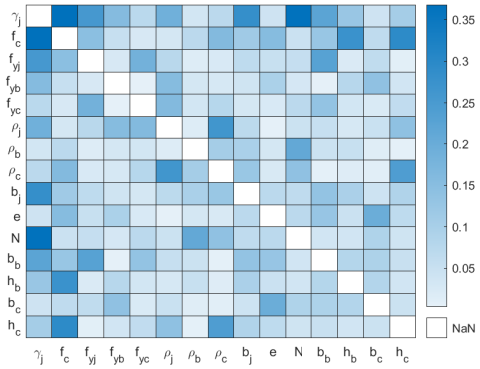

(b)

Figure 4.1 Visualization of correlation matrix between parameters presented in Table 4.1 and observed (a) joint shear strength τ_j and (b) shear strain when the joint shear strength is achieved

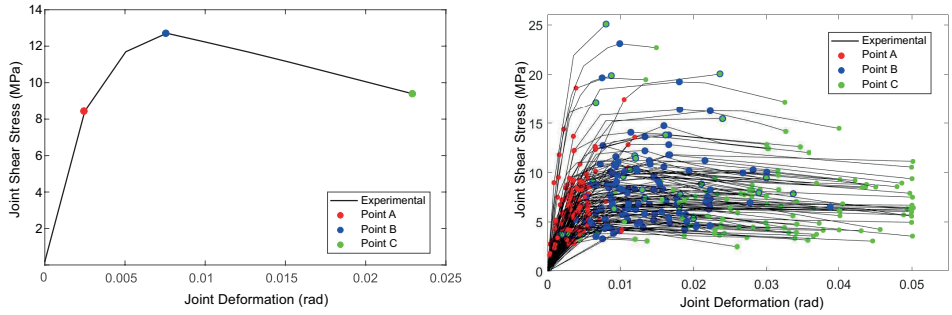

Figure 4.2 Points A, B and C for the experimental setup tested by (a) Meinheit and Jirsa [229] and overall database

articulation. In some cases, the capacity to quantify deformation may be restricted by experimental constraints and measurement instrumentation, which may result in the ultimate deformation value being a reflection of these limitations rather than the maximum observable deformation. Despite its imprecise representation of the ultimate deformation point, the determination of post-peak stiffness via Point C can provide sufficient information for establishing constitutional relationships in joint finite element simulations. The primary objective of this particular methodology is to ascertain a correlation between strain and stress by means of the anticipated data points.

In Figure 4.2 critical points are illustrated on the results of the experiment carried out by Meinheit and Jirsa [42] and the overall database.

4.3 Meta-Modelling

In this section, meta-modelling methodology for the relation between effective physical parameters for a reinforced joint sub-assemblage and characteristic points defining shear strain - stress curve are discussed through a test function for clarity and introduced for the mentioned problem. Test function is used for visualization of the results since the true mathematical expression for joint shear strain stress characteristic as a function of the aforementioned input parameters is quite complex and unknown for the particular case.

The main focus is on the detection of the most efficient neural network type, architecture and training method for the related problem which is defined in the previous section. For the sake of clarity and visualization, a complex test function is selected and expressed as $f(x) = \sum_i^N exp(a * (x-b)^2)$ where a and b are arbitrary scalars (e.g. $N = 4$, $a = [5,-1,-3,-1]$, $b = [-3,-6,-8,-11]$). Two different neural network types are investigated: feed-forward neural network and generalized

regression neural network. For each type, different internal parameters (e.g. number of hidden layers and neurons for FFNN and sigma parameter for GRNN) are used. For both neural network types random partition of database to training and validation and k-fold cross validation techniques are used. Pseudo-codes for the main procedure used to generate FFNNs and GRNNs during the approximation are given in Algorithm 4.3 and 4.4

In Figure 4.5, the function approximation results from Feed forward Neural Networks of different neural network architectures are displayed. Each figure corresponds to a distinct partition of a 5-fold cross-validation test. The true function, the approximation target is represented as a black solid line while the training samples are shown as scattered red points. The approximated functions created by FFNNs with 1 to 5 hidden layers are also depicted as dashed lines of varying colors. The ability to capture complex patterns in data is evaluated by comparing the approximations to the true function. Over-fitting risk, which tends to increase with the complexity of the model is managed by the cross-validation process. Through the Figures 4.5.(a)-(e), the performance of each network architecture on training data and its generalization to unseen data are assessed, guiding the selection of the optimal architecture for efficient and accurate function approximation.

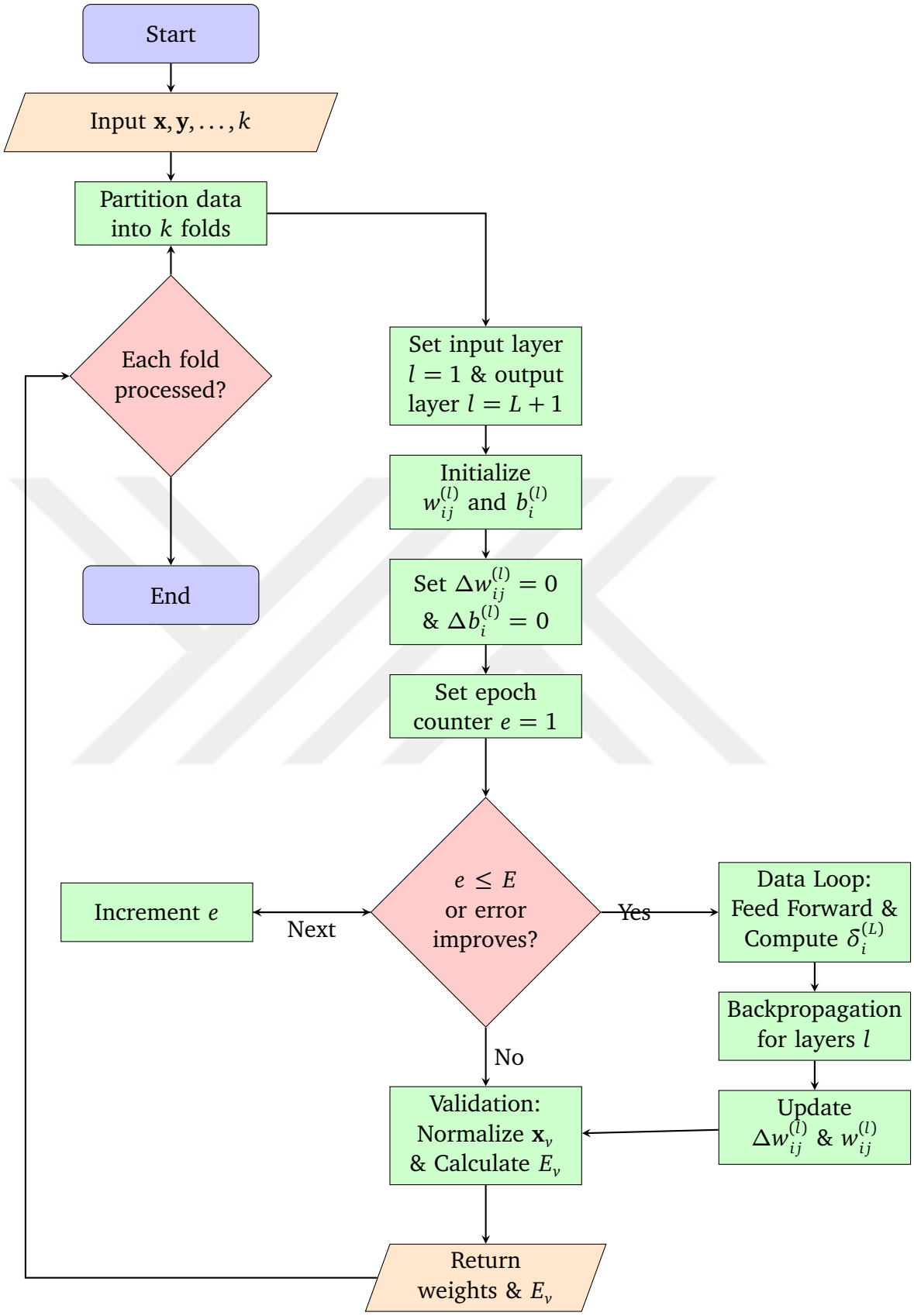

Figure 4.3 FFNN training using k-fold cross validation

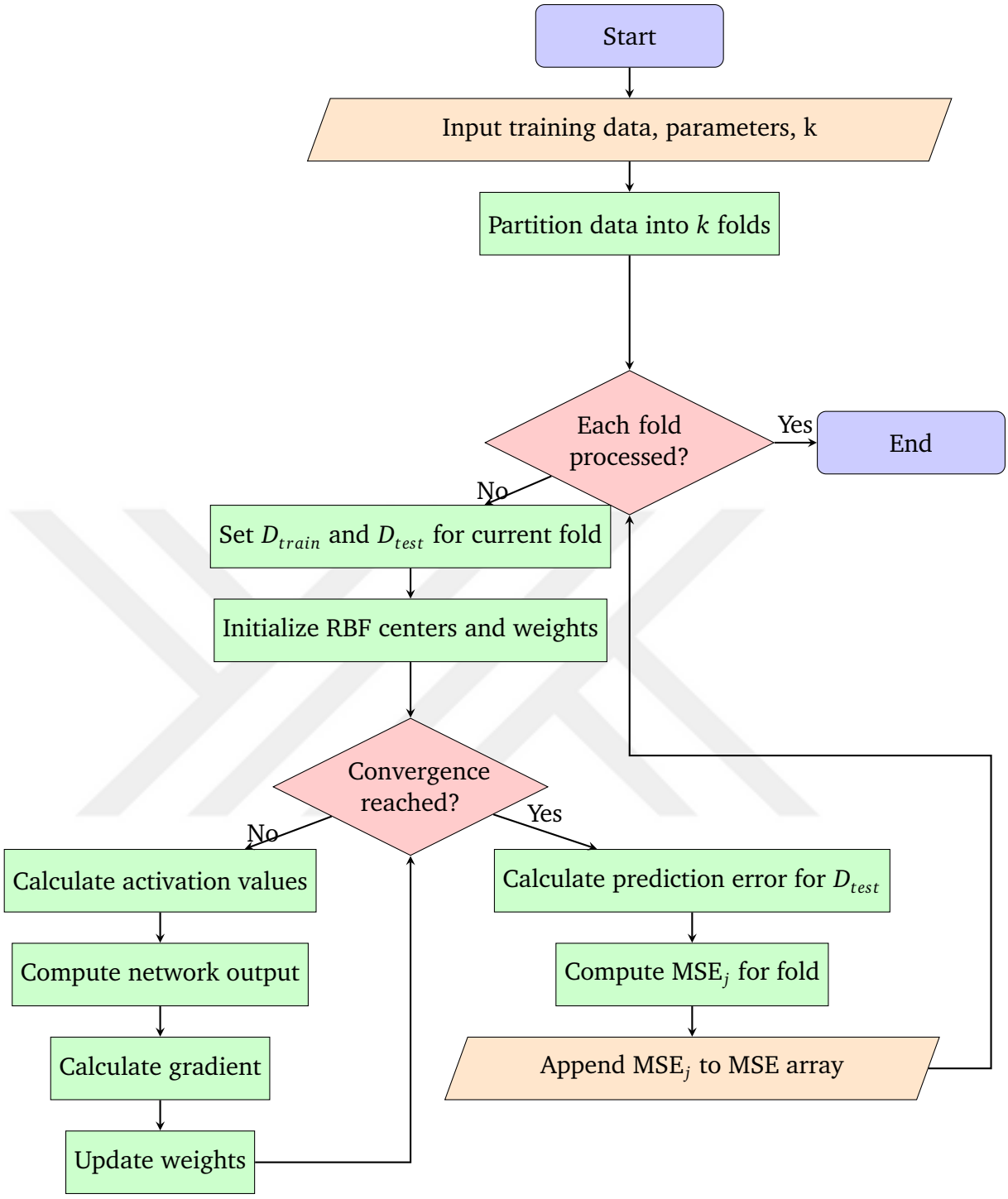

Figure 4.4 GRNN training using k-fold cross validation

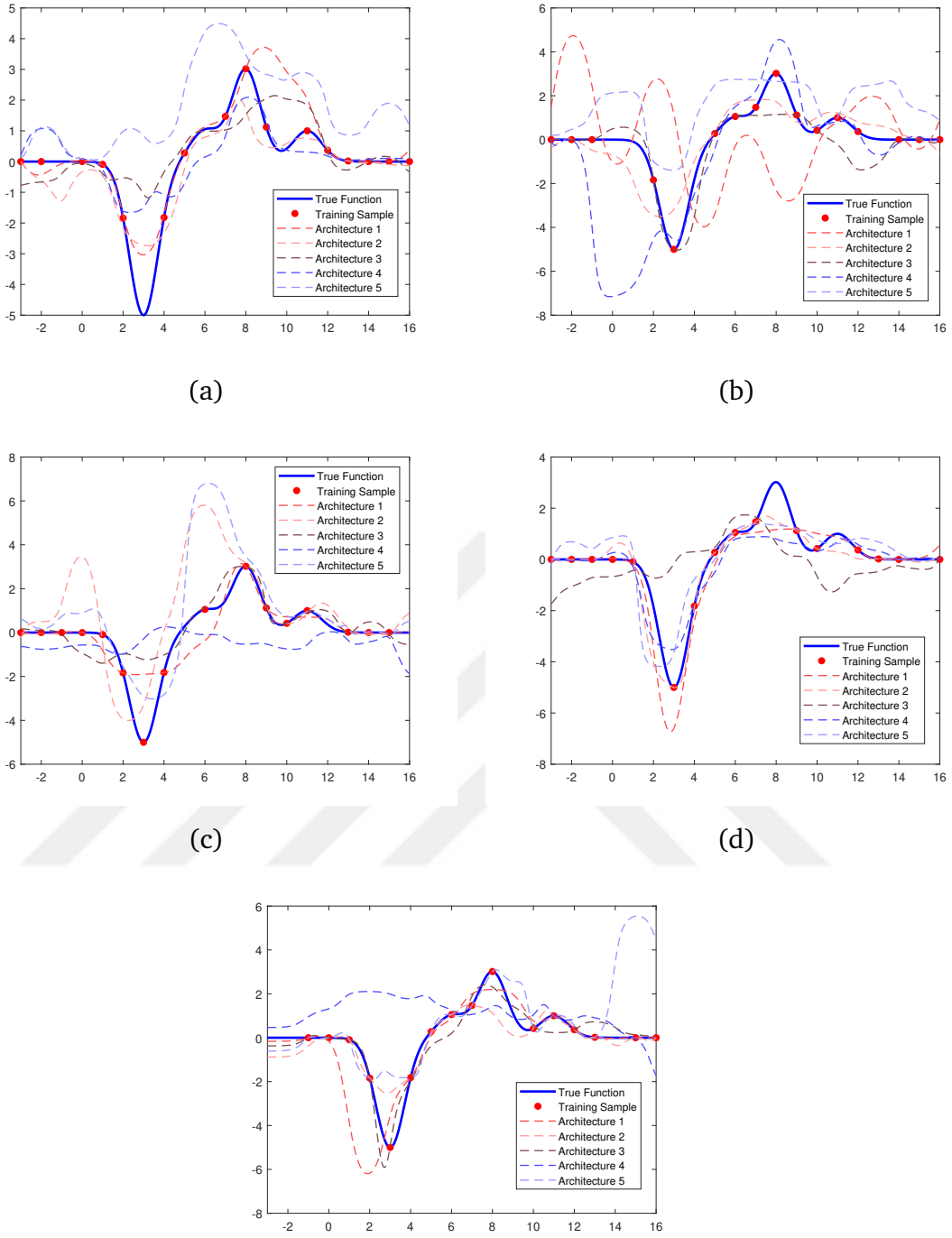

Figure 4.5 Comparison of true function approximation using FFNNs with varying number of hidden layers for (a) first, (b) second, (c) third, (d) fourth and (e) fifth data split in 5-fold cross validation

The MSE values indicate the average squared difference between the network's predictions and the true function values. Lower MSE values indicate a better fit of the model to the data. Therefore, the goal is to minimize the MSE for both the

training and test data. From the given data, it can be observed that FFNNs with more hidden layers generally achieve lower MSEs across different partitions. This suggests these networks may be more capable of capturing the complexity of the underlying function, leading to more accurate approximations. However, the MSEs are not consistently minimized with increasing hidden layers. For example, the MSE for the fourth partition significantly increases when moving from three to four hidden layers. This could be due to over-fitting, where the model becomes too complex and performs poorly on unseen data. The variance in MSE across different k-fold partitions indicates the model's performance variability with different splits of the data. This emphasizes the importance of cross-validation in assessing the model's robustness and its ability to generalize to unseen data.

Table 4.2 Mean Squared Errors for FFNNs with varying architectures and k-fold partitions

K-Fold	1 H.L.	2 H.L.	3 H.L.	4 H.L.	5 H.L.
1	2.5256	1.8502	0.5620	1.5289	0.1937
2	1.7263	1.1737	5.4463	1.9134	0.6565
3	4.5832	1.1471	0.5023	2.9629	0.1449
4	3.3717	23.7516	1.6592	1.6682	0.1847
5	12.3821	5.6178	5.6920	2.0789	3.6076

The same test function is approximated by several GRNNs built with varying σ parameter between 0.5 and 1.0. The analysis of mean squared error (MSE) results (see 4.3) comparing General Regression Neural Network and Feed-Forward Neural Network reveals a marked performance difference between the two approaches. On average, the MSE from GRNN is approximately an order of magnitude lower than that from FFNN. This remarkable distinction indicates that GRNN is far superior in prediction accuracy when compared to FFNN.

Table 4.3 Mean Squared Errors for GRNNs with varying spread parameter σ and k-fold partitions

K-Fold	$\sigma = 0.5$	$\sigma = 0.6$	$\sigma = 0.7$	$\sigma = 0.8$	$\sigma = 0.9$	$\sigma = 1.0$
1	3.2371	3.2014	3.0679	2.8124	2.4912	2.1805
2	0.2817	0.2806	0.2765	0.2689	0.2601	0.2530
3	0.1811	0.1811	0.1814	0.1817	0.1820	0.1812
4	3.1593	3.1677	3.2008	3.2736	3.3888	3.5416
5	0.0086	0.0088	0.0093	0.0106	0.0133	0.0178

The results provided in Table 4.3 suggests an evaluation of MSE across varying spread parameters for the GRNN for different runs of k-fold cross-validation (each row representing a separate run). Observations from the data indicate an initial decrease in MSE values as the spread parameter increases, reaching a minimum, and subsequently increasing. This behavior is consistent with the expectation that there exists an optimal spread parameter that minimizes the MSE, beyond which the model may start over-fitting, thereby increasing the MSE. For instance, the first row representing one

run of k-fold cross-validation shows MSE decreasing from 3.2371 to 2.1805 as the spread parameter is increased. Similar trends are observed in subsequent runs as well. The consistency of this trend across different runs suggests a robust behavior. It should be noted that, while each k-fold partition is random and independent, the consistency of trends across the different runs enhances the confidence in these observations.

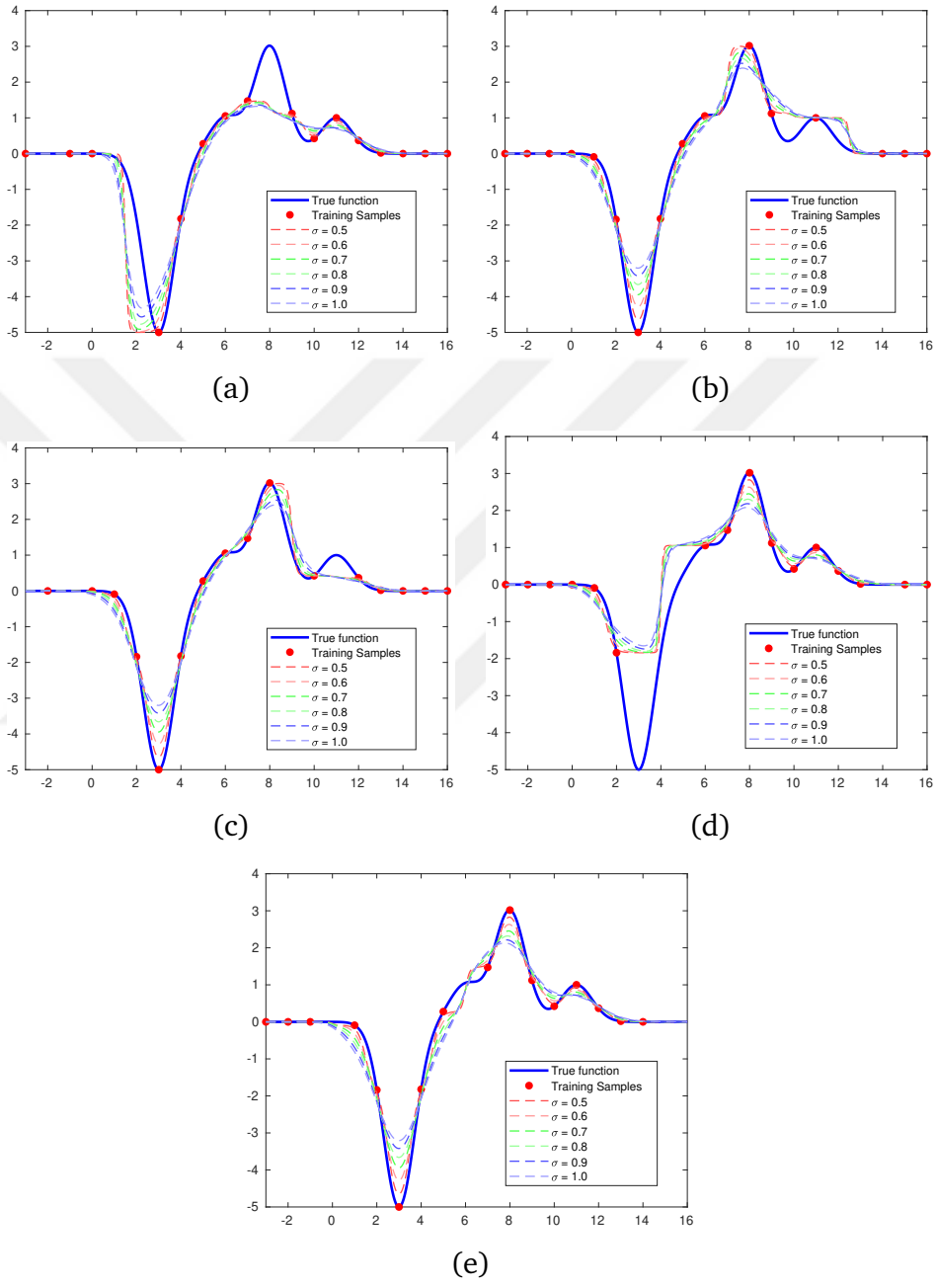

Figure 4.6 Comparison of true function approximation using GRNNs with varying σ for (a) first, (b) second, (c) third, (d) fourth and (e) fifth data split in 5-fold cross validation

The figures 4.6 provide a visual representation of the test function, the training sample data points from each k-fold partition and the GRNN approximations with varying sigma (σ) parameters depicted by dashed lines. Each figure provides insight into

the relationship between the true function the scattered training samples and the GRNN approximations. The second and the fifth k-fold partitions stand out with their performance. They seem to capture the underlying pattern of the true function more accurately than the other approximations, demonstrating a higher level of accuracy in replicating the test function. This result aligns with the observed performance metrics in the associated table. The dashed lines representing the GRNN approximations provide an important visualization of how the model's accuracy can vary with changes in the sigma parameter. The different dashed lines, therefore, help to identify optimal sigma values that result in the lowest discrepancies between the GRNN approximations and the true function.

Throughout the course of this section, an emphasis has been placed on the comparative analysis of different neural network types and architectures. A test function has been utilized for this purpose, primarily due to its capability for visualization. When a known function is used the accuracy of any approximation model can be assessed directly by comparing it with the true function. However, such comparison may not provide sufficient information to conclude which neural network type is most suitable for creating a meta-model of a complex approximation function which is intended to predict the response of a joint over multiple parameters. The complexities of this task might not be fully addressed by the test function alone.

In cases where visualization is not possible, other metrics like the mean squared error (MSE) and coefficient of determination (R^2) values are often calculated to assess the performance of the meta-model. These metrics offer a quantitative evaluation of the model's predictions in relation to the actual values. As part of the research outlined in this thesis, the best approaches for constructing approximation functions for joint shear and strain values are being explored. Two distinct approximation functions are sought: one for joint shear strength, and another for the corresponding shear strain value.

A low MSE, along with a small variation across different k-fold partitions may suggest an effective approach to meta-modelling this complex problem. This hypothesis is a fundamental part of the current research. The ultimate aim is to apply these findings in the construction of more accurate and reliable approximation functions for complex, multi-parameter problems.

In Figure 4.7 and Figure 4.8, mean values of MSE for different k-fold runs are plotted as bar charts for the FFNN and GRNN which are built to predict joint shear strength after training with the data provided in Table 4.1 respectively. While the blue bars show the mean values, variation in the various k-fold runs are shown with the solid

black lines.

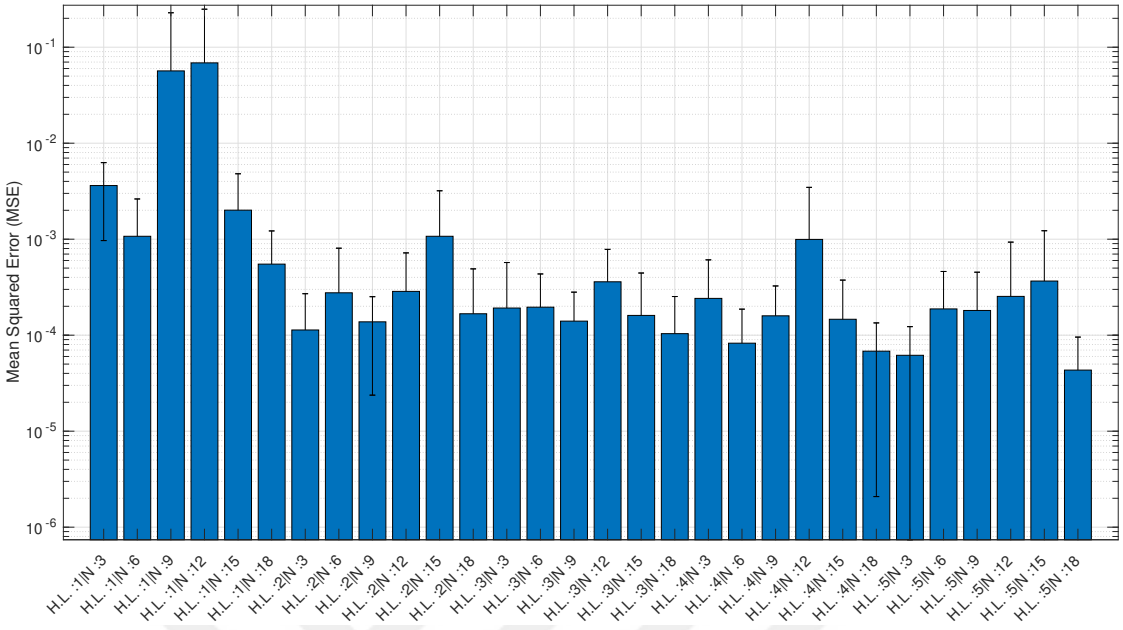

Figure 4.7 Mean MSE values obtained by approximation with FFNNs with varying architecture for joint shear prediction model

For joint strength prediction models, in the comparison of the Mean Squared Error (MSE) of feedforward neural networks (FFNNs) and generalized regression neural networks (GRNNs) in approximating joint shear strength, a discernible pattern arises. This study employed 30 different FFNN architectures and 20 sigma spread values in GRNN models, denoted as 'H.L. :i|N :j' and numeric values respectively, each corresponding to specific MSE results.

For the FFNNs, MSE values displayed a wide range, from as low as 0.0000433 to as high as 0.0686870, with no evident correlation between the MSE and the network architecture complexity. The highest MSE values were associated with relatively simple architectures ('H.L. :1|N :3' and 'H.L. :1|N :12'), while the lowest MSEs were found in more complex architectures ('H.L. :5|N :15' and 'H.L. :5|N :18'). It is also noteworthy that not all complex architectures resulted in low MSEs, indicating that complexity alone does not guarantee optimal performance.

On the other hand, the GRNNs exhibited a consistently increasing MSE as the spread value increased, ranging from 0.0007119 to 0.0200590. The lowest MSE was associated with the smallest spread (0.01) and the highest with the largest spread (0.5). The monotonic increase in MSE with spread value suggests a direct correlation between the two parameters in the context of the GRNN model's performance.

For the shear strain corresponds to joint strength prediction model (see Figure 4.9), it

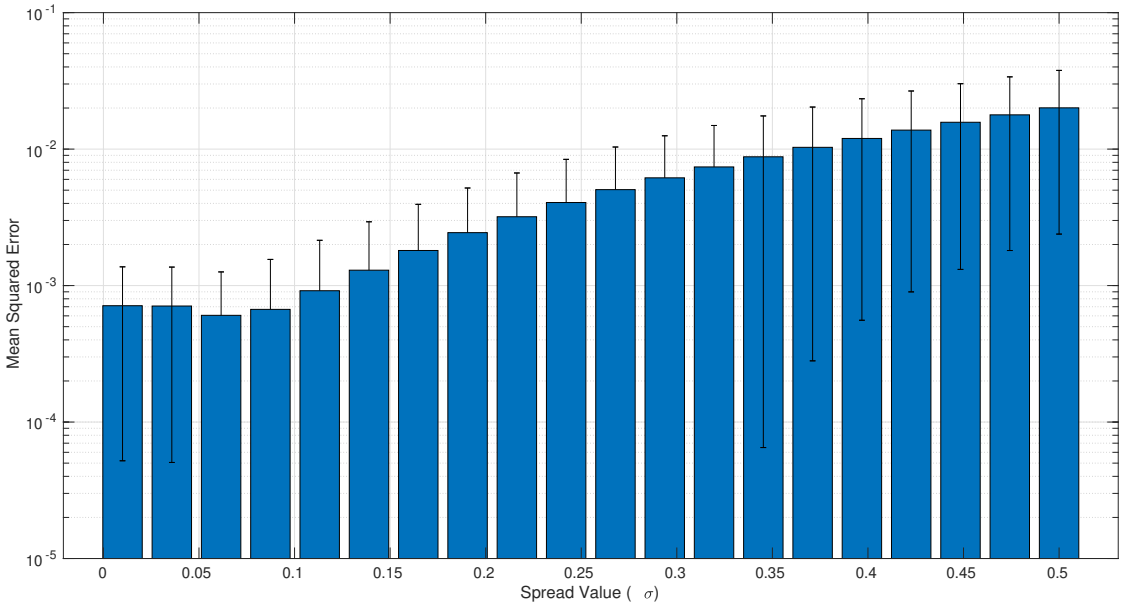

Figure 4.8 Mean MSE values obtained by approximation with GRNNs with varying spread parameter for joint shear prediction model

is observed that for FFNNs, the mean squared errors (MSE) vary widely across different architectures. For instance, MSE values are significantly low (close to zero) for many architectures such as 'H.L. :1|N :6', 'H.L. :2|N :6', and 'H.L. :3|N :9'. However, there are a few architectures like 'H.L. :1|N :15' and 'H.L. :5|N :12' which exhibit higher MSE values. This variation suggests that the architecture (number of hidden layers and neurons) greatly influences the performance of FFNNs. It also implies that a careful selection of architecture is required to obtain the optimal performance. For GRNNs (see Figure 4.10), MSE values increase progressively with the increase in sigma values from 0.1 to 0.5. The GRNN starts with a higher MSE value than FFNNs, but as the sigma value increases, the MSE shows a consistent upward trend. This indicates that the spread of the radial basis function, governed by the sigma parameter, significantly impacts the model's approximation accuracy. A larger sigma value causes the radial basis function to spread more, which might lead to underfitting, resulting in a higher MSE.

FFNN architectures showed varied performance, with the MSE not directly correlated to the complexity of the architecture. Conversely, GRNN models displayed a clear trend of increasing error with larger spread values. Overall, while both models provide viable avenues for joint shear strength approximation, their performance is highly dependent on the chosen parameters, underscoring the necessity of meticulous parameter selection in these machine learning techniques.

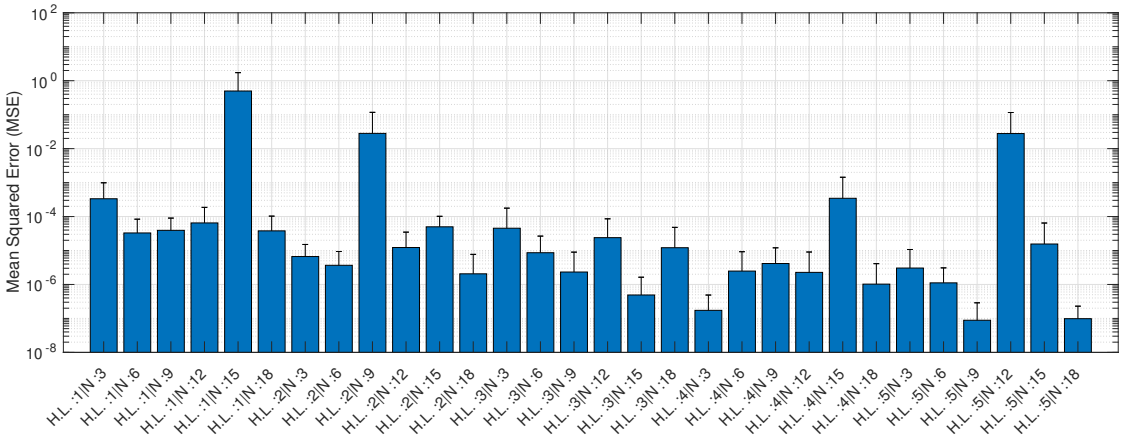

Figure 4.9 Mean MSE values obtained by approximation with FFNNs with varying architecture for joint shear strain value corresponding to the shear strength prediction model

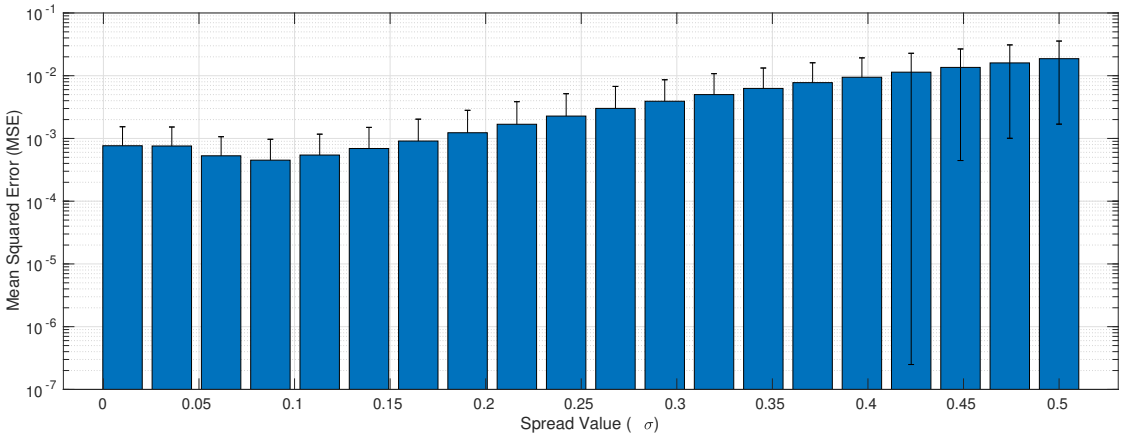

Figure 4.10 Mean MSE values obtained by approximation with GRNNs with varying spread parameter for joint shear strain value corresponding to the shear strength prediction model

Comparing two approaches, GRNNs have a simple and fast one-pass learning process. Unlike FFNNs that require iterative training methods such as backpropagation, GRNNs use the entire dataset in one step to adjust their weights. This results in a much faster training process, making GRNNs more efficient for large datasets or real-time applications. Although FFNNs with a large number of hidden layers may yield lower MSEs, they are also more prone to overfitting, especially when dealing with a limited amount of data. Overfitting is a situation where the model performs well on the training data but poorly on unseen data. GRNNs, due to their architecture and training process, are less prone to overfitting. GRNNs are known for providing smooth function approximations. They make use of radial basis functions, which result in smooth and continuous approximations. On the other hand, FFNNs with sigmoid or ReLU activation functions can sometimes create discontinuities or non-smooth approximations. GRNNs excel at capturing non-linear relationships in the data without the need for complex architectures. They are capable of forming

highly nonlinear decision boundaries, which is beneficial when dealing with complex function approximation problems.

4.4 Results

Six GRNN models which are trained to predict the coordinates of Point A, Point B and Point C on the strain-stress space. The training data-set is constructed from randomly selected samples from the total data-set presented in Table A.1. The ratio of numbers of test/training samples is 0.25 : 0.75, corresponds to 90 training and 30 testing samples. To investigate the reliability and applicability of the proposed prediction models, their performance are evaluated by the means of correlation coefficients (R) for predictions for different target parameters. Also, its accuracy is monitored through the mean values and coefficients of variation (C.O.V.) of ratio between predictions and experimental outputs.

$$R = \frac{\sum (x_i - \bar{x})(y_i - \bar{y})}{\sqrt{\sum (x_i - \bar{y})^2 \sum (y_i - \bar{y})^2}}$$

Correlation coefficient, theoretically shows the statistical dependence between two random variables. $R \approx 1$ indicate a perfect statistical dependence while $R \approx 0$ shows that two variables are not associated to each other. Considering the high number of input parameters, non-uniformity of the parameter samples in the dataset and differentiations related to experimentation and measurement techniques, models with $R \geq 0.75$ remarked as acceptable in this study. It is worth noting that higher performance can be achieved with customized databases, but for the sake of simplicity and the objective of implementing a generalized practical framework, this level of accuracy is adopted. The database presented in Table 4.1 is divided into subsets regarding to the specimens' framing type, failure mode and reinforcement ratio and accuracy measures for these subsets are presented to distinguish the performance of the models for different joint types, failure modes and joint ductility.

4.4.1 Point A

In the cases that large correlation coefficients are achieved in the training data, but significantly lower in the test data imply an over-fitted model to the training set, which is not able to make reasonable predictions for an arbitrary input, but fits almost perfectly to the inputs in training set. In other words, larger correlation coefficients for test data indicate an accurate model. Figure Figure 4.11 show model predictions

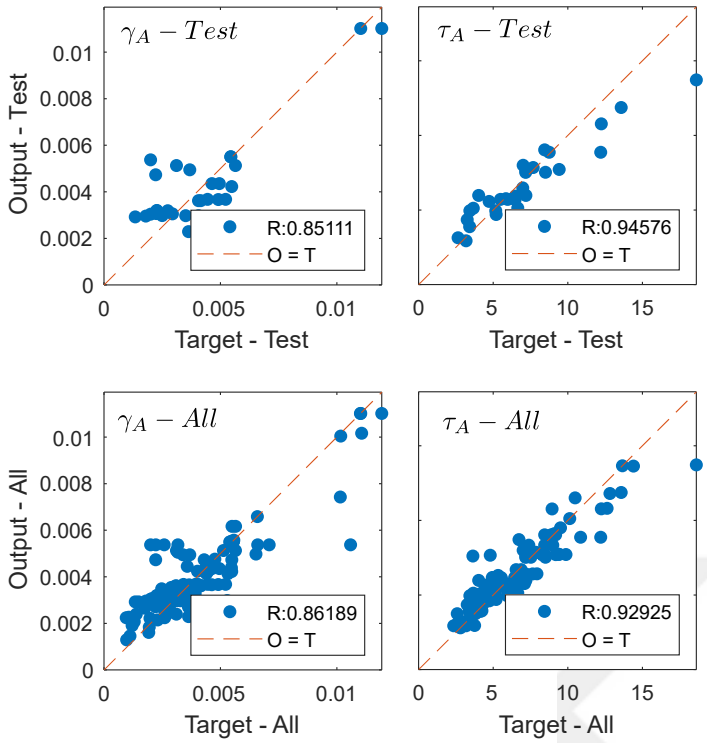

Figure 4.11 GRNN predictions versus experimentally observed values, training data (top) and all data (bottom) for Point A

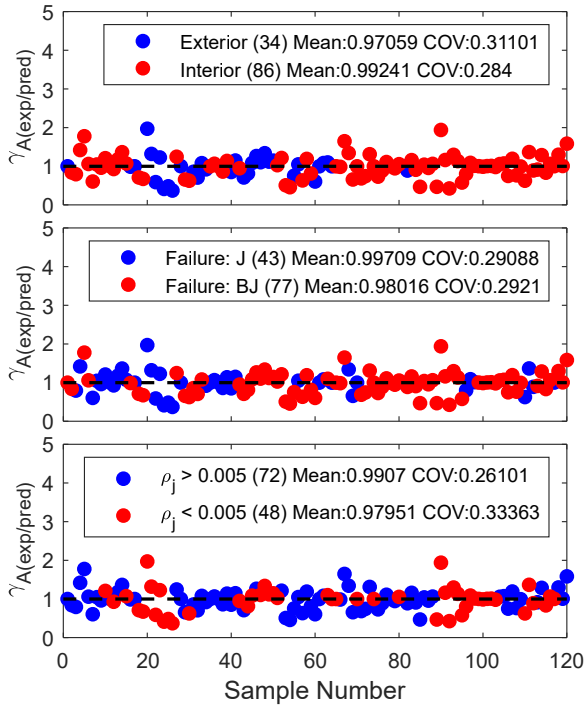

Figure 4.12 Scatter of γ_A GRNN predictions by type, failure type and reinforcement ratio

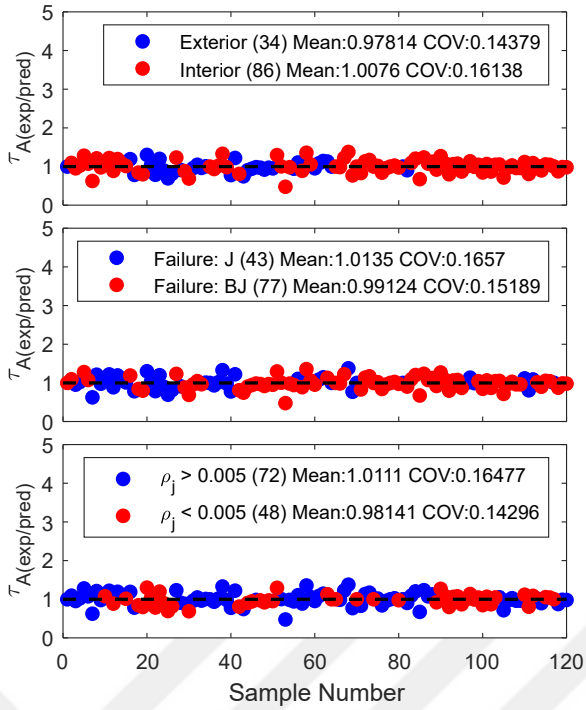

Figure 4.13 Scatter of τ_A GRNN predictions by type, failure type and reinforcement ratio

versus experimentally observed results for γ_A and τ_A. In both models, determined correlation coefficients for test and overall data are very close to each other, that fact notes that models (γ_A, τ_A) are properly trained and not over-fitted.

In Figure 4.12 and Figure 4.13, it is shown that the ratio between model predicted and experimentally observed values of γ_A and τ_A respectively scattered around the ideal value of 1. Mean values for different subsets varies between $0.97 - 1.01$ and no significant differences between subsets are observed. However, examination of coefficient of variations reveal that there is much larger dispersal in γ_A predictions in comparison with τ_A. Moreover, variation in predictions for exterior joints is significantly larger than the ones for interior joints, notes the proposed model is more accurate for interior joints. Variations between coefficients of variation in failure type and joint reinforcement subsets are statistically insignificant.

4.4.2 Point B

In Figure 4.14, scatter of the experimental versus predicted values are given for γ_B and τ_B. Close correlation coefficient values ($R_{test} = 0.80$, $R_{all} = 0.78$) are obtained for test and overall data for γ_B. Significantly larger correlation among predictions and experimental outputs for test and all data of τ_B is observed. Figure 4.15 and Figure 4.16 also verifies this significant difference between accuracy of shear strain (γ_B) and shear stress models (τ_B) respectively. Much larger dispersion

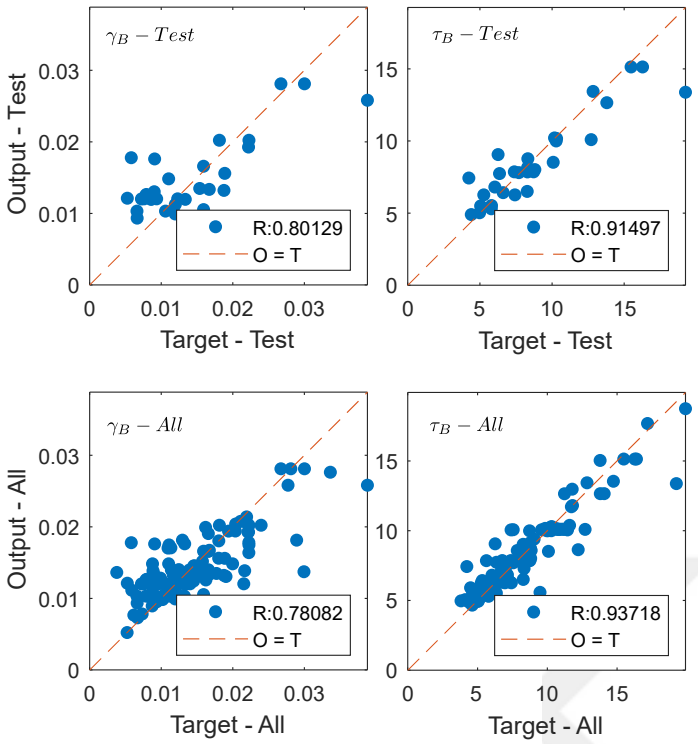

Figure 4.14 GRNN predictions versus experimentally observed values, training data (top) and all data (bottom) for Point B

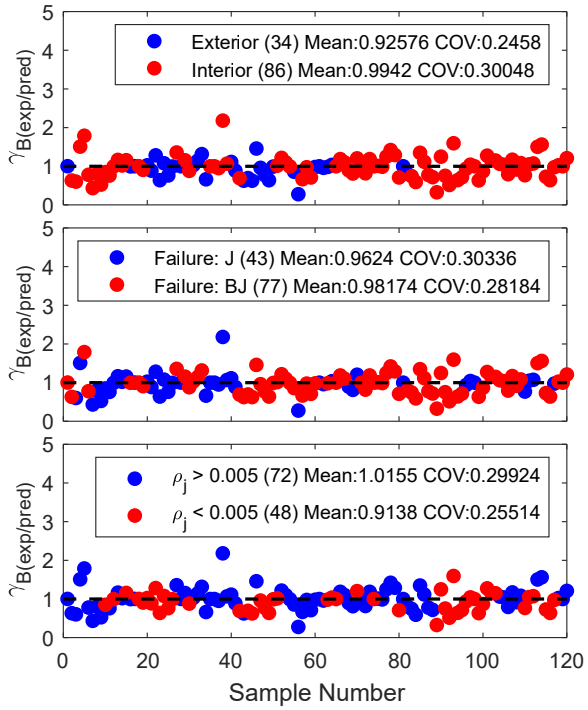

Figure 4.15 Scatter of γ_B GRNN predictions by type, failure type and reinforcement ratio

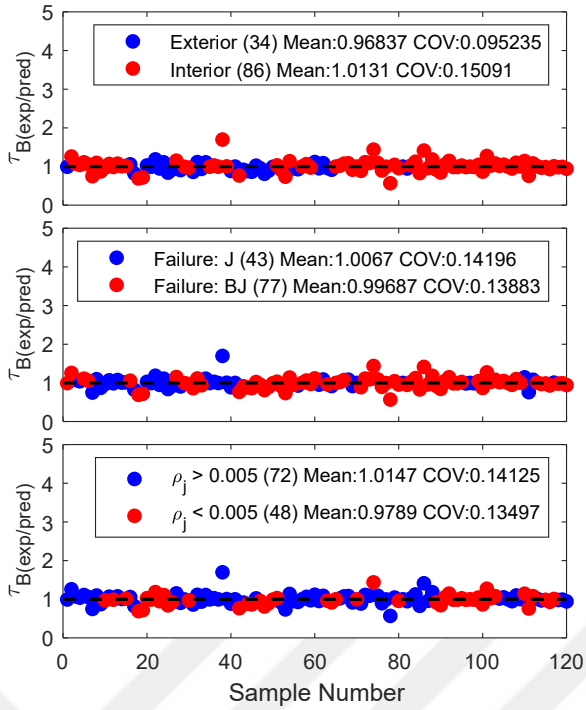

Figure 4.16 Scatter of τ_B GRNN predictions by type, failure type and reinforcement ratio

is observed in strain prediction output data in comparison with stress. Another fact to stress out, mean values for strain prediction of exterior joints (0.93) and joints with lower reinforcement ratio than 0.005 (0.91) are much lower than the mean values determined for other subsets. This fact implies that accuracy of the strain model should be improved with more well-quality data from these type of joints. Another important factor contributes to the relatively lower performance in strain predictions, after the first significant change in stiffness, stress response may exhibit only minor variations until the ultimate point (Point C). Detection of the strain level at the point with maximum stress response (Point B) may be challenging in cases that reported results have not sufficient resolution to represent these minor variations.

4.4.3 Point C

In Figure 4.17, scatter of the experimental versus predicted values are given for γ_C in which close correlation coefficient values $R_{test} = 0.87$ for test data and $R_{all} = 0.83$ for all data for γ_C predictions. As it was pointed in Point B results, there is a significant performance difference between γ_C and τ_C results, noting that prediction model for τ_C has $R_{test} = 0.92$ and $R_{all} = 0.94$ implying a higher performance. Among other uncertainties, a factor contribute to this fact is the limitation of the experimentation or measurement technique. As the congestion of experimental output in the range of $0.04-0.05$ points out, some of the deformation measurements in the database are limited to finite values close to 0.05, thus joint deformation capacity beyond this point

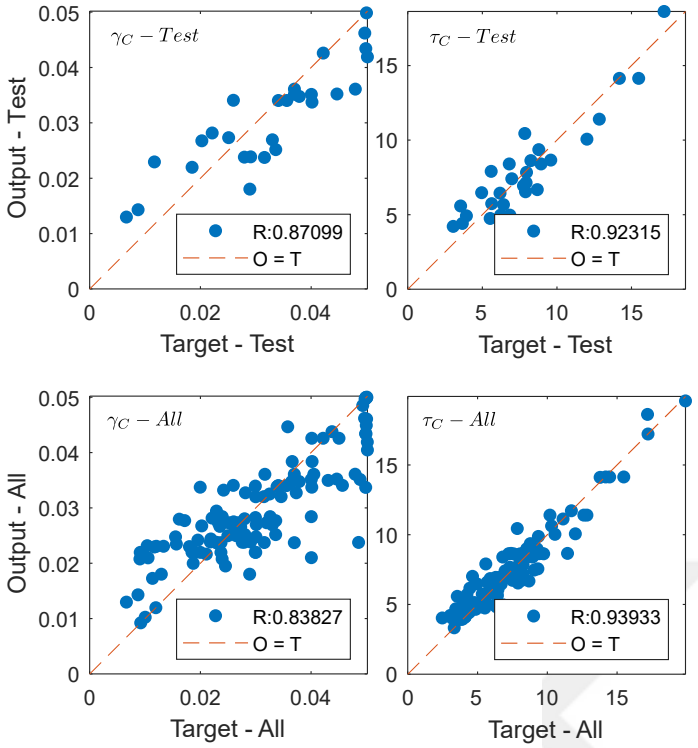

Figure 4.17 GRNN predictions versus experimentally observed values, training data (top) and all data (bottom) for Point C

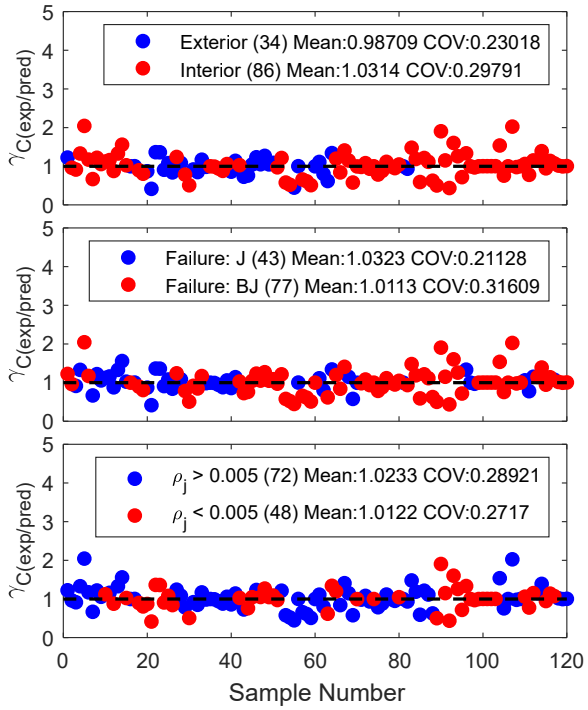

Figure 4.18 Scatter of γ_C GRNN predictions by type, failure type and reinforcement ratio

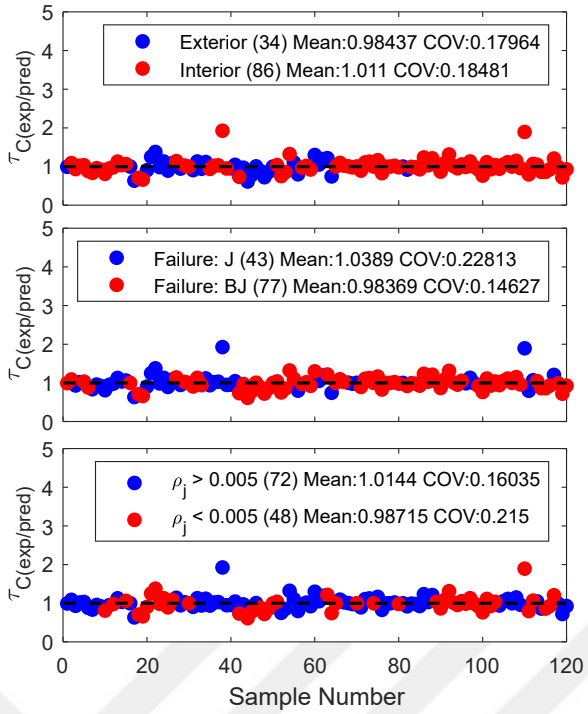

Figure 4.19 Scatter of τ_C GRNN predictions by type, failure type and reinforcement ratio

is ignored.

Figure 4.18 and Figure 4.19 show that mean values for Point C predictions to experimentally observed quantities vary between $0.98-1.04$. Coefficient of variations in τ_C exceeds 0.20 only for joint failure specimens. As expected, larger variation is observed in γ_C in which the larger C.O.V. is calculated as 0.31 in beam-joint failure joint specimen units.

To evaluate the accuracy of the proposed prediction method, joint shear strain-stress envelopes predicted by the models are compared with the experimental observations, analytical solution using MCFT [77] and statistical model based on Bayesian parameter estimation method by Kim and LaFave [25].

Table 4.4 Comparison of prediction/experiment values obtained by different methods

		γ_A	τ_A	γ_B	τ_B	γ_C	τ_C
MCFT [77]	Mean	1.00	0.99	0.59	0.81	0.88	0.63
	SD	0.93	0.51	0.49	0.29	0.56	0.27
Kim and LaFave [25]	Mean	1.61	1.19	1.12	1.02	1.11	1.08
	SD	1.04	0.33	0.43	0.14	0.78	0.22
GRNN (Proposed)	Mean	1.10	1.03	1.10	1.02	1.06	1.03
	SD	0.37	0.19	0.37	0.15	0.32	0.18

In Table 4.4, mean values and standard deviations of the ratio between predicted and experimentally observed values by MCFT, Kim and LaFave [25] equations and the proposed GRNN model. It is seen that Point A properties are estimated by MCFT

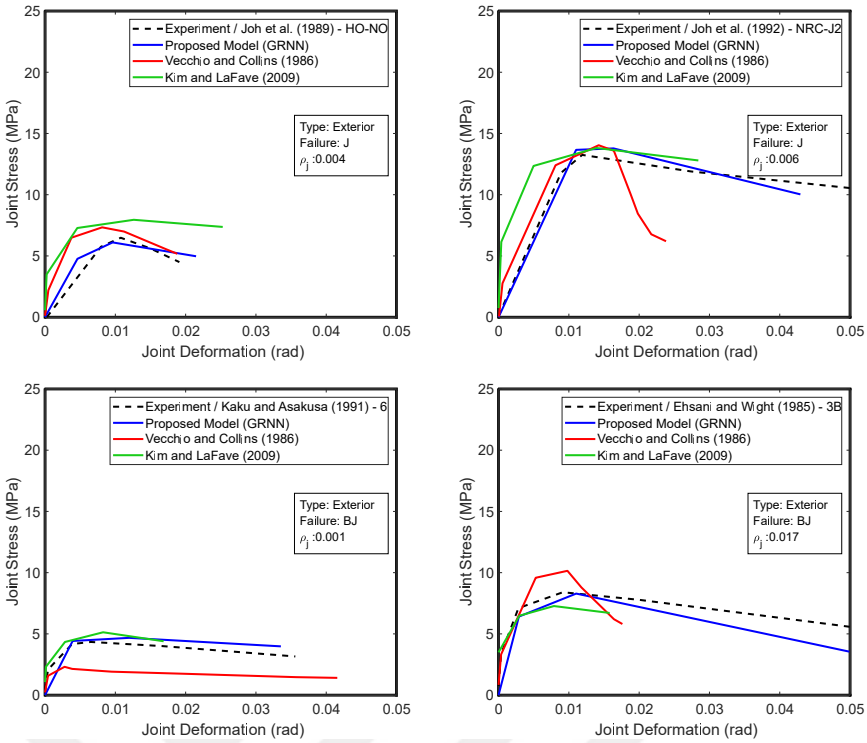

Figure 4.20 Comparison of experimental and predicted methods with various methods for exterior joints with joint shear (top) and beam-joint shear (bottom) failure modes

most accurately in average, however, large standard deviations of the estimations imply that MCFT can lead to misleading Point A predictions for some joint type and design configurations. GRNN predictions have mean value of 1.10 and 1.03 mean values for γ_A and τ_A respectively and relatively narrower band of predictions with 0.37 and 0.19 standard deviation in same respective order. Thus, it can be inferred that GRNN has the ability to yield more consistent predictions among these methods. In Point B, GRNN and Kim and LaFave [25] equations have almost identical statistical results overall in terms of mean values and standard deviations while MCFT [77] predictions are significantly less accurate for both γ_B and τ_B. For γ_C, proposed model yielded predictions with slightly better mean value accuracy ($mean(\gamma_{C-Kim})$: 1.11 and $mean(\gamma_{C-GRNN})$: 1.06) but significantly less disperse in terms of coefficient of variations ($SD(\gamma_{C-Kim})$: 0.78 and $SD(\gamma_{C-GRNN})$: 0.32).

Considering the large number of specimens, only selected results are presented in Figure 4.20 and Figure 4.21. Based on the plotted results for exterior joints in Figure 4.20, one can interpret that MCFT estimates joint shear strength with an acceptable accuracy except for the specimen tested by Joh *et al.* [226] which the joint failure was observed. In terms of deformation, MCFT underestimated the ultimate deformation for the specimens with relatively larger amount of joint horizontal reinforcement [52]. Despite the fact that accurate estimations by Kim and LaFave [25] of joint strength

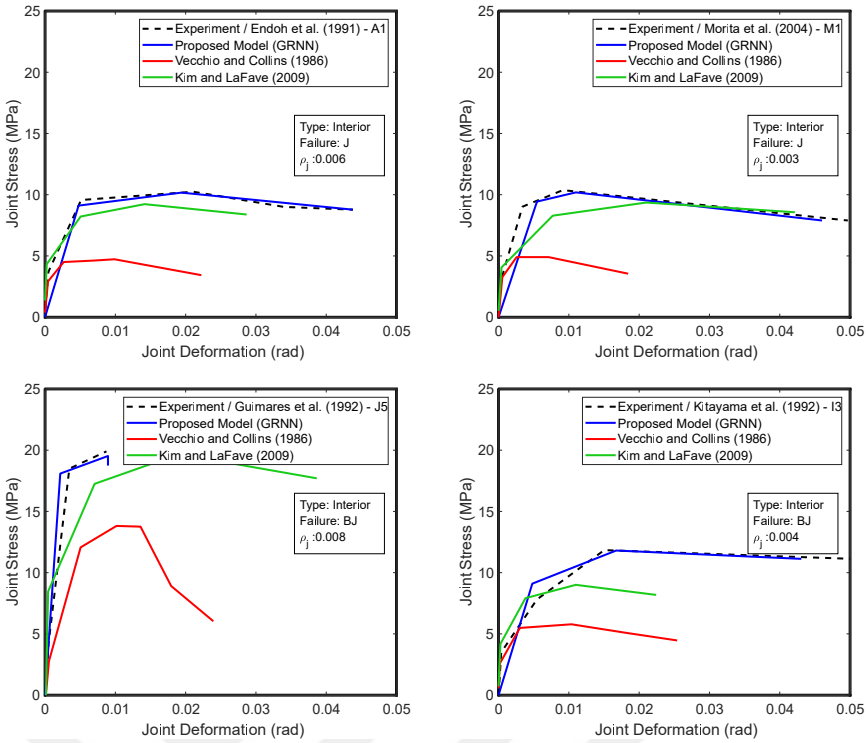

Figure 4.21 Comparison of experimental and predicted methods with various methods for interior joints with joint shear (top) and beam-joint shear (bottom) failure modes

for exterior joints are observed, joint deformation is only predicted for the specimen with low amount of reinforcement which exhibited joint failure. It is also observed that proposed model estimated joint strength and deformation significantly better for exterior joints with varying reinforcement level and failure types.

Figure 4.21 shows that MCFT failed to estimate joint strength and ultimate deformation level in interior joints for all plotted specimen results regardless of the failure type and reinforcement amount. In a similar way of exterior joint results, Kim and LaFave [25] model predicted joint shear strength level accurately, but failed to predict deformation except the specimen tested by Morita *et al.* [240] while proposed model predicts the full shear stress-strain envelope in an acceptable range.

Samples from different subsets are plotted to demonstrate the overall accuracy of the model is not significantly affected by the joint's type, failure mode or reinforcement ratio and can be used in practice to estimate shear strain - stress history envelope without any customization or modification on the structure of the framework.

4.5 Conclusions

A large experimental database of reinforced concrete joints has been collected. Joint specimens in the database were tested under static or quasi-static loading conditions and exhibited a dominant joint shear failure or beam failure followed by joint shear failure. Despite its upmost importance in finite element modelling of joints, there are only few studies available in the literature aiming to predict joint strain - stress envelope curve. A prediction framework is constructed in this study using specialized neural networks.

Investigation of the statistical correlation between experimental observations and model prediction output led to the conclusion that GRNN structure is capable of predicting essential key-points on the strain-stress curve using only general input data. Previous studies highlighted GRNN has strong priorities over conventional FFNN structures. The most importantly, the GRNN approximation algorithm is controlled by only one free parameter (σ) and optimization of the neural network structure is not required. Expectedly, GRNN yielded reasonably acceptable predictions by collection of 120 experiments, without any need for manual classification of data before training.

Comparison of the model results with a widely used analytical approach [77] and a statistical prediction model proposed by Kim and LaFave [25] demonstrated that the proposed model has the most accurate predictions among them. To demonstrate the capability of the proposed model in all various types of joints, the comparison was made for combinations of interior/exterior types, joint/beam-joint failure types and joints with smaller/greater reinforcement ratio than 0.005. For all comparison subsets, proposed model performed significantly better than the others.

As a conclusion, proposed GRNN joint shear strain - stress envelope prediction model is capable of making accurate predictions with only essential input and it has a good potential to contribute finite element analyses to be done with super-elements. A soft copy of the trained model is available in the Reference [246] in which the MATLAB users can use to predict joint shear strain-stress envelope using the required input parameters shown in Table 4.1.

5
ADVANCED FINITE ELEMENT ANALYSIS OF REINFORCED CONCRETE JOINTS

5.1 Overview

This chapter presents a detailed analysis and validation of microplane plasticity damage material models for reinforced concrete joints. The primary objective is to assess the accuracy and effectiveness of these models compared to other material models implemented in ANSYS Parametric Design Language (APDL). The chapter covers various aspects related to the analysis and validation process, highlighting the advantages of microplane models, discussing the element formulation, addressing limitations, and examining the practicality of these models in simulating cyclic effects on reinforced concrete. Essential notes on the theoretical background of these constitutive models can be found in Chapter 2, further details are available in the relevant references.

Microplane models offer significant advantages over classical plasticity-based models when simulating the behavior of concrete. These models excel at capturing the anisotropic and heterogeneous nature of concrete materials, providing a more accurate representation of their response. A key aspect of the analysis is the element formulation employed in the microplane models. The chapter explores the incorporation of additional degrees of freedom specifically designed to account for tension and compression damage separately. This enhanced formulation extends the accuracy of simulations by explicitly considering the damage behavior of concrete materials. Additionally, the concept of regularization is introduced, which addresses numerical challenges arising from the discontinuous nature of damage variables in microplane models, enhancing their numerical stability.

However, the limitations of microplane models in simulating cyclic effects on reinforced concrete structures are also addressed. The chapter examines the challenges associated with accurately capturing the bar-slip mechanism within these models. It emphasizes the need for further research to develop more realistic modeling

approaches capable of effectively representing cyclic behavior. The calibration process focuses on determining appropriate values for damage and non-local parameters within the microplane plasticity damage material models. Experimental data from laboratory tests on reinforced concrete structures are used for comparison and alignment with the model predictions. This ensures that the material models accurately represent the complex damage mechanisms occurring in reinforced concrete under different loading scenarios.

Furthermore, the chapter explores the definition and investigation of critical points along the joint strain-stress curve. These critical points are identified and analyzed to establish their relationship with joint dimensions, reinforcement, and concrete material properties. Nonlinear regression techniques are applied to understand the influence of these parameters on the behavior of reinforced concrete joints, providing valuable insights into their performance characteristics.

To enhance the accuracy of the regression analysis, the solution domain is divided into subdomains. This subdomain splitting approach allows for a more refined investigation, enabling a better understanding of the relationship between critical points and various influencing factors. By analyzing these subdomains separately, more robust regression models can be developed, improving the predictive capabilities of the microplane plasticity damage material models.

5.2 Aspects on the numerical modelling through plasticity and plasticity-damage material models

5.2.1 Unit Finite Element

A comprehensive parametric investigation was conducted to provide basic understanding of the relation between control parameters in material formulations introduced in Section 2.3.4.2 and corresponding output. The primary objective of this investigation was to identify the most capable material formulation for accurately reproducing the mechanical behavior of unreinforced concrete. Three distinct material formulations were considered for evaluation: Drucker-Prager with HSD06, MPLA (Elastic Microplane Material with Isotropic Damage and Implicit Gradient Regularization), and MPDP (Drucker-Prager Microplane with Anisotropic Damage and Implicit Gradient Regularization) [117].

To ensure simplicity in the analysis, the initial phase of the investigation utilized the most basic finite element unit, representing a 100 x 100 x 100 mm cube discretized with a single finite element (see Figure 5.1). This approach follows the methodology

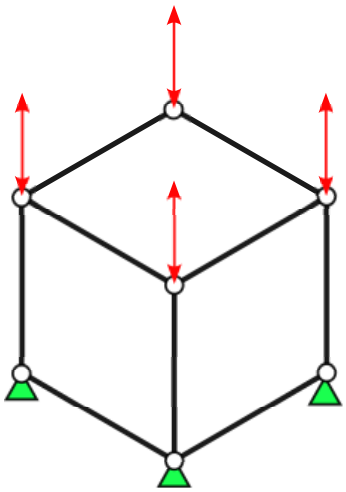

Figure 5.1 Sinlge finite element under cyclic displacement load

employed by Zreid and Kaliske [111]. The element is fixed at the bottom and cyclic displacement histories are applied at the top nodes. Two different loading protocol definitions were used to observe the response to different loading protocols. Accordingly, loading protocol I describes a cyclic loading with one step between -0.6 mm and +0.06 mm, while loading protocol II takes these values as the ultimate displacement and reaches these values incrementally with steps of -0.1 mm and +0.01 mm, respectively.

The investigation aimed to compare and assess the performance of the different material formulations in terms of their ability to accurately reproduce softening behavior under compression and tension, sensitivities to control parameters, the number of parameters governing changes in the stress-strain curve, and computational cost. The analyses were done and their results were compared to each other to evaluate the efficiency of the material formulations in capturing the desired behavior of unreinforced concrete. By considering various factors and metrics, this study aimed to provide valuable insights into the capabilities and limitations of different material formulations for simulating the mechanical response of unreinforced concrete. For the sake of clarity, a subset of simulations with a range of material model parameters is plotted in the following subsections, providing insight into the effect of these parameters on the material response; however, it should be noted that numerous other simulations have been conducted using a wider range of parameters.

5.2.1.1 Drucker-Prager combined with HSD06

As described in Section 2.3.4.2, plasticity based material models implemented in APDL can be used combined with a Hardening-Softening-Dilatation (HSD) definition. One of the most common HSD model is HSD06 which assumes linear softening after tension

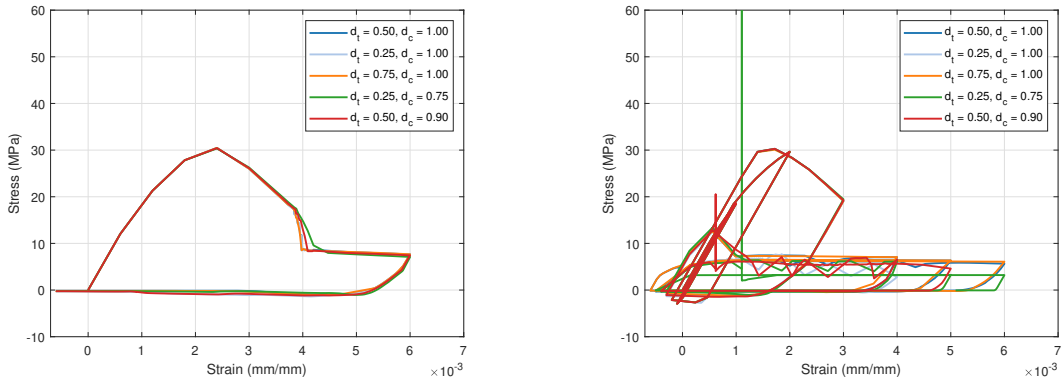

Figure 5.2 Stress strain curves of a unit finite element representing $f_c = 30MPa$ concrete material for various combinations of dilatation factors d_t, d_c (a) under loading protocol I and (b) loading protocol II

limit is exceeded.

The main advantage of using this combined material formulation is the intuitiveness of the model parameters that control the stress-strain relationship. The dependence of the control parameters on the compressive strength characterising the concrete leads to a significant reduction of the free variables within the formulation. Accordingly, a definition of plasticity can be made with uniaxial compressive strength f_c, tensile strength f_t, which is considered to be approximately $1/10$ of the compressive strength and biaxial concrete compressive strength f_b, which can be considered to be $1.15-1.20$ times the compressive strength [247], and dilatation factors d_t and d_c, which are defined separately for tension and compression. In addition, the softening that will occur after the strength is exceeded in compression and tension can be obtained by defining the relative stress ratios ($\Omega_{ci}, \Omega_{cm}, \Omega_{cr}$ and the plastic strain values ($\kappa_{cm}, \kappa_{cr}, \kappa_{tr}$) corresponding to the softening trend. A disadvantage is that the parameters controlling the softening trend must be estimated in advance and given to the model. However, it can be assumed that the physical quantities represented by these parameters are close to the values given by ANSYS Mechanical APDL Material Reference [117] for concrete materials in a wide range of compressive strengths.

Figure 5.2.(a) shows the response of a unit finite element with $30MPa$ compressive strength for Protocol I, which is a one-step cyclic loading targeting the endpoint displacement in tension and compression. Although there is no noticeable difference between the measured responses for different parameters, a significant difference was observed in the number of Newton-Raphson iterations performed to arrive at these solutions. For example, for the solution of the simulation with $d_t = 0.75, d_c = 1.00$, approximately half of the Newton Raphson iteration was performed for the solution

of the simulation with $d_t = 0.50, d_c = 1.00$, although it gave the same response results. Figure 5.2 plots the stress and strain responses of the unit finite element for incremental cyclic displacement loading procedure (Protocol II) for different dilatation factors. Accordingly, while the strength goes to infinity in simulations where the compressive dilatation factor d_c is below unit, meaningful results can be obtained only in simulations where the tensile dilatation factor d_t is close to 0 among the other cases.

5.2.1.2 Elastic Microplane Damage

The responses obtained from the material model constructed using the elastic microplane damage formulation are controlled by the variables k_0, k_1, and k_2, as well as the damage parameters (β, α, and γ_0) of the equivalent strain (see Equation 2.61) and the damage (see Equation 2.3.4.4) equations, respectively. This can be expressed as

$$I_1^2\left(\frac{k_o^2 - k_1^2}{k_2}\right) + I_1\left(\frac{-2\gamma k_0}{k_2}\right) + \frac{\gamma^2}{k_2} = J_2 \tag{5.1}$$

Simplifying this expression yields

$$I_1^2 X_1 + I_1 X_2 + X_3 = J_2 \tag{5.2}$$

$$\begin{pmatrix} I_t^2 & I_t & 1 \\ I_c^2 & I_c & 1 \\ I_{cb}^2 & I_{cb} & 1 \end{pmatrix} \cdot \begin{pmatrix} X_1 \\ X_2 \\ X_3 \end{pmatrix} = \begin{pmatrix} J_t \\ J_c \\ J_{cb} \end{pmatrix} \tag{5.3}$$

Solving the resulting linear equation system allows to obtain the damage surface in the invariant space (see Figure 2.12), thus k_0, k_1 and k_2.

For the purpose of comparison, considering a concrete material with a characteristic strength of $30MPa$, an elastic modulus of approximately $E = 30000$, a Poisson's ratio of approximately 0.2, and assuming that the tensile strength is approximately one-tenth of the compressive strength, as mentioned in Section 5.2.1.1, the variables k_0, k_1, and k_2 can be obtained as 0.703, 0.703, and 0.215, respectively.

Assuming the value of gamma is taken as suggested in the ANSYS Mechanical APDL Material Reference [117], f_t/E, the scope of this parametric study can be limited to

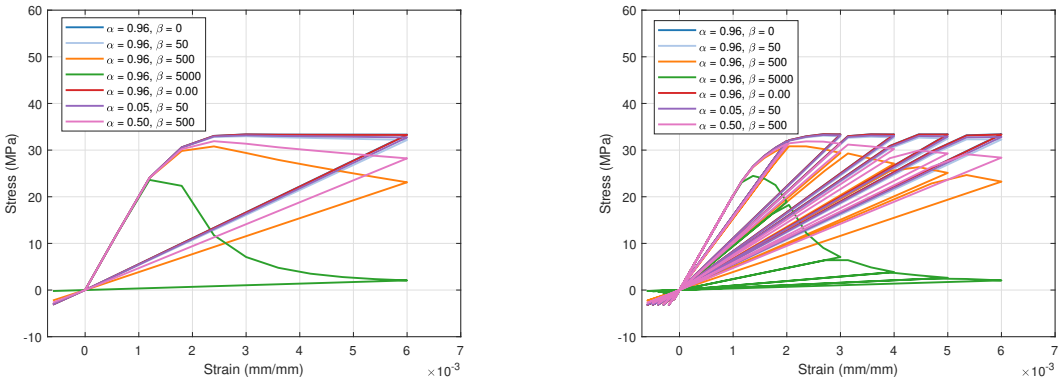

(a) **(b)**

Figure 5.3 Stress strain curves of a unit finite element representing $f_c = 30MPa$ concrete material for various combinations of damage parameter variables α, β (a) under loading protocol I and (b) loading protocol II

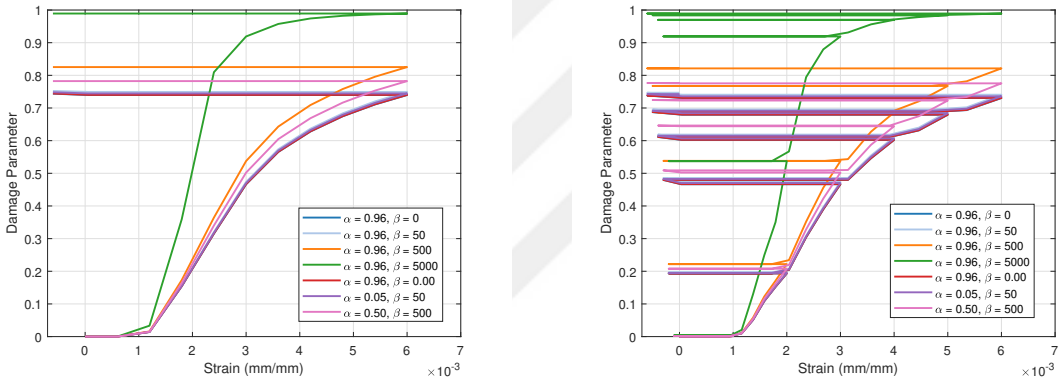

(a) **(b)**

Figure 5.4 Damage parameter with respect to strain of a unit finite element representing $f_c = 30MPa$ concrete material for various combinations of damage parameter variables α, β (a) under loading protocol I and (b) loading protocol II

investigating the influence of β and α parameters on the stress-strain response.

Finite element simulations conducted with CPT215 [124] element with an additional degree of freedom reserved for isotropic damage parameter d_{mic}. No implicit gradient regularization used in simulations.

Simulation results are shown in Figure 5.3. Firstly, contrary to the results obtained with the Drucker-Prager material model, it can be observed that the stress-strain curves and strain-damage parameter curves are independent of the displacement loading procedure. Additionally, during both unloading stages under compression and tension, it can be observed that the stiffness curve follows a zero-strain point target rather than the elastic or damaged stiffness.

The strain-damage parameter curves shown in Figure 5.4 also indicate that the material is more prone to damage for values of β ranging between 500 and 5000 compared to other parameter ranges. Furthermore, it was only possible to reach the state where the material's strength is completely exhausted by using a simulation model with $\beta = 5000$.

In terms of damage parameters, it is expected that the damage parameter will be close to $d_{mic} = 1$ for both loading procedures considering that the total ultimate strain values are exceeded for a standard $f_c = 30MPa$ concrete. This is demonstrated by the simulation conducted with a value of $\beta = 5000$, thereby supporting the conclusion that the sensitivity is relatively low for the remaining β values. Additionally, it is observed that the realistic representation of the material's stress behavior during unloading is not reflected in the results.

5.2.1.3 Drucker-Prager Microplane Damage

In a similar manner to the Elastic Microplane Damage model described in the previous section, the proposed material model by Zreid and Kaliske [111] includes damage parameters defined with an exponential function, coupled with stress-strain relationships. The loss of load-carrying capacity of the material occurs as these damage parameters approach unity. A notable difference is that the damage definition is separately formulated for tension and compression, which is considered to be more realistic. Steinke *et al.* [247] suggests a relationship between the tensile damage variable β_t and the compressive damage variable β_c as $\beta_t = 1.5\beta_c$

Additionally, definitions related to plastic yielding, hardening, and softening are described in Section 2.3.4.3, involving seven parameters, including f_c, f_t, and f_b. Steinke *et al.* [247] remarks low sensitivity to parameters R and R_t and, Zreid and Kaliske [111] suggest σ_{cV} as a function of f_c. As a result of this variable reduction, reactions for Procedure I and Procedure II were simulated and observed for different values of β_t (tensile damage variable) and D (material constant controls hardening), solely for a concrete material with a compressive strength of $30MPa$.

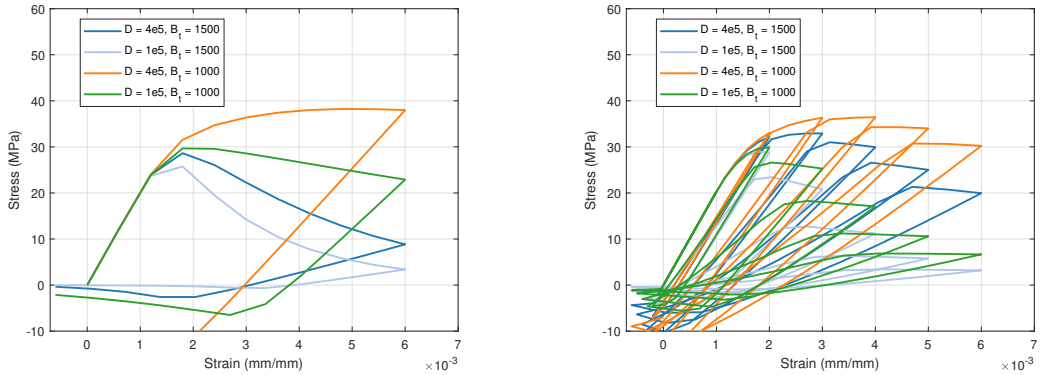

(a) **(b)**

Figure 5.5 Stress - strain curves of a unit finite element representing $f_c = 30MPa$ concrete material for various combinations of damage parameter variables β_t, D (a) under loading protocol I and (b) loading protocol II

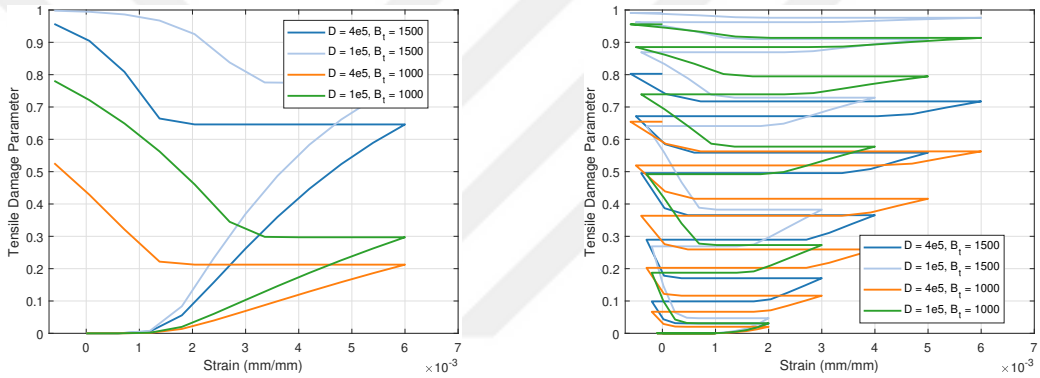

(a) **(b)**

Figure 5.6 Tensile damage parameter with respect to strain of a unit finite element representing $f_c = 30MPa$ concrete material for various combinations of damage parameter variables β_t, D (a) under loading protocol I and (b) loading protocol II

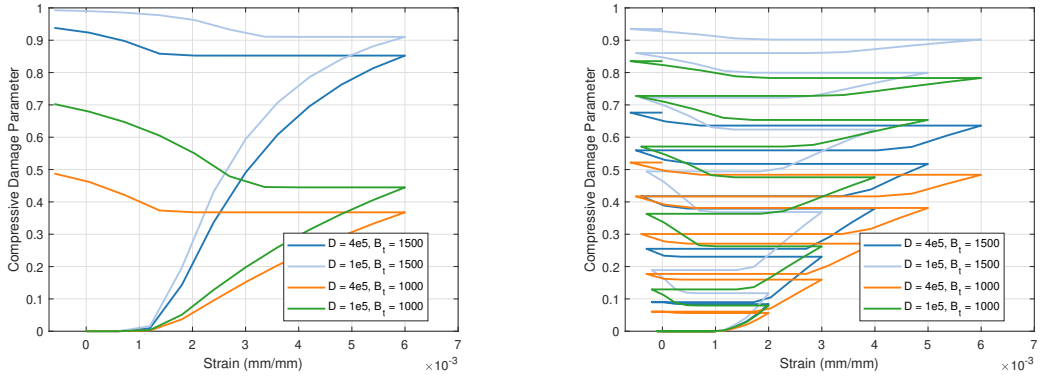

(a) **(b)**

Figure 5.7 Compressive damage parameter with respect to strain of a unit finite element representing $f_c = 30MPa$ concrete material for various combinations of damage parameter variables β_t, D (a) under loading protocol I and (b) loading protocol II

Figure 5.5 illustrates the strain-stress relationship for simulations with different MPDP model parameters. The simulations show varying stress levels as strain increases. The solid blue line exhibits a decreasing trend, indicating that stress decreases with increasing strain. The light blue line shows a similar trend but with a steeper slope. The orange line demonstrates a moderate decline in stress as strain increases, while the green line demonstrates a gradual decrease in stress. The stress-strain data reveals that varying the β_t and D parameters has distinct effects on the material's response to stress. Increasing the β_t parameter leads to a decrease in stress, indicating that the material becomes less resistant to deformation and requires less stress to produce a given strain. Conversely, as the D parameter decreases, there is a significant increase in stress, suggesting that the material becomes more susceptible to deformation and requires higher stress levels to achieve the same amount of strain. These observations highlight the importance of these parameters in influencing the material's behavior under stress, with higher β_t values leading to a weaker response and lower D values resulting in a stronger response. Alteration in slopes for the unloading sections indicates that distinct from MPLA material, the material unloads with a reduction in the initial stiffness. An important note about the effect of the loading history on the material response is clearly shown through the simulations for $D = 4e5$, $\beta_t = 1500$ and $D = 1e5$, $\beta_t = 1000$ model parameters run for Protocol I and II.

Figure 5.6 depicts the relationship between strain and the tensile damage parameter. The simulations reveal changes in the tensile damage parameter as strain magnitude escalates. The solid blue line shows an increasing trend, indicating that the tensile damage parameter rises with increasing strain. The light blue line displays a steeper increase, while the orange line exhibits a moderate increase. The green line demonstrates a gradual increase in the tensile damage parameter with increasing strain. Figure 5.7 represents the relationship between strain and the compressive damage parameter. The simulations reveal variations in the compressive damage parameter with increasing strain. The solid blue line showcases a gradual increase in the compressive damage parameter as strain magnitude increases. The light blue line displays a steeper incline, while the orange line exhibits a moderate increase. The green line demonstrates a gradual increase in the compressive damage parameter with increasing strain.

5.2.2 Exterior Joint Specimens Tested by Tsonos [8]

In order to extend the investigations carried out on the unit finite element to a real engineering problem, three finite element models were produced that reflect the geometry of the experimental studies carried out by Tsonos [8]. In the first of these, the

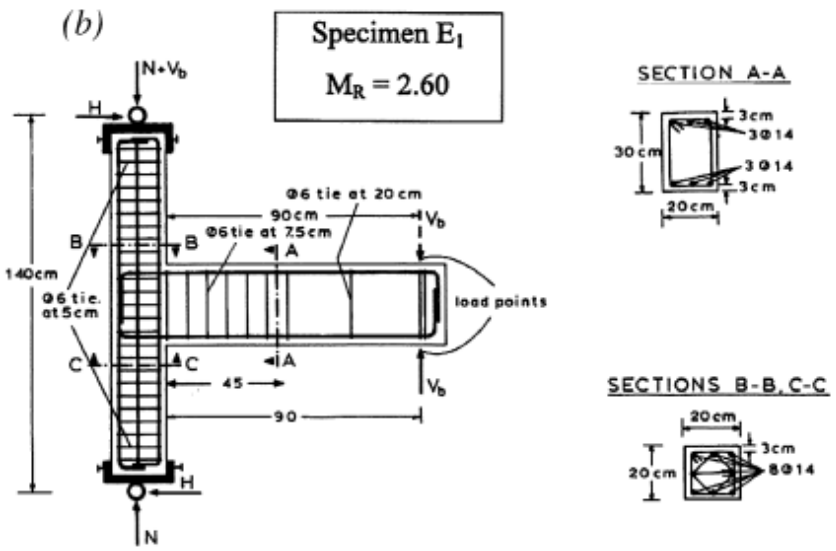

Figure 5.8 Experimental configuration of E1 specimen tested under cyclic loads [8]

concrete material was discretized using the SOLID186 finite element and the material formulation was made by combining the classical Drucker-Prager plasticity material model with the HSD06 dilatation definition. In the second model, the CPT215 finite element formulation was used and an additional degree of freedom was created for the isotropic damage formula, and in the third model, the same finite element formulation, two degrees of freedom were added for tensile and compressive damage.

In all three finite element models, flexural reinforcement and transverse reinforcement were modelled explicitly and BEAM188 element formulation was used for discretization. The stress-strain behaviour of the reinforcement is based on the yield strengths reported in the experimental study using a isotropic hardening bilinear material formulation. Full interlock between the reinforcement and the concrete material is assumed [65].

In order to realistically reflect the boundary conditions and loading protocol, it is considered that the loading jack is constituted by a rotatable mechanism and all nodal points on the beam end section surface are connected to an imaginary nodal point formed at the section centre with MPC184 elements with rigid link formulation and cyclic displacement loading is performed through this imaginary nodal point. The same arrangement was made for the supports at the column ends. The upper end of the column was not fixed vertically and a vertical load of 200 kN, which was kept constant throughout the experiment, was applied at the upper end of the column. 38160 elements are used to discretize the problem domain and symmetrical boundary conditions are applied to the vertical axis passing through the centroid of the beam section.

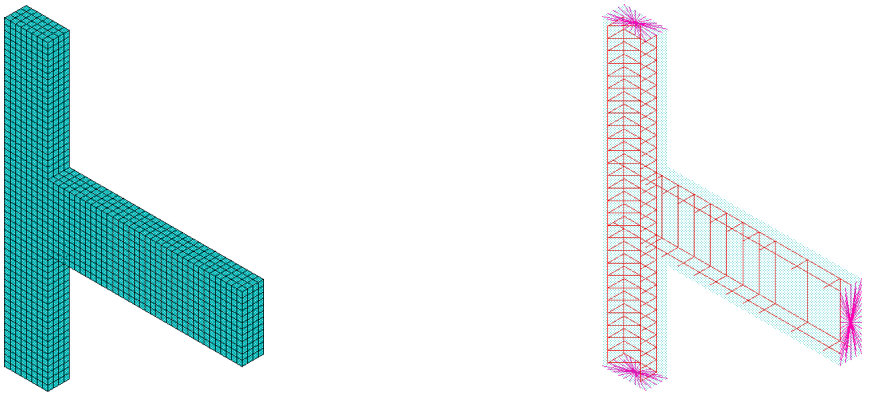

(a) **(b)**

Figure 5.9 Finite element model of E1 specimen [8] (a) concrete body (b) reinforcement and constraints (red) for boundary conditions (purple)

The simulation results of the finite element model of specimen E1, which was experimentally tested by Tsonos [8], using the introduced material models and the displacement loading procedure applied in the experiment are shown in Figure 5.10.The figure shows the simulation responses with the least error compared to the experimental results in the parametric analyses performed with the model parameters mentioned in the previous section. In the comparison, in addition to the numerical magnitude of the response, the prediction of the damage mode received by the joint region was also used. In Figure 5.11, the damage conditions at the joint region are presented for different loading steps of the experiment while Figure 5.13 displays the loading cycle and the measured amount of total strain of the yielding transverse reinforcement within the joint region, as observed in the experimental model. For comparison purposes, Figure 5.14 provides the total equivalent total strain map of the concrete body modeled using different material models in finite element models at various loading steps. Figure 5.13 illustrates the distribution of total principle strain in the transverse reinforcement observed in the simulation models.

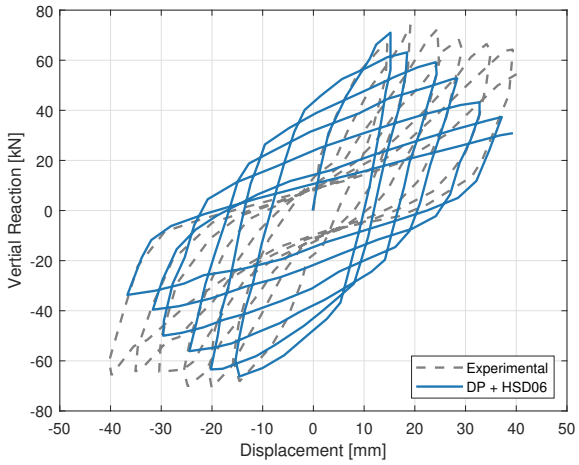

(a)

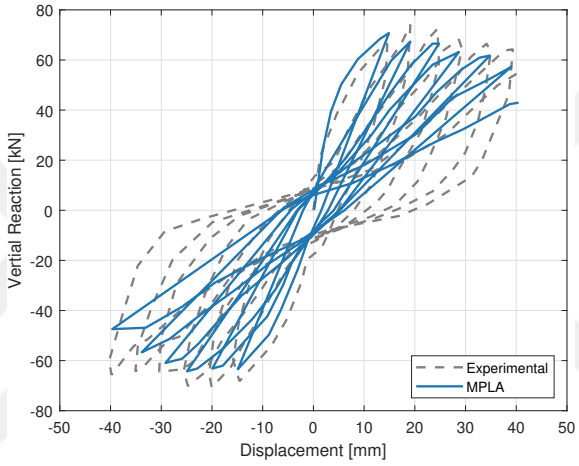

(b)

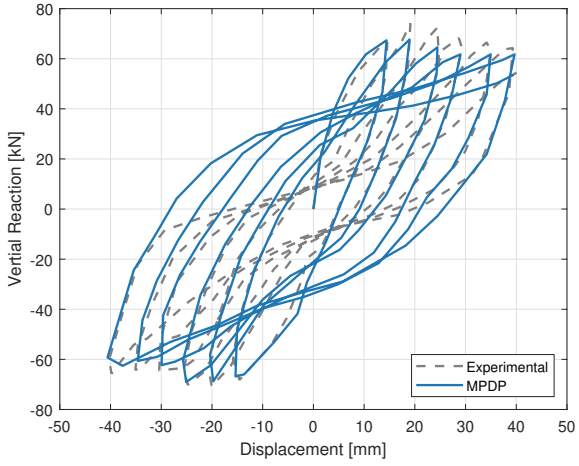

(c)

Figure 5.10 Comparison of the simulated response to the experimentally observed response for the simulation models built with (a) DP + HSD06, (b) MPLA, (c) MPDP material formulations

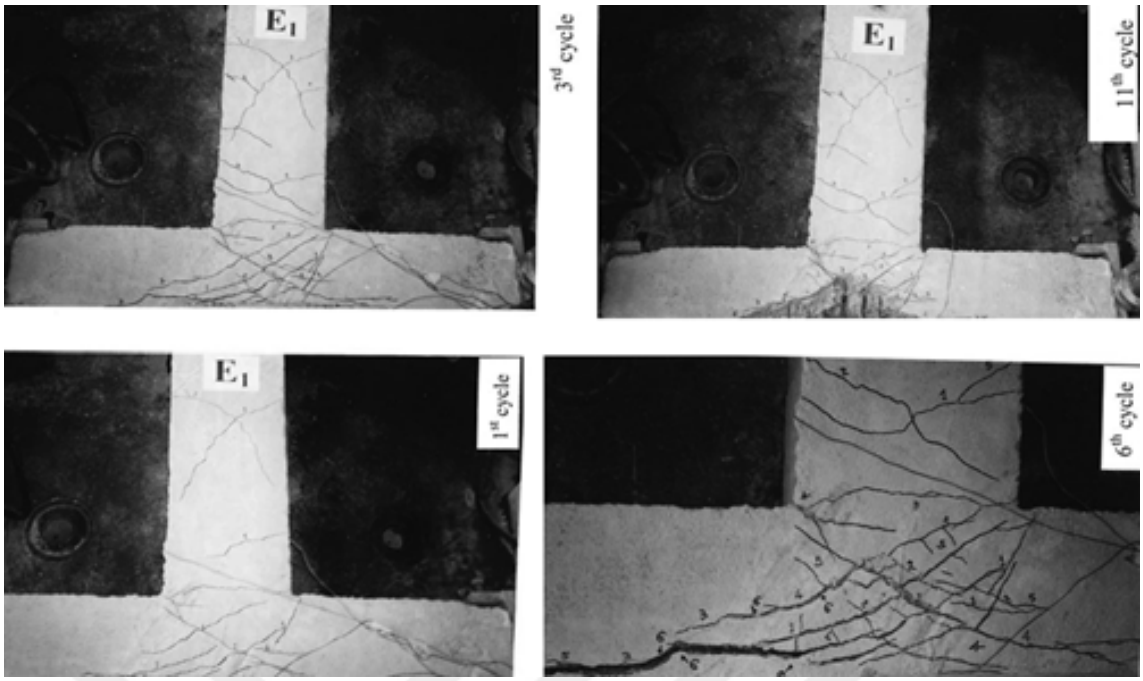

Figure 5.11 Observed damage in E1 specimen due to cyclic deformation in 1st, 3rd, 6th and 11th cycles [8]

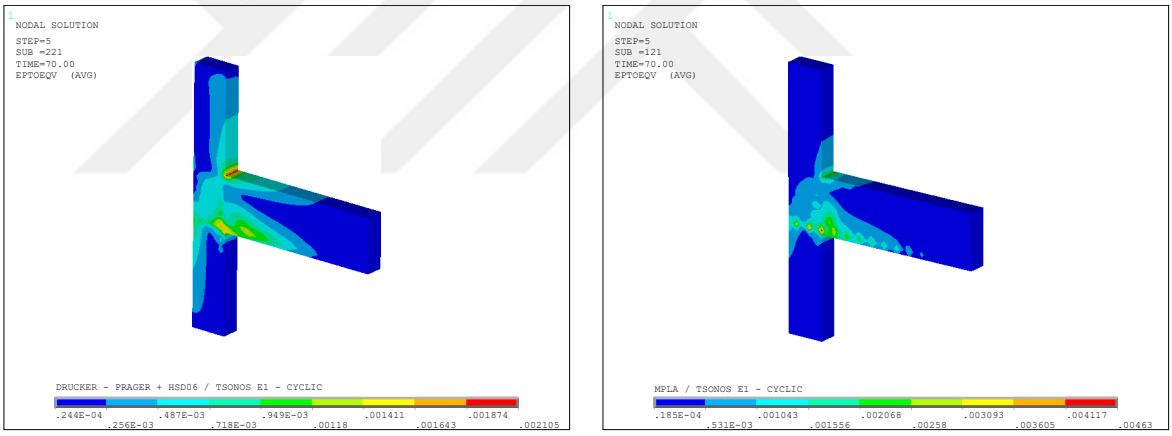

(a) (b)

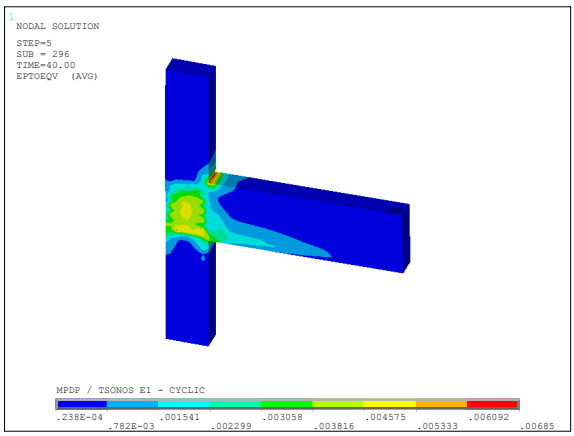

(c)

Figure 5.12 Total equivalent strains simulated with FE models using (a) DP + HSD06, (b) MPLA, (c) MPDP material formulations

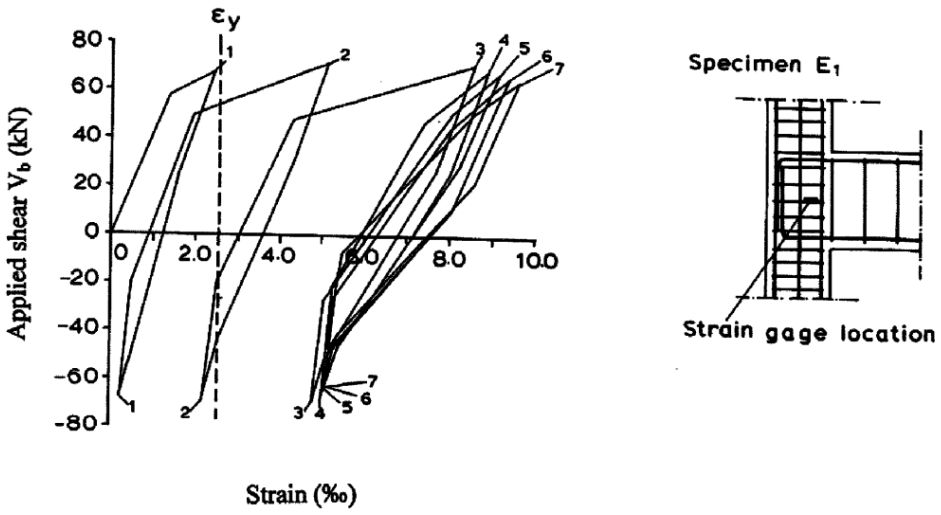

Figure 5.13 Total strain measurement versus total vertical reaction in transverse joint reinforcement of subassemblage E1 [8]

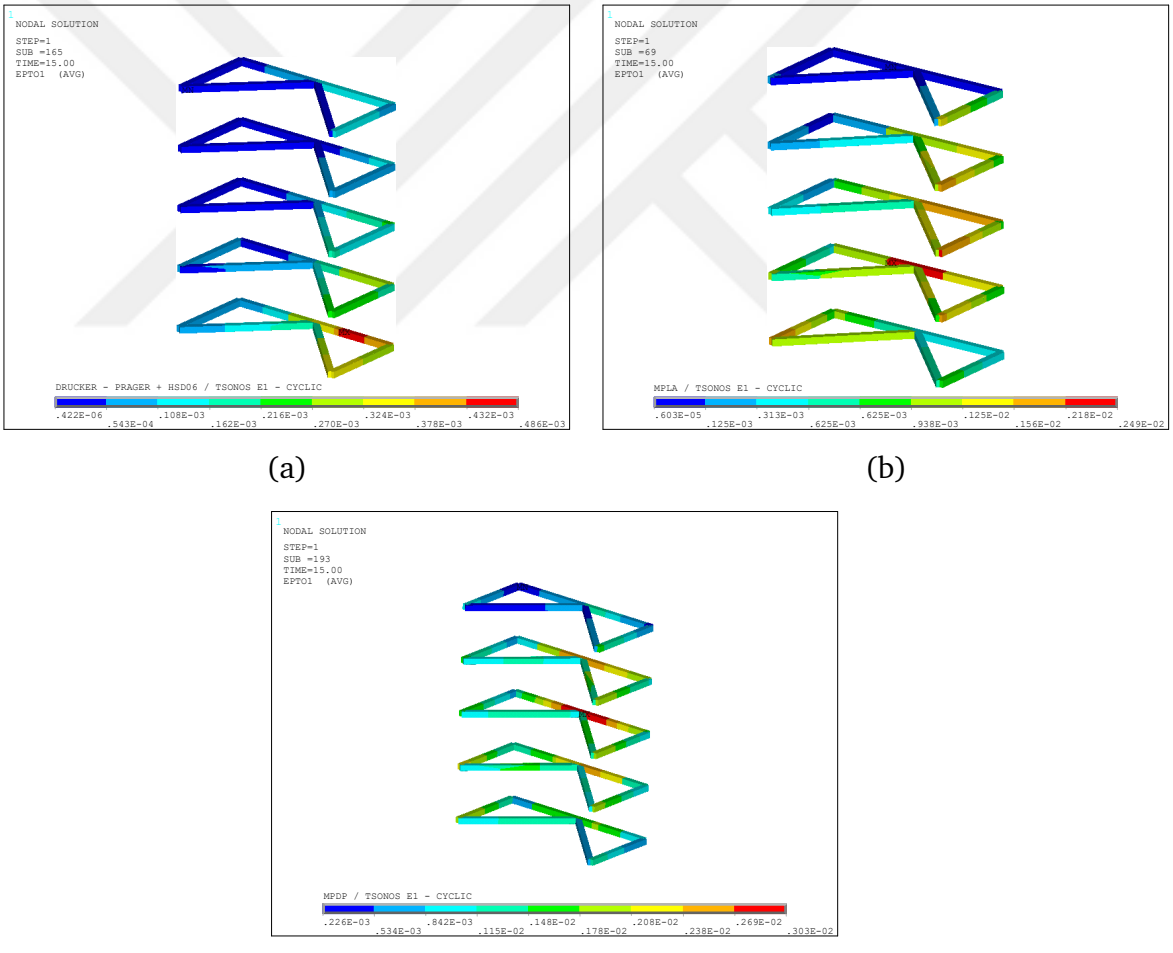

Figure 5.14 Total strains in joint transverse reinforcements simulated with FE models using (a) DP + HSD06, (b) MPLA, (c) MPDP material formulations

According to the results presented in Figure 5.10.(a), although the results obtained with the material model in which the Drucker-Prager plasticity model is used in combination with HSD06 have consistent responses for the initial cycle, the section reaches its bearing capacity by the yielding of the beam reinforcement at the end of the beam, not in the joint region, contrary to the experimental observation (see Figure 5.11 and 5.14.(a)). In addition, since the material model does not include any damage definition, the initial stiffness of the section is observed at the stages of unloading. On the other hand, it was observed experimentally that the stiffness decreased at each stage of loading. The cycle curve obtained by simulations using this material model is far from reflecting the actual plastic deformation.

In the simulations performed with the MPLA material model in Figure 5.10.(b), although the force response obtained in each cycle is observed realistically, it is observed that the stiffness is equal to the secant stiffness in all cases during the unloading phases of the loading. In accordance with the experimental observations, it was found that no beam hinge was observed in the joint and intense total equivalent deformations (EPTO) were observed in the joint region (see Figure 5.11 and 5.14.(b)). The phase in which the damage in the joint region is intensified can be determined as the phase in which the transverse reinforcement yields. As Figure 5.13 and 5.14 demonstrate, in the simulation results, there is a discrepancy between the total strain of the joint transverse reinforcement and the cycle in which this strain occurs.

When examining the results obtained from simulations using the MPDP material model plotted in Figure 5.10.(c), which provides the most realistic outcome, it can be concluded that there are fewer inconsistencies compared to other models. Analysis of the total equivalent strain values reveals that plastic deformations occur as expected in the joint region, and the actual force responses observed during all loading stages are better represented by this material model compared to others. Additionally, the damage parameters defined in the material model demonstrate a gradual decrease in stiffness during the unloading stages. Although there may not be a perfect match between the experimentally measured unit strain values and the simulated values, it is deemed acceptable that realistic results are obtained to a satisfactory extent.

The comparison between the results obtained from the simulation model built using the MPDP model and the experimental observations revealed the most significant difference to be the pinching behavior, which is one of the fundamental characteristics of hysteretic response in the joint region. Pinching, which appeared to be quite prominent in the experimental results, was observed to a limited extent in the simulation results. This can be interpreted as follows: there are two main sources for the occurrence of pinching in the hysteretic response. The first is the reversible

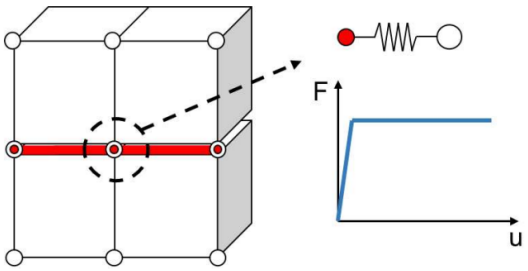

Figure 5.15 Illustration of non-linear spring definition [124]

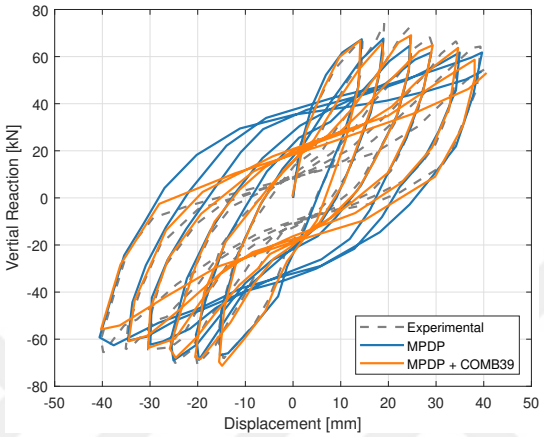

Figure 5.16 Comparison of the FEM results obtained by bond-spring and MPDP material definition

opening and closing of cracks in the concrete material, leading to changes in stiffness along the section during loading and unloading cycles, influencing the load transfer throughout the cycle. The second source is the bond-slip mechanism that controls the load transfer and slippage between the concrete and reinforcement. Incorporating the bond-slip mechanism in finite element analyses can be achieved by defining springs that represent the nonlinear load-displacement relationship along the reinforcement axis, rather than defining constraints acting in all directions between the finite element nodes representing the reinforcement and concrete material. In this regard, a parametric study was conducted and zero-length (COMB39) elements were defined between the node points corresponding to the same spatial coordinates (see Figure 5.15). The main challenge in establishing this definition lies in the uncertainty of the load-displacement relationship during loading and unloading phases. This definition was created by scaling the results of pull-out tests using the cyclic pinching material model within the framework of a super-element formulation. However, specifying the load-displacement characteristics of this mechanism for individual node points involves considerable uncertainty. The response results of the simulation model generated by incorporating this definition into the parametric investigation are provided in Figure 5.16, in comparison with the experimental responses.

The responses obtained from the solution of the simulation models are compared with experimental observations and presented in Figure 5.16. These models utilize the MPDP material model for concrete and the COMB39 zero-length uniaxial spring element. The bi-linear isotropic hardening load-displacement relationship is defined for the bond-slip mechanism. Bond strength values are fixed to the values defined in Table 2.1 and displacements are introduced as random variables. The comparisons demonstrate a certain level of agreement with experimental observations. However, the contribution of this definition to the complexity of the model outweights the realism effect. The increased complexity of the model results in an increase in computational effort required for achieving a single solution. Additionally, it involves the inclusion of new parameters that influence the behavior, and a significant effort is needed to create a simulation example that yields responses within acceptable error bounds. The parametric search at this stage follows the conventional trial and error method thus lacks an objective quantitative measurement of the increase in effort. Nevertheless, it is evident that the solutions obtained through this approach exceed the practical limits of the current study in terms of scope and objectives.

A secondary objective here is to simplify the material formulation and modelling technique, whose ability to represent the real problem has been validated, in order to meet the main objectives described in this thesis. Remembering that the purpose of the simulation models is to determine the boundaries (envelope) of the deformation likely to occur in the joint region, a more effective solution method in terms of practicality is to perform the displacement loading directly as the envelope of the cyclic displacement loading, instead of obtaining cyclic responses by simulation and using their envelope as the model output. In this case, it is clear that there will be some deviation in the internal forces and displacements to be obtained. However, as can be seen from the comparison of the computational effort required to realise an example of the simulations in Figure 5.17, it was order of magnitude more practical to apply the displacement loading in monotonic procedure. Validation tests for the monotonic loading case have shown that this deviation is acceptable. The validation tests presented in Section 5.3 cover the entire experimental database, not only the simulation model of specimen E1.

In order to obtain more statistically significant results for the validation and calibration process simulations performed for each sample in the experimental database as described in Appendix A, it is important to perform as many simulations as practicality allows. Therefore, in order to reduce the computational cost for each simulation run, the dimension in which the problem is defined within the validated assumptions is reduced from space to the plane. The strain in the cross-section due to the confinement effect can be considered close to the plane strain assumption. A comparison of the

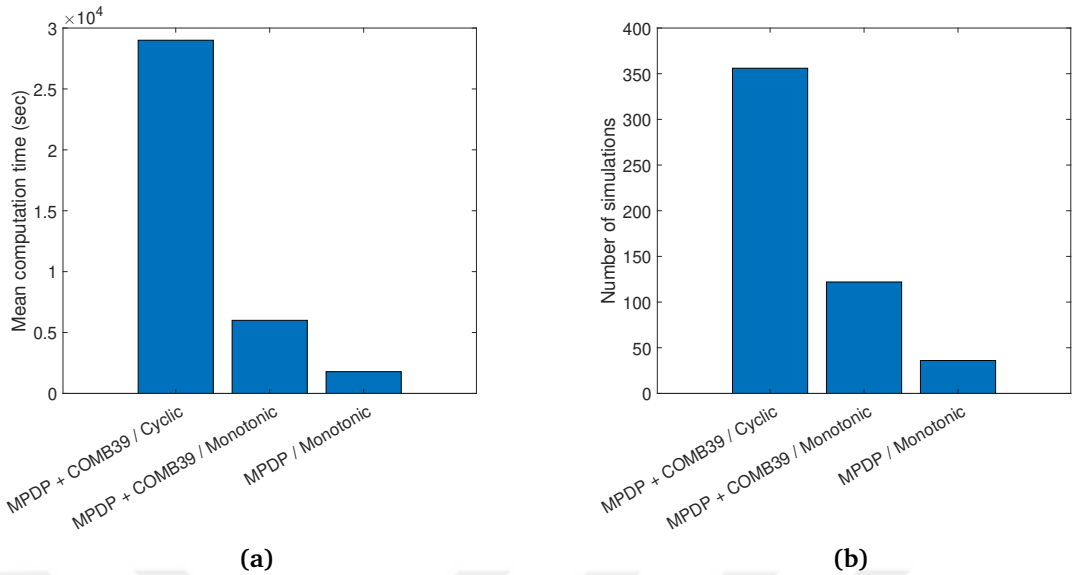

(a) **(b)**

Figure 5.17 (a) Mean computational time for simulations (b) Number of simulations to converge an accurate solution

simulation results in 3 dimensions (CPT215) and 2 dimensions (CPT213) with plane strain assumption under monotonic loading conditions is given in Figure 5.18. In the same figure, the results obtained from finite element models discretized with different number of elements are also given comparatively to verify finite element discretization technique used.

It should be noted that there is an order difference in the finite element models discretized with CPT213 and CPT215 due to the size of the problem and each discretization requires a regularisation process. For this reason, the interaction parameter c appropriate to the discretization dimension is used for each model whose result is shown in the Figure 5.18.

Using three different material models defined in ANSYS Parametric Design Language (APDL) Material reference, a finite element model comprising a unit element and an experimentally tested joint subassemblage was constructed. The objective was to qualitatively observe the sensitivity of these material models to the various parameters of the model. Through this analysis, it was determined that the Drucker-Prager Microplane Damage (MPDP) model offers a realistic description of concrete material behavior based on cyclic and monotonic tests conducted on the unit finite element. The MPDP model can be effectively controlled by adjusting the two most sensitive parameters associated with it. To achieve the most accurate representation of the joint specimen's response to cyclic displacement loads, which was supported by available experimental results, a modeling approach involving the definition of

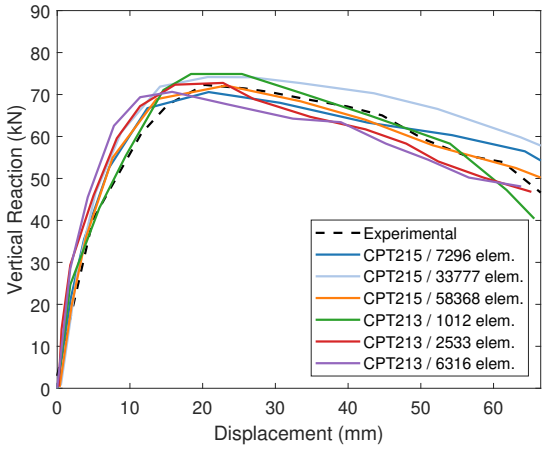

Figure 5.18 Load - displacement response of Tsonos E1 joint sub-assemblage under monotonic procedure using CPT215 3D model and CPT213 plane strain model

springs with nonlinear load-displacement characteristics at the nodes where the finite elements representing concrete and reinforcement coincide was employed. Although this approach yields a more realistic representation, it introduces limitations and increased complexity to the simulation process. When the expected magnitude of the output at the end of the simulations is specified as an envelope curve depicting joint deformation, the simulations conducted to achieve this outcome can be viewed as an envelope of the displacements that are cyclically applied. This approach enables a comprehensive assessment of the joint's behavior. Furthermore, the presence of the confinement effect allows for the assumption that the stress-strain state within the joint zone is a plane strain state, thereby significantly reducing the computational cost. This simplification contributes to more efficient calculations while still capturing the essential characteristics of the joint's response.

The MPDP material model exhibits the capability to provide realistic results in both unidirectional and cyclic simulations of joint regions, owing to its constitutive relations and implicit gradient regularization feature. Additionally, the model's advantageous characteristics include a small number of parameters governing material behavior and simplifications that effectively reduce computational costs. These benefits make the MPDP model particularly valuable for calibrating the models used in this approach.

5.3 Calibration of MPDP Model Parameters

As mentioned in the previous section, the parameters of the material model used in simulations need to be calibrated for each experiment. This calibration is done by classical trial-and-error in many studies in the literature. The necessity of the trial-and-error method in MPDP material is also emphasized by Zreid and Kaliske

[111] through the interaction parameter c that governs the regularization process. The interaction parameter controls the area of damage propagation and is related to the characteristic length of the material. The approach used by Bazant and Pijouder to determine the characteristic length by comparing the energy dissipation in cases where the damage is diffuse and localized is not possible in cases where the damage is diffuse, such as joint damage. On the other hand, the approach followed by Zreid and Kaliske [111], where damage (or plastic deformation) initiation and evolution and load-displacement characteristics are monitored and compared with experimental measurements, can lead to appropriate approximate regularization processes. In addition, since the damage patterns and finite element discretization magnitudes of the specimens forming the calibration sample pool are equivalent and there are no order of magnitude differences in terms of geometric dimensions and material character, a single characteristic length and hence interaction parameter can be assumed. In this case, the need for trial and error for the interaction parameter will be eliminated and a calibration process can be carried out based on the model parameters β_t and D of the MPDP material model as implemented in the previous section.

Another point that should be emphasized at this stage is that the damage generation and propagation should be equivalent for each specimen. This implies that the damage must occur in the joint region in all simulated joint region specimens. For this reason, in the experimental database table given in Appendix A, only the results of specimens showing "J" joint damage or "BJ" beam-joint combined damage are considered. In addition, the results of the experiment conducted by Vecchio and Collins [77] in which reinforced concrete panels were subjected to pure shear stresses were also added to the database. Material properties of the reinforced concrete panels tested by Vecchio and Collins [77] are given in the Table 5.1 Thus, finite element models of a total of 40 specimens experimentally determined to have shear damage were generated and 50 sets of β_t and D model parameters were generated for each model using LHS sampling for better representation of the sampling domain. The remaining control parameters were determined and used depending on the concrete compressive strength (f_c) as suggested by Steinke *et al.* [247]. The interaction parameter was taken equal to the value obtained by trial-and-error approach for the E1 joint specimen ($c = 625$) of Tsonos [8] in the previous section.

Within the 50 simulations performed for each specimen in the experimental dataset, the experimental response was considered as the envelope of the force response to cyclic displacement loading and an error value was calculated between the experimental and simulation results by interpolating the simulation response for each displacement point forming this curve. Among the 50 simulations performed for each

Table 5.1 Material properties of specimens experimentally tested by [77]

Specimen	fc	$f_{yx}(MPa)$	ρ_x	$f_{yy}(MPa)$	ρ_y
PV3	26.6	662	0.00483	662	0.00483
PV4	26.6	242	0.01056	242	0.01056
PV6	29.8	266	0.01785	266	0.01785
PV9	11.6	455	0.01785	455	0.01785
PV10	14.5	276	0.01785	276	0.00999
PV11	15.6	235	0.01785	235	0.01306
PV12	16	469	0.01785	269	0.00446
PV13	18.2	248	0.01785	-	0
PV16	21.7	255	0.0074	255	0.0074
PV18	19.5	431	0.01785	412	0.00315
PV19	19	458	0.01785	299	0.00713
PV20	19.6	460	0.01785	297	0.00885

specimen, the material model parameters belonging to the value with the least error were determined as the parameter set that most appropriately represents the response of the relevant specimen.

As mentioned in the previous section, the parameters of the material model used in simulations need to be calibrated for each experiment. This calibration is done by classical trial-and-error in many studies in the literature. The necessity of the trial-and-error method in MPDP material is also emphasised by Zreid and Kaliske [111] through the interaction parameter c, which controls the regularisation process. The interaction parameter controls the area of damage propagation and is associated with the characteristic length of the material. The approach used by Bazant and Pijaudier-Cabot [126] to determine the characteristic length by comparing the energy dissipation in cases where the damage is diffuse and localised is not possible in cases where the damage is diffuse, such as joint damage. On the other hand, the approach followed by Zreid and Kaliske [111], where damage (or plastic strain) formation and progression and load-displacement characteristics are monitored and compared with experimental measurements, can lead to appropriate approximate regularisation processes. In addition, since the damage patterns and finite element discretization magnitudes of the specimens forming the calibration sample pool are identical and there are no order of magnitude differences in terms of geometrical dimensions and material character, a single characteristic length and therefore interaction parameter can be assumed. In this case, the need for trial and error for the interaction parameter will be eliminated and a calibration process based on the model parameters β_t and D of the MPDP material model as applied in the previous section can be carried out.

Similar to Steinke *et al.* [247], where most of the material model parameters are obtained as a function of concrete compressive strength, the values of D and β_t

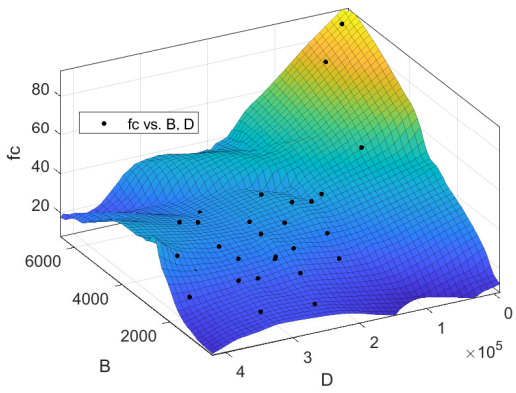

Figure 5.19 The surface fitted for the scatter of β_t, D values yielding the best result with respect to the concrete strength f_c of the corresponding specimen

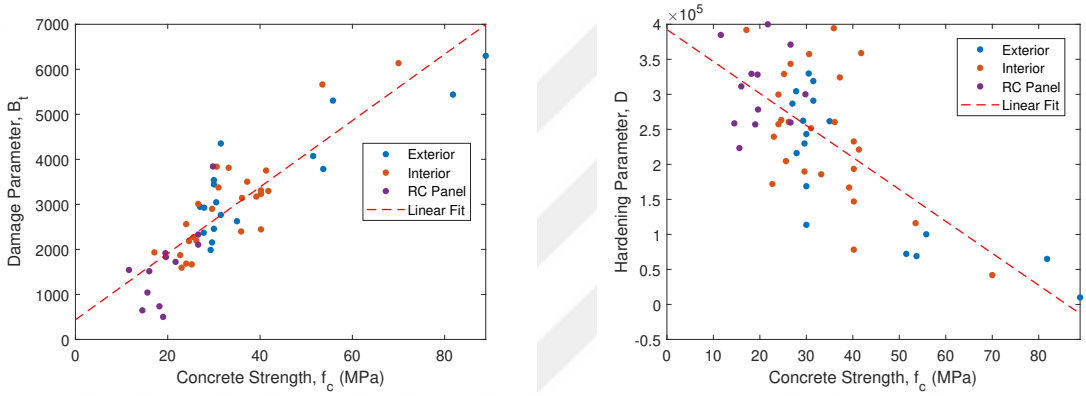

(a) **(b)**

Figure 5.20 (a) Scatter plot of damage parameter β_t versus concrete strength f_c (b) Scatter plot of hardening parameter D versus concrete strength f_c

parameters selected for the calibration of the material model, which give the most approximate result for each simulation, are given as a surface in the f_c-β_t-D space in Figure 5.19. The surface shows that a correlation can be established between the variable f_c and D and β_t.

For the sake of simplicity, linear regression technique is used to express the model parameters β_t and D as a function of concrete compressive strength. Figures 5.20 show the scatter plots of β_t-f_c and D-f_c and the nonlinear functions describing the relationship. Accordingly, Equation 5.4 is proposed for the β_t-f_c relationship and Equation 5.5 for the D-f_c relationship.

$$B_t = 73.76 f_c + 435.53 \tag{5.4}$$

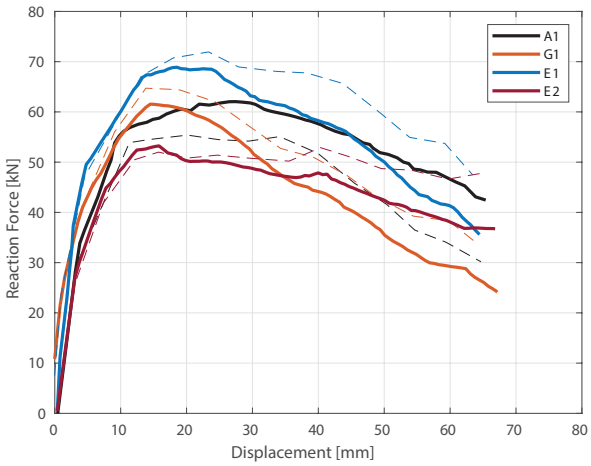

Figure 5.21 Comparison of the experimental responses to the simulated responses obtained through CPT213 Plane Strain MPDP models which β_t and D parameters are assigned with Equation 5.4 and 5.5

$$D = -4563.4 f_c + 39243 \tag{5.5}$$

The scatter plots given in Figure 5.20.(a) and Figure 5.20.(b) show that there is no statistically significant difference in the determination of β_t and D for the reinforced concrete panel, internal joint region or external joint region. Therefore, it is considered as appropriate to use Equation 5.4 and Equation 5.5 for all three types of simulations.

5.4 Validation

Proposed Equations 5.4 and 5.5 have been tested for all sub-assemblages and reinforced concrete panels tested by Tsonos [8] and Vecchio and Collins [77]. Figure 5.21 presents a comparison between the simulated responses and the experimentally measured responses for the models described in [8]. In simulation models A1 and E1, the initiation of plastic strains at the column face and their propagation to the beam body resulted in the formation of a flexural hinge, which aligns well with the observations from the experiment (see Figure 5.22.(a)). However, it should be noted that while specimen A1 remained intact even after a 4.5% drift, in the simulation model, plastic strains were formed in the joint region after 3.5% drift, indicating a coupled failure mode. For models G1 and E2, plastic strains were observed to initiate in the vicinity of the joint core and propagate inside the joint, resulting in a premature failure mode similar to the experimental observations (see Figure 5.22.(b)). The simulation models successfully captured the formation of this failure mode as well

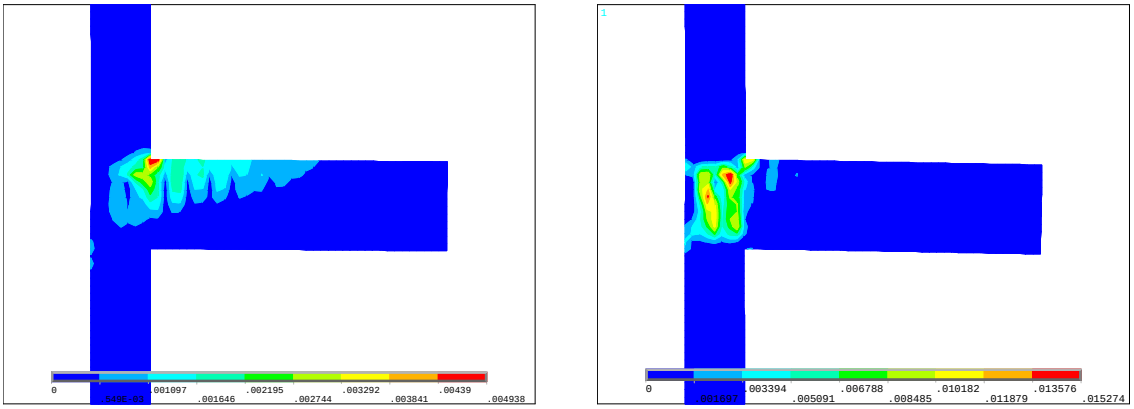

(a) **(b)**

Figure 5.22 Total strain plots for the simulations at the final state of (a) G1 and (b) E2 specimens tested by Tsonos [8]

as the overall response. However, there was a slight overestimation of the flexural capacity by approximately 15% in model A1, and in both models A1 and G1, a beam-joint failure mode was observed, whereas the severe joint failure was reported in the experiment. These findings indicate that the simulation models provide a reasonable representation of the structural behavior and can effectively predict the formation of failure modes observed in the experiments. Despite some discrepancies in flexural capacity estimation and the occurrence of specific failure modes, the overall response of the reinforced concrete panels under cyclic loading was well-predicted. These insights contribute to a better understanding of the structural response under shear effects and inform the design and assessment of reinforced concrete structures subjected to similar loading conditions.

The maximum shear stress, first principal stress, and second principal stress values obtained from the finite element analysis were compared with the corresponding experimentally observed values for the reinforced concrete panels. This comparison aimed to assess the accuracy and reliability of the numerical simulation. To visually illustrate the agreement between the measured and calculated values, scatter plots were generated, as shown in Figure 5.23. Each point on the scatter plot represents a specific panel configuration, and its position indicates the corresponding values of the maximum shear stress, first principal stress, and second principal stress obtained from both experimental measurements and finite element analysis. Upon analyzing the scatter plots, it was observed that there is a strong correlation between the measured and calculated values. The coefficients of determination (R-squared values) were determined to quantify this correlation. The coefficient of determination measures the proportion of the total variation in the experimental data that can be explained by the calculated values.

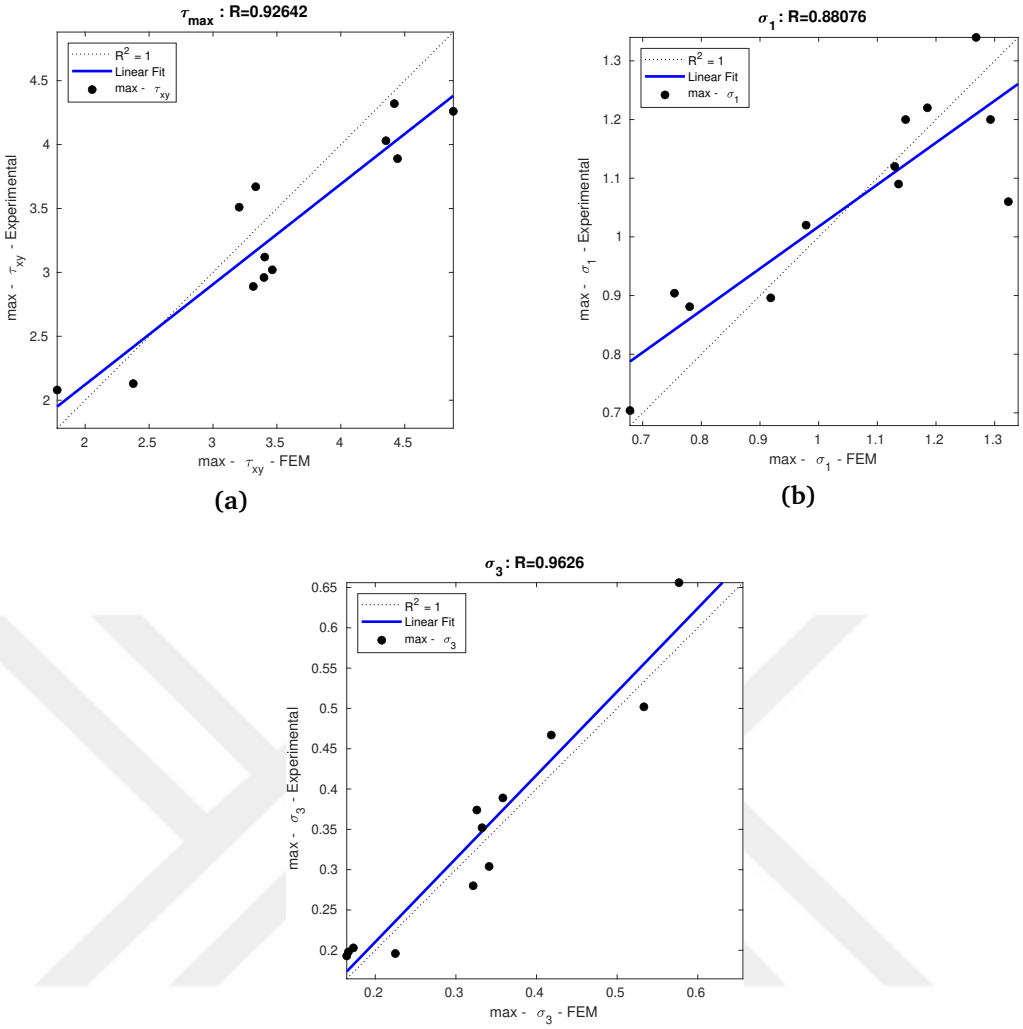

Figure 5.23 Comparison of experimentally reported and simulated (a) maximum shear stress (b) first principal stress and (c) second principal stress for the specimens tested by Vecchio and Collins [77]

The coefficients of determination between the measured and calculated maximum shear stresses, first principal stresses, and second principal stresses were found to be $R^2 = 0.92$, $R^2 = 0.96$, and $R^2 = 0.88$, respectively. These high R-squared values indicate a significant level of agreement between the experimental and numerical results, suggesting that the finite element analysis accurately predicts the response of the reinforced concrete panels under shear effects. The obtained coefficients of determination provide confidence in the reliability of the numerical simulation and demonstrate its capability to capture the essential features of the panel behavior. The strong correlation between the measured and calculated values confirms the suitability of the developed prediction model for estimating the characteristic points of joint shear strain-stress curves.

5.5 Parametric Simulations

This section focuses on the parametric analyses and the generation of a comprehensive dataset for the prediction model related to joint shear strain-stress curves' characteristic points. Three distinct simulation types were conducted, namely interior joint simulations, exterior joint simulations, and panel simulations. A substantial number of 500 simulations were performed for each simulation type, resulting in a comprehensive dataset comprising a total of 1500 simulations. The simulations aimed to analyze the influence of various model parameters on the response of these structural elements under varying loading conditions.

The interior and exterior joint simulations involved a meticulous examination of model parameters, excluding beam eccentricity due to the adoption of plane modeling and the limited variations observed in the dataset. Notably, the concrete body dimensions, including the width and depth of the joint in the plane (h_c, h_b), as well as the configuration of reinforcement in the beam and column, were thoroughly investigated. Additionally, the joint transverse reinforcement ratio and the material strength of the concrete were varied within prescribed ranges outlined in Table 5.2. For the purpose of analysis, the yielding strength of the reinforcement was maintained at 200 MPa for half of the simulations and 400 MPa for the remaining half, as the variability in this parameter was deemed relatively low when compared to the concrete material. Furthermore, the reinforcement configuration exhibited diversity as specified in Table 5.2, augmenting the comprehensiveness of the investigations. Alongside this, the panel simulations incorporated variations in panel dimensions, reinforcement ratio, and concrete material strength, all within the intervals prescribed in Table 5.2. Consistent with the joint simulations, the yielding strength of the reinforcement was divided into two groups: 200 MPa and 400 MPa, ensuring a comprehensive

Table 5.2 Descriptions and bounds of the input parameters of the panel parametric simulation set

Type	Parameter	Bounds	Units	Description
Int. and Ext. Joints	f_c	10 - 90	MPa	Compressive strength of the concrete
(see Fig. 5.24.(a-b))	f_{yb}	200, 400	MPa	Yield strength of the beam long. reinf.
	f_{yc}	200, 400	MPa	Yield strength of the column long. reinf.
	f_{yc}	200, 400	MPa	Yield strength of the joint trans. reinf.
	ρ_b	0.001 - 0.025		Beam reinforcement ratio
	ρ_c	0.001 - 0.025		Column reinforcement ratio
	ρ_j	0.000 - 0.025		Joint volumetric reinf. ratio
	ρ_{bt}	0.0005 - 0.002		Beam transverse reinf. ratio
	ρ_{ct}	0.0005 - 0.002		Column transverse reinf. ratio
	h_b	200 - 1300	mm	Beam height
	h_c	200 - 1300	mm	Column height
	b_b	200 - 600	mm	Beam width
	b_c	200 - 600	mm	Column width
	n	0 - 0.6		Column axial force to capacity ratio
RC Panels	f_c	10 - 90	MPa	Compressive strength of the concrete
(see Fig. 5.24.(c))	f_x	200, 400	MPa	Yield strength of the reinf. along x dir.
	f_y	200, 400	MPa	Yield strength of the reinf. along y dir.
	ρ_x	0.000 - 0.025		Reinforcement ratio in x dir.
	ρ_y	0.000 - 0.025		Reinforcement ratio in y dir.
	b	200 - 1300	mm	Panel width
	h	200 - 1300	mm	Panel height

examination of its effects. It is also worth noting that in panel simulations, number of reinforcement kept constant and different joint reinforcement ratios are obtained by altering the size of the reinforcement bars.

In order to effectively cover a larger portion of the sampling domain while minimizing the number of required samples, the generation of the simulation sampling space was conducted using Latin hypercube sampling. By leveraging Latin hypercube sampling, the simulation space was efficiently explored, ensuring a comprehensive representation of the varying model parameters and their effects on the structural behavior of reinforced concrete elements. This approach enabled the researchers to obtain meaningful and statistically significant results, despite the relatively limited number of simulations performed. It reduces the likelihood of missing important regions or clusters within the domain, allowing for a more representative sampling of the input variables. By partitioning the space into equally probable intervals along each dimension, LHS offers a higher level of coverage and exploration of the parameter space. Thus, the adoption of Latin hypercube sampling allowed for the efficient utilization of computational resources while maintaining a robust and extensive coverage of the parameter space, thereby enhancing the overall validity and reliability of the study's findings.

The collective outcomes of these simulations present a valuable contribution to the understanding of interior joints, exterior joints, and panels, shedding light on their

structural behavior under severe effects. To establish a relationship between the model parameters and the desired outputs, nonlinear regression techniques are employed. This approach allows for the identification of the interdependencies and correlations between the various parameters influencing the joint's behavior and the resulting characteristic points. By accurately modeling this relationship, a prediction model can be developed to estimate the joint shear strain-stress curve's characteristic points based on the input parameters.

5.5.1 Investigation of Critical Points along the Joint Strain-Stress Curve

In order to establish a relationship between the model input parameters defining the joint model and the shear strain-stress output, a selection process is used to identify multiple points that effectively characterize the shear strain-stress output. This selection is founded on predetermined criteria. These principles are defined using two separate methodologies. The first strategy focuses on the damage formulation of the concrete material model, which involves minimizing the load transformation capacity of the discrete elements that represent the concrete material. The results of this methodology are presented in the Section 5.5.1.1. Alternately, a method based on the stress limit conditions of both the concrete and the joint reinforcement material is developed. In the Section 5.5.1.2 the results of the analyses conducted using this methodology are presented.

The correlation analysis conducted in Section 4.2 reveals that the concrete strength, denoted by f_c, exerts a significantly greater influence on the shear strain and stress output than other model parameters. In order to assess the sensitivity of the aforementioned output to other influential model parameters, correlation coefficients between simulation outputs belong to the various sub-domains of the sampling domain and concrete strength, f_c. As a result, f_c is chosen as the principal variable upon which the input-output relation is constructed. To establish a mathematical representation of the obtained outputs in relation to concrete strength, curves are fit to the selected coordinates. Utilizing both nonlinear regression techniques, the most statistically robust relationship is determined.

An additional control subroutine is implemented for the damage-based method to arrange strain outputs in ascending order based on the damage index. Likewise, a control subroutine is implemented for the material strength-based method, permitting the shear strain points corresponding to intermediate limit states to be evaluated in any order. Although these control subroutines do not significantly improve the statistical metrics for the curve-fitting process, they effectively prevent overlapped strain point predictions.

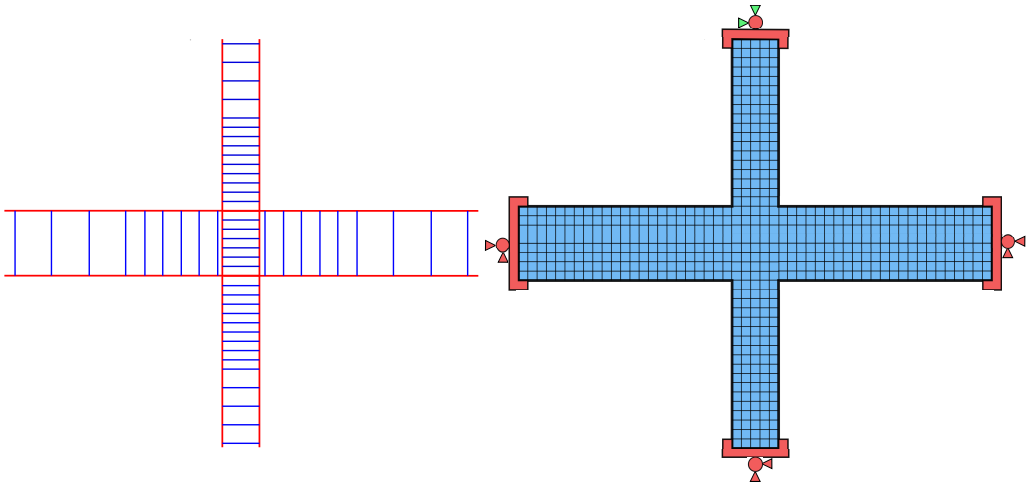

(a) Interior Joint reinforcement configuration (left) and concrete body (right)

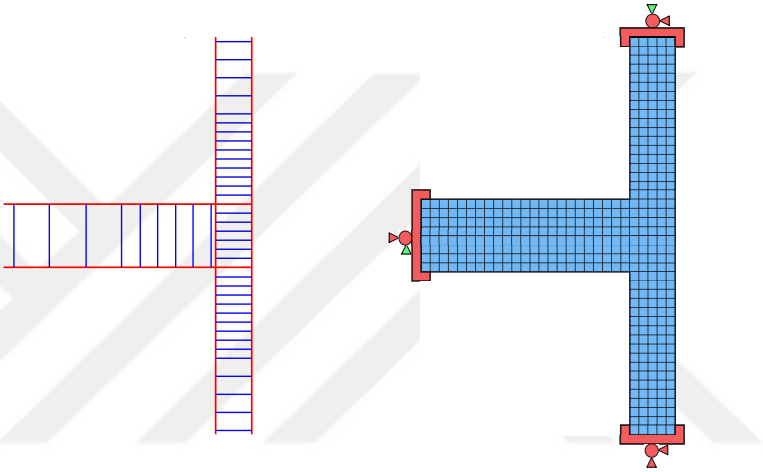

(b) Exterior Joint reinforcement configuration (left) and concrete body (right)

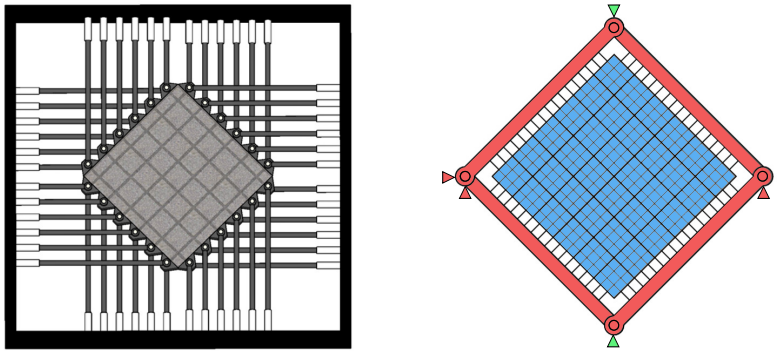

(c) Reinforced concrete panel subjected to pure shear

Figure 5.24 Illustration of discretization and boundary conditions of the finite element models

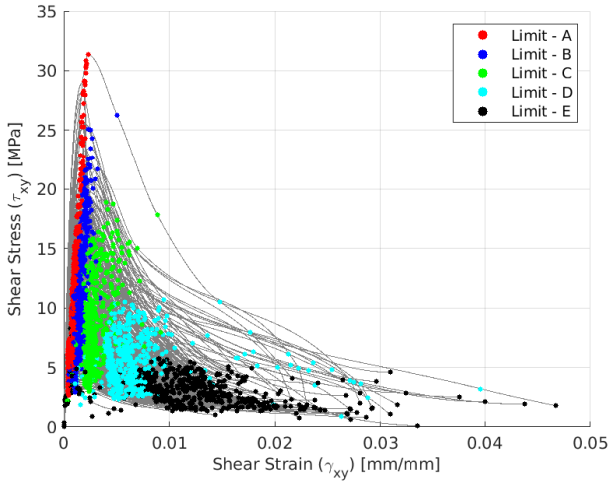

Figure 5.25 Shear strain - stress plots of simulations (gray solid lines) and scatters of the strain - stress values that specified material damage occurred for Limit A, Limit B, Limit C, Limit D and Limit E

5.5.1.1 Damage Index Based Approach

In this chapter, the primary objective is the development of explicit equations to provide a clear representation of the phenomena under study. To achieve this, a process of simplification and selection has been adopted. The most influential parameter, f_c, which stands for the concrete compressive strength, has been singled out for this purpose. All other quantities are then intended to be expressed as a function of this critical parameter. The selection of f_c as the central variable is due to its established role in significantly affecting the outcomes in the system.

While f_c serves as the central variable, it is also essential to acknowledge that the complexity of the system involves other parameters. These include the joint reinforcement ratio and the joint geometry (h_c/h_b), which have also been found to be influential, based on empirical evidence. These parameters have thus been included in the categorization of the subdomains of the sampling space.

A simple correlation analysis, similar to what was conducted in Chapter 4, would reveal the influence of these additional parameters. The inclusion of these factors adds depth to the analysis, ensuring that while f_c remains the primary variable, other significant parameters are also considered. This approach provides a more comprehensive, yet focused, method to understand and represent the system. The resulting explicit equations thus offer a balanced account of the complexity of the system, highlighting the predominant influence of f_c while acknowledging the roles of other critical parameters.

Two different approaches to the selection of critical points are developed

comparatively. In the first one, using the damage definition (d_{mic}, see Eq. 2.40) proposed by Zreid and Kaliske [111] for the material model, limit points with equal intervals between 0 (undamaged material) and 1 (0.99: damaged material) were selected. Although it does not have a direct physical meaning, d_{mic} is important in terms of representing the numerical equivalent of the damage state of concrete. Figure 5.25 shows the strain-stress pairs as scatter plots on the simulation bundle. In this approach, the values of $d_{mic} = 0.05, 0.25, 0.50, 0.75, 0.95$ are named as Limit A, Limit B, Limit C, Limit D and Limit E, respectively.

Regardless of the shear stress level received by the concrete material, it is observed that the limit described as Limit A is exceeded in a very narrow range, even at small loading steps. The points where the whole population reached Limit A had a mean value of $9.0029e-04$ and a standard deviation of $4.1462e-04$. Similarly, the Limit B value determined as $d_{mic} = 0.25$ was also realised in small loading steps and in a narrow band similar to Limit A. The mean of the points where the whole population reaches Limit B is 0.0015 and the standard deviation is $5.4522e-04$, similar to Limit A. The mean of the points where the whole population reaches Limit B is 0.0015 and the standard deviation is $5.4522e-04$, similar to Limit A. After reaching Limit B, it can be seen that the plateau to be covered On the strain axis, the mean values for Limit C, Limit D and Limit E are 0.0028, 0.0061, 0.0122 and the standard deviations are 0.0012, 0.0061, 0.0066. In stress terms, mean shear stress for the entire population values are 10.2018, 10.9540, 9.5885, 5.5338 and 3.1589 MPa for Limit A, B, C, D and E respectively. Standard deviations for the same limit points are 6.0278, 4.9655, 3.6581, 2.0355 and 1.2885. It was observed that the standard deviations of the stress values decreased with the stress value at which the limit exceedance occurred, but the standard deviations of the strain values increased as the strain value increased.

In the Figure 5.26, the relationship between the deformation values of the sub-populations separated according to aspect ratio h_c/h_b and joint reinforcement ratio ρ_j values and the concrete compressive strength f_c is expressed in terms of coefficient of correlation. Accordingly, regardless of the h_c/h_b values, it is seen that the simulated specimens reinforced with relatively lower reinforcement ratio are more sensitive to the concrete compressive strength. In the subdomain low level reinforcement is included in the joint region ($\rho < 0.0059$), the mean correlation coefficient calculated between f_c and shear strains for defined limit states is remarked very strong ($R^2_{mean} = 0.63$) It is considered that the correlation among the concrete strength f_c and the shear strain output for the high level reinforcement subdomain ($\rho > 0.0059$) is not equally powerful as it is seen in the low level reinforcement subdomain; but still accepted as a sufficient correlation ($R^2_{mean} = 0.41$) for including samples from all subdomains. Correlation between f_c and shear strength values did

not given since no significant difference with respect to the defined subdomains are observed.

The variables $\gamma_A(f_c)$, $\gamma_B(f_c)$, $\gamma_C(f_c)$, $\gamma_D(f_c)$, and $\gamma_E(f_c)$ indicate the shear strain as a function of concrete strength while indices denote the corresponding limits defined in this subsection. Table 5.3 shows fitted equations, proposed coefficients for 90% prediction bounds and correlation coefficients as goodness of fit measure for each equation fitted. For strain functions denote limit states A, B, C and E are represented with cubic polynomials while an exponential equation is fitted to the limit state D. Similarly, the variables $\tau_A(f_c)$, $\tau_B(f_c)$, $\tau_C(f_c)$, $\tau_D(f_c)$, and $\tau_E(f_c)$ are power-law curve fits, representing the relationship between concrete strength f_c and the expected shear stress values at limit states A, B, C, D and E, respectively. It is worth noting that all curves proposed for shear stress are power-law equations that predicts 0.5 for exponent coefficient of base variable f_c. The correspondence with numerous academic investigations and established design codes that suggests a potent correlation between the square root of concrete strength and ultimate shear strength is significant. Curve fitting results indicate that the that strong connection is valid for the other stress states corresponds to defined criteria. Stress values did not show a significant correlation difference within the decomposed population as was the case for strain values. Although the sensitivity of the different limit states to the compressive strength of concrete shows small differences, there is no dependence in terms of other parameters. The curve fitting study for shear stresses is given in Table 5.4.

Fitted curves are shown with scattered data and 90% prediction bounds are given in Figure 5.27 and Figure 5.28. As it was remarked in the results presented in Table 5.3 and Table 5.4, stress curves significantly better correlation with the scattered data compared to the strain curves.

As can be seen in the Tables 5.3 and 5.4 and Figures 5.27 and 5.28, the data based on the proposed curves show a large amount of dispersion. Therefore, the proposed curves for different strain or stress states, although statistically well representing the data they represent, may take inconsistent values with each other. In other words, accurate prediction of the shear strain stress curve requires sequential representation of limit states A, B, C, D and E (or at least one limit state to be chosen from B, C and D). This may not be straightforward for curves fitted separately for the data. In this study, each fitted curve is checked for the displacement equivalents of the different limit states to ensure that they do not cross each other in such a way as to create inconsistencies. With Figure 5.29, the strain prediction curves corresponding to each limit state are plotted on the same figure to show that the described logical order is not broken.

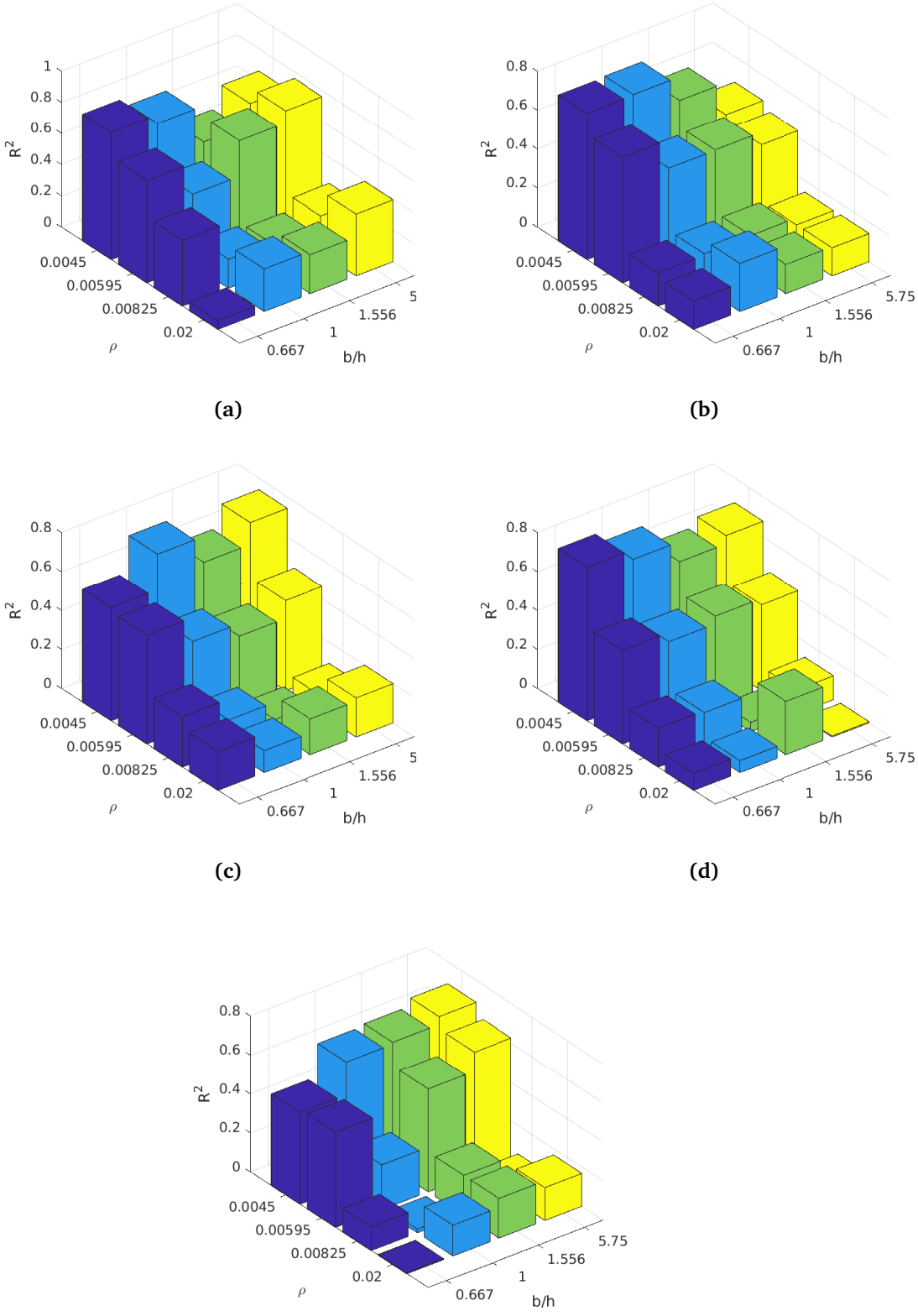

Figure 5.26 Coefficient of correlation between concrete compression strength f_c of the shear strains belong to different levels of average ρ and aspect ratio h_c/h_b

Considering that the determination coefficients representing goodness of fit of the fitted curves are not strong particularly for shear strain values corresponding to the intermediate steps of damage index based criteria; a surface fitting application based on cubic polynomials accepting other influential parameters, joint reinforcement ratio ρ_j and aspect ratio h_c/h_b as well as the concrete strength f_c. The surface fitting results are presented in Figure B.5 and Figure B.6, dependent on f_c and ρ_j, and f_c and h_c/h_b, respectively. Determination coefficients are calculated as $R^2 = 0.7501, 0.6961, 0.8106, 0.6828, 0.6150$ for the surface fitted between strains dependent on f_c and ρ_j while $R^2 = 0.7143, 0.8276, 0.6721, 0.7824, 0.6349$ for the surface fitted to strains dependent on f_c and h_c/h_b.

A similar surface fitting application is employed for the shear stress values corresponding to the damage index limit states. The resulting surfaces along with the scattered data are presented in Figure B.3 and Figure B.4 for the stress surfaces as three-degrees polynomials as functions of f_c and ρ_j and f_c and h_c/h_b. Their goodness of fit is demonstrated by determination coefficients $R^2 = 0.7291, 0.8632, 0.7924, 0.8197, 0.8803$ for the shear stress surfaces as functions of f_c and ρ_j while $R^2 = 0.7512, 0.9225, 0.8367, 0.7331, 0.9078$ for the shear stress surfaces as functions of f_c and h_c/h_b.

As a conclusion, specimens with lower reinforcement ratios demonstrated greater sensitivity to concrete compressive strength. This was evident from a stronger correlation between f_c and shear strain outputs for the subdomain with lower level reinforcement. Curve fitting studies involving shear strain and shear stress further revealed that while stress curves had a better correlation with scattered data compared to strain curves, data based on these curves displayed significant dispersion. This suggests that an accurate prediction of the shear strain-stress curve requires a sequential representation of all the limit states.

Surface fitting applications using cubic polynomials, which incorporated parameters such as joint reinforcement ratio, aspect ratio, and concrete strength, were conducted to address weaknesses in goodness of fit, particularly for shear strain values. Both stress and strain surfaces demonstrated a generally high determination coefficient, indicating good agreement with the data. As a whole, these findings underline the fact that of considering multiple factors and using complex methodologies can approximate better predictions but for the sake of simplicity and practicality, both shear strain and stress values corresponds to the predefined limit states can be predicted with acceptable accuracy using f_c as the governing variable.

Table 5.3 Descriptions of the fitted curves for simulation shear strain output based on damage index approach

Variable	Equation	Coefficient	Value	Lower Bound	Upper Bound	R^2
$\gamma_A(f_c)$	$p1 \cdot f_c^3 + p2 \cdot f_c^2 + p3 \cdot f_c + p4$	$p1$	-3.734×10^{-8}	-5.375×10^{-8}	-2.092×10^{-8}	0.5451
		$p2$	6.229×10^{-6}	3.68×10^{-6}	8.778×10^{-6}	
		$p3$	-0.0003308	-0.0004502	-0.0002113	
		$p4$	0.01131	0.009718	0.01289	
$\gamma_B(f_c)$	$p1 \cdot f_c^3 + p2 \cdot f_c^2 + p3 \cdot f_c + p4$	$p1$	-7.679×10^{-8}	-1.096×10^{-7}	-4.399×10^{-8}	0.5912
		$p2$	1.289×10^{-5}	7.793×10^{-6}	1.798×10^{-5}	
		$p3$	-0.0006843	-0.0009229	-0.0004456	
		$p4$	0.02287	0.0197	0.02604	
$\gamma_C(f_c)$	$p1 \cdot f_c^3 + p2 \cdot f_c^2 + p3 \cdot f_c + p4$	$p1$	-1.109×10^{-7}	-1.596×10^{-7}	-6.214×10^{-8}	0.4913
		$p2$	1.846×10^{-5}	1.089×10^{-5}	2.603×10^{-5}	
		$p3$	-0.0009835	-0.001338	-0.0006289	
		$p4$	0.03392	0.0292	0.03863	
$\gamma_D(f_c)$	$a \cdot \exp(b \cdot f_c) + c \cdot \exp(d \cdot f_c)$	a	1.083	-1.067	3.233	0.5561
		b	-0.3103	-0.4439	-0.1767	
		c	0.02556	0.02348	0.02765	
		d	-0.001936	-0.003267	-0.0006046	
$\gamma_E(f_c)$	$p1 \cdot f_c^3 + p2 \cdot f_c^2 + p3 \cdot f_c + p4$	$p1$	-1.898×10^{-7}	-2.709×10^{-7}	-1.088×10^{-7}	0.5136
		$p2$	3.183×10^{-5}	1.925×10^{-5}	4.441×10^{-5}	
		$p3$	-0.001701	-0.002291	-0.001112	
		$p4$	0.05736	0.04952	0.0652	

Table 5.4 Descriptions of the fitted curves for simulation shear stress output based on damage index approach

Variable	Equation	Coefficient	Value	Lower Bound	Upper Bound	R^2
$\tau_A(f_c)$	$a \cdot f_c^b + c$	a	13.78	-35.68	63.23	0.6711
		b	0.1522	-0.198	0.5024	
		c	-17.15	-72.44	38.14	
$\tau_B(f_c)$	$a \cdot f_c^b + c$	a	1.27	-0.684	3.224	0.7196
		b	0.5448	0.2697	0.82	
		c	-1.382	-6.13	3.367	
$\tau_C(f_c)$	$a \cdot f_c^b + c$	a	1.502	-0.8945	3.899	0.7233
		b	0.5157	0.2353	0.7961	
		c	-1.616	-7.045	3.813	
$\tau_D(f_c)$	$a \cdot f_c^b + c$	a	1.52	-0.6408	3.681	0.7425
		b	0.5275	0.2759	0.7792	
		c	-1.941	-6.976	3.095	
$\tau_E(f_c)$	$a \cdot f_c^b + c$	a	2.11	-1.007	5.228	0.6925
		b	0.4763	0.2234	0.7292	
		c	-3.166	-9.602	3.27	

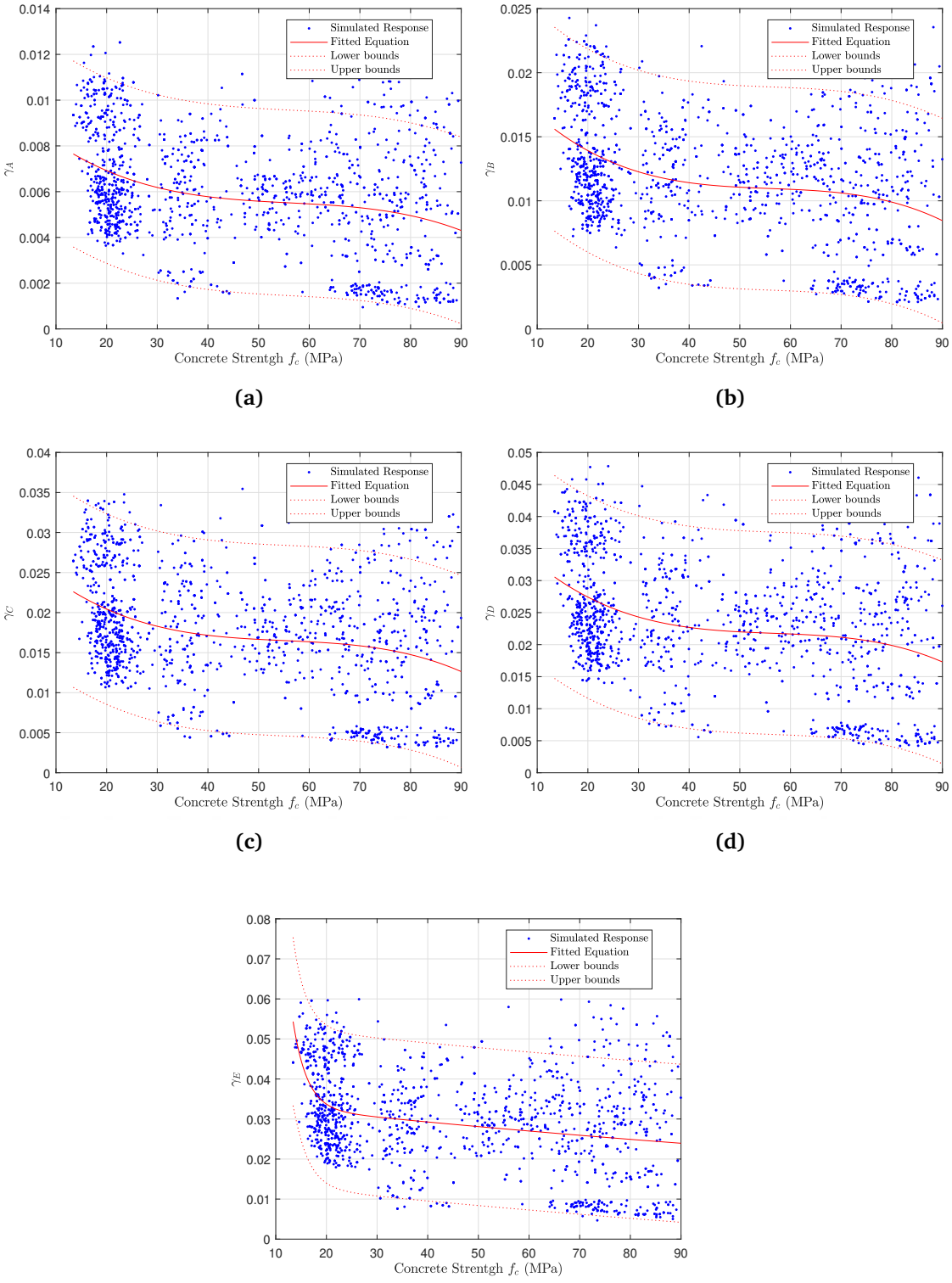

Figure 5.27 Scatter and fitted equations for shear strain values, γ_{xy}(y) and concrete strength values, f_c (x) for (a) Limit A, (b) Limit B, (c) Limit C, (d) Limit D and (e) Limit E

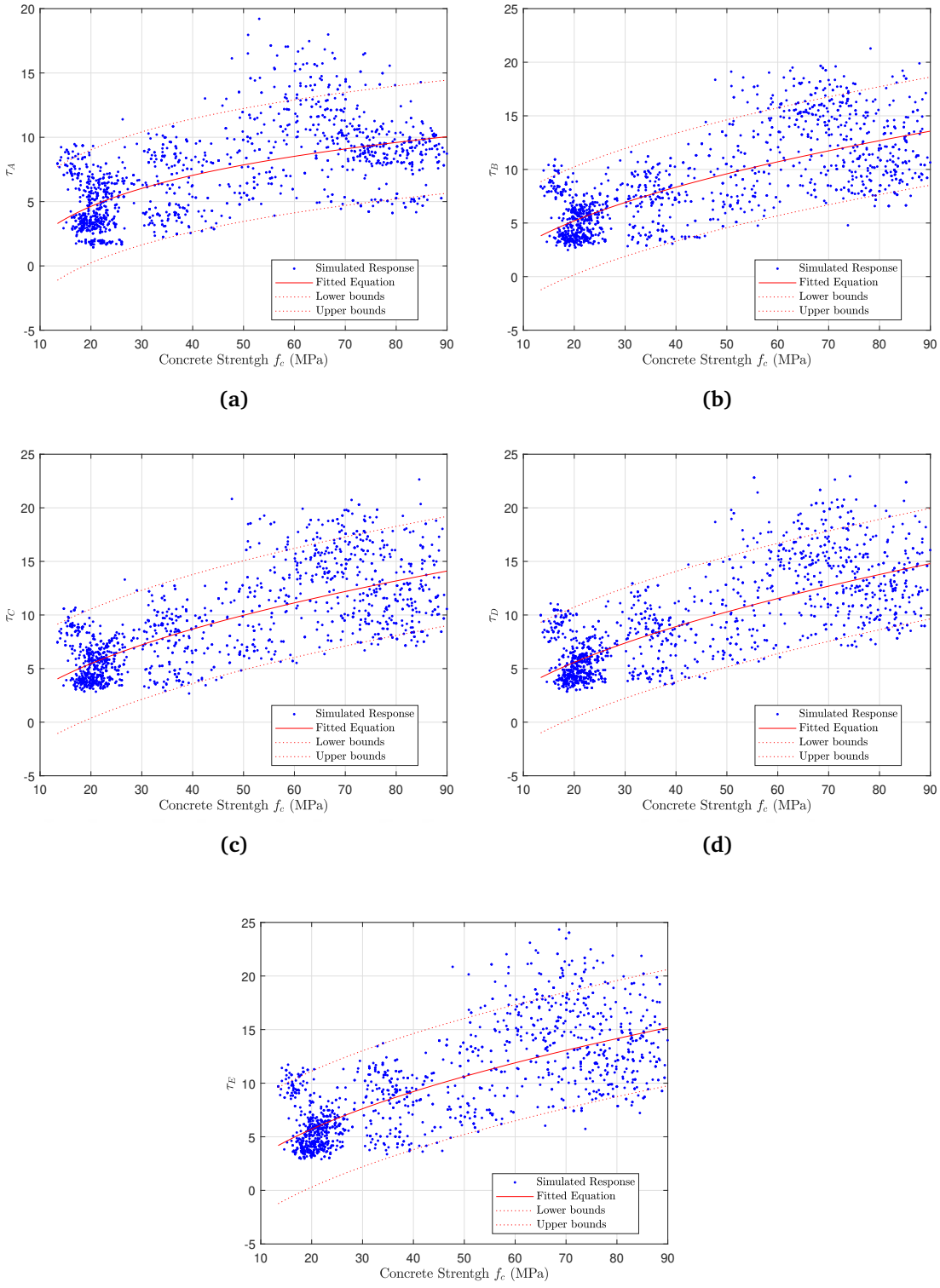

(a) **(b)**

(c) **(d)**

(e)

Figure 5.28 Scatter and fitted equations for shear strain values, τ_{xy}(y) and concrete strength values, f_c (x) for (a) Limit A, (b) Limit B, (c) Limit C, (d) Limit D and (e) Limit E

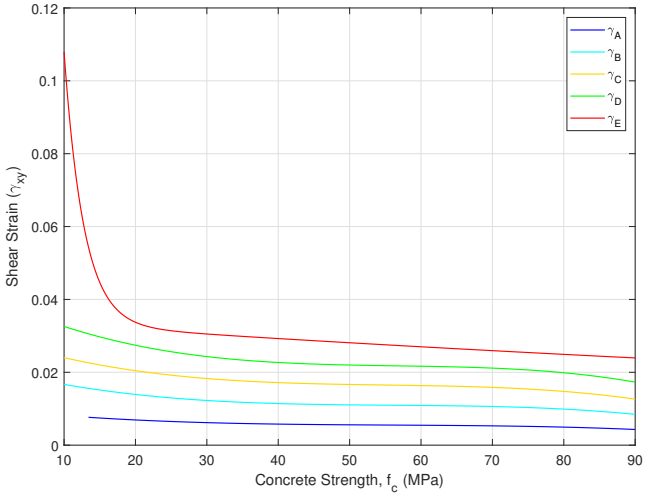

Figure 5.29 Strain prediction curves proposed for Limit A, Limit B, Limit C, Limit D and Limit E

5.5.1.2 Material Strength Based Approach

Within the scope of this study, in addition to the approach based on the concrete damage index, another approach based on the critical points of the material was developed. In figure, scatter of the strain stress pairs corresponding to the states that several limit states exceeded. These limit states are described as;

1. Limit I: Cracking of concrete, when the first principal stress exceeds the tensile strength.
2. Limit II: Rebar Yielding, first plastic strains developed in rebars in any direction.
3. Limit III: Crushing of concrete, second principal stress exceeds the compressive strength.
4. Limit IV: Maximum shear stress, state that maximum shear stress is observed over history
5. Limit V: Ultimate concrete stress, state that 50% of compressive strength achieved after softening plateau

In the Figure 5.30, the shear strain shear stress pairs are scattered where the described limit states are realized. The mean of the strain points where the whole population reaches Limit A is 0.0012 with a standard deviation of 7e-04. The mean of the strain points where the whole population reaches Limit B is 0.0060 with a standard deviation of 0.0109. The mean strain values for Limit C, Limit D, and Limit E are 0.0019, 0.0017, and 0.008 with standard deviations of 0.0015, 0.0012, and 0.0093,

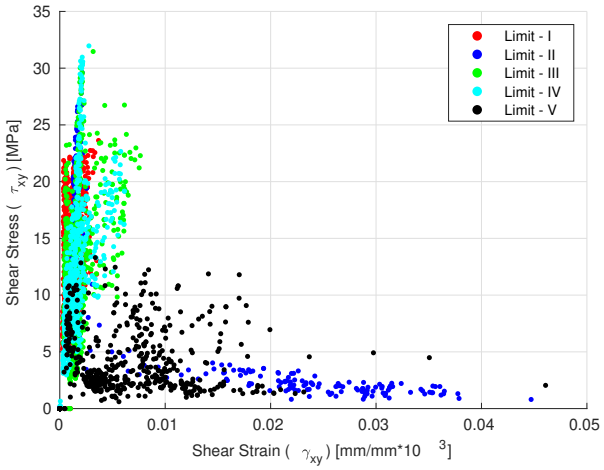

Figure 5.30 Shear strain and shear stress pairs scattered where the described limit states are occurred

respectively. In terms of shear stress in joint, the mean values for the entire population are $13.6843MPa$, $4.3329MPa$, $13.2673MPa$, $12.3657MPa$, and $3.9978MPa$ for Limit A, B, C, D, and E, respectively. The standard deviations for these limit points are 5.0510, 7.3714, 6.5619, 6.1159, and 3.1413, respectively.

When the 5.30 is analyzed in terms of shear stress, it is seen that the Limit I case is spread in a wide band between $5MPa$ and $15MPa$. This trend does not change for Limit III and Limit IV. However, Limit V is found to take values in a narrower stress band. Among these limit states, the propagation of Limit B is unique among the others, as is its definition. While the other limit cases are defined in terms of concrete material, Limit II is defined in terms of steel reinforcement yielding. Limit II, unlike the other limit states, is spread over the entire stress band. In strain terms, strain values that Limit I, Limit III and Limit IV are reached, are located in a narrow strain band, while Limit IV and Limit V are spread over a wider strain field.

The relationship between the limit states (I-V) based on stress and the damage index d_{mic} was investigated. A scatter plot of shear stress damage index pairs, shown in Figure 5.31.(b), was used to illustrate this relationship. Interestingly, the analysis indicated that the correlations between shear stress and damage for Limits I, III, IV, and V were quite weak. This was evidenced by the correlation coefficients of 0.0024, 0.0026, 0.0164, and 0.1123, respectively, suggesting an absence of a strong, direct relationship between these two parameters. A similar trend was observed when examining the relationships in terms of strain, with correlation coefficients of 0.0023, 0.1657, 0.2561, and 0.3015 for Limits I, III, IV, and V, respectively, further affirming the lack of substantial correlation. However, a significant exception was observed in the case of Limit II, which pertains to the yielding of the joint reinforcement.

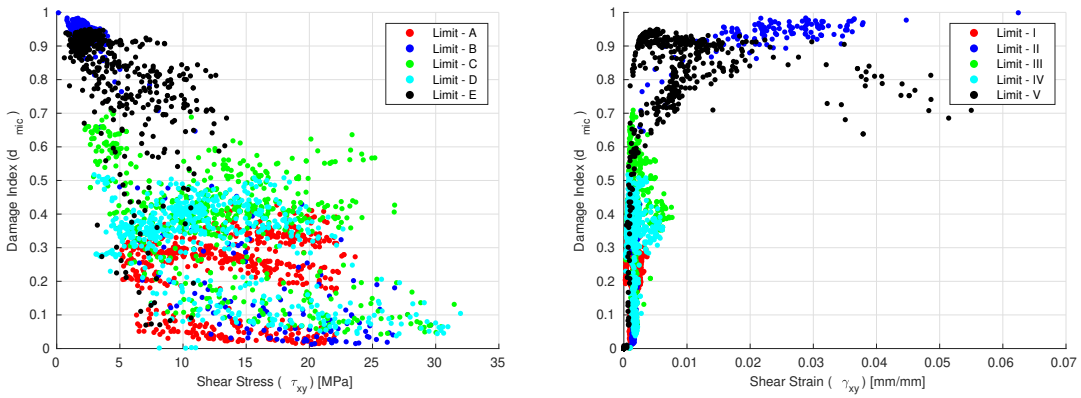

(a) **(b)**

Figure 5.31 Damage index with respect to shear stress (a) and damage index with respect to shear strain (b)

Here, a strong correlation was discovered between concrete strength f_c and both shear strain and shear stress, with a coefficient of determination (R^2) of 0.8515 for shear strain and 0.9154 for shear stress. Such a robust correlation suggested a potent linear relationship. This finding reveals that a strong direct relationship exists between the yielding of the reinforcement bars and the damage definition based on the concrete material. This finding may have practical implications, suggesting that valuable insights into the overall health and status of the concrete material could be provided by careful observation and monitoring of the strain and stress in the joint reinforcement. Consequently, this understanding may be instrumental in predictive maintenance and failure prevention in concrete structures.

The correlation between the deformation values of sub-domains, predicated on their h_c/h_b and ρ_j values, and the compressive strength of concrete is depicted in Figure 5.32. An interesting revelation made through this analysis is that the specimens with moderate aspect ratios (b_c/b_h) demonstrate a higher sensitivity to the compressive strength of concrete. This observation is valid irrespective of the variations in the average reinforcement ρ_j values, thereby establishing a consistent pattern. Furthermore, a distinctive segment within the population, characterized by aspect ratios ranging between 0.667 and 1.556, was identified. This sub-group displayed unique characteristics in relation to the concrete compressive strength, setting them apart from the rest of the population. With a similar reason explained in previous subsection, no significant difference between various subdomains is observed in terms of correlation coefficients, relation between concrete strength f_c and shear strength is not included.

However, it is worth noting that a residual segment of the population exists that falls outside this distinctive group. When a correlation analysis was performed on the shear

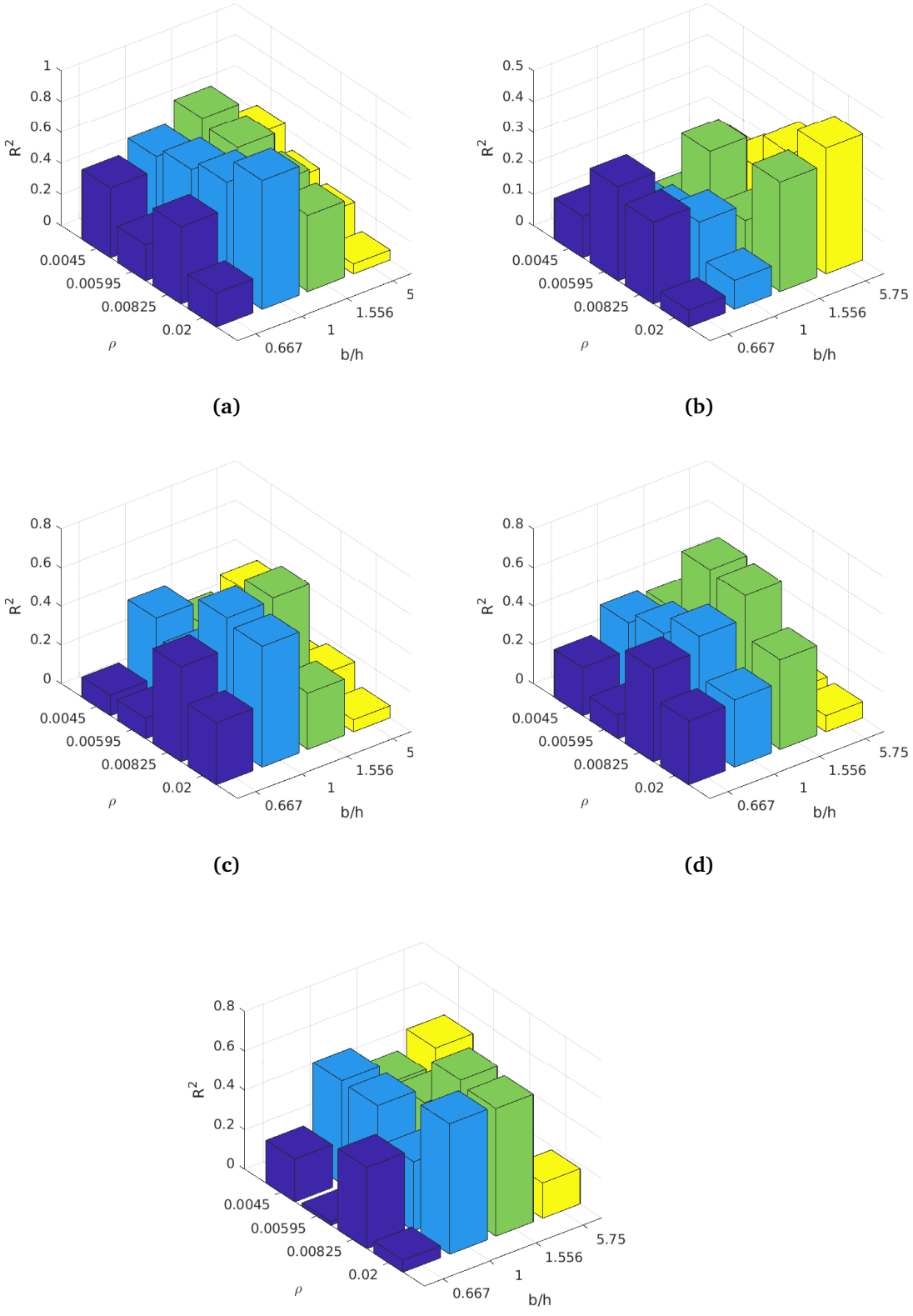

Figure 5.32 Coefficient of correlation between concrete compression strength f_c of the shear strains belong to different levels of average ρ and aspect ratio h_c/h_b

strain and stress responses from the simulation samples of this remaining segment, an R^2 value of 0.4191 and 0.6116 were obtained. This is considerably lower than the R^2 value of 0.6321 noted for the sub-domain with aspect ratios between 0.7364 and 1.556. This discrepancy suggests a more robust relationship between the aspect ratios and compressive strength in the distinguished sub-domain, as compared to the remaining population.

Table 5.5 illustrates the proposed strain prediction equations for the limit states I to V (γ_I to γ_V) as a function of the concrete compressive strength f_c. Different functional forms have been used for each limit state, reflecting the unique strain behaviors observed. For $\gamma_I(f_c)$, a cubic polynomial form has been employed. The coefficient values for $p1$, $p2$, $p3$, and $p4$ suggest that the response is highly sensitive to variations in f_c, with the coefficients covering a wide range of magnitudes. The strain prediction for $\gamma_{II}(f_c)$, meanwhile, is modeled by a sum of two exponential terms. The wide range of the coefficients of a, b, c, and d indicate complex exponential behavior, which may be indicative of the nonlinear behavior typically observed in steel reinforcement yielding. The function form used for $\gamma_{III}(f_c)$ is a power function. The parameter b takes a wide range of values between 0.4919 and 12.8, suggesting that f_c is raised to a higher power, indicating a potentially high sensitivity to f_c. For $\gamma_{IV}(f_c)$ and $\gamma_V(f_c)$, a cubic polynomial form is again used. The coefficients exhibit significant variability, which, akin to $\gamma_I(f_c)$, suggests a complex response to variations in f_c.

Table 5.6 presents the proposed stress prediction curves for the limit states I to V (τ_I to τ_V), as a function of the concrete compressive strength f_c. For all limit states, a power function has been employed, indicative of the nonlinear stress responses observed. For $\tau_I(f_c)$, the coefficients a, b, and c have values spanning from negative to positive, hinting at a complex relationship between stress and compressive strength. The coefficient of b lies in the range 0.9252 to 1.543, implying that f_c is predominantly raised to the first power, while the wide range for c may suggest a constant stress offset. The $\tau_{II}(f_c)$ curve, similar to $\tau_I(f_c)$, is modeled using a power function. The a and c coefficients exhibit a wider range, signifying potential variation in the underlying data. For $\tau_{III}(f_c)$, the coefficient b falls between 0.3001 and 0.7863, suggesting a less steep response curve to f_c changes. The coefficient c varies widely, with a negative lower bound, indicative of a possible shift in the stress response. The model for $\tau_{IV}(f_c)$ shows a smaller value for b between 0.06381 and 0.6109, indicating a potential lower degree of sensitivity to changes in f_c. The coefficient c varies from negative to positive, possibly indicating a shifted baseline for the stress values. Finally, the $\tau_V(f_c)$ model shares similar characteristics with $\tau_{III}(f_c)$ and $\tau_{IV}(f_c)$, with the b coefficient value ranging from 0.2327 to 0.7993 and the c coefficient ranging from negative to positive.

Fitted curves are shown with scattered data and 90% prediction bounds are given in Figure 5.34 and Figure 5.35. As it was remarked in the results presented in Table 5.5 and Table 5.6, stress curves significantly better correlation with the scattered data compared to the strain curves.

Table 5.5 Strain prediction curves proposed for Limit I, Limit II, Limit III, Limit IV and Limit V

Variable	Equation	Coefficient	Value	Lower Bound	Upper Bound	R^2
$\gamma_I)(f_c)$	$p1 \cdot f_c^3 + p2 \cdot f_c^2 + p3 \cdot f_c + p4$	$p1$	8.061×10^{-8}	6.733×10^{-8}	9.389×10^{-8}	0.6154
		$p2$	-9.033×10^{-6}	-1.11×10^{-5}	-6.971×10^{-6}	
		$p3$	0.0002745	0.0001779	0.0003711	
		$p4$	0.001618	0.0003333	0.002903	
$\gamma_{II}(f_c)$	$a \cdot e^{b \cdot f_c} + c \cdot e^{d \cdot f_c}$	a	-4.191×10^{-6}	-4.108×10^{-5}	3.27×10^{-5}	0.4685
		b	0.08135	−0.01272	0.1754	
		c	0.01464	0.01344	0.01585	
		d	0.001705	−0.001702	0.005111	
$\gamma_{III}(f_c)$	$a \cdot f_c^b + c$	a	-3.028×10^{-16}	-8.576×10^{-15}	7.971×10^{-15}	0.5631
		b	6.647	0.4919	12.8	
		c	0.01411	0.01373	0.01448	
$\gamma_{IV}(f_c)$	$p1 \cdot f_c^3 + p2 \cdot f_c^2 + p3 \cdot f_c + p4$	$p1$	-9.742×10^{-8}	-1.392×10^{-7}	-5.568×10^{-8}	0.6354
		$p2$	1.61×10^{-5}	9.621×10^{-6}	2.259×10^{-5}	
		$p3$	−0.000846	−0.00115	−0.0005423	
		$p4$	0.02845	0.02441	0.03249	
$\gamma_V(f_c)$	$p1 \cdot f_c^3 + p2 \cdot f_c^2 + p3 \cdot f_c + p4$	$p1$	-2.147×10^{-7}	-2.975×10^{-7}	-1.319×10^{-7}	0.5874
		$p2$	3.555×10^{-5}	2.269×10^{-5}	4.84×10^{-5}	
		$p3$	−0.001862	−0.002464	−0.00126	
		$p4$	0.05951	0.0515	0.06751	

Table 5.6 Stress prediction curves proposed for Limit I, Limit II, Limit III, Limit IV and Limit V

Variable	Equation	Coefficient	Value	Lower Bound	Upper Bound	R^2
$\tau_I(f_c)$	$a \cdot f_c^b + c$	a	0.03635	−0.0163	0.08901	0.7151
		b	1.234	0.9252	1.543	
		c	3.463	2.562	4.365	
$\tau_{II}(f_c)$	$a \cdot f_c^b + c$	a	0.1634	−0.1122	0.4391	0.6841
		b	0.9175	0.5742	1.261	
		c	2.795	0.9768	4.613	
$\tau_{III}(f_c)$	$a \cdot f_c^b + c$	a	1.485	−0.5351	3.504	0.6512
		b	0.5432	0.3001	0.7863	
		c	−2.002	−6.89	2.886	
$\tau_{IV}(f_c)$	$a \cdot f_c^b + c$	a	5.405	−4.472	15.28	0.7321
		b	0.3374	0.06381	0.6109	
		c	−8.7	−23.78	6.383	
$\tau_V(f_c)$	$a \cdot f_c^b + c$	a	1.459	−0.8922	3.811	0.6663
		b	0.516	0.2327	0.7993	
		c	−1.978	−7.308	3.351	

The coefficients and their corresponding ranges reveal the complex, nonlinear response of the system, while the different functional forms reflect the unique behavior observed at each limit state. However, it should be noted that these models are subject to the usual assumptions and limitations of curve fitting, and the ranges provided give a measure of the uncertainty inherent in the fitting process.

As described in the previous subsection, the order of occurrence of limit states in a prediction based on independent data must remain within the limits of logic. However, since no gradual change of a variable is taken into account here, as in the definition of the damage index, it is logically possible for all intermediate steps between Limit I and Limit V to transition to each other. Therefore, in this part of the method, it is

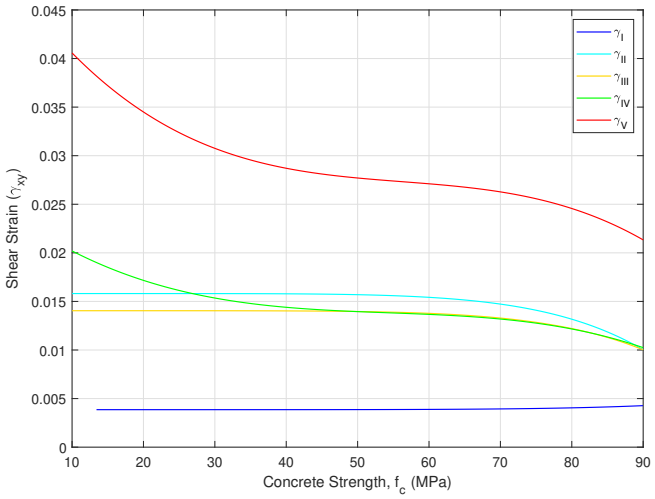

Figure 5.33 Strain prediction curves proposed for Limit I, Limit II, Limit III, Limit IV and Limit V

advisable to use the strain and stress values of limit states B, C or D in the intermediate steps. This can be seen by comparing the strain values corresponding to the boundary states for different values of f_c in the Figure 5.33.

5.6 Conclusion

In this chapter, the shear strain - stress envelope of reinforced concrete joints was investigated through the utilization of advanced finite element method simulations. The lack of unified experimental configurations in literature made it necessary to seek alternatives for the statistical implementation of strain stress prediction models.

The need for a solution led to the exploration of artificial intelligence techniques as a means to provide a connection between the physical characteristics of the RC joint sub-assemblages and the resulting shear strain-stress outcomes. Although these techniques often provide black-box solutions that can be effective in many modelling applications, they usually offer limited insight into the characteristics of the problem being defined. The approach in this study involved introducing a specialized type of artificial neural network structure in regression applications while also exploring basic statistical methods to establish a direct relationship between the aforementioned quantities. The lack of abundant data samples in literature necessitated the use of advanced finite element methods to create an accurate statistical model. The application of finite element modelling techniques which includes particularly sophisticated solutions for high-level nonlinear behavior of concrete material helped overcome the issues encountered due to the diversity of configurations, measurement techniques, design code alterations, and insufficient

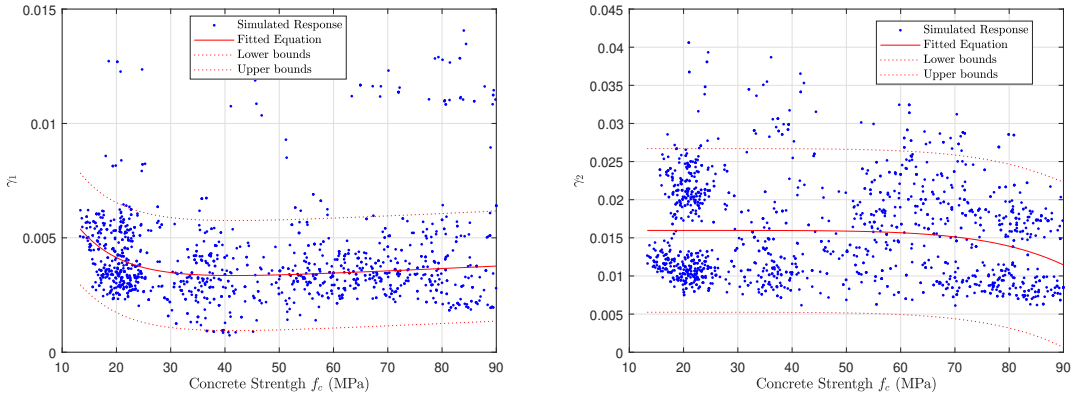

(a)

(b)

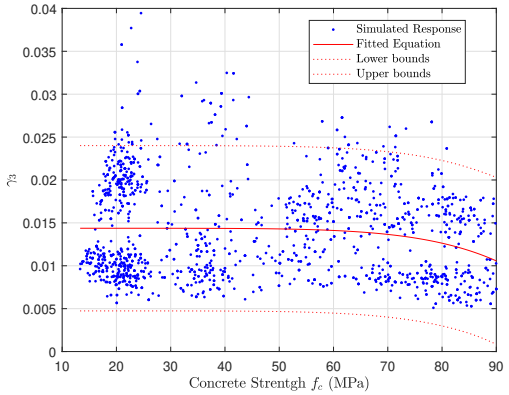

(c)

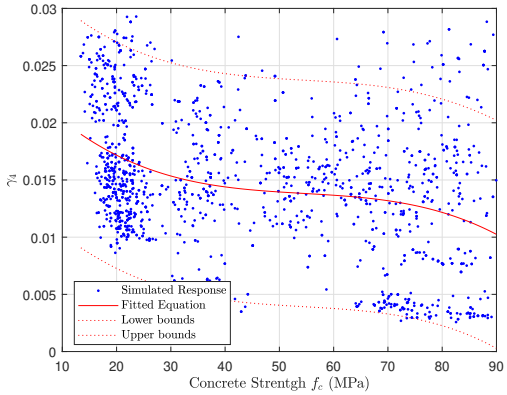

(d)

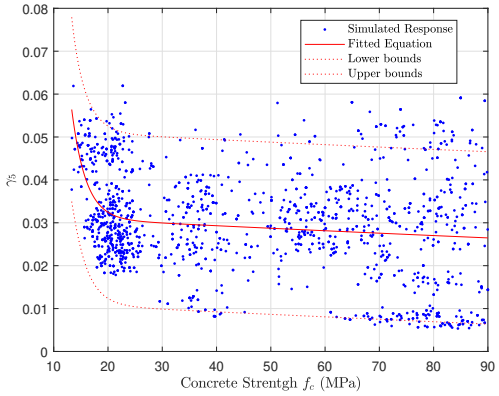

(e)

Figure 5.34 Scatter and fitted equations for shear strain values, γ_{xy}(y) and concrete strength values, f_c (x) for (a) Limit I, (b) Limit II, (c) Limit III, (d) Limit IV and (e) Limit V

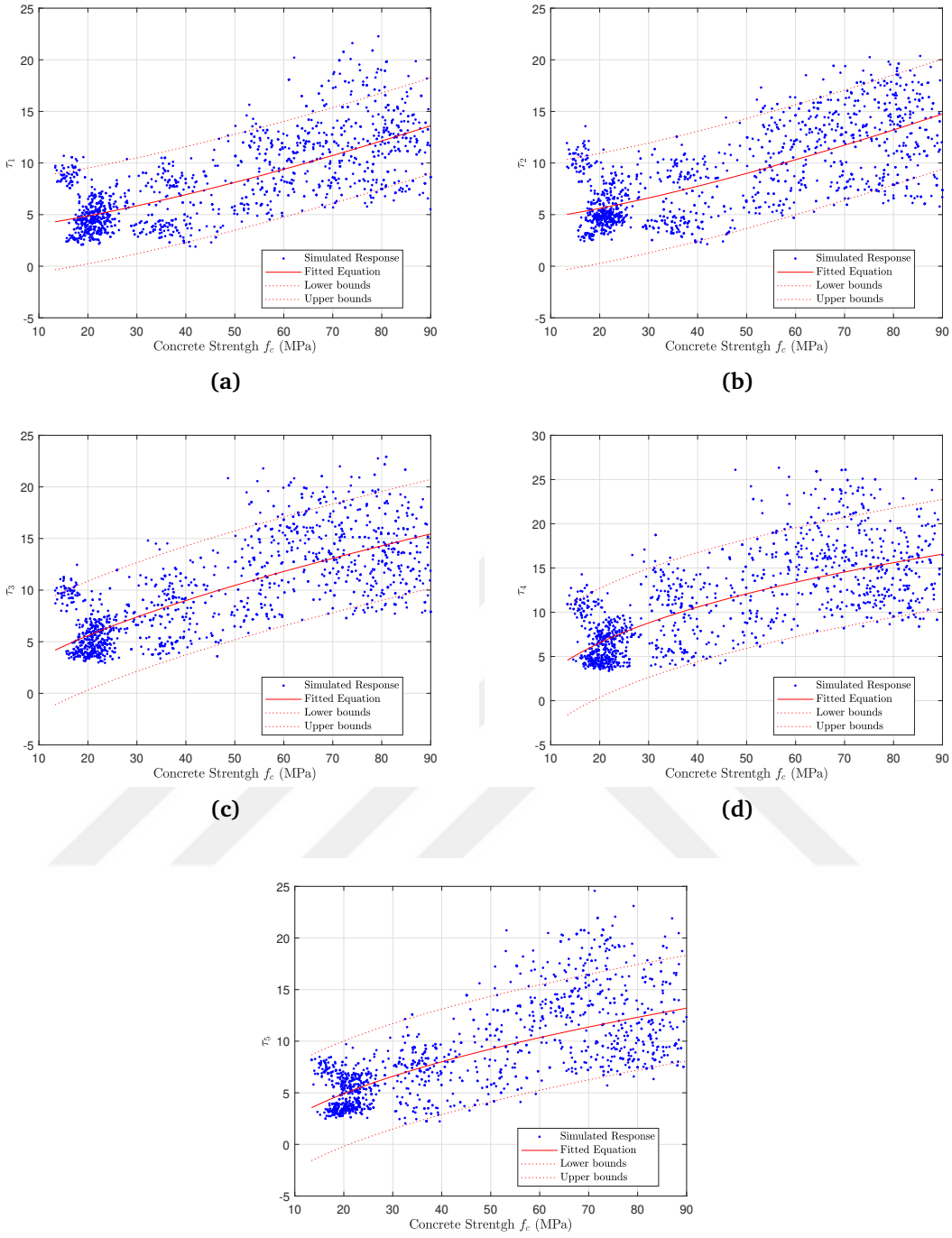

Figure 5.35 Scatter and fitted equations for shear strain values, τ_{xy}(y) and concrete strength values, f_c (x) for (a) Limit I, (b) Limit II, (c) Limit III, (d) Limit IV and (e) Limit V

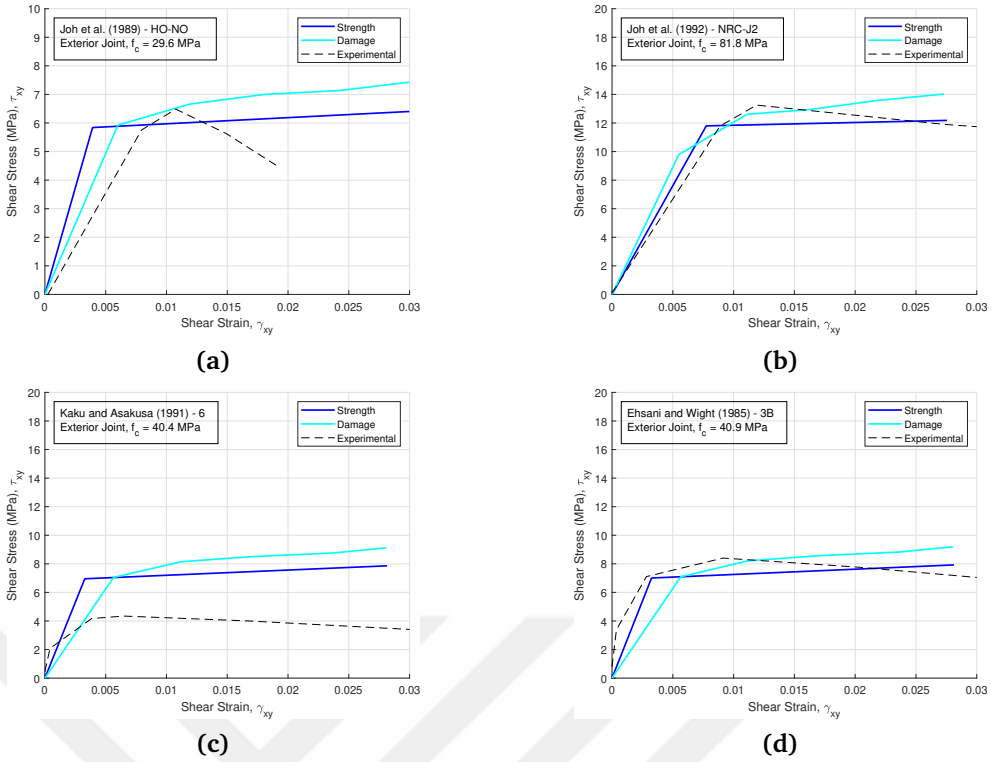

Figure 5.36 Comparison of experimental measurements with the predicted joint shear strain - shear stress response for interior joints with (a) $f_c = 29.6$ MPa (b) $f_c = 81.8$ MPa (c) $f_c = 40.4$ MPa (d) $f_c = 40.9$ MPa

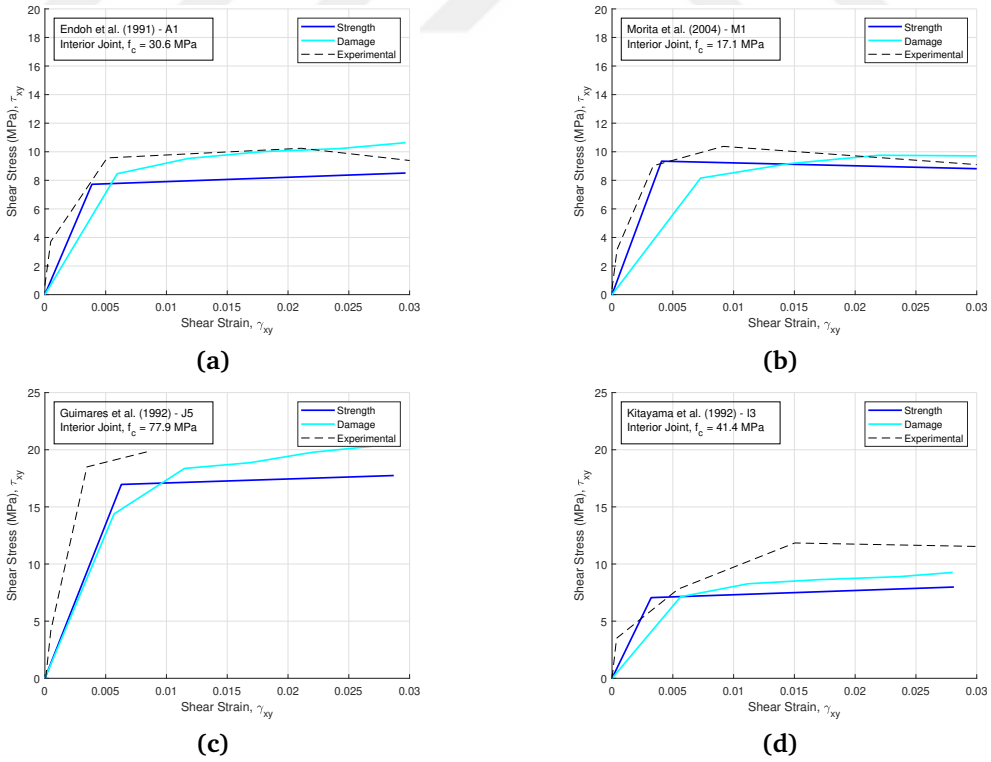

Figure 5.37 Comparison of experimental measurements with the predicted joint shear strain - shear stress response for interior joints with (a) $f_c = 30.6$ MPa (b) $f_c = 17.1$ MPa (c) $f_c = 77.9$ MPa (d) $f_c = 41.4$ MPa

information about test setups in the existing literature. A calibration procedure for the MPDP material model [111] was proposed, based solely on concrete strength, f_c, following the methodology introduced by Steinke *et al.* [247]. It was concluded that, with the use of equations provided by Steinke *et al.* [247] and this chapter, a test specimen expected to have joint panel damage or coupled joint panel beam flexure damage can be accurately simulated.

The generation of 1500 simulation samples under predefined assumptions was executed, with the results being classified based on limit states defined by the concrete material damage index and the exceedance of concrete or reinforcement material strength. Regression techniques were applied to these outcomes, and it was concluded that the shear strain-stress envelope of any given joint sub-assembly with a known concrete strength can be predicted with acceptable accuracy. It was found that the inclusion of auxiliary terms such as ρ_j and h_c/h_b could further enhance this accuracy. However, for the sake of simplicity, the proposed equations were determined to be adequate for the prediction of the mentioned quantities.

In conclusion, it was shown that the proposed equations are capable of calibrating the MPDP material for use in joint specimens. Furthermore, the fitted equations from the simulation results can predict the general characteristics of the joint shear strain-stress envelope within acceptable limits.

Overall, a significant contribution has been made towards the practical applications of joint modeling, with the insights gained from this work aiding in the further understanding of the shear strain-stress behavior of RC joints. These findings present opportunities for further refinement of these models and an expansion of understanding in future studies.

Table 5.7 Mean and standard deviation for the damage index based approach and material strength approach (Gamma γ Variables)

	γ_A		γ_B		γ_C	
	Mean	Std Dev	Mean	Std Dev	Mean	Std Dev
Damage Index Based Approach	1.2510	0.4645	1.5010	0.5328	1.7747	0.6750
Material Strength Based Approach	1.2062	0.3806	1.3960	0.5904	1.4198	0.6787

Table 5.8 Mean and standard deviation for the damage index based approach and material strength approach (Tau τ Variables)

	τ_A		τ_B		τ_C	
	Mean	Std Dev	Mean	Std Dev	Mean	Std Dev
Damage Index Based Approach	1.4644	0.5637	1.4703	0.5282	0.8645	0.2602
Material Strength Based Approach	0.9031	0.4213	1.5359	0.5478	0.9625	0.3364

In Table 5.7 and Table 5.8, mean values and standard deviations for ratio between joint shear strain and stress predictions and experimental observations based on the criteria defined in Chapter 4. The present definition was based on the geometrical properties of the shear strain - shear stress curve, enabling the objective comparison between experimental and simulated quantities. Even though the definition of the curves based on the limit states give more comprehensive insight on the mechanics of the joint deformation, due to the lack of reported objective information about the experimental observations on the limit state exceedence.

In Table 5.7 presenting the joint shear predictions, the Damage Index Based Approach shows higher mean values for each of γ_A, γ_B, and γ_C compared to the Material Strength Based Approach. This indicates that, on average, the Damage Index Based Approach predicts higher gamma values, suggesting a more severe damage. However, the standard deviation values for the Damage Index Based Approach are also consistently higher, implying greater variability or spread in the predicted values. This could mean that while the Damage Index Based Approach generally predicts more severe damage, it also comes with a higher level of uncertainty in the predictions.

In Figure 5.36 - 5.37, comparison between experimental results and predicted joint shear strain-stress curves of the specimens experimentally tested by various researchers are given. Table 5.8 displays the mean and standard deviation values for the joint shear stress predictions. Here, a mixed picture is presented. For τ_A, the Material Strength Based Approach predicts a lower mean value with lower variability, suggesting that it predicts less severe damage with less uncertainty. However, for τ_B and τ_C, the Material Strength Based Approach predicts higher mean values, which suggests it predicts more severe damage for these variables. In the case of τ_B, the standard deviation is slightly higher for the Material Strength Based Approach, implying slightly more variability or spread in these predictions. For τ_C, however, the standard deviation is higher for the Material Strength Based Approach, suggesting a higher degree of uncertainty in these predictions.

In summary, while the Damage Index Based Approach generally predicts higher levels of damage (as reflected in the shear strain and stress variables), it also exhibits higher variability, suggesting greater uncertainty in these predictions. The Material Strength Based Approach, on the other hand, shows mixed results with lower predicted levels of damage for some variables, but higher predicted levels for others. It also exhibits a generally lower degree of variability, indicating less uncertainty in these predictions. These considerations should be taken into account when choosing between these two approaches for predicting damage in reinforced concrete joints.

6
CALIBRATION OF JOINT MODEL THROUGH GENETIC ALGORITHM

6.1 Overview

Building on the detailed discussions in Chapter 3, the goal is to construct a mathematical model that is expected to be capable of predicting the inelastic response of any reinforced concrete joint with known basic physical properties. The model's purpose extends to its application in practical design and evaluation tasks. Apart from incorporating the envelope parameters estimated in the previous sections, it is also necessary to estimate the deterioration parameters. These parameters are critical in controlling the responses to cyclic loads.

In this chapter, a calibration method for the deterioration parameters (referred to as *deteriorationParams*) is proposed based on the collection of artificial intelligence algorithms. The objective is to estimate the deterioration parameters that control the joint panel shear deformation envelope for each experiment. Two methods are employed for parameter estimation: the Finite Element Method using the MPDP material model, introduced in Chapter 5, and generalized regression neural networks trained using experimental results, as discussed in Chapter 4.

The process begins by estimating the model parameters for each experiment using the aforementioned methods. Next, a set of *deteriorationParams* is generated for each experiment using Latin Hypercube Sampling (LHS). These *deteriorationParams* populations serve as the initial generation. The joint sub-assemblage model, constructed using the reported features, is then simulated using the simulation framework introduced in Chapter 3.

The simulated responses of the joint sub-assemblage model representing each sample introduced in Table A.2 are compared to the experimentally observed responses. A different experimental database is used in this process, since the all the samples of database used in Chapter 5 and Chapter 4 did not apply cyclic loading procedure. The

fitness or error of each simulation is assessed using several criteria explained in Section 6.2. Error assignment involves adopting two different methods: in the first, the error is directly evaluated based on the simulation results while in the second method, a relatively larger initial population is created, and an error meta-model is generated using artificial neural networks.

Based on the criteria introduced in Section 6.2, multiple objectives are evaluated, and the simulation that leads to the least error is determined using a non-dominated sorting algorithm. In the generations following the initial population, simulations for the new population are performed through the direct method in the first error assessment method (Method I). In the second method (Method II), the error meta-model is evaluated in each run. The *deteriorationParams* set that provide the best solution for each experimental test are listed and statistically investigated to establish a relationship between the physical features of the joint sub-assemblage. Nonlinear regression results are presented to analyze the obtained data.

This chapter presents a comprehensive method for calibrating deterioration parameters using artificial intelligence algorithms. The approach combines parameter estimation techniques, simulation frameworks, and error assessment methods to find the optimal solution for each experimental test. The results obtained provide valuable insights into the relationship between the physical features of the joint sub-assemblage and the corresponding deterioration parameters.

6.2 Problem Definition

A sub-assemblage is a portion of a moment frame isolated at approximate zero moment sections. General configuration a simulation model representing a testing unit is presented in Figure 6.1. In both exterior and interior joint models, both translational degrees of freedoms are fixed at the bottom column end while vertical translation is free at top column to allow axial loading. The cyclic displacement load is applied to the free beam ends.

In the given experimental setup configuration, experimentally measurable parameters (concrete strength (f_c), longitudinal reinforcement in beams and columns (ρ_b,ρ_c), transverse reinforcement in beams, columns and joint region (ρ_{bt}, ρ_{ct}, ρ_{jt}), section width and height in beams and columns (b_b,h_b,b_c,h_c) and clear length of beams and columns (L_b,L_c) are typically reported for the available test results in the literature. Despite the uncertainty consisted in the measurement of these quantities, these parameters are considered deterministic.

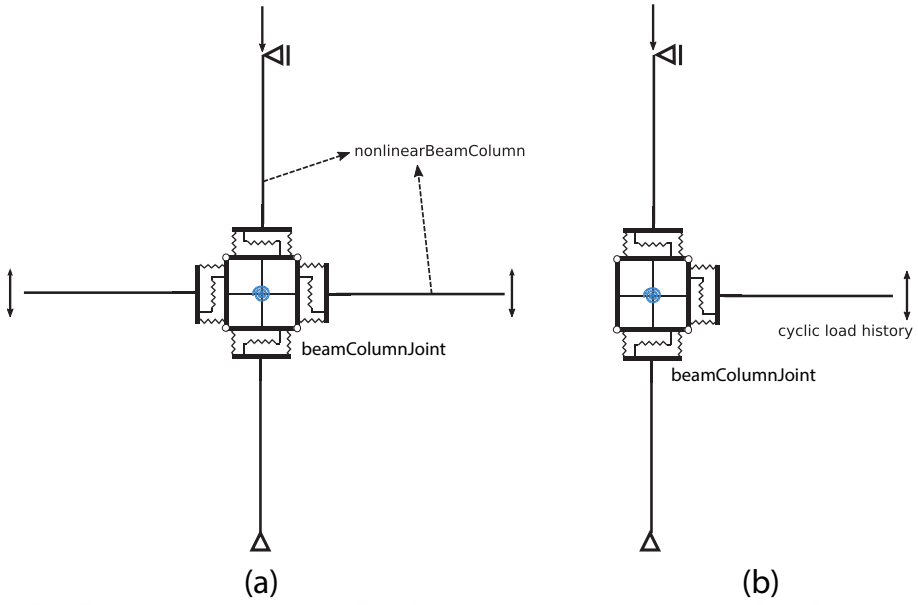

Figure 6.1 Idealization of the experimental setups for (a) interior and (b) exterior reinforced concrete frame joints

Concrete material properties are defined with uniaxial Kent-Scott-Park Model [33] which considers linear unloading/reloading stiffness and no tensile strength. Confined concrete properties are derived through the definition of unconfined concrete and provided reinforcement at any section according to Scott *et al.* [33] confinement model. In steel reinforcement, Menegotto and Pinto [219] steel model with isotropic strain hardening material model is used. Beside the basic characteristic parameters representing the bilinear load-deformation response curve of reinforcement steel material, a group of parameters are required to control the transition between elastic and plastic regions which has a strong impact in the hysteresis unloading and reloading behaviour. These parameters denoted by $R0$, $CR1$, $CR2$ and $a1-a4$ are considered as deterministic scalars of their recommended values [220].

Along with the deterministic input parameters representing measurable features of an arbitrary joint sub-assemblage, and prediction of the general characteristics defined with *envelopeParams* which are discussed in Chapter 4 and Chapter 5; a complete mathematical representation with *pinching4* in *OpenSees* require proper estimation of the damage rule defined in Equation 3.1 - 3.8. This process require proper estimation of aforementioned *deteriorationParams* which is inherently challenging due to the large number of combinations of the governing parameters and corresponding outcomes. Descriptions and bounds observed in the previous studies available in the literature are presented in Table 6.1.

In estimation of these parameters, conventional trial-error procedure is often followed in the literature, as it is discussed in further detail in Chapter 2. However, examination

Table 6.1 Description and bounds of the *deteriorationParams*

Parameter	Description	Bounds
rDisp	Pinching displacement reloading parameter	0.0 − 0.4
rForce	Pinching response reloading parameter	0.0 − 0.4
uForce	Pinching response unloading parameter	0.0 − 0.25
$gK_1 - gK_4$	Hysteresis stiffness degradation parameter	0.0 − 1.0
$gD_1 - gD_4$	Hysteresis displacement degradation parameter	0.0 − 1.0
$gF_1 - gF_4$	Hysteresis response degradation parameter	0.0 − 1.0
gE	Hysteresis energy degradation parameter	1.0 − 10.0

of the common approach reveals the lack of rational prediction through principles of structural mechanics in the numerical representation of stiffness and strength degradation phenomenon in reinforced concrete joints. Moreover, the same approach has led to the use of existing equations (see Equations 3.1 - 3.8) controlling deterioration only for the purpose of matching simulation results with experimental observations, thus ensuring full dependence on experimental results. The fact is, however, that there are practically no experimentally reported observations for each joint region sample for which civil engineers have to estimate inelastic responses during structural design or evaluation.

6.3 Methodology

The methodological framework presented in this chapter follows a structured and systematic process, ensuring a comprehensive exploration of the parameter space. Initially, an experimental database is compiled, encompassing only those specimens subjected to a cyclic displacement procedure.

Distinct from the experimental database used in the previous two chapters, the experimental database to be used for the intended purpose should include reported observations of cyclic loading protocols. A new database is collected from the available literature and the detailed information about the model parameters described experimental setups is given in Table A.2. Interior joint sub-assemblages of 52 different configurations tested by Fernandes [248], Lee *et al.* [249], Alaee and Li [250], Pantelides *et al.* [251], Liu [252], Noguchi and Kurusu [253], Dhakal and Pan [254], Xin *et al.* [255], RaffaelleE and Wight [256], Kurose *et al.* [257], and Kusuhara and Shiohara [258], 45 different exterior joint sub-assemblage tested by Tsonos [8], Kaku and Asakusa [52], Ehsani and Alameddine [54], Shafaei *et al.* [214], Ehsani and Wight [259], Ehsani *et al.* [260], and Chutarat and Aboutaha [261] are used as experimental database.

Subsequently, their envelope parameters are predicted utilizing the dual methodologies proposed in Chapters 4 and 5. A crucial aspect of the methodology

is the adoption of Latin Hypercube Sampling to sample deterioration parameters, aiming to achieve a comprehensive coverage of the sampling domain. The efficacy of LHS lies in its ability to ensure a uniformly distributed and representative sample across the entire problem space, thereby reducing the risks associated with overfitting or underfitting and enhancing the robustness of the derived models.

Subsequently, OpenSees models are built by the collected information, the predicted shear strain-stress curve, and randomly sampled deterioration parameters. Each simulation sample is then evaluated based on predefined error (or fitness) criteria, and a new generation of deterioration parameters is created following the principles of the non-dominated sorting genetic algorithm. The algorithm iteratively seeks the optimal solution until the convergence criteria are satisfied. Following this optimization process, the obtained deterioration parameters are associated with the physical features of the experimental specimens. This leads to the establishment of relationships between the measurable features of joint sub-assemblies and the detected deterioration parameters. The resulting correlations provide valuable insights, paving the way for more accurate and efficient prediction and analysis in future research and applications. In the subsections of this section, essential aspects of the developed methodology are introduced.

6.3.1 Parameter Sampling

Training data preparation is a critical step in the effective implementation of both feed-forward neural networks (FFNNs) and regression models, particularly in cases where the ability to design the learning database exists. In such instances, one does not merely rely on collected data, but can leverage the power of generated data, enabling the creation of rich, diverse, and balanced datasets. In this regard, the data generation process becomes a potent tool, enabling the provision of comprehensive and representative training sets which can facilitate improved learning and modeling of intricate underlying relationships. Along with the quality of data, the method employed for training sample selection is also of significant importance. Techniques such as Latin Hypercube Sampling (LHS) play a pivotal role in ensuring a uniformly distributed and representative sample from the entirety of the problem domain. This balanced sampling approach mitigates the risks of overfitting or underfitting, enhancing the robustness of the derived models. As such, the thoughtful design and generation of the training database, incorporating effective sampling strategies like LHS, are vital to enhancing the accuracy and performance of both FFNNs and regression models.

In Figure 6.2, two subfigures are observed, illustrating the performance of

feed-forward neural networks (FFNNs) in approximating a given true function, which is represented by a blue solid line. The effects of different training sample selection methods, namely uniform random sampling and Latin Hypercube Sampling (LHS), on the approximation accuracy are demonstrated by the subfigures. For the sake of clarity and visualization, a complex test function is selected and expressed as $f(x) = \sum_i^N exp(a*(x-b)^2)$ where a and b are arbitrary scalars (e.g. $N = 4$, $a = [5,-1,-3,-1]$, $b = [-3,-6,-8,-11]$). In the Figure 6.2.(a), the true function is compared with several approximation functions, which are derived from FFNNs with varying numbers of hidden layer neurons. These approximation functions are depicted as dashed lines of different colors. The training samples are generated by having random numbers drawn within the function's domain, following a uniform distribution. While some of the approximation functions closely follow the true function, a higher degree of deviation is exhibited by others, indicating the varying performance of the FFNNs with different architectures. In contrast, the performance of FFNNs with the same architectures as in the Figure 6.2.(a) is presented in the Figure 6.2.(b), but the training samples are now selected using LHS. This sampling method ensures that the training dataset is more evenly distributed across the entire input space, thus reducing the likelihood of overfitting or underfitting. As evident from the Figure 6.2.(b), a much closer adherence to the true function is exhibited by the approximation functions provided by the FFNNs trained with LHS samples, compared to their counterparts in the 6.2.(b).

By providing a more balanced and representative set of training samples, LHS allows the neural networks to learn the underlying patterns of the true function more efficiently. The utilization of LHS for sample selection in training dataset preparation can lead to improved performance and generalization in feed-forward neural network-based approximations, as demonstrated by the findings.

During the training of a feedforward neural network (FFNN), the weights and biases are adjusted to establish a relationship between the inputs and outputs presented in the training dataset (as explained in Section 2.4.1). The performance of the network is evaluated using an error function (such as mean squared error) by comparing the neural network response to the desired output. However, according to Celikoglu [262], FFNNs may struggle to find a global optimum solution or require a large amount of training data when many input parameters are involved, even when using advanced optimization algorithms (e.g., Newton or Levenberg-Marquardt). In such cases, finding an effective neural network structure (e.g., number of input and hidden layers, number of neurons, activation function) may require significant effort through trial-and-error. Additionally, Cigizoglu and Alp [263] notes that the accuracy of the neural network is heavily dependent on the random initialization of the input weights.

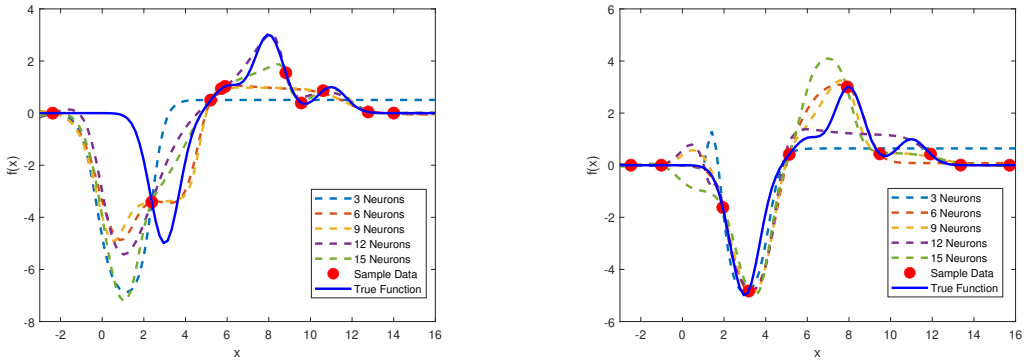

(a) (b)

Figure 6.2 Approximation to selected true function by FFNN through points sampled through the domain with (a) uniform distribution (b) Latin Hypercube Sampling

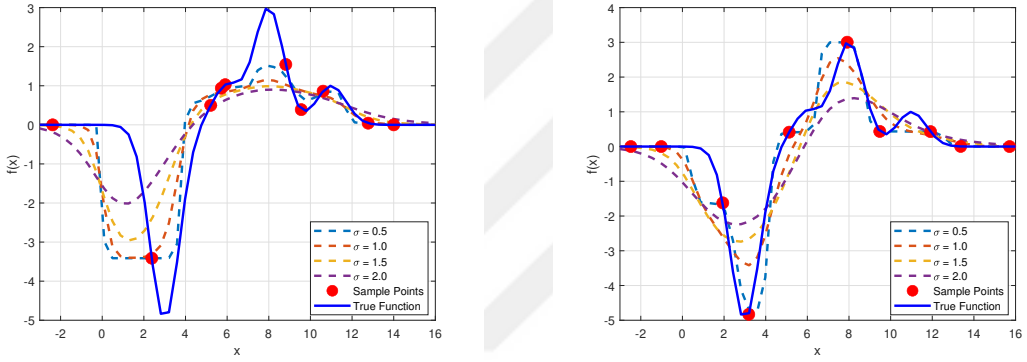

(a) (b)

Figure 6.3 Approximation to selected true function by GRNN through points sampled through the domain with (a) uniform distribution (b) Latin Hypercube Sampling

Furthermore, depending on the dataset and target, a unique FFNN structure may be required for each target parameter, as one structure may not be effective for all targets.

Figure 6.3 presents two subfigures comparing the performance of Generalized Regression Neural Networks (GRNNs) with varying spread parameters (σ), using uniform random sampling and Latin Hypercube Sampling (LHS) for training sample selection. The results highlight the superior approximation accuracy achieved by GRNNs trained with LHS samples, emphasizing the importance of LHS in enhancing performance and generalization in GRNN-based approximations.

6.3.2 Error Definition

In the evaluation of simulation accuracy, several critical fitness or error criteria are considered based on the investigation of experimental specimens listed in Table A.3, which offer a comprehensive understanding of how closely the simulated response

matches the experimentally observed response.

The first criterion, maximum strength (f_1), refers to the highest lateral load the sub-assemblage can resist. This measure is essential because it directly corresponds to the sub-assemblage's load-bearing capacity, a crucial factor in determining the robustness of the simulated response.

The second criterion is the drift at maximum lateral load (f_2), a measurement derived from the ratio of the lateral displacement at the column top to the total height of the sub-assemblage when the load is at its peak. This metric provides insight into the structural deformation under the maximum load, thereby revealing the structural integrity of the simulated response under peak stress conditions.

The strength loss at the last cycle (f_3), which signifies the reduction in strength from the maximum during the final load cycle, is the third criterion. This quantifies the progressive deterioration of the structure's load-bearing capability over successive load cycles, providing crucial information about the simulation's depiction of structural fatigue.

The fourth and fifth criteria are derived from the load-displacement history of the specimen. Tangent stiffness (f_4) offers a measure of the rate of change of loading with respect to displacement. It is influenced by multiple factors, including behavior within the joint core and the flexural stiffness of the beams and columns. Unloading stiffness (f_5), on the other hand, is indicative of the stiffness deterioration of the specimen linked to inelastic response within the joint core. Both measures offer vital information about the load-displacement characteristics and the stiffness deterioration of the structure under simulated conditions. The final criterion, (f_6), is the convex hull area of the load deformation history which has a particular importance to represent the accuracy in terms of pinching.

In conclusion, these six criteria, while individually providing unique insights into various aspects of the simulated structural response, collectively give a comprehensive understanding of how well the simulated response mirrors the experimentally observed response. As such, they serve as critical benchmarks for evaluating the accuracy of the simulations. Illustrative representation of the criteria is shown in Figure 6.4

One of the most essential aspects affecting the quality and accuracy is the definition of error or the fitness of the each individual simulation sample. In the present study, two approaches are proposed; the first defines the optimization problem based on the minimization error defined by one criterion, or the norm of the defined criteria. This

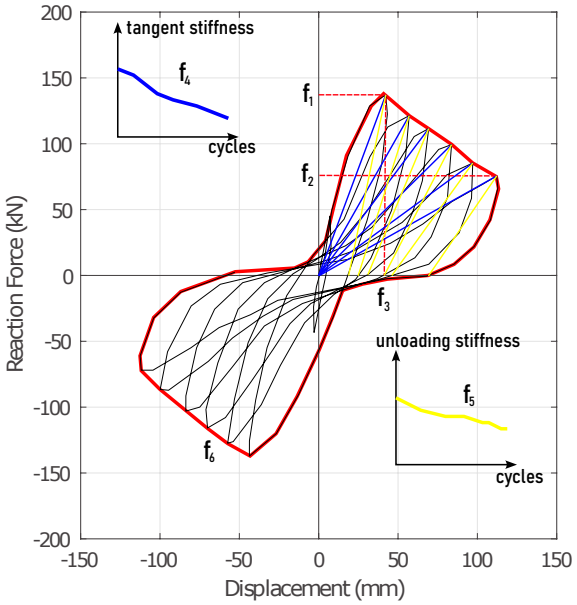

Figure 6.4 Illustration of the error definitions used in multi-objective error minimization problem

approach corresponds to a uni-objective unconstrained optimization problem which requires less sophisticated solutions compared to the second. The second approach aims to minimize a collection of error criteria simultaneously. In the result section, effect of the objective definition is investigated.

6.3.3 Optimization Problem

In the present study, the proper modeling of an arbitrary joint sub-assemblage is defined as an optimization problem where the best solution is aimed and the *deteriorationParams* leading to the optimal solution. After assessment of the *deteriorationParams* for the all specimens introduced in Table A.1, factors affecting the alteration of the members of this parameter set and its sensitivities to the joint features are investigated.

Among many, genetic algorithms are often adopted for such parameter identification problems [129]. One of the biggest benefits is that they can search the entire solution space which is particularly helpful in avoiding local optima, which are points that look like the best solution within a small sub-domain. What sets genetic algorithms apart is their adaptability. Genetic algorithms are not rigid, but rather capable of evolving over time, adjusting to changes in the problem space. This makes them particularly useful for dynamic optimization problems where the optimal solution might shift as time progresses. In addition, genetic algorithms shine due to their problem-independent nature. They don't demand specific knowledge about the problem in order to find solutions. As long as a fitness function is provided to guide the evolutionary

process, genetic algorithms can be employed to solve a wide array of optimization problems. Genetic algorithms are well-equipped to handle non-linear parameters and discontinuous search spaces, thanks to their robustness and flexibility. Even when a problem has complex interactions between variables, or numerous local optima, genetic algorithms can still navigate the solution space effectively. Notably, they also excel at multi-objective optimization. Through techniques like Pareto optimization, genetic algorithms can find solutions that optimize several conflicting objectives at once [146].

In the mathematical representation of the joint deformation problem, the i-th simulated response in the j-th population is expressed as

$$v_{ij} = f(d_{ij}, c_{ij}, s_{ij}, p_{ij}, t), i \in [1, n]^Z, j \in [1, m]^Z \tag{6.1}$$

where d_{ij}, c_{ij}, s_{ij} and p_{ij} are vectors of input parameters related to model dimensions, concrete material, steel (reinforcement) material and *pinching4* material respectively and f stands for structural analysis operator. While the d_{ij}, c_{ij} and s_{ij} are consisted of only deterministic scalar variables, p_{ij} consists of both deterministic scalars (p_{ij}^{det}) and a set of random scalars (p_{ij}^{rand}) which were recommended to be fitted to the experimental data.

The fitness of each simulation sample g_{ij} is defined as the squared error between simulated ($v_{ij}(t)$) and experimentally observed ($v_{exp}(t)$) response (the objective output defined in terms of various response quantities in the previous section).

$$g_{ij}(v_{ij}, v_{exp}) = (v_{ij} - v_{exp})^2 \tag{6.2}$$

The calibration process is adopted as an optimization problem that targets to minimize the fitness function. The squared error is used to define fitness to overcome the issue related to the fact negative error values may lead to inaccurate predictions of simulations' fitness.

After generation of the j-th population of n converged solutions, each sample is sorted in the respective order of their normalized fitness ($\hat{g}$) values. $p_s \in [0, 1]^R$ is a random variable to be returned for each selection while $F(\hat{g} = P(\hat{(}g) \leq p_s))$ corresponds to the selection case where F is the cumulative distribution function. Since simulation samples with less fitness values have higher $F(\hat{g})$ values returned, thus have greater chance to be selected in comparison with the other simulation samples.

After random selection of parent simulation samples, new sets of simulations samples (referred as child) of the next generation are generated with the crossover process. Probability of crossover is defined as $P(p_c \in [0,1]^R < \hat{p}_c)$ and exceedence of a given threshold $\hat{p}_c$ (typically assigned a high value e.g. 0.9 to enhance variation in solutions) corresponds to realization of generation of new random parameters deriving from selected solution samples.

$$y^k_{i,j+1} = \beta \cdot y^k_{\alpha,j} + (1-\beta) \cdot y^k_{b,j} \tag{6.3}$$

where a and b are indices of selected samples, $\beta \in [0,1]^R$ is a random parameter that controls contribution of parameters from genes and superscript indicates the kth component of model parameter vector. At last, generated model parameters (genes) are mutated to a value randomly generated within the sampling interval with probability defined as $P(p_m \in [0,1]^R < \hat{p}_m)$ to expand solution domain. Members of the mth population are expected to be consisted of the solution samples with the least error.

6.3.4 Multiobjective Optimization

Use of more than one objectives in optimization process turns the case to a multi-objective optimization problem. Within the scope of the present study, a collection of functions has been developed and implemented for the purpose of addressing multi-objective optimization problems as needed. These functions have been designed to be compatible with MATLAB's built-in 'gamultiobj' function, which utilizes the Non-dominated Sorting Genetic Algorithm II (NSGA-II) for solving multi-objective optimization problems [264]. Performance evaluation of the optimization process is carried out by monitoring the hypervolume metric across successive generations. This metric offers valuable insights into the convergence and diversity properties of the algorithm, thereby facilitating the assessment of the quality of the Pareto front approximations obtained during the optimization process.

A generic function is introduced to describe essential concepts used in the optimization process used in the present study. To evaluate the performance of the developed methodology, the well-established ZDT1 test problem (Equation **??**) has been employed as a benchmark [265]. This particular test problem has been extensively utilized in the literature for assessing the efficacy of various optimization algorithms. The ZDT1 function is challenging to optimize because it exhibits both convex and non-convex regions in the search space. The non-linear nature of the second objective function also adds to the difficulty. Therefore, optimization algorithms need to

be able to balance between exploring the search space to find diverse solutions and exploiting the solutions found to improve the objective values. Because of its complexity and difficulty, ZDT1 is widely used as a benchmark test function in the field of multi-objective optimization.

NSGA-II is an extension of the classical genetic algorithm framework, incorporating several key modifications to enhance its ability to address multi-objective optimization problems. These include a fast non-dominated sorting procedure, an elitist preservation strategy, and a crowding distance sorting mechanism. By integrating these features, NSGA-II effectively balances the exploration and exploitation aspects of the search process, allowing it to converge to the Pareto-optimal set more efficiently. A primary advantage of NSGA-II is its ability to generate a diverse set of Pareto-optimal solutions. This diversity stems from the crowding distance calculation, which serves to estimate the density of solutions surrounding a given individual in the objective space. By incorporating this measure into the selection process, NSGA-II promotes a more uniform distribution of solutions along the Pareto front, thereby enabling decision-makers to identify a wider range of trade-offs between conflicting objectives. An illustrative flowchart of NSGA-II algorithm is presented with Figure 6.5.

Regardless of the used algorithm, in multi-objective optimization, the Pareto front is described a set of solutions that are not dominated by any other solution in terms of all objective functions. Specifically, a solution is Pareto optimal if there is no other solution that is better in all objectives, and there is at least one objective in which the other solution is worse. The Pareto front is the set of all Pareto optimal solutions.

The Pareto front is a useful tool for decision making, as it represents the trade-offs between the different objectives. A decision maker can choose a solution from the Pareto front based on their preferences or priorities for the different objectives. Figure 6.6 displays the Pareto fronts of different generations during the optimization process. The x-axis represents the first objective, while the y-axis represents the second objective. Each dot represents a solution, and the Pareto fronts are shown in different colors. As the optimization progresses, the Pareto fronts move closer to the true Pareto front, which might be not available in all cases. The figure demonstrates the convergence of the optimization algorithm towards the true Pareto front and provides insight into the trade-offs between the different objectives.

In a Pareto front, there is no single "best" solution that dominates all others in terms of all objectives. Instead, the best solution for a particular decision maker or problem depends on their preferences and priorities for the different objectives.

One approach to finding the best solution among a Pareto front using Euclidean

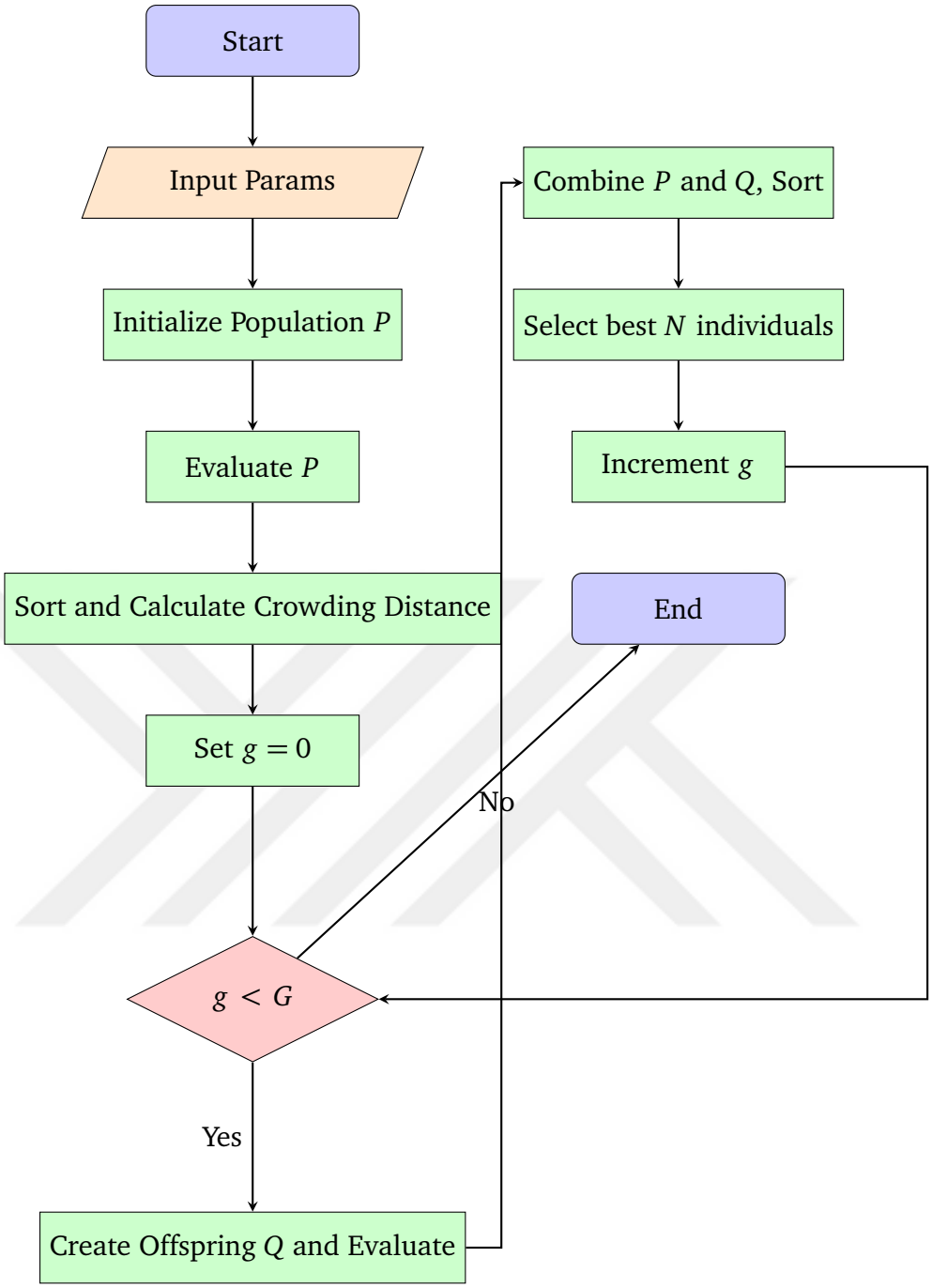

Figure 6.5 Non-dominated Sorting Algorithm - II flowchart

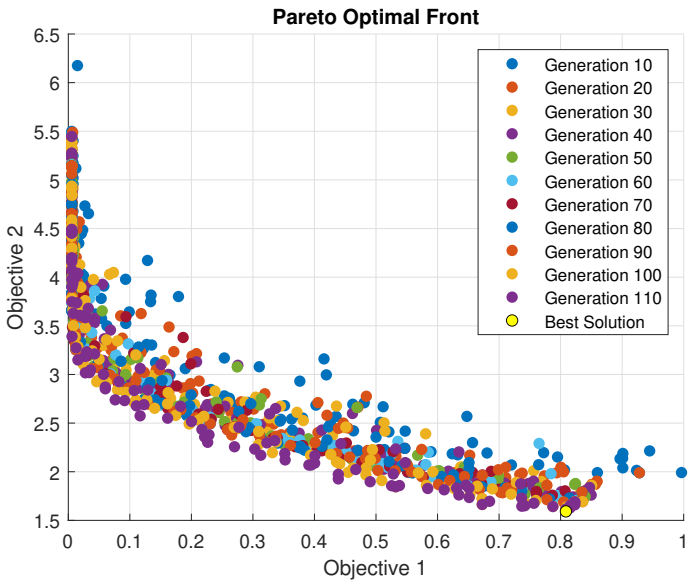

Figure 6.6 Pareto front of bi-objective ZDT1 problem

distance to the origin is to first normalize the objective values of each solution in the Pareto front by subtracting the ideal solution and dividing by the range between the ideal solution and the Nadir point. This normalization transforms the Pareto front into a unit hypercube centered at the origin.

Supposing a Pareto front with m objectives and n solutions. Let $\mathbf{y}_i \in \mathbb{R}^m$ denote the objective values of the i-th solution in the Pareto front, where $i = 1, \ldots, n$.

Ideal solution $\mathbf{y}^{ideal}$ and the Nadir point $\mathbf{y}^{nadir}$ are defined as follows:

$$\mathbf{y}^{ideal} = \min_{i=1,\ldots,n} \mathbf{y}_i \tag{6.4}$$

$$\mathbf{y}^{nadir} = \max_{i=1,\ldots,n} \mathbf{y}_i \tag{6.5}$$

Next, objective values can be normalized of each solution in the Pareto front as follows:

$$\mathbf{y}'_i = \frac{\mathbf{y}_i - \mathbf{y}^{ideal}}{\mathbf{y}^{nadir} - \mathbf{y}^{ideal}} \tag{6.6}$$

This normalization transforms the Pareto front into a unit hypercube centered at the origin. Then, the Euclidean distance can be calculated of each solution to the origin as follows:

$$d_i = \sqrt{\sum_{j=1}^{m} (y'_{ij})^2} \tag{6.7}$$

The solution with the smallest Euclidean distance to the origin is considered the best solution among the Pareto front in terms of Euclidean distance:

$$i^* = \arg \min_{i=1,\ldots,n} d_i \tag{6.8}$$

The best solution among the solutions in the Pareto front of the last generation is remarked in yellow in Figure 6.6.

6.3.5 Performance Metrics and Validation

Generational Distance (GD) and Hypervolume (HV) are two popular performance indicators used to evaluate the quality of solutions obtained from multiobjective optimization algorithms. They provide quantitative measures of the performance of the algorithms and help in comparing their effectiveness [266].

Generational Distance is a measure of the average distance between the obtained Pareto front and the true Pareto front while Hypervolume is a measure of the size of the space dominated by the obtained Pareto front. It quantifies the convergence of the algorithm towards the true Pareto front. Both Generational Distance and Hypervolume are valuable performance indicators in multiobjective optimization. While Generational Distance focuses on convergence to the true Pareto front, Hypervolume takes into account both convergence and diversity of the solutions. By tracking the indicators over generations, you can observe how the algorithm converges towards the true Pareto front. If the hypervolume value increases rapidly at first and then starts to plateau, it's an indication that the algorithm has converged to a reasonable approximation of the Pareto front.

In most inverse analysis problems, analytical form of objective functions may not be available thus true Pareto front is unknown. Deb and Jain [267] remark the limitations of generational distance and propose the use of hypervolume as a more suitable performance indicator, especially when the true Pareto front in such cases. The authors argue that hypervolume has some desirable properties that make it a convenient choice for evaluating the quality of the Pareto front approximations.

Hypervolume provides information about both the convergence of the algorithm

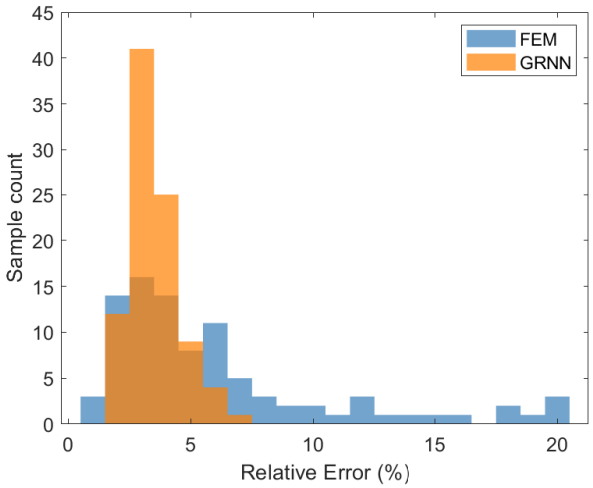

Figure 6.7 Histogram of the norm of error vector minimized for the entire dataset through uni-objective optimization (Method I)

(how close the obtained Pareto front is to the true Pareto front) and the diversity of the solutions (how well the solutions are spread along the Pareto front). A larger hypervolume indicates better performance in terms of convergence and diversity. To calculate the hypervolume, a reference point is required, which should be strictly worse than any point in the true Pareto front. The hypervolume is then calculated as the volume of the space enclosed between the obtained Pareto front and the reference point.

6.4 Results

In this section, the optimization processes carried out with different objective functions and modelling approaches are evaluated in terms of efficiency and obtained coefficients. In these processes, firstly, the problem is considered as a single objective function optimisation problem and the optimum result is sought by using the modelling approaches presented in Chapter 4 and Chapter 5. The single objective function chosen can be defined as the norm of the vector of scalar values of the criteria defined in Section 6.3.2. The operation carried out here is referred to as Method I. In the second part of the analysis, the aim is to simultaneously minimize the quantities constituting the error vector as separate objective functions. Similar to Method I, both GRNN predictions and equations obtained from FEM are used as modelling approach.

Since the accurate prediction of the cyclic response in both methods depends to a great extent on the correct estimation of the envelope curve, an objective comparison can only be made on the results using the same assumptions.

Firstly, in order to compare the effectiveness of both approaches, Figure 6.7-6.9

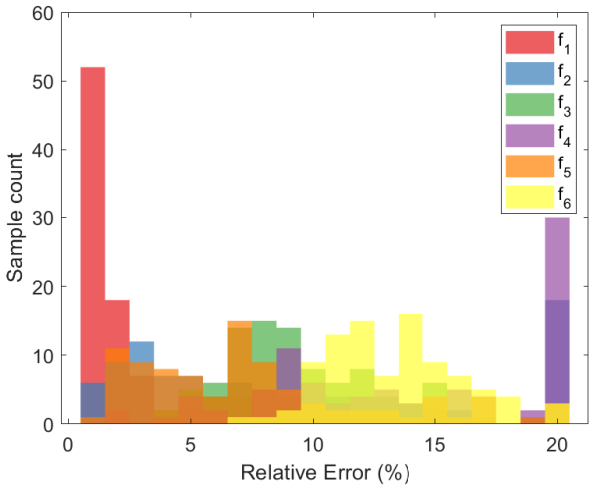

Figure 6.8 Histograms of the objective functions minimized for the entire dataset through multi-objective optimization (Method II) based on the FEM predicted shear strain stress curve

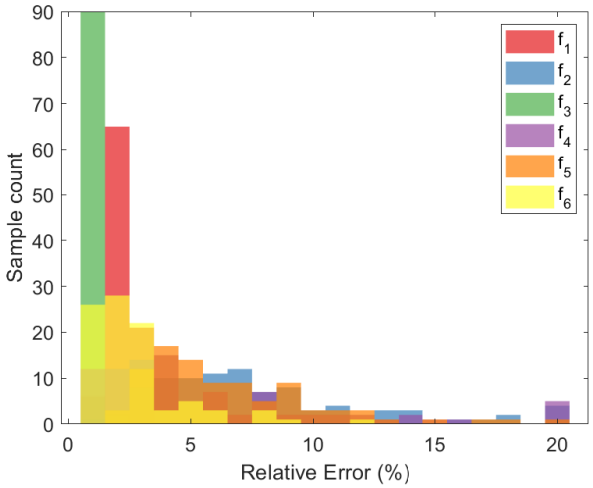

Figure 6.9 Histograms of the objective functions minimized for the entire dataset through multi-objective optimization (Method II) based on the GRNN predicted shear strain stress curve

show the lowest relative error (see Section 6.3.2) obtained in simulations with 50 generations of 50 individuals each, for each sample in the database characterised in Tables A.2 and A.3. The distributions of the relative error vector generated from the defined criteria f_1 - f_6 for the two different modelling approaches performed in Method I are given in Figure 6.7. Accordingly, it is seen that the results obtained from the optimisation scheme based on the envelope estimation with GRNN can obtain more convergent results at the same number of function cycles compared to the models based on the envelope estimation with FEM. In the results obtained with FEM, there are also results around 20% in the relative error vector, whereas there are very few simulation examples with errors beyond 5% relative error in the results obtained by GRNN.

Secondly, the relative error distributions obtained as a result of the multi-objective optimisation process based on the joint deformation envelope obtained by FEM in the Method II application, which includes 6 different objective functions, are shown in Figure 6.8. According to this, it is seen that the function f_1, which is based only on the strength value, converged to the minimum values for most of the specimens, and the objective functions remained far from the acceptable convergence range within the defined number of function cycles. On the other hand, it is seen in Figure 6.9 that with the error minimization process carried out over the joint deformation envelope predictions made by GRNN, relative errors at reasonable levels can be obtained for almost all discrete objective functions within the defined number of common function cycles.

Accordingly, it is obvious that running both optimization methods with the predictions made with GRNN is more efficient. In the comparison of the optimisation processes carried out with Method I and Method II using the predictions from GRNN, it can be suggested that more convergent results can be obtained with the multiobjective optimization process based on the relevant results.

6.4.1 Estimation of *deteriorationParams*

Due to the nature of the problem, it is not entirely possible to relate the results obtained as a result of the optimisation process carried out in this chapter to measurable quantities describing the simulation models, or the corresponding experimental samples, as was done in Chapters 4 and 5. Since the set of parameters obtained in each solution work together to create a damage description, it is not acceptable to relate the parameters obtained separately from the individual solutions to different quantities. Nevertheless, it is still possible to make certain inferences by examining the outputs obtained through the optimization process of these parameters.

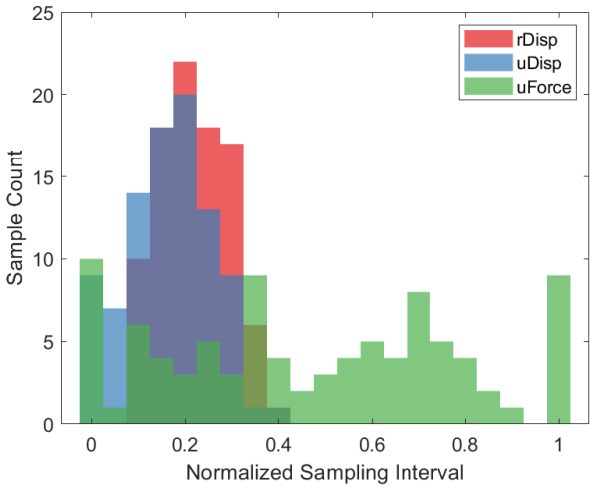

Figure 6.10 Histograms of the pinching parameters resulted from the optimization procedure of Method II GRNN approach

In Figure 6.10, strong accumulations are observed between the values of 0.20 - 0.25 for the pinching parameters $rDisp, rForce$ while $uForce$ is highly dissipated along the sampling space. However, no distinguishable difference is observed based on concrete strength f_c, reinforcement ratio ρ_j, aspect ratio b/h or joint type. On the other hand the distribution of second to fourth terms of cyclic unloading stiffness degradation parameters $(gK2, gK3, gK4)$, cyclic reloading stiffness degradation parameters $(gD2, gD3, gD4)$, cyclic strength degradation parameters $(gF2, gF3, gF4)$ and maximum energy dissipation under cyclic loading parameter (gE) have shown very large variance almost approximating an uniform distribution along the space. The dissipation of the parameters along the sampling interval can indicate the low sensitivity of the simulation model to the listed parameters.

When the distribution of the parameter $gK1$, which is outside the listed parameters, is examined separately according to the type of the joint area, it is observed that the values best approximating the result form two distinct clusters as it is shown in Figure 6.11. The data for the interior joints varies significantly, suggesting a diverse range of behaviors within this category. The values, while predominantly centering around the mid-range, have a wide span. Conversely, the $gK1$ values for exterior joints appear to be generally higher, indicating a potential difference in the behavioral characteristics between interior and exterior joints. This observation might suggest that exterior joints generally exhibit higher $gK1$ values.

A similar clustering is also present for the $gD1$ values, albeit in a more variant form. When a distinction is made specific to the type of joint, a notable separation is observed in the distribution of parameters that yield convergent results. Upon analyzing the $gD1$ values for interior and exterior joints, we can observe a couple of distinct features.

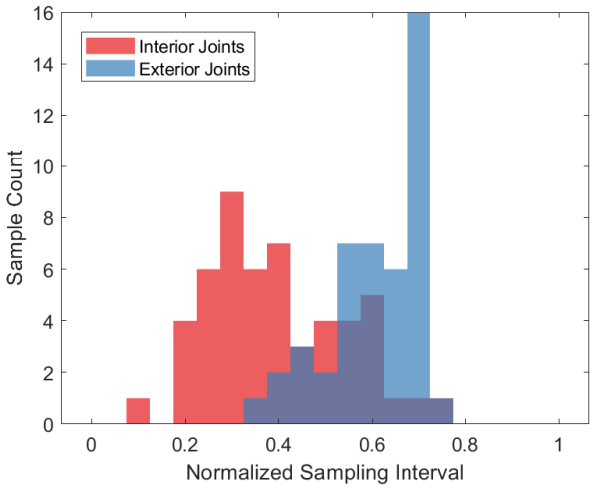

Figure 6.11 Histograms of $gK1$ parameters resulted from the optimization procedure of Method II GRNN approach split data based on the joint type

For interior joints, the data seems to vary more widely than that of exterior joints. The mean value for gD1 for interior joints is approximately 0.39, suggesting that most of the data points cluster around this value. However, the standard deviation of approximately 0.17 indicates a high level of variance, showing that the data is spread out over a large range. The minimum and maximum values lie between approximately 0.07 and 0.78 respectively, thus indicating the wide dispersion.

On the other hand, for exterior joints, the mean value is around 0.72, which is significantly higher than that of interior joints. This suggests that the gD1 values for exterior joints tend to be higher on average. The standard deviation is approximately 0.20, indicating a more spread out data set than the interior joint data, but also, it is consistent with the larger mean value. The minimum and maximum values span from approximately 0.30 to 1.00.

The $gF1$ parameter exhibits a certain level of consistency across both interior and exterior joints, indicating that this specific parameter might not be significantly influenced by the joint type. The parameter is characterized by a relatively low mean value of around 0.15, suggesting that the majority of $gF1$ values are clustered in this region. Furthermore, the standard deviation of 0.21, though higher than the mean, indicates a reasonable level of dispersion around this mean value. However, it is noteworthy to mention that no discernible patterns or clusters specific to either interior or exterior joints have been observed within the data for $gF1$. This signifies that the $gF1$ values remain relatively consistent regardless of the joint type, hinting at a level of universality for this particular parameter across different types of joints in the studied system. This can be an intriguing area of study to understand the underlying factors causing such uniformity and its implications on the overall behavior of the

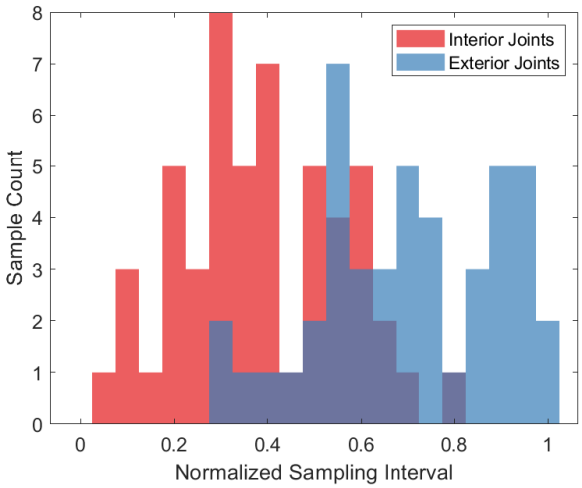

Figure 6.12 Histograms of $gD1$ parameters resulted from the optimization procedure of Method II GRNN approach split data based on the joint type

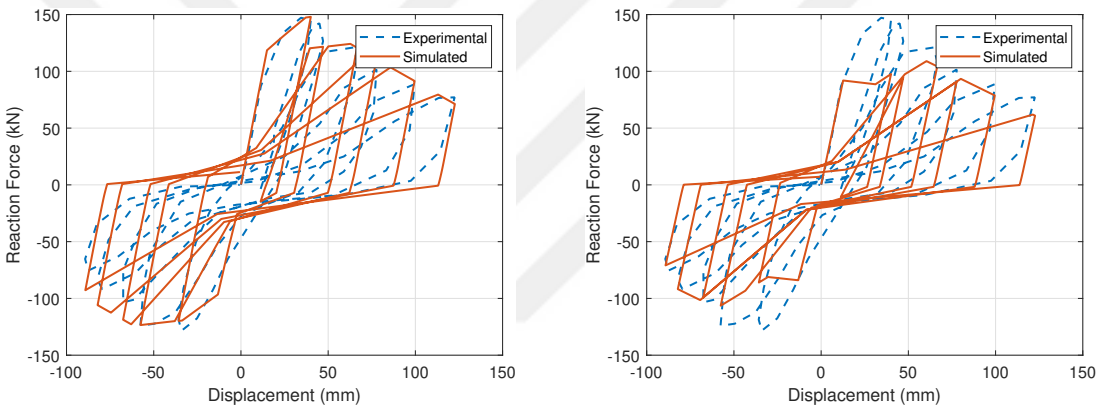

Figure 6.13 Comparative presentation of experimental and simulated responses for Specimen 1B [259], (a) Optimized *deteriorationParams* through Method I GRNN Approach (b) Predicted through rDisp = 0.2, uDisp = 0.2, gK1 = 0.65 and gD1 = 0.72

system.

6.4.2 Numerical Examples

The conclusions drawn from the findings of this section are tested on an experimental set, with an optimised interior and exterior joint sub-assemblages. In the previous section, it was evaluated that it was appropriate to use the norms of both criteria as the objective function in the genetic algorithm in the evaluation made on the relative errors obtained over the whole data set through scatter plots. In Figure 6.13.(a), a simulation result obtained with the Method I GRNN approach is shown in comparison with experimental observations reported by Ehsani and Wight [259] about Specimen 1B.

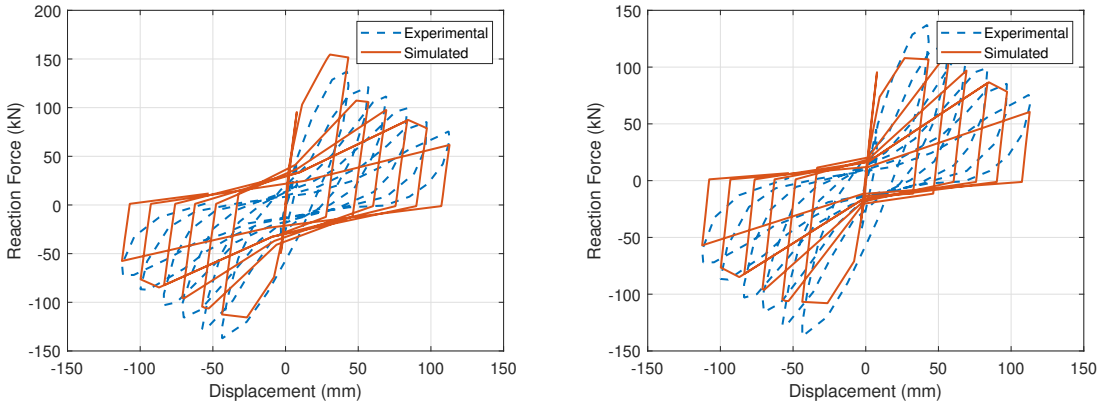

Figure 6.14 Comparative presentation of experimental and simulated responses for Specimen LL1 [54], (a) Optimized *deteriorationParams* through Method I GRNN Approach (b) Predicted through rDisp = 0.2, uDisp = 0.2, gK1 = 0.65 and gD1 = 0.72

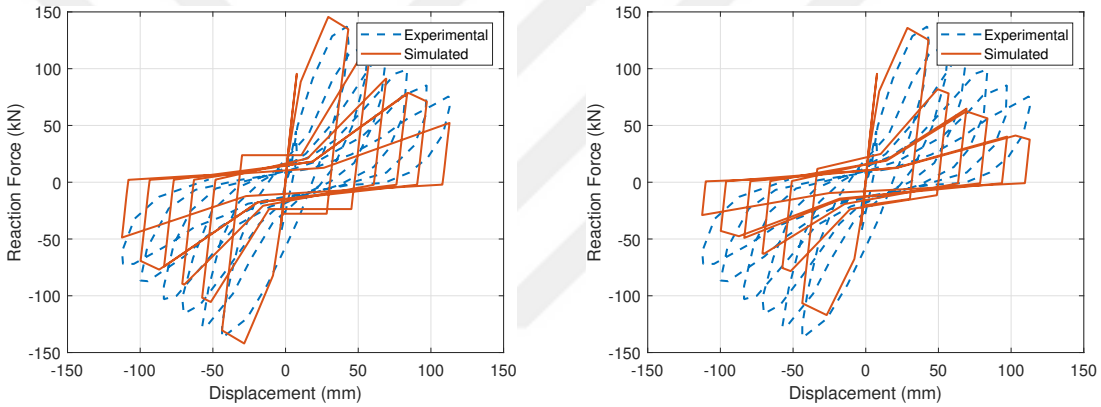

Figure 6.15 Comparative presentation of experimental and simulated responses for Specimen LL1 [53], (a) Optimized *deteriorationParams* through Method I GRNN Approach (b) Predicted through rDisp = 0.2, uDisp = 0.2, gK1 = 0.65 and gD1 = 0.72

Figure 6.13.(b) shows the result of a simulation with the proposed values of the 4 effective parameters (rDisp = 0.2, uDisp = 0.2, gK1 = 0.65 and gD1 = 0.72) for an external joint region without optimisation based on simple estimations based on inferences made from the distribution of the parameters. Comparison between error norms between two simulations lead to 21% increase in the relative error.

Figure 6.14, Figure 6.15 and Figure 6.16 show the optimized and predicted simulation responses in comparison with experimental measurements reported by Ehsani and Alameddine [54], Kaku and Asakusa [53] and Kaku and Asakusa [52] in respective order. Commonly, Method I with GRNN approach is used for joint deformation envelope prediction.

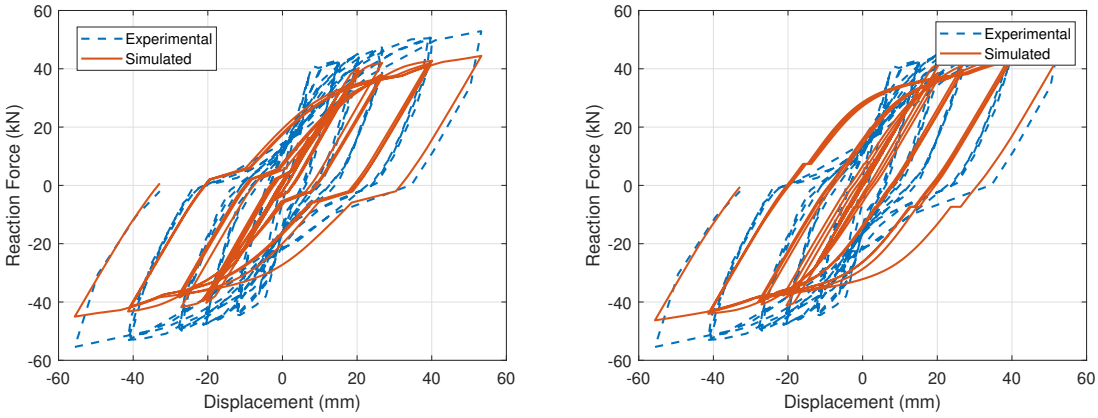

Figure 6.16 Comparative presentation of experimental and simulated responses for Specimen 6 [52], (a) Optimized *deteriorationParams* through Method I GRNN Approach (b) Predicted through rDisp = 0.2, uDisp = 0.2, gK1 = 0.30 and gD1 = 0.39

6.5 Conclusion

In conclusion, this chapter has conducted a thorough investigation into the application of genetic algorithms for the problem of reinforced concrete joint modelling. Two distinct genetic algorithm forms were employed and the divergence between simulated and observed responses was systematically classified to delineate different aspects of joint deformation characteristics. A meticulous search was undertaken for the parameter set that would yield the minimum error.

The techniques applied were twofold: the first method aimed for the minimization of the norm of the error criteria (Method I), while the second one took a more complex approach in minimizing all the objective functions simultaneously using the principles of NSGA-II (Method II). Both techniques were tested using two different joint deformation prediction models proposed in the preceding chapters, with findings indicating superior accuracy from the GRNN-based prediction model.

The results clearly indicate that the employment of both methods in conjunction with the GRNN joint deformation prediction model is capable of producing highly approximate solutions, leveraging the robust capabilities of the Genetic Algorithm.

A comprehensive exploration of the procured deterioration parameters demonstrated that the vast majority of parameters have minimal impact on the joint response. However, four parameters — rDisp, uDisp, gK1, and gD1 — were found to significantly influence the joint response. The effect of these crucial parameters was analyzed separately based on the joint type, and their effective ranges were identified.

The mean values obtained from this statistical analysis were subsequently applied

to both interior and exterior specimens. The results were found to be suitable for practical applications, reinforcing the validity and efficacy of the methods and models adopted in this study. This research lays a substantial foundation for further exploration and improvement in the field of reinforced concrete joint modeling.

7
DISCUSSION and FUTURE WORK

In summary, this thesis presents a comprehensive exploration into the shear strain-stress envelope of reinforced concrete joints, leveraging advanced finite element method simulations and artificial intelligence techniques. The research was necessitated by the lack of unified experimental configurations in the literature, resulting in the need for alternative statistical implementation of strain stress prediction models.

In response to this, the study introduced a specialized type of artificial neural network structure and explored basic statistical methods to establish a relationship between the physical characteristics of the RC joint sub-assemblies and the resulting shear strain-stress outcomes. The scarcity of data samples from the literature led to the utilization of advanced finite element methods to create an accurate statistical model, which was achieved by applying intricate solutions for high-level nonlinear behavior of concrete material.

The study generated a significant number of simulation samples under predefined assumptions. These results were systematically classified and regression techniques were applied, leading to the conclusion that the shear strain-stress envelope of any given joint sub-assembly can be predicted with acceptable accuracy. It was further observed that including auxiliary terms could enhance this accuracy, although for the sake of simplicity, the proposed equations were deemed sufficient.

The thesis subsequently delved into the practical application of genetic algorithms for reinforced concrete joint modeling. Employing two distinct forms of genetic algorithms, the study systematically classified the divergence between simulated and observed responses to delineate different aspects of joint deformation characteristics. It was found that a combination of these genetic algorithm forms and the GRNN joint deformation prediction model could produce highly approximate solutions. Further analysis revealed that the majority of deterioration parameters had minimal impact on joint response. However, a select few – rDisp, uDisp, gK1, and gD1 – were found

to have a significant effect, laying the groundwork for future research in this area.

The study has demonstrated that the GRNN-based model provides the most accurate predictions among existing models, thereby showcasing the potential of the GRNN model in enhancing the understanding of joint deformation characteristics and aiding practical applications of joint modeling. A publicly accessible version of the trained model has been provided to facilitate its wider use and further improvements.

Continuing from the findings of this thesis, a comprehensive parametric study of joint mechanics is an important next step. The proposed methods, tools, and equations in this thesis form a foundation for this study, allowing for the inclusion of more factors in the exploration. By considering a broader range of parameters, a more detailed understanding of joint mechanics may be achieved, which could lead to even more accurate predictive models.

Microplane material formulation and bond springs under cyclic loading conditions have shown significant potential. However, their application is often restricted due to the high computational demands. Therefore, a future focus is to develop a calibration technique to replace the current laborious trial and error fine-tuning process. This could simplify the implementation of more comprehensive models and allow for more detailed investigations.

Moreover, the proposed approach from this study could be adapted and integrated into the existing design and assessment processes described in seismic codes and provisions. Embedding these advanced modeling techniques into industry standards could streamline the design process and possibly lead to structures that are more efficient and safer. Based on the results of the parametric analyses, the possibility of considering joint failures in force-based assessment methods through the use of reduction factors will also be examined. Incorporating joint failures into these methods could offer a more realistic representation of joint behavior under different loads. This could contribute to the development of more accurate and safer structural designs.

Incremental dynamic analyses and similar methods also present an interesting area for future study. These methods could be used to represent the failure probabilities of joints with varying characteristics in the form of fragility curves. This could provide important insights for engineers and architects when assessing structural resilience under different loading conditions.

In conclusion, this thesis has made a substantial contribution to the understanding of the shear strain-stress behavior of RC joints. It has shown the feasibility of advanced

AI techniques in predicting the strain-stress envelope, the effectiveness of genetic algorithms in finding the most appropriate parameter set, and the superiority of the GRNN model in predicting joint deformation. The insights and methods provided by this study will certainly aid in the further understanding and improvement of reinforced concrete joint modeling. Future research directions promise to significantly contribute to the ongoing development and refinement of reinforced concrete joint modeling. They offer a promising path towards enhancing our understanding of joint behavior, leading to safer and more resilient structures.

REFERENCES

[1] SEAOC, "Performance based seismic engineering of buildings," *Sacramento (CA): Structural Engineers Association of California, USA*, 1995.

[2] E. Miranda and H. Aslani, "Building specific loss estimation for performance based design," in *2003 Pacific Conf. on Earthquake Engineering, New Zealand Society for Earthquake Engineering, Wellington, New Zealand*, 2003.

[3] S. Hakuto, R. Park, and H. Tanaka, "Seismic load tests on interior and exterior beam-column joints with substandard reinforcing details," *Structural Journal*, vol. 97, no. 1, pp. 11–25, 2000.

[4] M. O. Yılmaz, S. Bekiroğlu, Ç. Mollamahmutoğlu, M. Öztürk, and Y. Şahinkaya, "Kahramanmaraş depremleri sonrası bölgedeki deprem yalıtım birimli binalar ile abyyhy-1998 sonrası yapılmış binaların incelenmesi, Investigation of buildings with earthquake isolation units in the region after kahramanmaraş earthquakes and buildings constructed after abyyhy-1998," Turkish, TUBITAK, Ankara, Turkey, 1002-C Proje Sonuç Raporu, 2023.

[5] M. d. A. Ferreira, "Deformabilidade de ligações viga-pilar de concreto pré-moldado," in Portuguese, Master's Thesis, Universidade de São Paulo, São Carlos, 1999.

[6] M. Geradin and P. Negro, "The european laboratory for structural assessment (elsa) and its role for the validation of european seismic codes," in *Second Euro Conference on Global Change and Catastrophe Risk Management: Earthquake Risks in Europe*, Luxembourg, 2000, pp. 1–8.

[7] G. Alva, "Estudo teórico-experimental do comportamento de nós de pórtico de concreto armado submetidos a ações cíclicas," in Portuguese, PhD Thesis, Universidade de São Paulo, São Carlos, 2006.

[8] A. G. Tsonos, "Cyclic load behaviour of reinforced concrete beam-column subassemblages of modern structures," *ACI Structural Journal*, vol. 104, no. 4, 2007.

[9] A. Amirsardari, H. Goldsworthy, and E. Lumantarna, "Modelling non-ductile reinforced concrete beam-column joints," in *Proceedings of the Tenth Pacific Conference on Earthquake Engineering*, 2015.

[10] A. Amirsardari, E. Lumantarna, P. Rajeev, and H. M. Goldsworthy, "Seismic fragility assessment of non-ductile reinforced concrete buildings in australia," *Journal of Earthquake Engineering*, vol. 26, no. 4, pp. 1941–1975, 2022.

[11] A. Y. Rahmani, S. H. Boukhalkhal, and M. Badaoui, "Effect of beam-column joints flexibility on the seismic response of setback rc buildings designed according to the algerian seismic code," *Frattura ed Integrita Strutturale*, vol. 16, no. 61, pp. 394–409, 2022.

[12] ACI318-71, “Commentary on building code requirements for reinforced concrete,” 1971.

[13] ACI352-76, “Recommendations for design of beam-column connections in monolithic reinforced concrete structures,” 1976.

[14] W. Nadir, A. Y. Ali, and M. M. Kadhim, “Structural behavior of hybrid reinforced concrete beam-column joints under cyclic load: State of the art review,” *Case Studies in Construction Materials*, vol. 15, e00707, 2021.

[15] R. Park and T. Paulay, *Reinforced concrete structures*. John Wiley and Sons, 1991.

[16] L. N. Lowes and A. Altoontash, “Modeling reinforced-concrete beam-column joints subjected to cyclic loading,” *Journal of Structural Engineering*, vol. 129, no. 12, pp. 1686–1697, 2003.

[17] J. Bonacci and S. Pantazoupoulou, “Parametric investigation of joint mechanics,” *Structural Journal*, vol. 90, no. 1, pp. 61–71, 1993.

[18] T. Kamimura, S. Takeda, and M. Tochio, “Influence of joint reinforcement on strength and deformation of interior beam-column subassemblages,” in *12 th World Conference on Earthquake Engineering*, 2000.

[19] G. Thermou, S. J. Pantazopoulou, and A. S. Elnashai, “Analytical modeling of interface behavior in reinforced concrete jacketed members,” in *Structures 2004: Building on the Past, Securing the Future*, 2004, pp. 1–8.

[20] M. Priestley, “Performance based seismic design,” *Bulletin of the New Zealand society for earthquake engineering*, vol. 33, no. 3, pp. 325–346, 2000.

[21] ACI352-R02, “Recommendations for design of beam-column connections in monolithic reinforced concrete structures,” 2002.

[22] T. Paulay, R. Park, and M. J. N. Preistley, “Reinforced concrete beam-column joints under seismic actions,” in *Journal Proceedings*, vol. 75, 1978, pp. 585–593.

[23] N. W Hanson and H. W Conner, “Seismic resistance of reinforced concrete beam-column joints,” *Journal of the Structural Division*, vol. 93, no. 5, pp. 533–560, 1967.

[24] R. Park and T. Paulay, “Ductile reinforced concrete frames: Some comments on the special provisions for seismic design of aci 318-71 and on capacity design,” *Bulletin of the New Zealand Society for Earthquake Engineering*, vol. 8, no. 1, pp. 70–90, 1975.

[25] J. Kim and J. M. LaFave, “Joint shear behaviour of reinforced concrete beam-column connections,” *Mag Concr Res*, vol. 61, no. 2, pp. 119–132, 2009.

[26] S.-J. Hwang and H.-J. Lee, “Analytical model for predicting shear strengths of exterior reinforced concrete beam-column joints for sesimic resistance,” *ACI Structural Journal*, vol. 96, pp. 846–857, 1999.

[27] H. Murakami, S. Fujii, Y. Ishiwata, and S. Morita, “Shear strength and deformation capacity of interior r/c beam-column joint subassemblage,” in *Proceedings*, 2000.

[28] FEMA356, “Prestandard and commentary for the seismic rehabilitation of buildings (fema 356),” *ASCE*, 2000.

[29] G. Parra-Montesinos and J. Wight, “Prediction of strength and shear distortion in r/c beam-column joints,” *ACI Special Publications*, vol. 197, pp. 191–214, 2001.

[30] S. A. Attaalla, “General analytical model for nominal shear stress of type 2 normal-and high-strength concrete beam-column joints,” *Structural Journal*, vol. 101, no. 1, pp. 65–75, 2004.

[31] G. Russo and G. Somma, “A design formula for predicting the shear strength of exterior beam column joints under seismic loading,” in *13 th World Conference of Earthquake Engineering*, 2004.

[32] H. Shiohara, “Quadruple flexural resistance in r/c beam-column joints,” in *13th World Conference on Earthquake Engineering*, 2004, p. 491.

[33] B. D. Scott, R. Park, and M. J. Priestley, “Stress-strain behavior of concrete confined by overlapping hoops at low and high strain rates,” in *Journal Proceedings*, vol. 79, 1982, pp. 13–27.

[34] O. Joh, Y. Goto, and T. Shibata, “Influence of transverse joint and beam reinforcement and relocation of plastic hinge region onbeam column joint stiffness deterioration,” *Special Publication*, vol. 123, pp. 187–224, 1991.

[35] ASCE41-17, “Seismic evaluation and retrofit of existing buildings,” American Society of Civil Engineers, 2017.

[36] ACI318-19, “Building code requirements for structural concrete:(aci 318-19) and commentary (aci 318-19),” American Concrete Institute, 2019.

[37] TBDY-2018, *Turkish seismic design code 2018*, Official Gazette of the Republic of Turkey, Published as "Turkish Earthquake Code of Practice for Buildings (TEC-2018)", 2018.

[38] EC8, “Eurocode8: Earthquake resistance design of structures work-ing draft 18.02.2021,” CEN: Bruxelles, Belgium, 2021.

[39] EC8, “Eurocode8: Design of structures for earthquake resistance,” 2004.

[40] NZSEE-17, “The seismic assessment of existing buildings,” 2017.

[41] Y. Higashi and Y. Ohwada, “Failing behaviors of reinforced concrete beam-column connections subjected to lateral load,” *Memoris of Faculty of Technology Tokyo Metropolitan University*, vol. 19, pp. 91–101, 1969.

[42] D. F. Meinheit and J. O. Jirsa, “The shear strength of reinforced concrete beam-column joints,” University of Texas at Austin, Technical Report CESRL Report No. 77-1, 1977.

[43] G. R. Birss, “The elastic behavior of earthquake resistant reinforced concrete interior beam-column joints,” University of Canterbury, New Zealand, Technical Report Research report 78-13, 1978.

[44] C. W. Beckingsale, “Post elastic behavior of reinforced concrete beam-column joints,” PhD Thesis, University of Canterbury, Christchurch, New Zealand, 1980.

[45] R. Park and J. R. Milburn, "Comparison of recent new zealand and united states seismic design provisions for reinforced concrete beam-column joints and test results from four units designed according to the new zealand code," *Bulletin of the New Zealand National Society of Earthquake Engineering*, vol. 16, no. 1, pp. 3–24, 1983.

[46] S. Otani, Y. Kobayashi, and H. Aoyama, *Reinforced concrete interior beam-column joints under simulated earthquake loading*. University of Tokyo, Department of Architecture, 1984.

[47] A. J. Durrani and J. K. Wight, "Behavior of interior beam-to-column connections under earthquake-type loading," in *Journal Proceedings*, vol. 82, 1985, pp. 343–349.

[48] M. Ehsani and J. Wight, "Exterior reinforced concrete beam-to-column connections subjected to earthquake-type loading," in *Journal Proceedings*, vol. 82, 1985, pp. 492–499.

[49] K. Kitayama, S. Otani, and H. Aoyama, "Earthquake resistant design criteria for reinforced concrete interior beam-column joints," in *Pacific Conference on Earthquake Engineering*, Wairakei, New Zealand, 1987, pp. 315–326.

[50] Y. Endoh, T. Kamura, S. Otani, and H. Aoyama, "Behavior of rc beam-column connections using light-weight concrete," *Transactions of Japan Concrete Institute*, vol. 13, pp. 319–326, 1991.

[51] S. Fujii and S. Morita, "Comparison between interior and exterior r/c beam-column joint behavior," *Special Publication*, vol. 123, pp. 145–166, 1991.

[52] T. Kaku and H. Asakusa, "Ductility estimation of exterior beam-column subassemblages in reinforced concrete frames," *Special Publication*, vol. 123, pp. 167–186, 1991.

[53] T. Kaku and H. Asakusa, "Bond and anchorage of bars in reinforced concrete beam-column joints," *Special Publication*, vol. 123, pp. 401–424, 1991.

[54] M. R. Ehsani and F. Alameddine, "Design recommendations for type 2 high-strength reinforced concrete connections," *ACI Structural Journal*, vol. 88, no. 3, pp. 277–291, 1991.

[55] H. Noguchi and T. Kashiwazaki, "Experimental studies on shear performances of rc interior column-beam joints," in *Tenth World Conference on Earthquake Engineering*, Madrid, Spain, 1992, pp. 3163–3168.

[56] K. Oka and H. Shiohara, "Tests on high-strength concrete interior beam-column joint subassemblages," in *Tenth World Conference on Earthquake Engineering*, Madrid, Spain, 1992, pp. 3211–3217.

[57] G. N. Guimaraes, M. E. Kreger, and J. O. Jirsa, "Evaluation of joint-shear provisions for interior beam-column-slab connections using high-strength materials," *Structural Journal*, vol. 89, no. 1, pp. 89–98, 1993.

[58] K. Hayashi, M. Teraoka, A. A. Mollick, and Y. Kanoh, "Bond properties of main reinforcing bars and restoring force characteristics in rc interior beam column subassemblages using high strength materials," in *Proceedings, Second US-Japan-New Zealand-Canada multilateral meeting on structural performance of high strength concrete in seismic regions*, Honolulu, Hawaii, 1994, pp. 15–27.

[59] M. Teraoka, Y. Kanoh, K. Tanaka, and K. Hayashi, "Strength and deformation behavior of rc interior beam-column joint using high strength concrete," in *Proceedings, Second US-Japan-New Zealand-Canada multilateral meeting on structural performance of high strength concrete in seismic regions*, Honolulu, Hawaii, 1994, pp. 1–14.

[60] S. G. Walker, "Seismic performance of existing reinforced concrete beam-column joints," Master's Thesis, University of Washington, Seattle, 2001.

[61] R. Park and D. Ruitong, "A comparison of the behavior of reinforced concrete beam column joints designed for ductility and limited ductility," *Bulletin of the New-Zealand national society for Earthquake Engineering*, vol. 21, no. 4, pp. 255–278, 1988.

[62] S. S. S. Zaid, "Behavior of reinforced concrete beam-column connections under earthquake loading," PhD Thesis, University of Tokyo, Japan, 2001.

[63] H. Shiohara, "New model for shear failure of rc interior beam-column connections," *Journal of Structural Engineering*, 2001.

[64] C. P. Pantelides, C. Clyde, and L. D. Reaveley, "Performance-based evaluation of reinforced concrete building exterior joints for seismic excitation," *Earthquake Spectra*, vol. 18, no. 3, pp. 449–480, 2002.

[65] N. Mitra, "An analytical study of reinforced concrete beam-column joint behavior under seismic loading," PhD Thesis, University of Washington, Seattle, Washington, 2007.

[66] R. D. Cook *et al.*, *Concepts and applications of finite element analysis*. John wiley and sons, 2007.

[67] A. Amirsardari, "Seismic assessment of reinforced concrete buildings in australia including," 2018.

[68] S. El-Metwally and W. Chen, "Moment-rotation modeling of reinforced concrete beam-column connections," *Structural Journal*, vol. 85, no. 4, pp. 384–394, 1988.

[69] S. Alath and S. Kunnath, "Modeling inelastic shear deformation in rc beam-column joints," in *Proceedings of the Tenth Pacific Conference on Earthquake Engineering*, Proceedings of the 10th Engineering Mechanics Conference, Boulder, CO, 1995.

[70] A. Biddah and A. Ghobarah, "Modelling of shear deformation and bond slip in reinforced concrete joints," *Structural Engineering and Mechanics*, vol. 7, no. 4, pp. 413–432, 1999.

[71] T. T. Hsu, "Softened truss model theory for shear and torsion," *Structural Journal*, vol. 85, no. 6, pp. 624–635, 1988.

[72] M. Youssef and A. Ghobarah, "Modelling of rc beam-column joints and structural walls," *Journal of earthquake engineering*, vol. 5, no. 01, pp. 93–111, 2001.

[73] O. C. Celik and B. R. Ellingwood, "Modeling beam-column joints in fragility assessment of gravity load designed reinforced concrete frames," *Journal of Earthquake Engineering*, vol. 12, no. 3, pp. 357–381, 2008.

[74] M. Shin and J. M. LaFave, "Modeling of cyclic joint shear deformation contributions in rc beam-column connections to overall frame behavior," *Structural Engineering and Mechanics*, vol. 18, no. 5, pp. 645–670, 2004.

[75] A. Altoontash, *Simulation and damage models for performance assessment of reinforced concrete beam-column joints*. Stanford university, 2004.

[76] F. McKenna, G. L. Fenves, M. H. Scott, *et al.*, "Open system for earthquake engineering simulation," *University of California, Berkeley, CA*, 2000.

[77] F. Vecchio and M. P. Collins, "The modified compression-field theory for reinforced concrete elements subjected to shear," *ACI Journal*, vol. 83, no. 22, pp. 219–231, 1986.

[78] N. Stevens, S. Uzumeri, and M. Collins, "Reinforced concrete subjected to reversed cyclic shear–experiments and constitutive model," *Structural Journal*, vol. 88, no. 2, pp. 135–146, 1991.

[79] N. Mitra and L. N. Lowes, "Evaluation, calibration, and verification of a reinforced concrete beam–column joint model," *Journal of Structural Engineering*, vol. 133, no. 1, pp. 105–120, 2007.

[80] S. Park and K. M. Mosalam, "Experimental investigation of nonductile rc corner beam-column joints with floor slabs," *Journal of Structural Engineering*, vol. 139, no. 1, pp. 1–14, 2013. DOI: 10.1061/(ASCE)ST.1943-541X.0000591.

[81] S. Park and K. M. Mosalam, "Simulation of reinforced concrete frames with nonductile beam-column joints," *Earthquake Spectra*, vol. 29, no. 1, pp. 233–257, 2013. DOI: 10.1193/1.4000100.

[82] J.-S. Jeon, L. N. Lowes, R. DesRoches, and I. Brilakis, "Fragility curves for non-ductile reinforced concrete frames that exhibit different component response mechanisms," *Engineering Structures*, vol. 85, pp. 127–143, 2015. DOI: 10.1016/j.engstruct.2014.12.009.

[83] W. M. Hassan, "Analytical and experimental assessment of seismic vulnerability of beam-column joints without transverse reinforcement in concrete buildings," Ph.D. dissertation, University of California, Berkeley, Department of Civil and Environmental Engineering, 2011.

[84] W. M. Hassan and J. P. Moehle, "A cyclic nonlinear macro model for numerical simulation of beam-column joints in existing concrete buildings," in *15th World Conference on Earthquake Engineering*, Lisbon, Portugal, 2012.

[85] R. Eligehausen, V. Bertero, and E. Popov, "Local bond stress-slip relationships of deformed bars under generalized excitations: Tests and analytical model," *Earthquake Engineering Research Center, Univ. of California, Berkeley, Calif., Report No. EERC*, pp. 83–23, 1983.

[86] R. Eligehausen, R. Mallee, and J. F. Silva, *Anchorage in concrete construction*. John Wiley and Sons, 2006, vol. 10.

[87] N. M. Hawkins, I. J. Lin, and F. J. Jean, "Local bond strength of concrete for cycle reversed loadings," in *Bond in Concrete*, 1982, pp. 151–161.

[88] S. Y. M. Ma, V. V. Bertero, and E. P. Popov, *Experimental and analytical studies on the hysteretic behavior of reinforced concrete rectangular and T-beams*. Earthquake Engineering Research Center, College of Engineering, University of California, 1976.

[89] J. Walraven, "Rough cracks subjected to earthquake loading," *Journal of Structural Engineering*, vol. 120, no. 5, pp. 1510–1524, 1994.

[90] L. N. Lowes, N. Mitra, and A. Altoontash, *A Beam-Column Joint Model for Simulating the Earthquake Response of Reinforced Concrete Frames*. 2004, vol. 88, p. 421, ISBN: FEMA P-695. DOI: 10.1016/j.compstruc.2009.08.001.

[91] C.-L. Ning, B. Yu, and B. Li, "Beam-column joint model for nonlinear analysis of non-seismically detailed reinforced concrete frame," *Journal of Earthquake Engineering*, vol. 20, no. 3, pp. 476–502, 2016.

[92] P. Sengupta and B. Li, "Modified bouc–wen model for hysteresis behavior of rc beam–column joints with limited transverse reinforcement," *Engineering Structures*, vol. 46, pp. 392–406, 2013.

[93] FEMA-P440A, "Effects of strength and stiffness degradation on seismic response," Washington, DC, Technical Report FEMA-P440A, 2009.

[94] T. Takeda, M. A. Sozen, and N. N. Nielsen, "Reinforced concrete response to simulated earthquakes," *Journal of Structural Division*, vol. 96, no. 12, pp. 2557–2573, 1970.

[95] L. F. Ibarra, R. A. Medina, and H. Krawinkler, "Hysteretic models that incorporate strength and stiffness deterioration," *Earthquake Engineering and Structural Dynamics*, vol. 34, no. 12, pp. 1489–1511, 2005. DOI: 10.1002/eqe.495.

[96] L. Lowes, N. Mitra, and A. Altoontash, "A beam-column joint model for simulating the earthquake response of reinforced concrete frames," Pacific Earthquake Engineering Center, University of California, Berkeley, PEER Report 2003/10, 2004.

[97] R. Leon, "Shear strength and hysteretic behavior of interior beam-column joints," *Struct. J.*, vol. 87, pp. 3–11, 1990.

[98] S. Viwathanatepa, E. P. Popov, and V. V. Bertero, *Effects of generalized loadings on bond of reinforcing bars embedded in confined concrete blocks*. University of California, Earthquake Engineering Research Center, 1979.

[99] H. Shiohara, "New model for shear failure of rc interior beam-column connections," *Journal of Structural Engineering*, vol. 127, no. 2, pp. 152–160, 2001.

[100] C. Xing, I. Koutromanos, R. Leon, and M. Moharrami, "Computational simulation of rc beam-to-column connections under earthquake loading," in *Eleventh US National Conference on Earthquake Engineering*, Los Angeles, CA, USA, 2018.

[101] J.-H. Kim and J. B. Mander, "Truss modeling of reinforced concrete shear–flexure behaviour," Multidisciplinary Center for Earthquake Engineering Research, University at Buffalo, State University of New York, Technical Report 99-0005, 1999.

[102] T. Miki and J. Niwa, "Nonlinear analysis of rc structural members using 3d lattice model," *Journal of Advanced Concrete Technology*, vol. 2, no. 3, pp. 343–358, 2004.

[103] H. J. Park and T. W. Eom, "Truss model for nonlinear analysis of rc members subject to cyclic loading," *Journal of Structural Engineering*, vol. 133, no. 10, pp. 1351–1363, 2007.

[104] M. Panagiotou, J. I. Restrepo, M. Schoettler, and G. Kim, "Nonlinear cyclic truss model for reinforced concrete walls.," *ACI Structural Journal*, vol. 109, no. 2, 2012.

[105] M. Moharrami, I. Koutromanos, M. Panagiotou, and S. C. Girgin, "Analysis of shear-dominated rc columns using the nonlinear truss analogy," *Earthquake Engineering and Structural Dynamics*, vol. 44, no. 5, pp. 677–694, 2015.

[106] J. T. Bowers, "Nonlinear cyclic truss model for beam-column joints of non-ductile rc frames," Ph.D. dissertation, Virginia Tech, 2014.

[107] A. E.-n. Atta, S. E.-d. F. Taher, A.-h. A. Khalil, and S. E.-d. El-metwally, "Behavior of reinforced high strength concrete beam-column joint; part ii: Numerical simulation," *Struct. Concr.*, vol. 5, pp. 101–112, 2004.

[108] R. H. Scott, "Intrinsic mechanisms in reinforced concrete beam-column connection behavior," *ACI Struct. J.*, 1996.

[109] S. M. Allam, H. M. Elbakry, and I. S. Arab, "Exterior reinforced concrete beam column joint subjected to monotonic loading," *Alexandria Eng. J.*, vol. 57, no. 4, pp. 4133–4144, 2018. DOI: 10.1016/j.aej.2018.10.015.

[110] M. Kaliske and I. Zreid, "Objective modeling of multixial softening of concrete," *PAMM*, vol. 18, no. 1, e201800394, 2018.

[111] I. Zreid and M. Kaliske, "A gradient enhanced plasticity–damage microplane model for concrete," *Computational Mechanics*, vol. 62, no. 5, pp. 1239–1257, 2018.

[112] C. E. Chalioris, M. J. Favvata, and C. G. Karayannis, "Reinforced concrete beam-column joints with crossed inclined bars under cyclic deformations," *Earthq. Eng. Struct. Dyn.*, 2008.

[113] J. Ozbolt, V. Li, and R. Eligehausen, "3d cyclic fracture analysis of beam-column connections j," in *Fracture Mechanics of Concrete Structures Proceedings*, 2000, pp. 1523–1536.

[114] M. Yılmaz, A. Demirbağ, and S. Bekiroğlu, "Investigation of reinforced concrete beam-column joint behaviour through numerical simulations," in *International Civil Engineering and Architecture Conference*, Trabzon, Turkey, Apr. 2019.

[115] R. Vonk, "Softening of concrete loaded in compression," Ph.D. dissertation, Technische Universiteit Eindhoven, Eindhoven, the Netherlands, 1992.

[116] P. Grassl, "Modelling the dynamic response of concrete with the damage plasticity model cdpm2," 2019.

[117] ANSYS Mechanical APDL Material Reference, *Mechanical apdl material reference*, Release 19.R1, 2019.

[118] M. Moharrami and I. Koutromanos, "Finite element analysis of damage and failure of reinforced concrete members under earthquake loading," *Earthquake Engineering and Structural Dynamics*, vol. 46, no. 15, pp. 2811–2829, 2017. DOI: 10.1002/eqe.2914.

[119] R. von Mises, "Mechanik der festen körper im plastisch-deformablen zustand," *Nachrichten von der Gesellschaft der Wissenschaften zu Göttingen, Mathematisch-Physikalische Klasse*, pp. 582–592, 1913.

[120] P. Feenstra and R. De Borst, "Constitutive model for reinforced concrete," *Journal of Engineering Mechanics*, vol. 121, no. 5, pp. 587–595, 1995.

[121] D. Drucker and W. Prager, "Soil mechanics and plastic analysis or limit design," *Quarterly of applied mathematics*, vol. 10, no. 2, pp. 157–165, 1952.

[122] M. Jirasek and Z. Bazant, *Inelastic Analysis of Structures*. Chichester, West Sussex, England, UK: John Wiley and Sons, 2002.

[123] Z. P. Bazant, "Instability, ductility, and size effect in strain-softening concrete," *ASCE J Eng Mech Div*, vol. 102, no. 2, pp. 331–344, 1976.

[124] A. Inc., "Element reference, release 2019 r1," ANSYS Inc., Southpointe, PA, Tech. Rep., 2019.

[125] Z. P. Bažant and P. C. Prat, "Microplane model for brittle-plastic material: I. theory," *Journal of Engineering Mechanics*, vol. 114, no. 10, pp. 1672–1688, 1988.

[126] Z. P. Bazant and G. Pijaudier-Cabot, "Measurement of characteristic length of nonlocal continuum," *Journal of Engineering Mechanics*, vol. 115, no. 4, pp. 755–767, 1989.

[127] D. Lehky and D. Novak, "Identification of material model parameters using stochastic training of neural network," *Unknown*, 2004.

[128] L. Ljung, *System Identification—Theory for the User*, second. Upper Saddle River, NJ: PTR Prentice Hall, 1999.

[129] A. Kučerová, "Identification of nonlinear mechanical model parameters based on softcomputing methods," Ph.D. Thesis, Ecole Normale Supérieure de CACHAN, 2007. [Online]. Available: http://tel.archives-ouvertes.fr/tel-00256025/fr.

[130] L. Ingber, "Simulated annealing: Practice versus theory," *Mathematical and Computer Modelling*, vol. 18, no. 11, pp. 29–57, 1993.

[131] D. Goldberg, *Genetic Algorithms in Search, Optimization and Machine Learning*. Addison-Wesley, 1989.

[132] Z. Michalewicz, *Genetic Algorithms + Data Structures = Evolution Programs*, 3rd ed. Springer-Verlag, 1999.

[133] K. Deb, A. Pratap, S. Agarwal, and T. A. M. T. Meyarivan, "A fast and elitist multiobjective genetic algorithm: Nsga-ii," *IEEE Transactions on Evolutionary Computation*, vol. 6, no. 2, pp. 182–197, 2002.

[134] S. W. Mahfoud, "Niching methods for genetic algorithms," Ph.D. dissertation, University of Illinois at Urbana-Champaign, 1995.

[135] G. Maier, M. Bocciarelli, G. Bolzon, and R. Fedele, "Inverse analyses in fracture mechanics," *International Journal of Fracture*, vol. 138, pp. 47–73, 2006.

[136] C. A. C. Coello, "Constraint-handling using an evolutionary multiobjective optimization technique," *Engineering Optimization*, vol. 33, no. 5, pp. 551–570, 2000.

[137] Y. F. Zheng, L. L. Zhang, and J. Zhang, "Parameter identification of consolidation settlement based on multi-objective optimization," in *Geotechnical Safety and Risk V*, 2015, pp. 394–399.

[138] D. Novak and D. Lehky, "Ann inverse analysis based on stochastic small-sample training set simulation," *Engineering Applications of Artificial Intelligence*, vol. 19, no. 7, pp. 731–740, 2006.

[139] E. Fairban, C. Paz, N. Ebecken, and F. Ulm, "Use of neural networks for fitting of fe probabilistic scaling model parameters," *International Journal of Fracture*, vol. 95, pp. 315–324, 1999.

[140] T. Gajewski and T. Garbowski, "Calibration of concrete parameters based on digital image correlation and inverse analysis," *Archives of Civil and Mechanical Engineering*, vol. 14, pp. 170–180, 2014.

[141] L. Guo, S. Li, L. Zhong, L. Guo, and L. Wang, "Inverse analysis of concrete meso-constitutive model parameters considering aggregate size effect," *Science and Engineering of Composite Materials*, vol. 27, no. 1, pp. 397–404, 2020.

[142] F. Kang, X. Liu, J. Li, and H. Li, "Multi-parameter inverse analysis of concrete dams using kernel extreme learning machines-based response surface model," *Engineering Structures*, vol. 256, p. 113 999, 2022.

[143] C. Iacono, L. Sluys, and J. van Mier, "Development of an inverse procedure for parameters estimates of numerical models," in *Proceedings of the Euro-C Conference*, 2003, pp. 259–268.

[144] D. Novak and D. Lehku, "Inverse analysis based on small-sample stochastic training of neural network," in *9th International Conference on Engineering Applications of Neural Networks*, 2005, pp. 155–162.

[145] D. Novak *et al.*, "Virtual stochastic simulation of fiber reinforced concrete experiments," in *Proceedings of First Central European Congress on Concrete Engineering 2005*, Graz, Austria, 2005, pp. 35–38.

[146] A. Kucerova, M. Leps, and J. Zeman, "Soft computing methods for estimation of microplane model parameters," in *Computational Mechanics Conference, WCCM VI in conjunction with APCOM'04*, Tsinghua University Press and Springer, Berlin, Beijing, China, Sep. 2004.

[147] V. Cervenka, D. Novak, D. Lehky, and R. Pukl, "Identification of shear wall failure mode," in *CD-ROM proceedings of 11th International Conference on Fracture, ICF XI*, Torino, Italy, 2005, p. 209.

[148] A. Strauss, D. Lehky, D. Novak, K. Bergmeister, and U. Santa, "Probabilistic response identification and monitoring of concrete structures," in *Third European Conference on Structural Control, 3ECSC*, Vienna University of Technology, Vienna, Austria, 2004.

[149] J. Zhang, C. K. Y. Leung, and S. Xu, "Evaluation of fracture parameters of concrete from bending test using inverse analysis approach," *Materials and structures*, vol. 43, pp. 857–874, 2010.

[150] Q. Peng and W. Liu, "Inverse analysis of related parameters in calculation of concrete drying shrinkage based on ansys design optimization," *Journal of Materials in Civil Engineering*, vol. 25, no. 6, pp. 683–692, 2013.

[151] W. S. McCulloch and W. Pitts, "A logical calculus of the ideas immanent in nervous activity," *Bulletin of Mathematical Biophysics*, vol. 5, no. 4, pp. 115–133, 1943.

[152] F. Rosenblatt, "The perceptron: A probabilistic model for information storage and organization in the brain," *Psychological Review*, vol. 65, no. 6, pp. 386–408, 1958.

[153] B. Widrow and M. E. Hoff, "Adaptive switching circuits," in *IRE WESCON Convention Record*, IEEE, vol. 4, 1960, pp. 96–104.

[154] J. J. Hopfield, "Neural networks and physical systems with emergent collective computational abilities," *Proceedings of the National Academy of Sciences*, vol. 79, no. 8, pp. 2554–2558, 1982.

[155] D. E. Rumelhart, G. E. Hinton, and R. J. Williams, "Learning representations by back-propagating errors," *Nature*, vol. 323, no. 6088, pp. 533–536, 1986.

[156] I. Goodfellow, Y. Bengio, and A. Courville, *Deep Learning*. MIT Press, 2016.

[157] S. Haykin, *Neural Networks and Learning Machines*, 3rd. Pearson, 2009.

[158] C. M. Bishop, *Pattern Recognition and Machine Learning*. Springer, 2006.

[159] X. Glorot, A. Bordes, and Y. Bengio, "Deep sparse rectifier neural networks," in *Proceedings of the 14th International Conference on Artificial Intelligence and Statistics (AISTATS 2011)*, 2011, pp. 315–323.

[160] Y. LeCun, L. Bottou, G. B. Orr, and K.-R. Müller, "Efficient backprop," in *Neural Networks: Tricks of the Trade*, Springer, 1998, pp. 9–50.

[161] D. P. Kingma and J. Ba, "Adam: A method for stochastic optimization," in *Proceedings of the 3rd International Conference on Learning Representations (ICLR 2015)*, 2015.

[162] A. Krizhevsky, I. Sutskever, and G. E. Hinton, "Imagenet classification with deep convolutional neural networks," in *Advances in Neural Information Processing Systems 25 (NIPS 2012)*, 2012, pp. 1097–1105.

[163] R. Collobert and J. Weston, "A unified architecture for natural language processing: Deep neural networks with multitask learning," in *Proceedings of the 25th International Conference on Machine Learning (ICML 2008)*, 2008, pp. 160–167.

[164] E. Guresen, G. Kayakutlu, and T. U. Daim, "Using artificial neural network models in stock market index prediction," *Expert Systems with Applications*, vol. 38, no. 8, pp. 10 389–10 397, 2011.

[165] G. Cybenko, "Approximation by superpositions of a sigmoidal function," *Mathematics of Control, Signals, and Systems*, vol. 2, no. 4, pp. 303–314, 1989.

[166] S. Hochreiter and J. Schmidhuber, "Long short-term memory," *Neural Computation*, vol. 9, no. 8, pp. 1735–1780, 1997.

[167] D. S. Broomhead and D. Lowe, "Multivariable functional interpolation and adaptive networks," *Complex Systems*, vol. 2, no. 3, pp. 321–355, 1988.

[168] J. Moody and C. J. Darken, "Fast learning in networks of locally-tuned processing units," *Neural Computation*, vol. 1, no. 2, pp. 281–294, 1989.

[169] J. Park and I. W. Sandberg, "Universal approximation using radial-basis-function networks," *Neural Computation*, vol. 3, no. 2, pp. 246–257, 1991.

[170] T. Poggio and F. Girosi, "Networks for approximation and learning," *Proceedings of the IEEE*, vol. 78, no. 9, pp. 1481–1497, 1990.

[171] B. Schölkopf and A. J. Smola, *Learning with Kernels: Support Vector Machines, Regularization, Optimization, and Beyond*. MIT Press, 2002.

[172] D. F. Specht *et al.*, "A general regression neural network," *IEEE transactions on neural networks*, vol. 2, no. 6, pp. 568–576, 1991.

[173] T. Kohonen, "Self-organized formation of topologically correct feature maps," *Biological cybernetics*, vol. 43, no. 1, pp. 59–69, 1982.

[174] T. Kohonen, *Self-Organizing Maps*. Springer, 2001.

[175] J. L. Elman, "Finding structure in time," *Cognitive science*, vol. 14, no. 2, pp. 179–211, 1990.

[176] T. Mikolov, M. Karafiat, L. Burget, J. Cernocky, and S. Khudanpur, "Recurrent neural network based language model," in *Eleventh Annual Conference of the International Speech Communication Association*, 2010.

[177] A. Graves, A.-r. Mohamed, and G. Hinton, "Speech recognition with deep recurrent neural networks," *IEEE international conference on acoustics, speech and signal processing*, vol. 2013, pp. 6645–6649, 2013.

[178] J. Chung, C. Gulcehre, K. Cho, and Y. Bengio, "Empirical evaluation of gated recurrent neural networks on sequence modeling," *arXiv preprint arXiv:1412.3555*, 2014.

[179] J. J. Hopfield and D. W. Tank, ""neural" computation of decisions in optimization problems," *Biological cybernetics*, vol. 52, no. 3, pp. 141–152, 1985.

[180] J.-S. Jang, "Anfis: Adaptive-network-based fuzzy inference system," *IEEE transactions on systems, man, and cybernetics*, vol. 23, no. 3, pp. 665–685, 1993.

[181] J.-S. R. Jang, C.-T. Sun, and E. Mizutani, "Neuro-fuzzy and soft computing-a computational approach to learning and machine intelligence [book review]," *IEEE Transactions on automatic control*, vol. 42, no. 10, pp. 1482–1484, 1997.

[182] R. Kohavi, "A study of cross-validation and bootstrap for accuracy estimation and model selection," in *International Joint Conference on Artificial Intelligence*, Morgan Kaufmann Publishers Inc., vol. 14, 1995, pp. 1137–1145.

[183] M. D. McKay, R. J. Beckman, and W. Conover, "Comparison of three methods for selecting values of input variables in the analysis of output from a computer code," *Technometrics*, vol. 21, no. 2, pp. 239–245, 1979.

[184] M. Stein, "Large sample properties of simulations using latin hypercube sampling," *Technometrics*, vol. 29, no. 2, pp. 143–151, 1987.

[185] J. C. Helton and F. J. Davis, "Latin hypercube sampling and the propagation of uncertainty in analyses of complex systems," *Reliability Engineering and System Safety*, vol. 81, no. 1, pp. 23–69, 2002.

[186] Y. Bengio, R. Ducharme, P. Vincent, and C. Janvin, "A neural probabilistic language model," *Journal of Machine Learning Research*, vol. 3, no. Feb, pp. 1137–1155, 2003.

[187] J. H. Holland, *Adaptation in natural and artificial systems*. University of Michigan Press, 1975.

[188] M. Mitchell, *An introduction to genetic algorithms*. MIT Press, 1998.

[189] A. E. Eiben and J. E. Smith, *Introduction to evolutionary computing*. Springer-Verlag, 2003.

[190] K. Deb, *Multi-objective optimization using evolutionary algorithms*. John Wiley & Sons, 2001.

[191] D. E. Goldberg and K. Deb, "A comparative analysis of selection schemes used in genetic algorithms," in *Foundations of Genetic Algorithms*, vol. 1, Morgan Kaufmann, 1991, pp. 69–93.

[192] J. E. Baker, "Adaptive selection methods for genetic algorithms," in *Proceedings of an International Conference on Genetic Algorithms and their Applications*, 1985, pp. 101–111.

[193] K. A. De Jong, "An analysis of the behavior of a class of genetic adaptive systems," Ph.D. dissertation, University of Michigan, 1975.

[194] G. Syswerda, "Uniform crossover in genetic algorithms," in *Proceedings of the Third International Conference on Genetic Algorithms*, 1989, pp. 2–9.

[195] D. E. Goldberg and R. Lingle, "Alleles, loci, and the traveling salesman problem," in *Proceedings of an International Conference on Genetic Algorithms and their Applications*, 1985, pp. 154–159.

[196] I. M. Oliver, D. J. Smith, and J. R. C. Holland, "A study of permutation crossover operators on the traveling salesman problem," in *Genetic Algorithms and their Applications: Proceedings of the Second International Conference on Genetic Algorithms*, 1987, pp. 224–230.

[197] A. Tarantola, *Inverse problem theory and methods for model parameter estimation*. SIAM, 2005.

[198] M. Sambridge and K. Mosegaard, "Monte carlo methods in geophysical inverse problems," *Reviews of Geophysics*, vol. 40, no. 3, pp. 3–1, 2002.

[199] I. Yilmaz and O. Kaynar, "Multiple regression, ann (rbf, mlp) and anfis models for prediction of swell potential of clayey soils," *Expert systems with applications*, vol. 38, no. 5, pp. 5958–5966, 2011.

[200] C. Dong, M. Wang, and J. Yan, "Inverse analysis of material parameters for solid mechanics using hybrid genetic algorithm," *Inverse Problems in Science and Engineering*, vol. 19, no. 3, pp. 323–340, 2011.

[201] C. A. Coello Coello, G. B. Lamont, and D. A. Van Veldhuizen, *Evolutionary Algorithms for Solving Multi-Objective Problems*. Springer, 2007.

[202] M. Ehrgott, *Multicriteria Optimization*. Springer, 2005.

[203] K. Deb, A. Pratap, S. Agarwal, and T. Meyarivan, "A fast and elitist multiobjective genetic algorithm: Nsga-ii," *IEEE Transactions on Evolutionary Computation*, vol. 6, no. 2, pp. 182–197, 2002.

[204] E. Zitzler, M. Laumanns, and L. Thiele, "Spea2: Improving the strength pareto evolutionary algorithm," *TIK-report*, vol. 103, 2001.

[205] Q. Zhang and H. Li, "Moea/d: A multiobjective evolutionary algorithm based on decomposition," *IEEE Transactions on Evolutionary Computation*, vol. 11, no. 6, pp. 712–731, 2007.

[206] E. Zitzler, L. Thiele, M. Laumanns, C. M. Fonseca, and V. G. Da Fonseca, "Performance assessment of multiobjective optimizers: An analysis and review," *IEEE Transactions on evolutionary computation*, vol. 7, no. 2, pp. 117–132, 2003.

[207] J. H. Holland, "Genetic algorithms," *Scientific american*, vol. 267, no. 1, pp. 66–73, 1992.

[208] A. E. Eiben and J. E. Smith, *Introduction to evolutionary computing*. Springer, 2015.

[209] A. I. Forrester, A. Sobester, and A. J. Keane, *Engineering design via surrogate modelling: A practical guide*. John Wiley & Sons, 2008.

[210] T. W. Simpson, J. Peplinski, P. N. Koch, and J. K. Allen, "Metamodels for computer-based engineering design: Survey and recommendations," *Engineering with Computers*, vol. 17, no. 2, pp. 129–150, 2001.

[211] M. C. Kennedy and A. O'Hagan, "Bayesian calibration of computer models," *Journal of the Royal Statistical Society: Series B (Statistical Methodology)*, vol. 63, no. 3, pp. 425–464, 2001.

[212] B. Iooss, L. Boussouf, V. Feuillard, and A. Marrel, "Numerical studies of the metamodel fitting and validation processes," *arXiv preprint arXiv:1001.1049*, 2010.

[213] N. Mitra and L. N. Lowes, "Evaluation and advancement of a reinforced concrete beam-column joint model," in *13th. World Conference on Earthquake Engineering*, Paper No. 1001, Vancouver, B.C., Canada, 2004.

[214] J. Shafaei, M. S. Zareian, A. Hosseini, and M. S. Marefat, "Effects of joint flexibility on lateral response of reinforced concrete frames," *Engineering Structures*, vol. 81, pp. 412–431, 2014.

[215] A. Calabrese, J. P. Almeida, and R. Pinho, "Numerical issues in distributed inelasticity modeling of rc frame elements for seismic analysis," *Journal of Earthquake Engineering*, vol. 14, no. S1, pp. 38–68, 2010.

[216] H. Roh, A. M. Reinhorn, and J. S. Lee, "Power spread plasticity model for inelastic analysis of reinforced concrete structures," *Engineering Structures*, vol. 39, pp. 148–161, 2012.

[217] I. D. Karsan and J. O. Jirsa, "Behavior of concrete under compressive loading," *Journal of the Structural Division*, vol. 95, no. ST12, 1969.

[218] S. Popovics, "A numerical approach to the complete stress strain curve for concrete," *Cement and Concrete Research*, vol. 3, no. 5, pp. 583–599, 1973.

[219] M. Menegotto and P. Pinto, "Method of analysis for cyclically loaded r.c. plane frames including changes in geometry and non-elastic behavior of elements under combined normal force and bending," in *Symposium on the Resistance and Ultimate Deformability of Structures Acted on by Well Defined Repeated Loads*, International Association for Bridge and Structural Engineering, Zurich, Switzerland, 1973, pp. 15–22.

[220] F. Filippou, E. Popov, and V. Bertero, "Effects of bond deterioration on hysteretic behavior of reinforced concrete joints," Earthquake Engineering Research Center, University of California, Berkeley, California, USA, Tech. Rep. UCB/EERC-83/19, 1983.

[221] Z. Yang, C. Li, L. Liu, H. Yang, and T. Zhong, "Study on modeling method of reinforced concrete pier based on opensees," in *Journal of Physics: Conference Series*, IOP Publishing, vol. 1838, 2021, p. 012 034.

[222] S. Mazzoni, F. McKenna, M. H. Scott, and G. L. Fenves, *The open system for earthquake engineering simulation (opensees) user command-language manual*, 2006.

[223] W. Kassem, "Strut-and-tie modelling for the analysis and design of RC beam-column joints," *Materials and Structures*, vol. 49, no. 8, pp. 3459–3476, 2016.

[224] G. Genesio, "Seismic assessment of RC exterior beam-column joints and retrofit with haunches using post-installed anchors," 2012.

[225] L. Megget, "Cyclic behaviour of exterior reinforced concrete beam-column joints," *Bull. N. Zeal. Natl. Soc. Earthq. Eng.*, vol. 7, pp. 22–47, 1974.

[226] O. Joh, Y. Goto, and T. Shibata, "Shear resistance performance in rc exterior beam-column connection using high strength materials," *Proc. Jpn. Concrete Inst.*, vol. 14, pp. 391–395, 1992.

[227] K. Kitayama, S. Otani, and H. Aoyama, "Develop of design criteria for rc interior beam-column joints," in *Design of Beam-Column Joints for Seismic Resistance*, 1991, pp. 145–165.

[228] Y. Kurose, G. Guimaraes, L. Zuhua, M. Kreger, and J. Jirsa, "Evaluation of slab-beam-column connections subjected to bidirectional loading," *Spec. Publ.*, vol. 123, pp. 39–68, 1991.

[229] D. Meinheit and J. Jirsa, "Shear strength of r/c beam-column connections," *J. Struct. Div.*, vol. 107, pp. 2227–2244, 1981.

[230] K. Kitayama, S. Lee, S. Otani, and H. Aoyama, "Behavior of high-strength r/c beam-column joints," in *Tenth World Conference of Earthquake engineering*, Balkana, Rotterdam, 1992.

[231] H. Tsubosaki, H. Shiohara, K. Oka, and J. Furukawa, “Evaluation of slab-beam-column joints subjected to bi-directional loading,” in *Proceedings of Architectural Institute of Japan*, 1993.

[232] G. Raffaelle and J. Wight, “Reinforced concrete eccentric beam-column connections subjected to earthquake-type loading,” *Struct. J.*, vol. 92, pp. 45–55, 1995.

[233] Y. Goto and O. Joh, “An experimental study of shear failure mechanism of rc interior beam-column joints,” in *11th World Conference on Earthquake Engineering*, 1996.

[234] K. Ishida, S. Fujii, S. Morita, and G. Choi, “Shear strength of exterior beam column connection under bi-axial earthquake loading,” *Proc. Jpn. Concrete Inst.*, vol. 18, pp. 953–958, 1996.

[235] M. Yoshino, S. Takeda, and T. Kamimura, “Behavior of interior rc beam-column connections after yielding of longitudinal beam reinforcement,” *Proc. Jpn. Concrete Inst.*, vol. 19, pp. 987–992, 1997.

[236] K. Suzuki and et al., “Experimental study on seismic performance of the rc eccentric beam-column joint,” in *Proceedings of Architectural Institute of Japan*, 2002.

[237] Y. Goto and O. Joh, “Shear resistance of rc interior eccentric beam-column joints,” in *13th World Conference on Earthquake Engineering*, 2004, pp. 1–6.

[238] S. Teng and H. Zhou, “Eccentric reinforced concrete beam-column joints subjected to cyclic loading,” *Struct. J.*, 2004.

[239] F. Kusuhara, K. Azukawa, H. Shiohara, and S. Otani, “Tests of reinforced concrete interior beam-column joint subassemblage with eccentric beams,” in *13th World Conference on Earthquake Engineering*, Vancouver, BC, Canada, 2004.

[240] S. Morita, K. Kitayama, S. Kishida, and T. Nishikawa, “Shear force and capacity in reinforced concrete beam-column joints with good bond along beam and column bars,” in *13th World Conference on Earthquake Engineering*, 2004.

[241] K. Watanabe, K. Abe, J. Murakawa, and H. Noguchi, “Strength and deformation of reinforced concrete interior beam-column joints,” *Trans. Jpn. Concrete Inst.*, vol. 10, pp. 183–188, 1988.

[242] H. Noguchi and K. Kurusu, “Correlation of bond and shear in rc beam-column connections subjected to seismic forces,” in *9th World Conference on Earthquake Engineering*, 1988, pp. 597–602.

[243] O. Joh, Y. Goto, and T. Shibata, “Influence of joint reinforcement to shear resistance characteristic in rc exterior beam column connection,” *Proc. Jpn. Concrete Inst.*, vol. 11, pp. 537–542, 1989.

[244] O. Joh, Y. Goto, and T. Shibata, “Behavior of reinforced concrete beam-column joints with eccentricity,” *Spec. Publ.*, vol. 123, pp. 317–358, 1991.

[245] O. Joh, Y. Goto, and T. Shibata, “Shear resistance characteristic of exterior beam column connection using high strength concrete,” *Proc. Jpn. Concrete Inst.*, vol. 12, pp. 639–644, 1990.

[246] M. O. Yilmaz, *GRNN Predictor for Joint Strain-Stress Curves*, https://www.mathworks.com/matlabcentral/fileexchange/80302-grnn-predictor-for-joint-strain-stress-curves, Accessed: 18.06.2023, 2020.

[247] C. Steinke, I. Zreid, W. Graf, and M. Kaliske, "Zur fortentwicklung des microplane-modells für die numerische analyse von betonstrukturen," *Bautechnik*, vol. 96, no. 5, pp. 415–423, 2019.

[248] C. A. L. Fernandes, "Cyclic behaviour of rc elements with plain reinforcing bars," Ph.D. dissertation, Universidade de Aveiro (Portugal), 2012.

[249] J.-Y. Lee, J.-Y. Kim, and G.-J. Oh, "Strength deterioration of reinforced concrete beam–column joints subjected to cyclic loading," *Engineering Structures*, vol. 31, no. 9, pp. 2070–2085, 2009.

[250] P. Alaee and B. Li, "High-strength concrete interior beam-column joints with high-yield-strength steel reinforcements," *Journal of Structural Engineering*, vol. 143, no. 7, p. 04 017 038, 2017.

[251] C. P. Pantelides, Y. Okahashi, and L. Reaveley, "Seismic rehabilitation of reinforced concrete frame interior beam-column joints with frp composites," *Journal of composites for construction*, vol. 12, no. 4, pp. 435–445, 2008.

[252] A. Liu, "Seismic assessment and retrofit of pre-1970s reinforced concrete frame structures," 2001.

[253] H. Noguchi and K. Kurusu, "Correlation of bond and shear in rc beam-column connections subjected to seismic forces," in *Proceedings of the 9th world conference on earthquake engineering. Tokyo-Kyoto, Japan*, 1988, pp. 597–602.

[254] R. Dhakal and T.-C. Pan, "Cyclic behavior of interior beam-column connections in non-seismic rc frames at different loading rates," 2006.

[255] X. Z. Xin, R. Park, and H. Tanaka, *Behaviour of Reinforced Concrete Interior Beam-column Joints Designed Using High Strength Concrete and Steel: A Research Report*. Department of Civil Engineering, University of Canterbury, 1992.

[256] G. S. RaffaelleE and J. K. Wight, "Reinforced concrete eccentric beam-column connections subjected to earthquake-type loading," *Structural Journal*, vol. 92, no. 1, pp. 45–55, 1995.

[257] Y. Kurose, K. Nagami, and Y. Saito, "Beam-column joints in precast concrete construction in japan," *Special Publication*, vol. 123, pp. 493–514, 1991.

[258] F. Kusuhara and H. Shiohara, "Tests of r/c beam-column joint with variant boundary conditions and irregular details on anchorage of beam bars," in *The 14th World conference on earthquake engineering October*, 2008, pp. 12–17.

[259] M. Ehsani and J. Wight, "Exterior reinforced concrete beam-to-column connections subjected to earthquake-type loading," *ACI J.*, vol. 82, pp. 492–499, 1985.

[260] M. Ehsani, A. Moussa, and C. Valenilla, "Comparison of inelastic behavior of reinforced ordinary-and high-strength concrete frames," *Structural Journal*, vol. 84, no. 2, pp. 161–169, 1987.

[261] N. Chutarat and R. S. Aboutaha, "Cyclic response of exterior reinforced concrete beam-column joints reinforced with headed bars—experimental investigation," *Structural Journal*, vol. 100, no. 2, pp. 259–264, 2003.

[262] H. B. Celikoglu, "Application of radial basis function and generalized regression neural networks in non-linear utility function specification for travel mode choice modelling," *Mathematical and Computer Modelling*, vol. 44, no. 5-6, pp. 640–658, 2006.

[263] H. K. Cigizoglu and M. Alp, "Generalized regression neural network in modelling river sediment yield," *Advances in Engineering Software*, vol. 37, no. 1, pp. 63–70, 2006.

[264] A. Auger, D. Brockhoff, N. Hansen, D. Tušar, T. Tušar, and T. Wagner, "Benchmarking matlab's gamultiobj (nsga-ii) on the bi-objective bbob-2016 test suite," in *Proceedings of the 2016 on Genetic and Evolutionary Computation Conference Companion*, 2016, pp. 1233–1239.

[265] E. Zitzler, K. Deb, and L. Thiele, "Comparison of multiobjective evolutionary algorithms: Empirical results," *Evolutionary computation*, vol. 8, no. 2, pp. 173–195, 2000.

[266] Y. Liu, J. Wei, X. Li, and M. Li, "Generational distance indicator-based evolutionary algorithm with an improved niching method for many-objective optimization problems," *IEEE Access*, vol. 7, pp. 63 881–63 891, 2019.

[267] K. Deb and H. Jain, "An evolutionary many-objective optimization algorithm using reference-point-based nondominated sorting approach, part i: Solving problems with box constraints," *IEEE transactions on evolutionary computation*, vol. 18, no. 4, pp. 577–601, 2013.

[268] A. Kaku, K. Maso, T. Kutoka, and T. Muguruma, "Experimental study about deformation characteristic of beam column connection in rc structure," *Proc. Jpn. Concrete Inst.*, vol. 15, pp. 559–564, 1993.

[269] Y. Ishikawa and T. Kamimura, "Experimental study on shear resistance of rc interior beam-column connections," *Vol. 12 of Proc., Japan Concrete Institute*, pp. 669–674, 1990.

[270] K. Oka and H. Shiohara, "Tests of high-strength concrete interior beam-column joint subassemblages," in *Proceedings of the 10th World Conference on Earthquake Engineering*, 1992, pp. 3211–3217.

[271] Y. Goto and O. Joh, "Experimental study on shear resistance of rc interior eccentric beam-column joints," in *9th East Asia-Pacific Conference on Structural Engineering and Construction*, 2003.

A
EXPERIMENTAL DATABASES

In this appendix chapter, experimental database collected from the available literature are presented. In Table A.1, database used for generalized regression neural network training and validation is shown. The sub-assemblages in this collection include only experimental studies which reported joint shear strain versus shear stress in an explicit form. Further details are given in Chapter 4. The same database, with addition of reinforced concrete panel test carried out by Vecchio and Collins [77] is used in calibration and validation of the method introduced in Chapter 5.

The second collection of experimental studies is presented in Table A.2 and Table A.3, indicating the joint and column properties of the sub-assemblages and beam configuration in respective order. In this database, all the sub-assemblages are subjected to cyclic loads at least 5% drift ratio and their overall response are reported in the cited references. The experimental results are used to evaluate and minimize the error based on the defined criteria according to the method introduced in Chapter 6 through the simulation framework introduced in Chapter 3.

Table A.1 Experimental Database

Ref	Unit	Joint Type	# TB	fcj	fyj	sj	rhoj	bj	fcb	fyb	rhob	hb	bb	fcc	fyc	rhoc	hc	bc	n	Failure Type
Meinheit and Jirsa [229]	12	INT	0	35.2	423	51	0.024	305	35.2	449	0.022	457	279	35.2	449	0.043	457	330	0.3	BJ
Watanabe *et al.* [241]	WJ-1	INT	0	29	364	36	0.013	250	29	326	0.008	300	200	29	358	0.026	300	300	0.07	BJ
Watanabe *et al.* [241]	WJ-3	INT	0	29	364	36	0.013	250	29	364	0.008	300	200	29	373	0.026	300	300	0.07	BJ
Leon [97]	BCJ2	INT	0	27.6	414	51	0.005	229	27.6	414	0.009	305	203	27.6	414	0.028	254	254	0	BJ
Leon [97]	BCJ3	INT	0	27.6	414	51	0.004	254	27.6	414	0.009	305	203	27.6	414	0.023	254	305	0	BJ
Noguchi and Kashiwazaki [55]	OKJ-1	INT	0	70	955	50	0.009	250	70	718	0.023	300	200	70	718	0.028	300	300	0.12	BJ
Noguchi and Kashiwazaki [55]	OKJ-4	INT	0	70	955	50	0.009	250	70	718	0.018	300	200	70	718	0.028	300	300	0.12	BJ
Goto and Joh [233]	BJ-PH	INT	0	30.5	326	40	0.009	250	30.5	395	0.014	350	200	30.5	640	0.031	300	300	0.17	BJ
Kaku *et al.* [268]	J11A	INT	0	57.6	893	86	0.005	280	57.6	371	0.022	350	260	57.6	371	0.033	400	300	0.24	BJ
Kaku *et al.* [268]	J12A	INT	0	56.6	893	86	0.005	280	56.6	371	0.03	350	260	56.6	371	0.033	400	300	0.25	BJ
Kaku *et al.* [268]	J32A	INT	0	55.2	893	65	0.006	280	55.2	363	0.032	350	260	55.2	371	0.033	400	300	0.25	BJ
Ishikawa and Kamimura [269]	No.3	INT	0	23.3	330	50	0.01	215	23.3	373	0.016	250	180	23.3	373	0.032	250	250	0.18	BJ
Kitayama *et al.* [227]	B2	INT	0	24.5	235	54	0.003	250	24.5	371	0.021	300	200	24.5	351	0.035	300	300	0.08	BJ
Meinheit and Jirsa [229]	13	INT	0	41.3	409	51	0.015	305	41.3	449	0.022	457	279	41.3	449	0.043	457	330	0.25	J
Meinheit and Jirsa [229]	14	INT	0	33.2	409	51	0.011	432	33.2	449	0.015	457	406	33.2	438	0.043	330	457	0.32	J
Watanabe *et al.* [241]	WJ-6	INT	0	29	364	36	0.013	250	29	358	0.012	300	200	29	373	0.04	300	300	0.07	BJ
Fujii and Morita [51]	A1	INT	0	40.2	291	52	0.005	190	40.2	1069	0.017	250	160	40.2	643	0.042	220	220	0.08	J
Noguchi and Kashiwazaki [55]	OKJ-5	INT	0	70	955	50	0.009	250	70	718	0.025	300	200	70	718	0.034	300	300	0.12	J
Noguchi and Kashiwazaki [55]	OKJ-6	INT	0	53.5	955	50	0.009	250	53.5	718	0.02	300	200	53.5	718	0.028	300	300	0.12	J
Morita *et al.* [240]	M1	INT	0	17.1	344	80	0.003	300	17.1	520	0.019	400	300	17.1	520	0.059	350	300	0	J
Oka and Shiohara [270]	J-10	INT	0	39.2	598	50	0.004	270	39.2	687	0.019	300	240	39.2	687	0.034	300	300	0.12	J
Megget [225]	Unit A	EXT	0	22.1	317	50	0.016	293	22.1	374	0.017	460	255	22.1	365	0.025	380	330	0.07	BJ
Ehsani and Wight [259]	3B	EXT	0	40.9	437	84	0.017	279	40.9	331	0.018	480	259	40.9	490	0.025	300	300	0.06	BJ
Ehsani and Alameddine [54]	LH8	EXT	0	55.8	437	61	0.02	337	55.8	437	0.019	508	318	55.8	437	0.028	356	356	0.04	BJ
Ehsani and Alameddine [54]	HH8	EXT	0	55.8	437	61	0.02	337	55.8	437	0.019	508	318	55.8	437	0.032	356	356	0.07	BJ
Joh *et al.* [226]	NRC-J13	EXT	0	79.4	770	36	0.006	225	79.4	698	0.025	250	200	79.4	698	0.024	250	250	0.02	BJ
Ehsani and Alameddine [54]	LL8	EXT	0	55.8	437	102	0.012	337	55.8	437	0.015	508	318	55.8	437	0.028	356	356	0.04	BJ
Ehsani and Wight [259]	2B	EXT	0	35	437	99	0.015	279	35	331	0.02	439	259	35	490	0.032	300	300	0.07	J
Joh *et al.* [243]	HO-NO	EXT	0	29.6	380	38	0.004	275	29.6	606	0.024	350	200	29.6	581	0.025	260	350	0.02	J
Joh *et al.* [243]	MM-NO	EXT	0	27.8	380	38	0.004	275	27.8	606	0.024	350	200	27.8	581	0.028	260	350	0.02	J
Joh *et al.* [243]	HH-NO	EXT	0	29.3	380	38	0.004	275	29.3	606	0.024	350	200	29.3	581	0.025	260	350	0.02	J
Joh *et al.* [243]	H'O-NO	EXT	0	31.5	380	38	0.004	275	31.5	606	0.024	350	200	31.5	581	0.025	260	350	0.02	J
Joh *et al.* [243]	HH-N96	EXT	0	30.5	380	38	0.004	275	30.5	606	0.024	350	200	30.5	581	0.034	260	350	0.31	J
Joh *et al.* [245]	NRC-J1	EXT	0	51.5	815	36	0.006	225	51.5	1091	0.032	250	200	51.5	1091	0.024	250	250	0.02	J

Continued on next page

Table A.1 Experimental Database – (continued from previous page)

Ref	Unit	Joint Type	# TB	fcj	fyj	sj	rhoj	bj	fcb	fyb	rhob	hb	bb	fcc	fyc	rhoc	hc	bc	n	Failure Type
Ishida *et al.* [234]	A0	EXT	0	27	271	50	0.005	190	27	700	0.015	250	160	27	700	0.031	220	220	0.15	J
Ishida *et al.* [234]	A0F	EXT	0	27	271	50	0.005	190	27	467	0.015	250	160	27	467	0.031	220	220	0.15	BJ
Ehsani and Alameddine [54]	HL8	EXT	0	55.8	437	102	0.012	337	55.8	437	0.019	508	318	55.8	437	0.032	356	356	0.07	J
Joh *et al.* [226]	NRC-J2	EXT	0	81.8	815	36	0.006	225	81.8	1091	0.032	250	200	81.8	1091	0.024	250	250	0.02	J
Joh *et al.* [226]	NRC-J4	EXT	0	88.9	815	36	0.006	225	88.9	1091	0.032	250	200	88.9	1091	0.024	250	250	0.3	J
Kurose *et al.* [228]	J1	INT	0	24.1	550	102	0.007	457	24.1	463	0.011	508	406	24.1	463	0.024	508	508	0	BJ
Kurose *et al.* [228]	J3N	INT	1	27.6	409	152	0.008	305	27.6	463	0.02	457	279	27.6	459	0.051	457	330	0	BJ
Shin and LaFave [74]	SL4	INT	1	31.2	448	64	0.012	279	31.2	510	0.008	406	279	31.5	503	0.026	368	279	0	BJ
Meinheit and Jirsa [229]	8	INT	2	33.1	409	152	0.005	305	33.1	449	0.022	457	279	33.1	449	0.043	457	330	0.32	BJ
Kurose *et al.* [228]	J2E	INT	2	27.6	409	152	0.008	305	27.6	463	0.028	457	279	27.6	459	0.068	457	330	0	BJ
Guimaraes *et al.* [57]	J4	INT	2	31.6	550	102	0.008	457	31.6	463	0.01	508	406	29.1	523	0.04	508	508	0	BJ
Guimaraes *et al.* [57]	J5	INT	2	77.9	550	102	0.008	457	77.9	561	0.023	508	406	95.1	543	0.063	508	508	0	BJ
Guimaraes *et al.* [57]	J6	INT	2	92.1	570	64	0.016	457	92.1	523	0.019	508	406	70.3	561	0.063	508	508	0	BJ
Tsubosaki *et al.* [231]	J12NS	INT	2	60.3	800	50	0.004	270	60.3	711	0.02	320	240	60.3	973	0.044	300	300	0.29	BJ
Kurose *et al.* [228]	J3E	EXT	2	27.6	409	152	0.008	305	27.6	459	0.029	457	279	27.6	459	0.051	457	330	0	BJ
Goto and Joh [237]	HM-125	INT	0	28.9	411	50	0.003	325	28.9	413	0.016	350	200	28.9	379	0.018	300	450	0.17	BJ
Goto and Joh [237]	HH-125	INT	0	31.4	411	32	0.004	325	31.4	413	0.016	350	200	31.4	379	0.018	300	450	0.17	BJ
Goto and Joh [237]	HU-125	INT	0	22.2	355	24	0.005	325	22.2	408	0.016	350	200	22.2	388	0.017	300	450	0.17	BJ
Teng and Zhou [238]	S2	INT	0	34	440	75	0.008	300	34	510	0.014	400	200	34	530	0.031	300	400	0.11	BJ
Teng and Zhou [238]	S3	INT	0	35	440	75	0.008	300	35	510	0.014	400	200	35	530	0.031	300	400	0.11	BJ
Teng and Zhou [238]	S5	INT	0	39	440	50	0.012	300	39	425	0.009	400	200	39	530	0.047	200	400	0.11	BJ
Teng and Zhou [238]	S6	INT	0	38	440	50	0.012	300	38	425	0.009	400	200	38	530	0.047	200	400	0.11	BJ
Kusuhara *et al.* [239]	JE-55S	INT	0	27	364	37	0.009	250	27	387	0.016	300	180	27	345	0.023	280	320	0	BJ
Raffaelle and Wight [232]	1	INT	0	28.6	476	89	0.008	305	28.6	441	0.01	381	254	28.6	441	0.018	356	356	0.02	BJ
Raffaelle and Wight [232]	2	INT	0	26.8	476	89	0.008	267	26.8	441	0.009	381	178	26.8	441	0.018	356	356	0.03	BJ
Raffaelle and Wight [232]	3	INT	0	37.7	476	89	0.008	273	37.7	441	0.009	381	191	37.7	441	0.018	356	356	0.02	BJ
Raffaelle and Wight [232]	4	INT	0	19.3	476	89	0.008	273	19.3	441	0.006	559	191	19.3	441	0.018	356	356	0.04	BJ
Shin and LaFave [74]	SL1	INT	1	29.9	448	79	0.006	368	29.9	503	0.008	406	279	35.8	538	0.015	330	457	0	BJ
Shin and LaFave [74]	SL2	INT	1	36.2	448	79	0.006	318	36.2	503	0.012	406	178	40.7	538	0.015	330	457	0	BJ
Meinheit and Jirsa [229]	6	INT	0	36.7	409	152	0.005	305	36.7	449	0.022	457	279	36.7	449	0.043	457	330	0.48	BJ
Noguchi and Kurusu [242]	No2	INT	0	34.1	354	150	0.001	250	34.1	325	0.015	300	200	34.1	388	0.023	300	300	0.06	BJ
Noguchi and Kurusu [242]	No4	INT	0	34.1	354	150	0.001	250	34.1	388	0.012	300	200	34.1	388	0.023	300	300	0.06	BJ
Joh *et al.* [244]	JXO-B1	INT	0	21.3	307	88	0.002	225	21.3	371	0.008	350	150	21.3	371	0.011	300	300	0.16	BJ
Kitayama *et al.* [230]	I3	INT	0	41.4	360	75	0.004	250	41.4	799	0.024	300	200	41.4	361	0.035	300	300	0.03	BJ
Goto and Joh [233]	BJ-PL	INT	0	29.7	326	50	0.004	250	29.7	395	0.014	350	200	29.7	640	0.031	300	300	0.17	BJ

Continued on next page

Table A.1 Experimental Database – (continued from previous page)

Ref	Unit	Joint Type	# TB	fcj	fyj	sj	rhoj	bj	fcb	fyb	rhob	hb	bb	fcc	fyc	rhoc	hc	bc	n	Failure Type
Yoshino *et al.* [235]	1	INT	0	28.6	420	50	0.005	215	28.6	382	0.013	250	180	28.6	379	0.025	250	250	0.16	BJ
Yoshino *et al.* [235]	3	INT	0	28.6	420	50	0.005	215	28.6	379	0.016	250	180	28.6	379	0.025	250	250	0.16	BJ
Yoshino *et al.* [235]	4	INT	0	28.6	420	50	0.005	215	28.6	379	0.011	250	180	28.6	379	0.025	250	250	0.16	BJ
Suzuki and al. [236]	E00	INT	0	24	358	100	0.004	315	24	384	0.018	500	230	24	384	0.014	500	400	0.25	J
Teng and Zhou [238]	S1	INT	0	33	440	75	0.008	300	33	510	0.014	400	200	33	530	0.031	300	400	0.11	BJ
Kusuhara *et al.* [239]	JE-0	INT	0	27	364	74	0.003	250	27	387	0.016	300	180	27	345	0.023	280	320	0	BJ
Meinheit and Jirsa [229]	1	INT	0	26.2	409	152	0.005	305	26.2	449	0.022	457	279	26.2	457	0.021	457	330	0.4	J
Meinheit and Jirsa [229]	2	INT	0	41.8	409	152	0.005	305	41.8	449	0.022	457	279	41.8	449	0.043	457	330	0.25	J
Meinheit and Jirsa [229]	3	INT	0	26.6	409	152	0.005	305	26.6	449	0.022	457	279	26.6	402	0.067	457	330	0.39	J
Meinheit and Jirsa [229]	4	INT	0	36.1	409	152	0.004	432	36.1	449	0.015	457	406	36.1	438	0.043	330	457	0.3	J
Meinheit and Jirsa [229]	5	INT	0	35.9	409	152	0.005	305	35.9	449	0.022	457	279	35.9	449	0.043	457	330	0.04	J
Meinheit and Jirsa [229]	7	INT	0	37.2	409	152	0.004	432	37.2	449	0.015	457	406	37.2	438	0.043	330	457	0.47	J
Endoh *et al.* [50]	A1	INT	0	30.6	320	45	0.006	250	30.6	780	0.02	300	200	30.6	539	0.035	300	300	0.06	J
Fujii and Morita [51]	A1	INT	0	40.2	291	52	0.005	190	40.2	1069	0.017	250	160	40.2	643	0.042	220	220	0.08	J
Fujii and Morita [51]	A2	INT	0	40.2	291	52	0.005	190	40.2	409	0.016	250	160	40.2	387	0.042	220	220	0.08	J
Fujii and Morita [51]	A3	INT	0	40.2	291	52	0.005	190	40.2	1069	0.017	250	160	40.2	643	0.042	220	220	0.23	J
Goto and Joh [237]	UM-0	INT	0	24	355	50	0.003	325	24	697	0.018	350	200	24	388	0.02	300	450	0.17	J
Kaku and Asakusa [53]	3	EXT	0	41.7	250	52	0.005	190	41.7	381	0.016	220	160	41.7	360	0.016	220	220	0	BJ
Kaku and Asakusa [53]	5	EXT	0	36.7	281	52	0.001	190	36.7	381	0.016	220	160	36.7	360	0.016	220	220	0.09	BJ
Kaku and Asakusa [53]	6	EXT	0	40.4	281	52	0.001	190	40.4	381	0.016	220	160	40.4	360	0.016	220	220	0	BJ
Kaku and Asakusa [53]	9	EXT	0	40.6	250	52	0.005	190	40.6	381	0.016	220	160	40.6	395	0.018	220	220	0	BJ
Kaku and Asakusa [53]	11	EXT	0	41.9	281	52	0.001	190	41.9	381	0.016	220	160	41.9	395	0.018	220	220	0.08	BJ
Kaku and Asakusa [53]	12	EXT	0	35.1	281	52	0.001	190	35.1	381	0.016	220	160	35.1	395	0.018	220	220	0	BJ
Kaku and Asakusa [53]	14	EXT	0	41	281	52	0.001	190	41	381	0.016	220	160	41	381	0.016	220	220	0.08	BJ
Kaku and Asakusa [53]	15	EXT	0	39.7	281	52	0.001	190	39.7	381	0.016	220	160	39.7	381	0.016	220	220	0.08	BJ
Fujii and Morita [51]	B2	EXT	0	30	291	52	0.005	190	30	409	0.016	250	160	30	387	0.031	220	220	0.07	J
Joh *et al.* [243]	NRC-J12	EXT	0	83.7	717	42	0.002	225	83.7	698	0.025	250	200	83.7	698	0.024	250	250	0.02	BJ
Joh *et al.* [243]	LO-NO	EXT	0	27.9	380	110	0.001	275	27.9	606	0.024	350	200	27.9	581	0.025	260	350	0.02	J
Joh *et al.* [243]	LO-N96	EXT	0	31.5	380	100	0.002	275	31.5	606	0.024	350	200	31.5	581	0.034	260	350	0.3	J
Fujii and Morita [51]	B1	EXT	0	30	291	52	0.005	190	30	1069	0.017	250	160	30	387	0.031	220	220	0.07	J
Fujii and Morita [51]	B3	EXT	0	30	291	52	0.005	190	30	1069	0.017	250	160	30	387	0.031	220	220	0.24	J
Joh *et al.* [226]	NRC-J8	EXT	0	53.7	717	42	0.002	225	53.7	675	0.025	250	200	53.7	675	0.028	250	250	0.02	J
Meinheit and Jirsa [229]	9	INT	2	31	409	152	0.005	305	31	449	0.022	457	279	31	449	0.043	457	330	0.35	J
Meinheit and Jirsa [229]	10	INT	2	29.6	409	152	0.005	305	29.6	449	0.022	457	279	29.6	449	0.043	457	330	0.36	J
Meinheit and Jirsa [229]	11	INT	2	25.6	409	152	0.004	432	25.6	449	0.015	457	406	25.6	438	0.043	330	457	0.42	J

Continued on next page

Table A.1 Experimental Database – (continued from previous page)

Ref	Unit	Joint Type	# TB	fcj	fyj	sj	rhoj	bj	fcb	fyb	rhob	hb	bb	fcc	fyc	rhoc	hc	bc	n	Failure Type
Goto and Joh [271]	LM-60	INT	0	26.4	411	50	0.003	325	26.4	396	0.016	350	200	26.4	379	0.018	300	450	0.17	BJ
Goto and Joh [271]	LM-125	INT	0	26	411	50	0.003	325	26	396	0.012	350	200	26	379	0.018	300	450	0.17	BJ
Goto and Joh [271]	HM-60	INT	0	24.3	411	50	0.003	325	24.3	396	0.02	350	200	24.3	379	0.018	300	450	0.17	BJ
Kusuhara *et al.* [239]	JE-55	INT	0	27	364	74	0.003	250	27	387	0.016	300	180	27	345	0.023	280	320	0	BJ
Suzuki and al. [236]	E085	INT	0	23	358	100	0.004	315	23	384	0.018	500	230	23	384	0.014	500	400	0.25	J
Suzuki and al. [236]	E135	INT	0	22.7	358	100	0.003	365	22.7	384	0.013	450	230	22.7	384	0.019	300	500	0.25	J
Goto and Joh [237]	UM-60	INT	0	24.6	355	50	0.003	325	24.6	697	0.018	350	200	24.6	388	0.02	300	450	0.17	J
Goto and Joh [237]	UM-125	INT	0	25.2	355	50	0.003	325	25.2	697	0.018	350	200	25.2	388	0.02	300	450	0.17	J
Goto and Joh [237]	UU-125	INT	0	25.4	355	24	0.005	325	25.4	697	0.018	350	200	25.4	388	0.02	300	450	0.17	BJ
Walker [60]	PEER14	INT	0	31.8	31.8	508	0	406	31.8	423	0.009	508	406	31.8	423	0.014	457	406	0.11	BJ
Walker [60]	CD1514	INT	0	29.8	29.8	508	0	406	29.8	423	0.009	508	406	29.8	423	0.014	457	406	0.12	BJ
Walker [60]	CD3014	INT	0	42.5	42.5	508	0	406	42.5	423	0.009	508	406	42.5	423	0.014	457	406	0.08	BJ
Walker [60]	PADH14	INT	0	42.9	42.9	508	0	406	42.9	423	0.009	508	406	42.9	423	0.014	457	406	0.09	BJ
Walker [60]	PEER22	INT	0	38.4	38.4	508	0	406	38.4	527	0.013	508	406	38.4	538	0.028	457	406	0.09	BJ

Table A.2 Experimental Database

Authors	Unit	f_c	ρ_j	N	L_c	h_c	b_c	c_c	ϕ	$ntop_c$	$nmid_c$	$nbot_c$	F_{yc}	ϕ_t	s_c	$Ltot_c$	F_{ty}
Fernandes [248]	JPA-1	19.8	0.0000	200	1600	300	300	20	12	2	0	2	590	8	250	1040	590
Fernandes [248]	JPA-2	19.8	0.0000	200	1600	300	300	20	12	2	0	2	590	8	250	1040	590
Fernandes [248]	JPA-3	19.8	0.0000	450	1600	300	300	20	12	2	0	2	590	8	250	1040	590
Fernandes [248]	JPB	19.8	0.0000	450	1600	300	300	20	12	3	2	3	590	8	250	1040	590
Fernandes [248]	JPC	19.8	0.0000	450	1600	300	300	20	12	2	0	2	590	8	250	1040	590
Fernandes [248]	JD	19.8	0.0000	200	1600	300	300	20	12	3	2	3	480	8	100	1040	480
Pantelides *et al.* [251]	Type I	43	0.0000	708.7948	1295	406	406	30	32	2	0	2	454	10	406	1504	454
Pantelides *et al.* [251]	Type II	43	0.0000	708.7948	1397	406	406	30	32	2	0	2	454	10	406	1504	454
Liu [252]	Unit 1	44	0.0000	0	1500	300	460	40	24	3	0	3	321	6	230	1760	318
Liu [252]	Unit 2	49	0.0000	811.44	1500	300	460	40	24	3	0	3	321	6	230	1760	318
Noguchi and Kurusu [242]	No 2	34.1	0.0001	294	585	300	300	20	13	6	4	6	388	10	100	2200	354
Noguchi and Kurusu [242]	No 4	34.1	0.0001	294	585	300	300	20	13	6	4	6	388	10	100	2200	354
Noguchi and Kurusu [242]	No 5	29.3	0.0001	294	585	300	300	20	13	6	4	6	374	10	100	2200	322
Noguchi and Kurusu [242]	No 7	29.3	0.0001	294	585	300	300	20	13	6	4	6	374	10	100	2200	322
Dhakal and Pan [254]	QS1	31.7	0.0000	600	1575	500	350	30	25	3	2	3	576	10	150	1680	364
Dhakal and Pan [254]	QS2	32.8	0.0000	600	1575	400	400	30	25	3	2	3	576	10	150	1500	364
Xin *et al.* [255]	Unit 1	20	0.0025	0	837	450	300	39	20	5.36	2	5.36	492	10	60	2027	348
Xin *et al.* [255]	Unit 2	20	0.0025	0	837	450	300	39	16	5.5	2	5.5	445	10	60	2027	348
Xin *et al.* [255]	Unit 3	40	0.0025	0	837	450	300	39	20	6.12	2	6.12	492	10	90	2027	348
Xin *et al.* [255]	Unit 4	40	0.0025	0	837	450	300	39	20	4.92	1.28	4.92	492	10	90	2027	348
Xin *et al.* [255]	Unit 5	60	0.0036	0	837	450	300	39	20	6.12	2	6.12	492	12	80	2027	327
Xin *et al.* [255]	Unit 6	60	0.0036	0	837	450	300	39	20	6.12	2	6.12	492	12	80	2027	327
Raffaelle and Wight [232]	S1	28.59	0.0013	89	876.3	355.6	355.6	25.4	19	3	2	3	440	9.53	88.9	2057	475
Raffaelle and Wight [232]	S2	26.8	0.0012	89	876.3	355.6	355.6	25.4	19	3	2	3	440	9.53	88.9	2057	475
Raffaelle and Wight [232]	S3	37.69	0.0017	89	876.3	355.6	355.6	25.4	19	3	2	3	440	9.53	88.9	2057	475
Raffaelle and Wight [232]	S4	19.29	0.0006	89	787.4	355.6	355.6	25.4	19	3	2	3	440	9.53	88.9	2057	475
Kurose *et al.* [228]	B1	24.4	0.0016	353	700	300	300	20	13	3	2	3	378	6	50	1040	378
Kurose *et al.* [228]	B2	24.4	0.0016	353	700	300	300	20	13	3	2	3	378	6	50	1040	378
Kurose *et al.* [228]	B3	24.4	0.0016	353	700	300	300	20	13	3	2	3	378	6	50	1040	378
Kurose *et al.* [228]	B4	24.4	0.0011	353	700	300	300	20	13	3	2	3	378	6	87.5	1040	378
Kurose *et al.* [228]	B5	24.4	0.0016	353	700	300	300	20	13	3	2	3	378	6	50	1040	378
Kurose *et al.* [228]	B6	24.4	0.0016	353	700	300	300	20	13	3	2	3	378	6	50	1040	378
Kurose *et al.* [228]	B8	24.4	0.0016	353	700	300	300	20	13	4	6	4	378	6	50	1040	378
Kurose *et al.* [228]	B9	24.4	0.0016	353	700	300	300	20	13	4	6	4	378	6	50	1040	378
Kurose *et al.* [228]	B10	24.4	0.0016	353	700	300	300	20	13	4	6	4	378	6	50	1040	378
Kurose *et al.* [228]	B11	24.4	0.0016	353	700	300	300	20	13	4	6	4	378	6	50	1040	378
Kusuhara and Shiohara [258]	A1	28.3	0.0025	216	585	300	300	20	13	5	6	5	345	6	50	1040	295
Kusuhara and Shiohara [258]	C1	28.3	0.0025	216	585	300	300	20	13	5	6	5	345	6	50	1040	295
Kusuhara and Shiohara [258]	D1	30.4	0.0025	216	585	300	300	20	13	5	4	5	345	6	50	1040	295
Kusuhara and Shiohara [258]	D2	30.4	0.0025	216	585	300	300	20	13	5	4	5	345	6	50	1040	295
Lee *et al.* [249]	J1	40	0.0081	0	880	350	350	20	29	4	4	4	514.4	10	50	1240	510.4
Lee *et al.* [249]	BJ1	40	0.0081	0	880	350	350	20	29	4	4	4	514.4	10	50	1240	510.4
Lee *et al.* [249]	BJ2	40	0.0054	0	880	350	350	20	29	4	4	4	514.4	10	75	1240	510.4

Continued on next page

Table A.2 Experimental Database – (continued from previous page)

Authors	Unit	f_c	ρ_j	N	L_c	h_c	b_c	c_c	ϕ	$ntop_c$	$nmid_c$	$nbot_c$	F_{yc}	ϕ_t	s_c	$Ltot_c$	F_{ty}
Lee *et al.* [249]	BJ3	40	0.0054	0	880	350	350	20	29	4	4	4	514.4	10	75	1240	510.4
Lee *et al.* [249]	B1	40	0.0054	0	880	350	350	20	29	4	4	4	514.4	10	75	1240	510.4
Alaee and Li [250]	IN80	80	0.0116	1863	1400	450	300	20	25	2.41	0.82	2.41	500	10	60	2310	700
Alaee and Li [250]	IH80	80	0.0093	1903.5	1400	450	300	20	25	2.92	1.28	2.92	500	10	60	2310	700
Alaee and Li [250]	IH80A	80	0.0093	1944	1400	450	300	20	25	2.92	1.28	2.92	500	10	60	2310	700
Alaee and Li [250]	IN100	100	0.0116	1984.5	1400	450	300	20	25	2.41	0.82	2.41	500	10	60	2310	700
Alaee and Li [250]	IH100	100	0.0116	2025	1400	450	300	20	25	2.92	1.28	2.92	500	10	60	2310	700
Alaee and Li [250]	IH60	60	0.0093	2065.5	1400	450	300	20	25	2.92	1.28	2.92	500	10	60	2310	700
Alaee and Li [250]	IH60A	60	0.0093	2106	1400	450	300	20	25	2.92	1.28	2.92	500	10	60	2310	700
Ehsani and Wight [259]	1B	-33.55	0.009047831	180	827	300	300	45	19.05	3	2	3	488	13	63.5	886	413
Ehsani and Wight [259]	2B	-34.93	0.009999121	222	827	300	300	45	19.05	4	2	4	488	13	63.5	886	413
Ehsani and Wight [259]	3B	-40.86	0.012063774	222	827	300	300	45	19.05	3	2	3	488	13	63.5	1329	413
Ehsani and Wight [259]	4B	-44.58	0.013332162	222	827	300	300	45	19.05	4	2	4	488	13	63.5	1329	413
Ehsani and Wight [259]	5B	-24.32	0.009047831	355.23	865	340	340	50.8	25.4	4	2	4	413	13	63.5	886	413
Ehsani and Wight [259]	6B	-39.78	0.009047831	302.66	865	340	340	50.8	25.4	3	2	3	413	13	63.5	886	413
Ehsani and Alameddine [54]	LL11	-75.8	0.012837267	285	1536	356	356	63.5	25.4	3	2	3	496	13	63.5	1460	446
Ehsani and Alameddine [54]	LL14	-96.5	0.012837267	236	1536	356	356	63.5	25.4	3	2	3	496	13	63.5	1460	446
Ehsani and Alameddine [54]	LH11	-75.8	0.017972174	276	1536	356	356	63.5	25.4	3	2	3	496	13	63.5	1460	446
Ehsani and Alameddine [54]	LH14	-96.5	0.017972174	223	1536	356	356	63.5	25.4	3	2	3	496	13	63.5	1460	446
Ehsani and Alameddine [54]	HL11	-75.8	0.012837267	687	1536	356	356	63.5	25.4	3	2	3	496	13	63.5	1460	446
Ehsani and Alameddine [54]	HH14	-96.5	0.017972174	476	1536	356	356	63.5	25.4	3	2	3	496	13	63.5	1460	446
Kaku and Asakusa [52]	4D16H617	-31.1	0.0049	258	660	220	220	19	16	2	0	2	360	12	52	728	250
Kaku and Asakusa [52]	4D16H610	-41.7	0.0049	199	660	220	220	19	16	2	0	2	360	12	52	728	250
Kaku and Asakusa [52]	4D16H600	-41.7	0.0049	0	660	220	220	19	16	2	0	2	360	12	52	728	250
Kaku and Asakusa [52]	4D16H317	-44.7	0.0012	360	660	220	220	19	16	2	0	2	360	6	52	728	281
Kaku and Asakusa [52]	4D16H309	-36.7	0.0012	160	660	220	220	19	16	2	0	2	360	6	52	728	281
Kaku and Asakusa [52]	4D16H300	-40.4	0.0012	0	660	220	220	19	16	2	0	2	360	6	52	728	281
Kaku and Asakusa [52]	4D108D10H612	-32.2	0.0049	194	660	220	220	16	10	4	4	4	395	12	52	752	250
Kaku and Asakusa [52]	4D108D10H608	-41.2	0.0049	160	660	220	220	16	10	4	4	4	395	12	52	752	250
Kaku and Asakusa [52]	4D108D10H600	-40.6	0.0049	0	660	220	220	16	10	4	4	4	395	12	52	752	250
Kaku and Asakusa [52]	4D108D10H317	-44.4	0.0012	360	660	220	220	16	10	4	4	4	395	6	52	752	281
Kaku and Asakusa [52]	4D10 8D10 H3 08	-41.9	0.0012	160	660	220	220	16	10	4	4	4	395	6	52	752	281
Kaku and Asakusa [52]	4D10 8D10 H3 00	-35.1	0.0012	0	660	220	220	16	10	4	4	4	395	6	52	752	281
Kaku and Asakusa [52]	4D10 8D10 H3 -04	-46.4	0.0049	-100	660	220	220	16	10	4	4	4	395	12	52	752	250
Shafaei *et al.* [214]	J1	-23	0.012932627	220	925	250	250	15	14	3	2	3	460	8	60	880	350
Shafaei *et al.* [214]	J2	-23.3	0	220	925	250	250	15	14	3	2	3	460	8	60	880	350
Shafaei *et al.* [214]	J3	-24.7	0	220	925	250	250	15	14	3	2	3	460	8	60	880	350
Chutarat and Aboutaha [261]	I1	-27.6	0.013594346	0	1194	406	406	25.4	22.23	4	4	4	482.7	13	88.89	2845	365.4
Chutarat and Aboutaha [261]	A2	-33.1	0.013594346	0	1194	508	406	25.4	22.23	3	2	3	482.7	13	88.89	2845	365.4
Ehsani *et al.* [260]	1	-64.72	0.011949747	133.447	1487.2	340	340	50.8	22.23	3	2	3	413	13	120	1630	413
Ehsani *et al.* [260]	2	-67.34	0.011949747	338.065	1487.2	340	340	50.8	22.23	3	2	3	413	13	120	1630	413
Ehsani *et al.* [260]	3	-64.72	0.01504164	382.547	1507.5	300	300	50.8	22.23	3	2	3	413	13	110	1352	413
Ehsani *et al.* [260]	4	-67.34	0.01504164	324.72	1507.5	300	300	50.8	25.4	3	2	3	413	13	110	1352	413
Ehsani *et al.* [260]	5	-44.64	0.01504164	222.411	849.1	300	300	50.8	19.05	3	2	3	413	13	110	1352	413

Continued on next page

Table A.2 Experimental Database – (continued from previous page)

Authors	Unit	f_c	ρ_j	N	L_c	h_c	b_c	c_c	ϕ	$ntop_c$	$nmid_c$	$nbot_c$	F_{yc}	ϕ_t	s_c	$Ltot_c$	F_{ty}
Tsonos [8]	A1	-35	0.009559798	200	550	200	200	30	10	3	2	3	500	6	50	792	540
Tsonos [8]	E1	-22	0.009559798	200	550	200	200	30	14	3	2	3	500	6	50	792	540
Tsonos [8]	E2	-35	0.009958123	200	550	200	200	30	14	3	2	3	495	6	48	792	540
Tsonos [8]	G1	-22	0.008535534	200	550	200	200	30	14	3	2	3	495	8	100	792	540

Table A.3 Experimental Database

Authors	Unit	L_b	h_b	b_b	c_b	ϕ	$ntop_b$	$nmid_b$	$nbot_b$	F_{yb}	$\phi_t b$	s_b	$Ltot_b$	F_{tyb}
Fernandes [248]	JPA-1	2150	400	300	20	12	2	0	4	590	8	200	1040	590
Fernandes [248]	JPA-2	2150	400	300	20	12	2	0	4	590	8	200	1040	590
Fernandes [248]	JPA-3	2150	400	300	20	12	2	0	4	590	8	200	1040	590
Fernandes [248]	JPB	2150	400	300	20	12	2	0	4	590	8	200	1040	590
Fernandes [248]	JPC	2150	400	300	20	12	2	0	4	590	8	100	1040	590
Fernandes [248]	JD	2150	400	300	20	12	2	0	4	480	8	200	1040	480
Pantelides *et al.* [251]	Type I	1677	610	406	30	13	17.34	1.18	2	454	10	229	1912	454
Pantelides *et al.* [251]	Type II	1677	406	406	30	13	12.08	1.18	3	454	10	229	1504	454
Liu [252]	Unit 1	1605	500	300	40	24	4	0	2	321	12	380	1280	318
Liu [252]	Unit 2	1605	500	300	40	24	4	0	2	321	12	380	1280	318
Noguchi and Kurusu [242]	No 2	1200	300	200	20	10	10	0	10	325	6	100	1800	354
Noguchi and Kurusu [242]	No 4	1200	300	200	20	13	5	0	5	388	6	100	1800	354
Noguchi and Kurusu [242]	No 5	1200	300	200	20	10	10	0	10	325	6	100	1800	322
Noguchi and Kurusu [242]	No 7	1200	300	200	20	13	5	0	5	374	6	100	1800	322
Dhakal and Pan [254]	QS1	2450	550	300	30	25	5	0	2	538	10	200	1500	264
Dhakal and Pan [254]	QS2	2500	550	300	30	25	6	0	2	538	10	200	1500	264
Xin *et al.* [255]	Unit 1	1855	500	250	44	12	7	0	7	453	6	70	1140	356
Xin *et al.* [255]	Unit 2	1855	500	250	44	16	4	0	2	445	10	90	1140	348
Xin *et al.* [255]	Unit 3	1855	500	250	44	16	4	0	4	445	10	90	1140	348
Xin *et al.* [255]	Unit 4	1855	500	250	44	20	2	0	1.28	492	10	90	1140	348
Xin *et al.* [255]	Unit 5	1855	500	250	44	20	3	0	3	492	10	90	1140	348
Xin *et al.* [255]	Unit 6	1855	500	250	44	20	3.92	0	2	492	10	90	1140	348
Raffaelle and Wight [232]	S1	2089	381	254	25.4	15.88	4.32	0	3	440	6.35	82.55	1068.8	475
Raffaelle and Wight [232]	S2	2089	381	177.8	25.4	15.88	2.88	0	2	440	6.35	82.55	914.4	475
Raffaelle and Wight [232]	S3	2089	381	190.5	25.4	15.88	3	0	2	440	6.35	82.55	939.8	475
Raffaelle and Wight [232]	S4	2089	558.8	190.5	25.4	15.88	3	0	2	440	6.35	127	1295.4	475
Kurose *et al.* [228]	B1	1350	350	150	20	13	3	0	3	378	6	75	840	378
Kurose *et al.* [228]	B2	1350	350	150	20	13	3	0	3	378	6	75	840	378
Kurose *et al.* [228]	B3	1350	350	150	20	13	3	0	3	378	6	75	840	378
Kurose *et al.* [228]	B4	1350	350	150	20	13	3	0	3	378	6	75	840	378
Kurose *et al.* [228]	B5	1350	350	150	20	13	3	0	3	378	6	75	840	378
Kurose *et al.* [228]	B6	1350	350	150	20	13	3	0	3	378	6	75	840	378
Kurose *et al.* [228]	B8	1350	350	200	20	13	3	0	3	378	6	50	1190	378
Kurose *et al.* [228]	B9	1350	350	200	20	13	3	0	3	378	6	100	900	378
Kurose *et al.* [228]	B10	1350	350	200	20	13	5	0	5	378	6	50	1190	378
Kurose *et al.* [228]	B11	1350	350	200	20	13	5	0	3	378	6	50	1190	378
Kusuhara and Shiohara [258]	A1	1350	300	300	20	13	8	0	8	345	6	50	1040	295
Kusuhara and Shiohara [258]	C1	1350	300	300	20	13	8	0	8	345	6	50	1040	295
Kusuhara and Shiohara [258]	D1	1350	300	300	20	16	6	0	6	345	6	50	1040	295
Kusuhara and Shiohara [258]	D2	1350	300	300	20	16	6	0	6	345	6	50	1040	295
Lee *et al.* [249]	J1	1375	400	300	20	16	10	0	10	509.9	10	100	1240	510.4
Lee *et al.* [249]	BJ1	1375	400	300	20	16	6	0	6	509.9	10	100	1240	510.4
Lee *et al.* [249]	BJ2	1375	400	300	20	16	5	0	5	509.9	10	200	1240	510.4

Continued on next page

Table A.3 Experimental Database – (continued from previous page)

Authors	Unit	L_b	h_b	b_b	c_b	ϕ	$ntop_b$	$nmid_b$	$nbot_b$	F_{yb}	$\phi_t b$	s_b	$Ltot_b$	F_{tyb}
Lee *et al.* [249]	BJ3	1375	400	300	20	16	4	0	4	509.9	10	200	1240	510.4
Lee *et al.* [249]	B1	1375	400	300	20	16	3	0	3	509.9	10	200	1240	510.4
Alaee and Li [250]	IN80	2175	500	250	20	16	4	0	2	500	10	65	1340	500
Alaee and Li [250]	IH80	2175	500	250	20	16	4	0	2	700	10	85	1340	700
Alaee and Li [250]	IH80A	2175	500	250	20	16	4	0	2	700	10	65	1340	700
Alaee and Li [250]	IN100	2175	500	250	20	16	4	0	2	700	10	65	1340	700
Alaee and Li [250]	IH100	2175	500	250	20	16	4	0	2	700	10	65	1340	700
Alaee and Li [250]	IH60	2175	500	250	20	16	2	0	2	700	10	85	1340	700
Alaee and Li [250]	IH60A	2175	500	250	20	16	2	0	2	700	10	85	1340	700
Ehsani and Wight [259]	1B	762	480	259	76	20.63	6	0	6	340	13	101.6	1072	413
Ehsani and Wight [259]	2B	762	439	259	48.3	20.63	6	0	6	340	13	88.9	1072	413
Ehsani and Wight [259]	3B	762	480	259	50.8	20.63	6	0	6	340	13	101.6	1072	413
Ehsani and Wight [259]	4B	762	439	259	48.3	20.63	6	0	6	340	13	88.9	1072	413
Ehsani and Wight [259]	5B	534	480	300	50.8	22.23	6	0	6	340	13	101.6	1072	413
Ehsani and Wight [259]	6B	534	480	300	50.8	20.63	6	0	6	340	13	76.2	1072	413
Ehsani and Alameddine [54]	LL11	800	508	311	76.2	25.4	4	0	4	496	13	88.9	1092	446
Ehsani and Alameddine [54]	LL14	800	508	311	76.2	25.4	4	0	4	496	13	88.9	1092	446
Ehsani and Alameddine [54]	LH11	800	508	311	76.2	25.4	4	0	4	496	13	63.5	1092	446
Ehsani and Alameddine [54]	LH14	800	508	311	76.2	25.4	4	0	4	496	13	63.5	1092	446
Ehsani and Alameddine [54]	HL11	800	508	311	76.2	28.58	4	0	4	496	13	88.9	1092	446
Ehsani and Alameddine [54]	HH14	800	508	311	76.2	28.58	4	0	4	496	13	63.5	1092	446
Kaku and Asakusa [52]	4D16H617	445	220	160	17	13	4	0	4	391	12	50	624	250
Kaku and Asakusa [52]	4D16H610	445	220	160	17	13	4	0	4	391	12	50	624	250
Kaku and Asakusa [52]	4D16H600	445	220	160	17	13	4	0	4	391	12	50	624	250
Kaku and Asakusa [52]	4D16H317	445	220	160	17	13	4	0	4	391	6	50	624	281
Kaku and Asakusa [52]	4D16H309	445	220	160	17	13	4	0	4	391	6	50	624	281
Kaku and Asakusa [52]	4D16H300	445	220	160	17	13	4	0	4	391	6	50	624	281
Kaku and Asakusa [52]	4D108D10H612	445	220	160	17	13	4	0	4	391	12	50	624	250
Kaku and Asakusa [52]	4D108D10H608	445	220	160	17	13	4	0	4	391	12	50	624	250
Kaku and Asakusa [52]	4D108D10H600	445	220	160	17	13	4	0	4	391	12	50	624	250
Kaku and Asakusa [52]	4D108D10H317	445	220	160	17	13	4	0	4	391	6	50	624	281
Kaku and Asakusa [52]	4D10 8D10 H3 08	445	220	160	17	13	4	0	4	391	6	50	624	281
Kaku and Asakusa [52]	4D10 8D10 H3 00	445	220	160	17	13	4	0	4	391	6	50	624	281
Kaku and Asakusa [52]	4D10 8D10 H3 -04	445	220	160	17	13	4	0	4	391	12	50	624	250
Shafaei *et al.* [214]	J1	575	250	220	15	14	4	0	3	460	8	60	820	350
Shafaei *et al.* [214]	J2	575	250	220	15	14	4	0	3	460	8	60	820	350
Shafaei *et al.* [214]	J3	575	250	220	15	14	4	0	3	460	8	60	820	350
Chutarat and Aboutaha [261]	I1	1067	457	356	25.4	22.23	4	0	4	482.7	13	88.9	2235	365.4
Chutarat and Aboutaha [261]	A2	1067	457	356	25.4	22.23	4	0	4	482.7	13	88.9	2235	365.4
Ehsani *et al.* [260]	1	787	480	300	50.8	20.96	5	0	5	413	13	120	774.7	413
Ehsani *et al.* [260]	2	787	480	300	50.8	19.05	5	0	5	413	13	120	774.7	413
Ehsani *et al.* [260]	3	787	440	260	50.8	17.78	5	0	5	413	13	110	990.6	413
Ehsani *et al.* [260]	4	787	440	260	50.8	19.69	5	0	5	413	13	110	990.6	413
Ehsani *et al.* [260]	5	787	440	260	50.8	20.64	6	0	6	275	13	110	990.6	413

Continued on next page

Table A.3 Experimental Database – (continued from previous page)

Authors	Unit	L_b	h_b	b_b	c_b	ϕ	$ntop_b$	$nmid_b$	$nbot_b$	F_{yb}	$\phi_t b$	s_b	$Ltot_b$	F_{tyb}
Tsonos [8]	A1	450	300	200	30	10	4	0	4	500	6	65	760	540
Tsonos [8]	E1	450	300	200	30	14	3	0	3	500	6	75	760	540
Tsonos [8]	E2	450	300	200	30	14	2	0	2	495	6	75	760	540
Tsonos [8]	G1	450	300	200	30	14	3	0	3	495	8	100	760	540

B
FITTED SURFACES ON THE FE SIMULATION OUTPUT

This appendix chapter presents the fitted surfaces for the simulation results obtained in the context of concrete behavior analysis. The surfaces are generated using cubic surfaces and capture the relationship between shear strain and stress values with respect to concrete strength, aspect ratio, and joint reinforcement ratio. A total of 1500 simulation results were utilized for the fitting process. The polynomial coefficients used to construct the surfaces are listed in Table 1, while Table 2 presents the metrics indicating the goodness of fit for the constructed surfaces.

To establish the relationships between shear strain and stress values, cubic surfaces were employed. These surfaces allow for the representation of complex three-dimensional interactions between the variables of interest, namely concrete strength, aspect ratio, and joint reinforcement ratio. By fitting the cubic surfaces to the simulation results, a comprehensive understanding of the concrete behavior under the defined criteria can be obtained.

Table 1 provides the polynomial coefficients obtained from the surface fitting process. These coefficients are crucial for accurately reproducing the fitted surfaces. Each term in the polynomial equation contributes to the overall shape and characteristics of the surfaces. By incorporating these coefficients, researchers and practitioners can efficiently utilize the fitted surfaces for further analysis and decision-making processes.

Table 2 presents the metrics used to evaluate the goodness of fit for the constructed surfaces. These metrics provide insights into the accuracy and reliability of the fitted surfaces in representing the simulation results. Commonly used metrics, such as root mean square error (RMSE), coefficient of determination (R^2), and mean absolute error (MAE), are reported. These metrics allow for an objective assessment of the quality of the fitted surfaces and aid in understanding the level of agreement between the simulation results and the fitted models.

This appendix chapter demonstrates the fitting of cubic surfaces to 1500 simulation results, which represent shear strain and stress values under defined criteria. By employing polynomial coefficients listed in Table 1, the fitted surfaces accurately capture the complex interdependencies between concrete strength, aspect ratio, and joint reinforcement ratio. The goodness of fit metrics presented in Table 2 assure the reliability of the fitted surfaces. Researchers and practitioners can utilize these surfaces to gain insights into concrete behavior and make informed decisions based on the defined criteria.

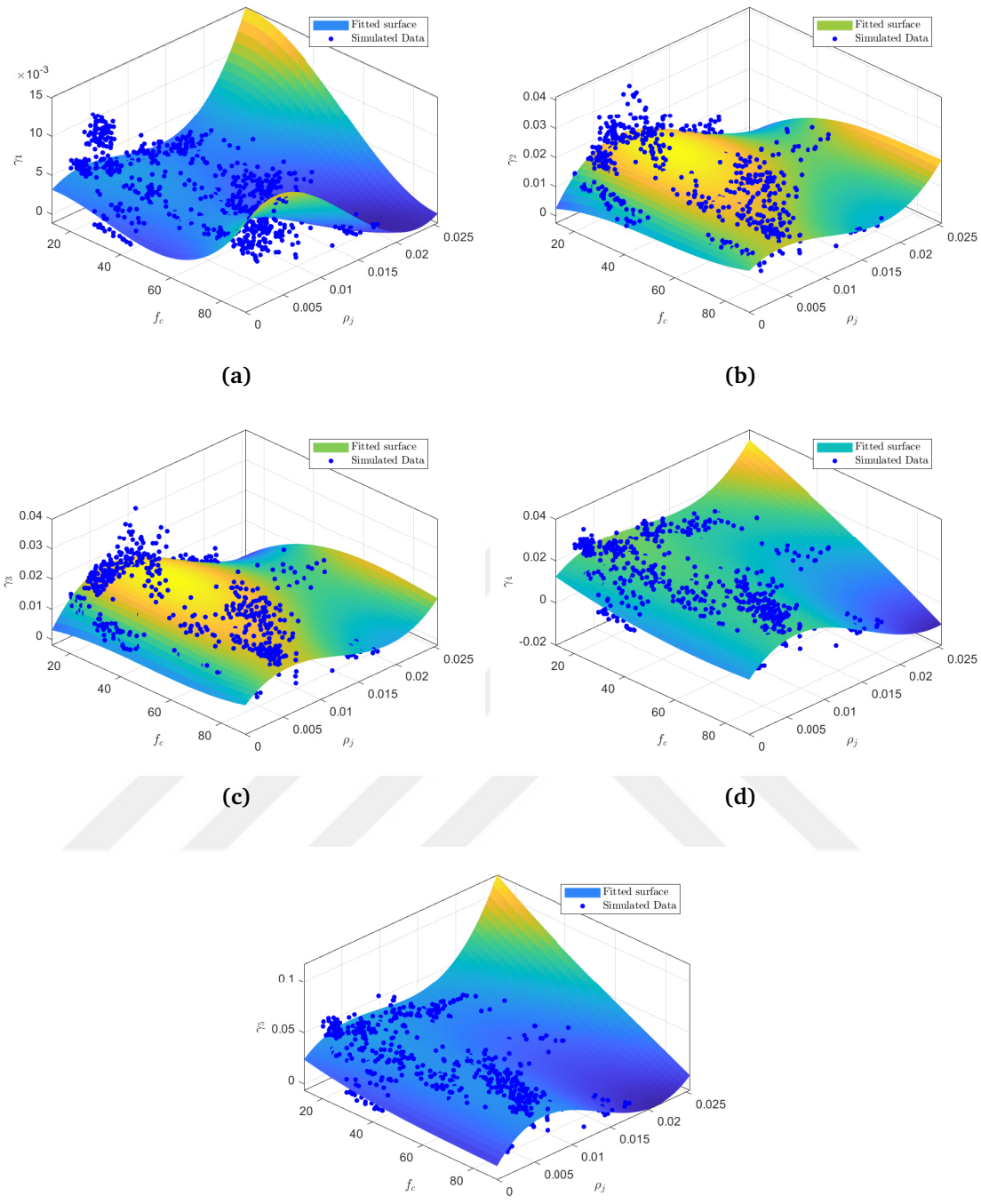

Figure B.1 Scatter and fitted surfaces for shear strain values, γ_{xy}(z) and concrete strength values, f_c (x) and joint reinforcement ratio, ρ_j (y) for (a) Limit I, (b) Limit II, (c) Limit III, (d) Limit IV and (e) Limit V

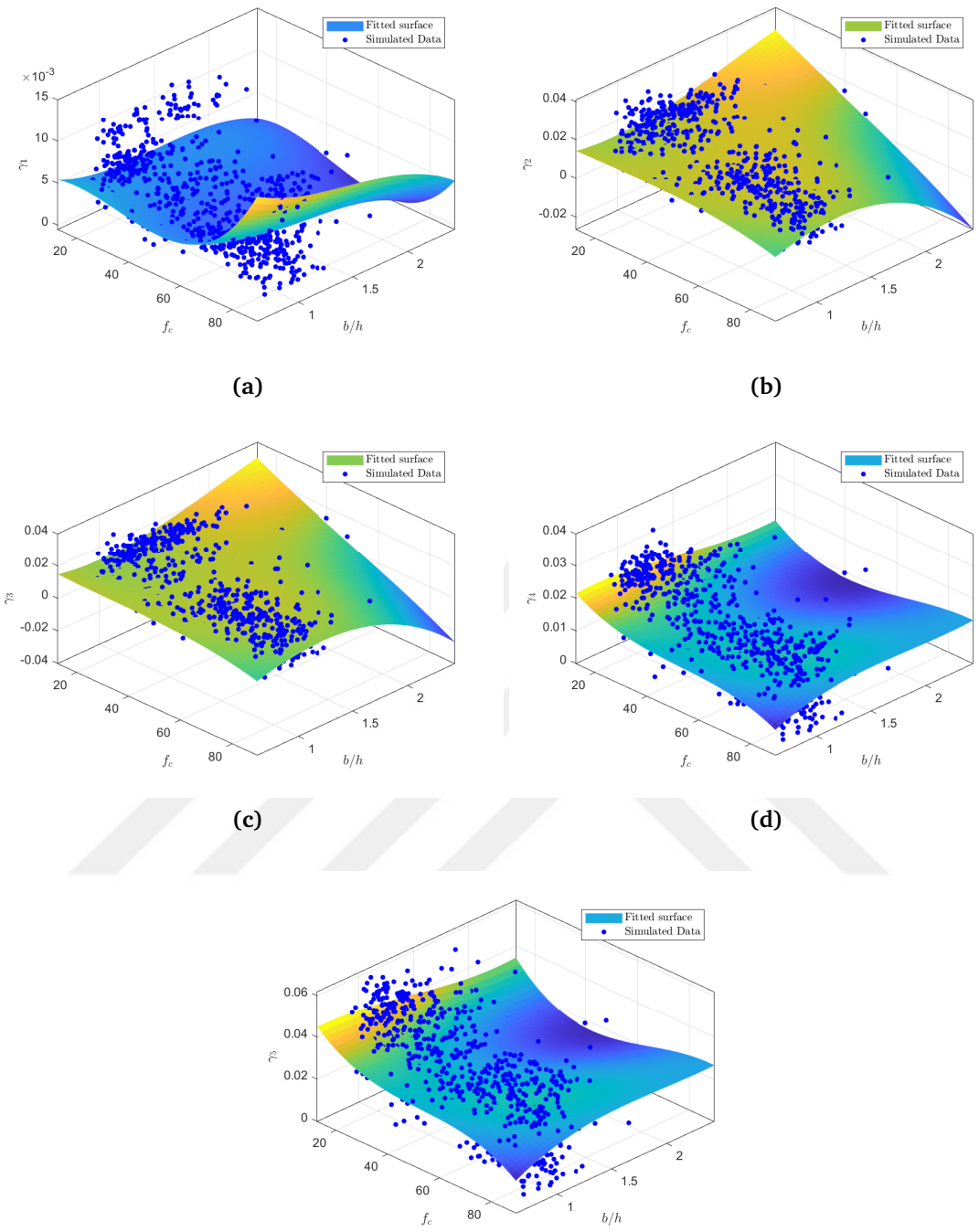

Figure B.2 Scatter and fitted surfaces for shear strain values, γ_{xy}(z) and concrete strength values, f_c (x) and aspect ratio, b/h (y) for (a) Limit I, (b) Limit II, (c) Limit III, (d) Limit IV and (e) Limit V

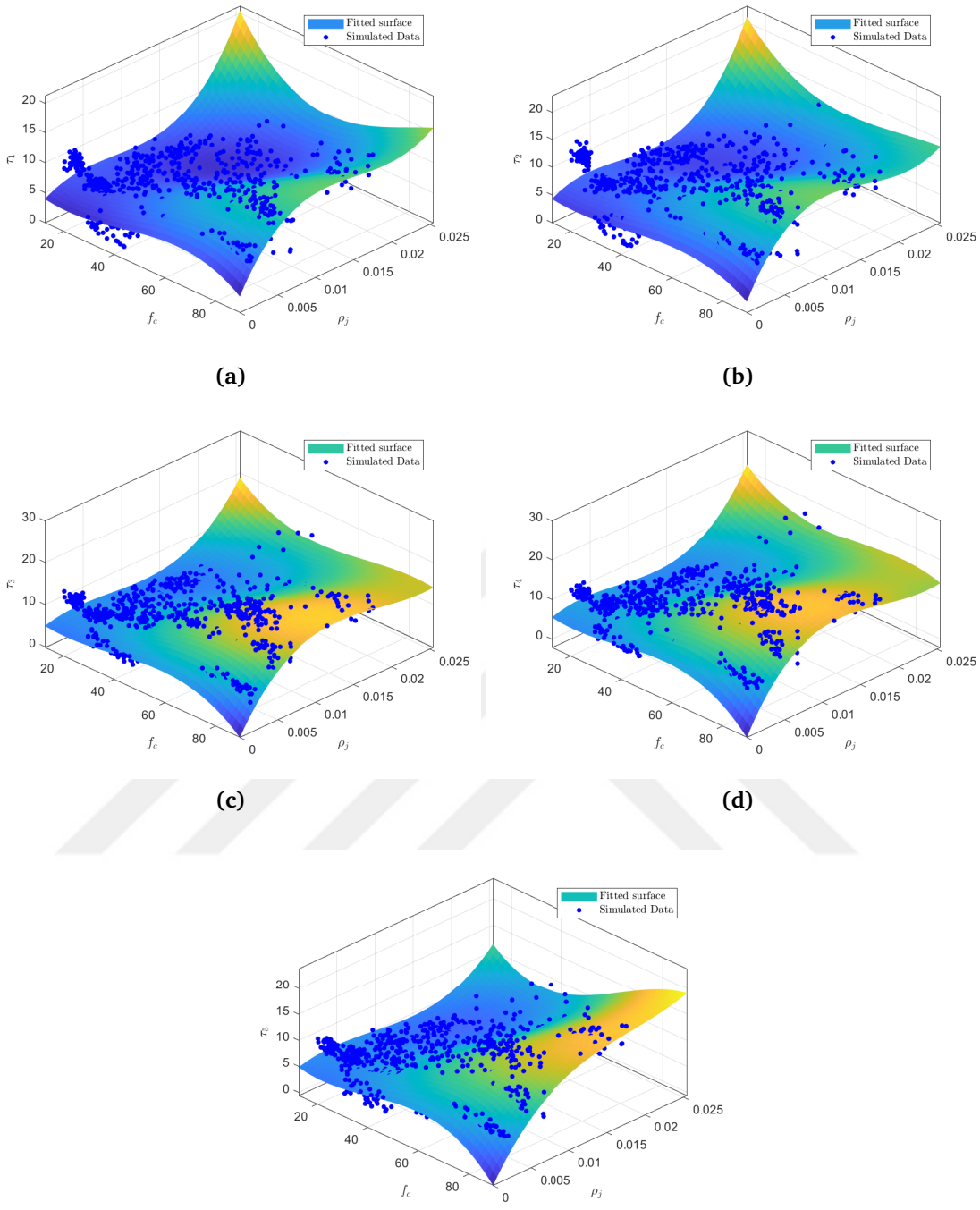

Figure B.3 Scatter and fitted surfaces for shear stress values, τ_{xy}(z) and concrete strength values, f_c (x) and aspect ratio, ρ_j (y) for (a) Limit I, (b) Limit II, (c) Limit III, (d) Limit IV and (e) Limit V

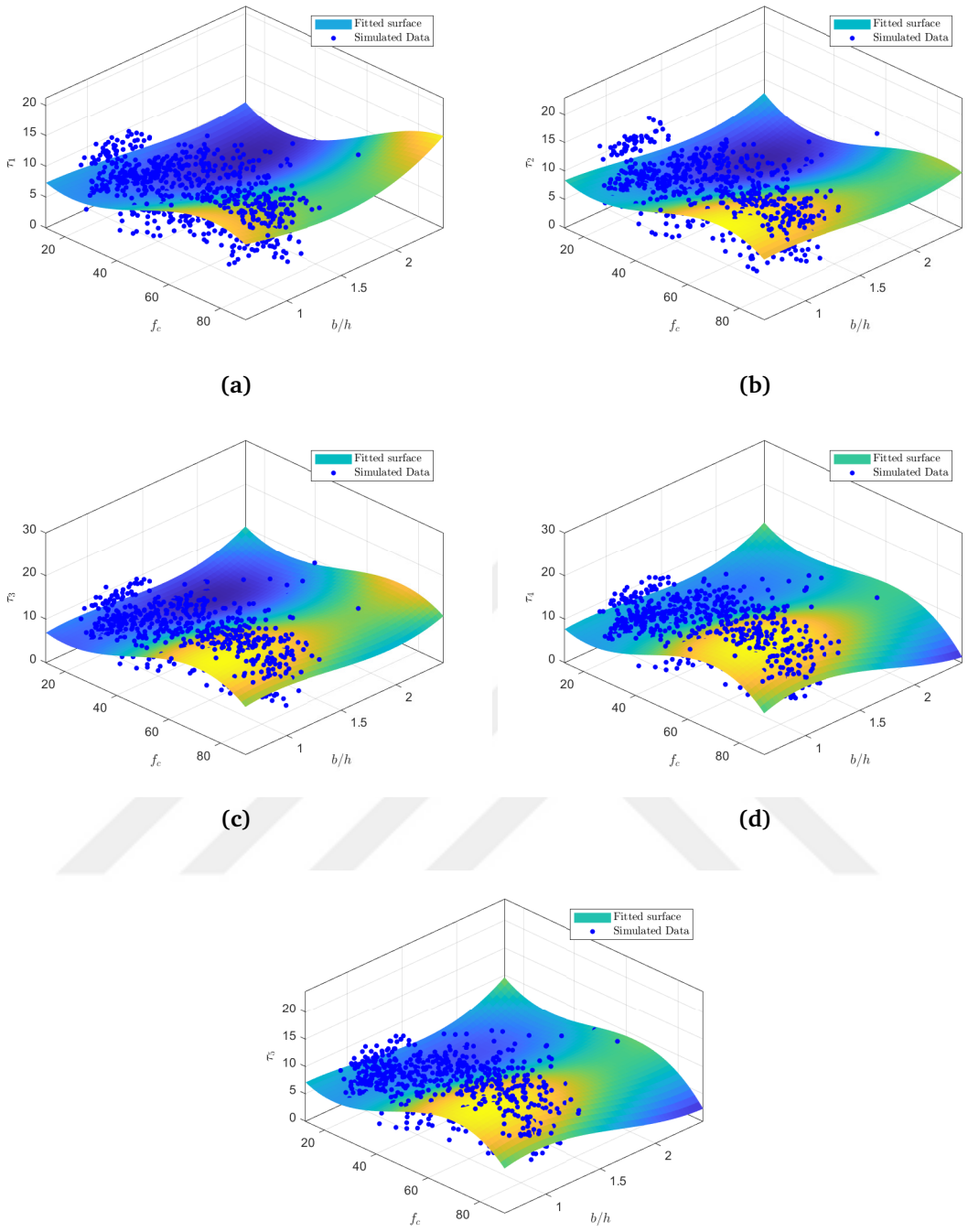

(a) **(b)**

(c) **(d)**

(e)

Figure B.4 Scatter and fitted surfaces for shear stress values, τ_{xy}(z) and concrete strength values, f_c (x) and aspect ratio, b/h (y) for (a) Limit I, (b) Limit II, (c) Limit III, (d) Limit IV and (e) Limit V

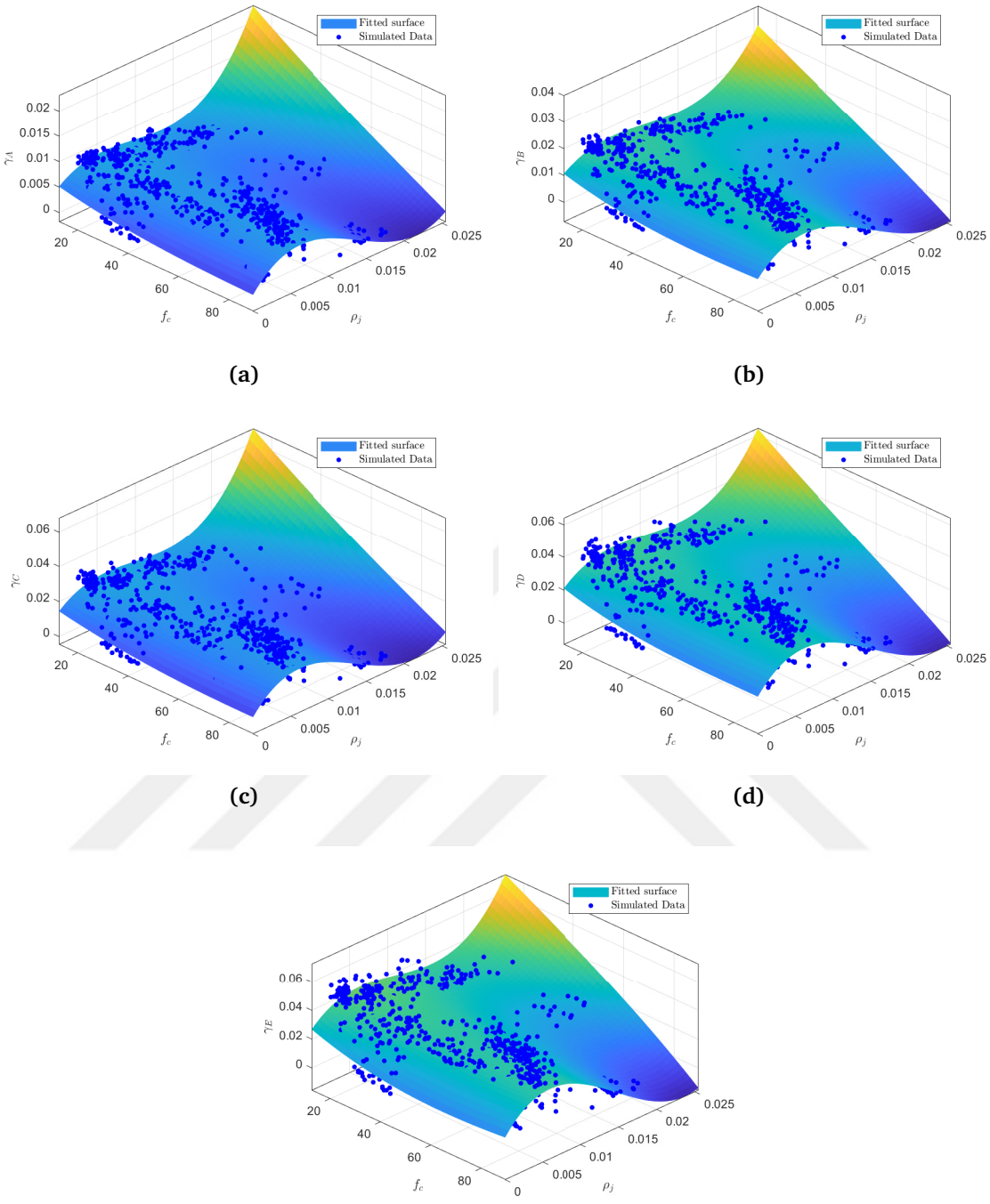

Figure B.5 Scatter and fitted surfaces for shear strain values, γ_{xy}(z) and concrete strength values, f_c (x) and joint reinforcement ratio, ρ_j (y) for (a) Limit A, (b) Limit B, (c) Limit C, (d) Limit D and (e) Limit E

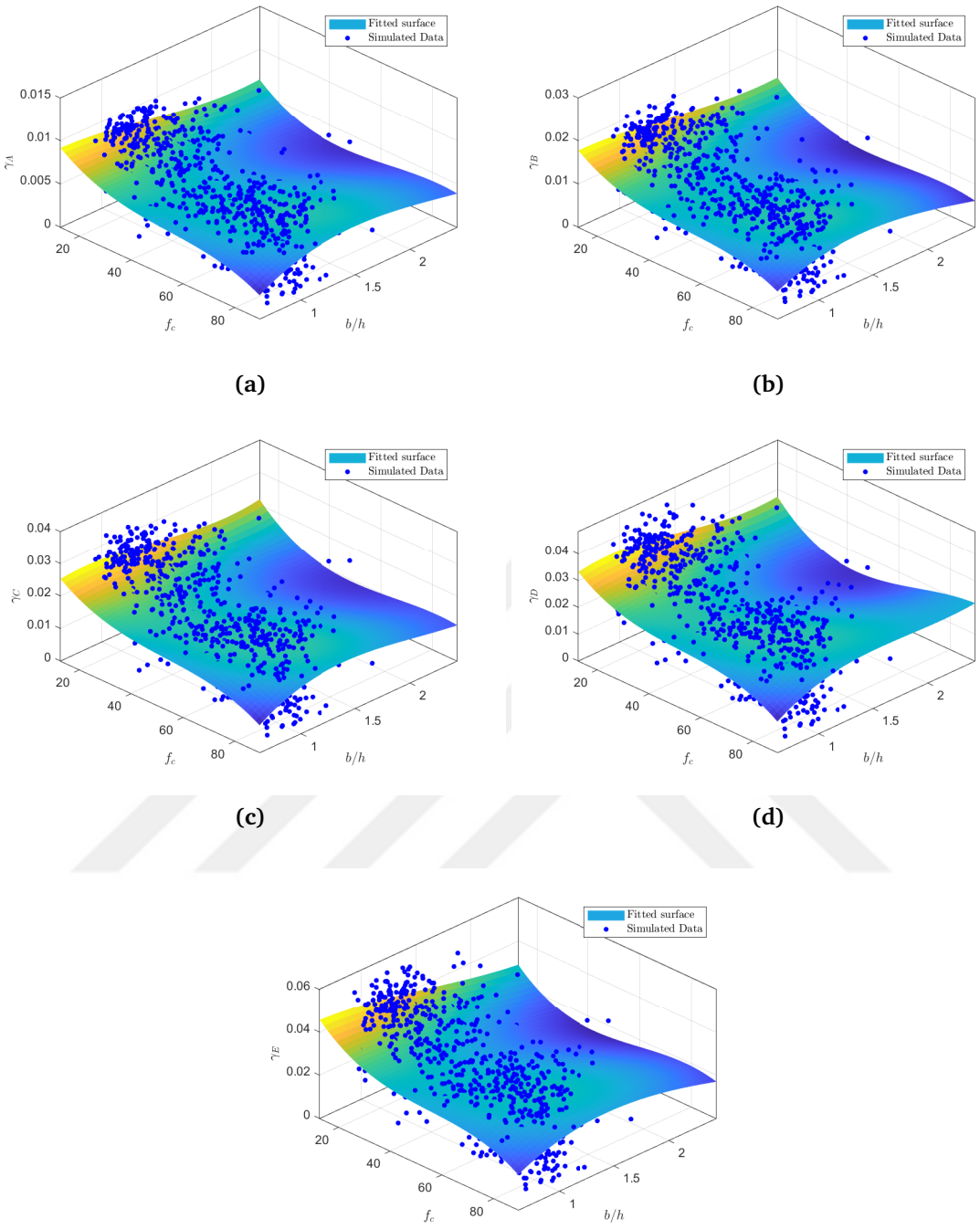

Figure B.6 Scatter and fitted surfaces for shear strain values, γ_{xy}(z) and concrete strength values, f_c (x) and aspect ratio, b/h (y) for (a) Limit A, (b) Limit B, (c) Limit C, (d) Limit D and (e) Limit E

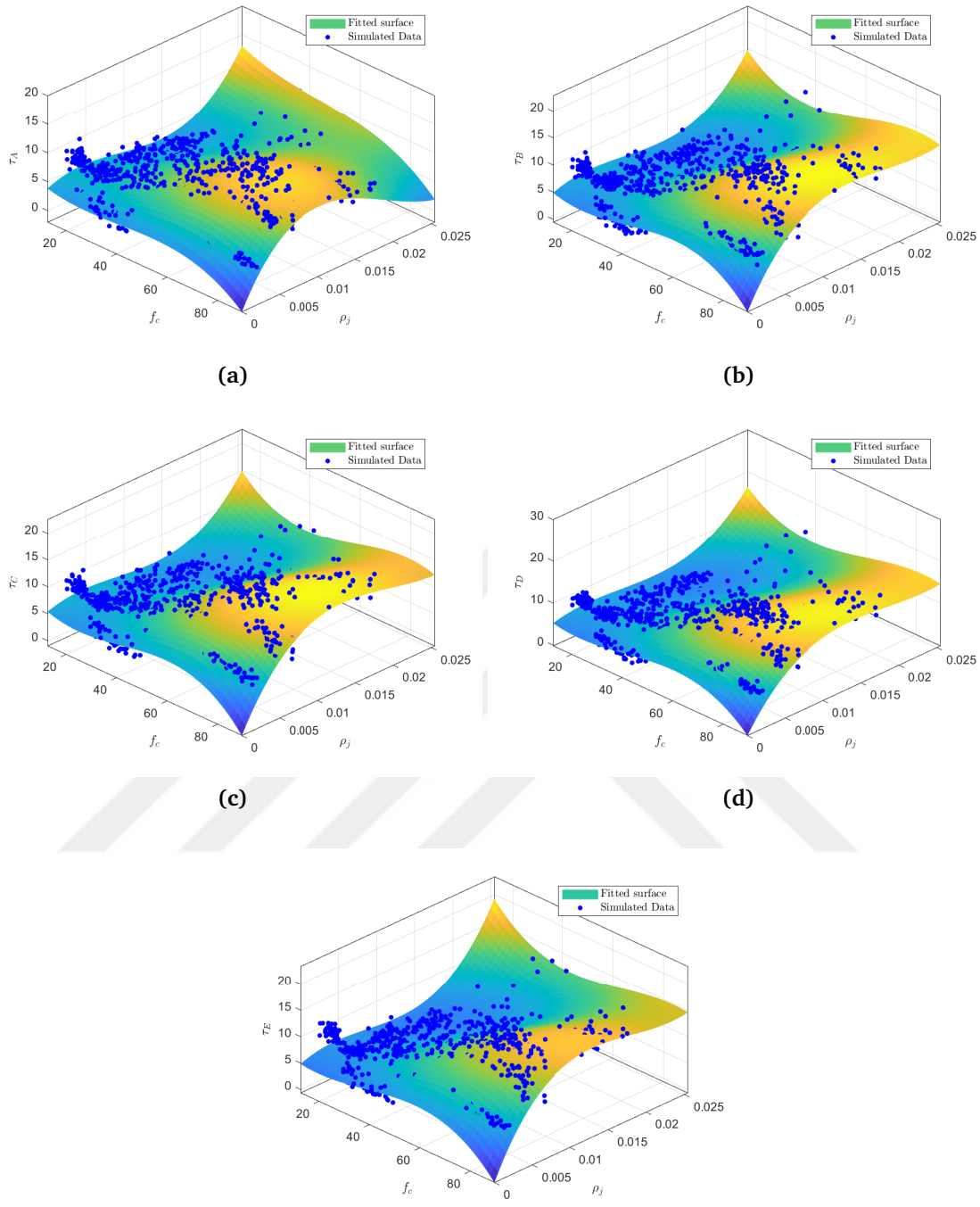

Figure B.7 Scatter and fitted surfaces for shear stress values, τ_{xy}(z) and concrete strength values, f_c (x) and aspect ratio, ρ_j (y) for (a) Limit A, (b) Limit B, (c) Limit C, (d) Limit D and (e) Limit E

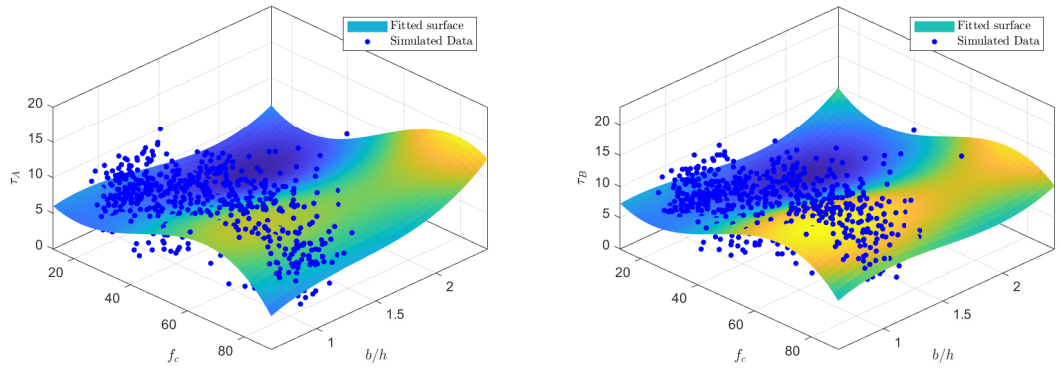

(a)

(b)

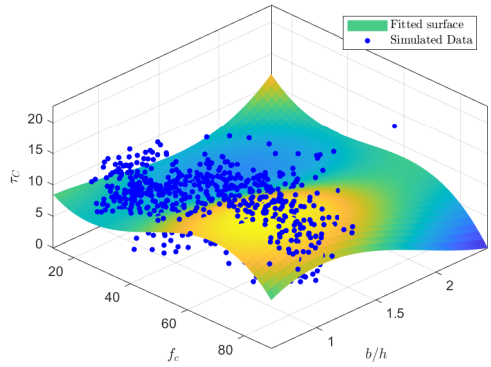

(c)

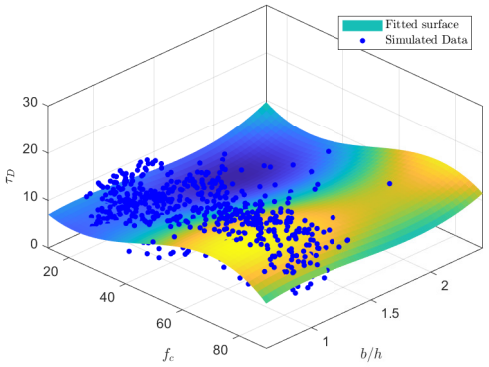

(d)

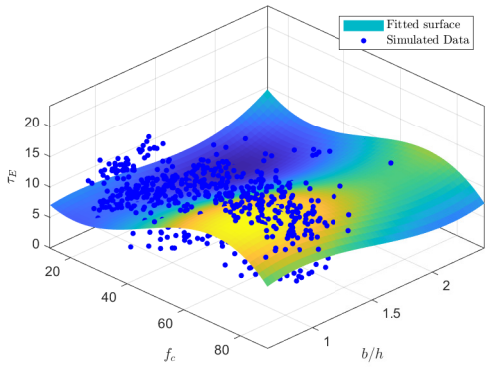

(e)

Figure B.8 Scatter and fitted surfaces for shear stress values, τ_{xy}(z) and concrete strength values, f_c (x) and aspect ratio, b/h (y) for (a) Limit A, (b) Limit B, (c) Limit C, (d) Limit D and (e) Limit E

Table B.1 Polynomial coefficients for surfaces fitted to shear strain data for material strength limit states

Function	p00	p10	p01	p20	p11	p02	p30	p21	p12	p03
$\gamma_1(f_c, \rho_j)$	0.0033	-4.112e-05	-0.0002053	0.0006908	-0.000551	-0.0002384	-0.0003309	-0.0001274	0.0002409	6.86e-05
$\gamma_1(f_c, b/h)$	0.003101	0.0002183	-0.0001638	0.0006495	1.702e-06	-4.011e-05	-0.0004901	-2.479e-05	-2.133e-05	-5.898e-07
$\gamma_2(f_c, \rho_j)$	0.01894	-0.00259	0.002112	-0.0007852	-0.000997	-0.003427	0.0001952	-0.0003786	0.0006939	0.0006018
$\gamma_2(f_c, b/h)$	0.01485	0.001379	0.0006839	0.0004231	-0.0008556	7.56e-05	-0.001423	0.0003254	-0.0004777	-0.0001216
$\gamma_3(f_c, \rho_j)$	0.01774	-0.002028	0.001869	-0.001839	-0.0007375	-0.003099	0.0005747	-0.0004858	0.0006154	0.0005675
$\gamma_3(f_c, b/h)$	0.0142	0.001712	0.0009086	-0.000702	-0.0006058	-4.534e-05	-0.001018	8.567e-05	-0.0003545	-8.825e-05
$\gamma_4(f_c, \rho_j)$	0.01566	-0.001882	0.0007032	0.001268	-0.0007421	-0.002525	-0.0004526	-0.0005993	-0.0001408	0.0005171
$\gamma_4(f_c, b/h)$	0.01339	-0.00038	-0.00068	0.002231	0.0005144	-0.0001225	-0.001762	3.42e-06	0.0003972	8.53e-05
$\gamma_5(f_c, \rho_j)$	0.03127	-0.003141	0.001123	0.002238	-0.001313	-0.005321	-0.001084	-0.0009177	-0.000348	0.001132
$\gamma_5(f_c, b/h)$	0.02651	-0.0002491	-0.001331	0.004128	0.0009772	-0.0001194	-0.003658	9.446e-05	2.452e-05	-2.031e-05

Table B.2 Polynomial coefficients for surfaces fitted to shear stress data for material strength limit states

Function	p00	p10	p01	p20	p11	p02	p30	p21	p12	p03
$\tau_1(f_c, \rho_j)$	7.776	4.249	-0.4513	0.962	0.964	-1.255	-1.144	0.801	-0.4556	0.3774
$\tau_1(f_c, b/h)$	6.928	3.822	-0.8362	1.27	0.1863	0.04634	-1.244	-0.06645	0.0364	0.01045
$\tau_2(f_c, \rho_j)$	8.017	4.536	-0.6713	1.455	0.7698	-1.109	-1.245	0.8317	-0.3291	0.3672
$\tau_2(f_c, b/h)$	7.361	4.096	-0.7794	1.655	0.2027	-0.008256	-1.237	-0.01441	0.002448	0.01899
$\tau_3(f_c, \rho_j)$	10.58	5.581	0.289	-0.05377	1.809	-1.382	-1.171	0.6123	-0.8274	0.367
$\tau_3(f_c, b/h)$	9.747	5.673	-0.6991	0.574	0.3026	-0.07089	-1.605	0.05769	-0.01784	0.04216
$\tau_4(f_c, \rho_j)$	11.63	6.354	0.2334	-0.1422	2.192	-1.552	-1.638	0.7242	-0.9584	0.4095
$\tau_4(f_c, b/h)$	10.67	6.665	-0.6862	0.718	0.5297	-0.09116	-2.343	-0.1966	-0.1376	0.04213
$\tau_5(f_c, \rho_j)$	9.575	5.141	0.1778	-0.2527	1.83	-1.202	-1.204	0.7929	-0.6392	0.3089
$\tau_5(f_c, b/h)$	9.015	5.216	-0.459	0.08087	0.1225	-0.1602	-1.561	-0.2967	-0.1354	0.03524

Table B.3 Polynomial coefficients for surfaces fitted to shear strain data for damage index limit states

Function	p00	p10	p01	p20	p11	p02	p30	p21	p12	p03
$\gamma_A(f_c, \rho_j)$	0.006314	-0.00063	0.0002713	0.0004164	-0.0002495	-0.001058	-0.0002276	-0.0001989	-7.01E-05	0.0002226
$\gamma_A(f_c, b/h)$	0.00529	-5.81E-05	-0.0003207	0.0008392	0.0002031	1.69E-05	-0.0007392	6.50E-05	1.92E-05	-7.26E-06
$\gamma_B(f_c, \rho_j)$	0.01236	-0.001265	0.0005464	0.001068	-0.0004876	-0.002089	-0.0004459	-0.0004115	-0.0001664	0.000432
$\gamma_B(f_c, b/h)$	0.01045	-5.59E-05	-0.0005274	0.00188	0.0004495	-4.38E-05	-0.001476	6.10E-05	-2.28E-05	-5.28E-06
$\gamma_C(f_c, \rho_j)$	0.01929	-0.002189	0.0007622	0.001234	-0.000879	-0.003454	-0.0004709	-0.0005024	-0.0002087	0.0007375
$\gamma_C(f_c, b/h)$	0.01616	-0.0001237	-0.0008607	0.002561	0.0006998	-0.0001407	-0.002169	0.0001087	-8.49E-05	-3.74E-06
$\gamma_D(f_c, \rho_j)$	0.02534	-0.002657	0.0007263	0.001906	-0.001209	-0.004402	-0.0009437	-0.0006457	-0.0002205	0.0009644
$\gamma_D(f_c, b/h)$	0.02125	-0.0002908	-0.001031	0.003643	0.0008168	-1.26E-05	-0.003023	0.0003097	0.000248	-2.50E-05
$\gamma_E(f_c, \rho_j)$	0.03153	-0.003657	0.0012	0.002029	-0.001044	-0.005741	-0.0004928	-0.001019	-0.0006002	0.001303
$\gamma_E(f_c, b/h)$	0.0263	-0.0006348	-0.001504	0.004207	0.001086	5.29E-05	-0.003223	0.000525	0.0001241	-3.27E-05

Table B.4 Polynomial coefficients for surfaces fitted to shear stress data for damage index limit states

Function	p00	p10	p01	p20	p11	p02	p30	p21	p12	p03
$\tau_A(f_c, \rho_j)$	8.585	3.702	0.556	-0.5013	1.261	-1.511	-0.8869	0.228	-0.6478	0.3855
$\tau_A(f_c, b/h)$	7.42	4.202	-0.7059	0.2298	0.3282	0.139	-1.543	0.1529	0.0924	-0.000301
$\tau_B(f_c, \rho_j)$	9.666	5.317	0.3724	-0.04375	1.61	-1.343	-1.404	0.5734	-0.6305	0.3473
$\tau_B(f_c, b/h)$	8.807	5.506	-0.4864	0.5066	0.2912	-0.04197	-1.837	-0.1697	-0.04739	0.02003
$\tau_C(f_c, \rho_j)$	10.02	5.219	0.3758	-0.07415	1.76	-1.327	-1.285	0.6703	-0.716	0.3393
$\tau_C(f_c, b/h)$	9.229	5.391	-0.773	0.5109	0.3021	-0.08456	-1.719	0.1501	0.001166	0.04528
$\tau_D(f_c, \rho_j)$	10.26	5.298	0.5842	-0.06859	1.866	-1.337	-1.154	0.5283	-0.8333	0.2995
$\tau_D(f_c, b/h)$	9.471	5.587	-0.5934	0.547	0.294	-0.1096	-1.717	-0.09267	-0.08499	0.04034
$\tau_E(f_c, \rho_j)$	10.69	5.569	0.1865	-0.1236	1.84	-1.482	-1.238	0.7417	-0.836	0.3895
$\tau_E(f_c, b/h)$	9.89	5.755	-0.5912	0.4369	0.1901	-0.1828	-1.755	-0.207	-0.1284	0.048

PUBLICATIONS FROM THE THESIS

Papers

1. M. O. Yılmaz and S. Bekiroğlu, "Prediction of Joint Shear Strain–Stress Envelope Through Generalized Regression Neural Networks", Arabian Journal for Science and Engineering, vol. 46, pp. 10819–10833, 2021.

Conference Papers

1. M. O. Yılmaz and S. Bekiroğlu, "Calibration of Coupled Plasticity-Damage Microplane Material Properties with Artificial Neural Networks", Proceedings 1st fib Italy YMG Symposium on Concrete and Concrete Structures, Parma, Italy, Oct. 15., 2019.

2. M. O. Yılmaz, A. T. Demirbağ, and S. Bekiroğlu, "Investigation of Reinforced Concrete Beam-column Joint Behaviour through Numerical Simulations", International Civil Engineering and Architecture Conference, Trabzon, Turkey, April 17-19, 2019.